Sensors and Electronic Instrumentation Advances

Proceedings

of the 9th International Conference on Sensors and Electronic Instrumentation Advances (SEIA' 2023)

20-22 September 2023
Funchal (Madeira Island), Portugal

MADEIRA SEIA'23

MADEIRA SEIA'23

Sensors and Electronic Instrumentation Advances:

Proceedings of the 9th International Conference on Sensors and Electronic Instrumentation Advances

20-22 September 2023
Funchal (Madeira Island), Portugal

Edited by Sergey Y. Yurish

IFSA Publishing

Sergey Y. Yurish, *Editor*
Sensors and Electronic Instrumentation Advances
SEIA' 2023 Conference Proceedings

Copyright © 2023
by International Frequency Sensor Association (IFSA) Publishing, S. L.

E-mail (for orders and customer service enquires): ifsa.books@sensorsportal.com

Visit our Home Page on http://www.sensorsportal.com

All rights reserved. This work may not be translated or copied in whole or in part without the written permission of the publisher (IFSA Publishing, S. L., Barcelona, Spain).

Neither the authors nor International Frequency Sensor Association Publishing accept any responsibility or liability for loss or damage occasioned to any person or property through using the material, instructions, methods or ideas contained herein, or acting or refraining from acting as a result of such use.

The use in this publication of trade names, trademarks, service marks, and similar terms, even if they are not identifies as such, is not to be taken as an expression of opinion as to whether or not they are subject to proprietary rights.

ISBN: 978-84-09-53746-4
BN-20230915-XX
BIC: TJFC

Contents

Foreword

On behalf of the SEIA' 2023 Organizing Committee, we introduce with pleasure these proceedings devoted to contributions from the 9th International Conference on Sensors and Electronic Instrumentation Advances 20223 held in Funchal (Madeira Island), Portugal. The conference is organized by the International Frequency Sensor Association (IFSA) in technical cooperation with *IFSA Publishing, S. L.* (Barcelona, Spain) and media partners MDPI *'Sensors'*, *'Chemosensors'* and *'Biosensors'* and open access journals (Switzerland).

The proceedings contain all papers of both: oral and poster presentations, which were presented at the conference. We hope that these proceedings will give readers an excellent overview of important and diversity topics discussed at the conference.

We thank all authors for submitting their latest work, thus contributing to the excellent technical contents of the Conference. Especially, we would like to thank the individuals and organizations that worked together diligently to make this Conference a success, and to the members of the International Program Committee for the thorough and careful review of the papers. It is important to point out that the great majority of the efforts in organizing the technical program of the Conference came from volunteers.

Prof., Dr. Sergey Y. Yurish,
SEIA' 2023 Conference Chairman

(001)

Fiber Optic Current Sensor Based on 22.5° Faraday Rotator and Polarizing Beam Splitter

A. Madaschi, P. Martelli and P. Boffi
Politecnico di Milano, Policom Lab, DEIB Department, via Ponzio 34/5, 20133 Milan, Italy
E-mail: andrea.madaschi@polimi.it

Summary: In this work a novel implementation of a polarimetric fiber optic current sensor scheme based on a polarizing beam splitter and a 22.5° Faraday rotator will be presented. The developed sensor employs a compact and pigtailed component realized by joining a polarizing beam splitter and a Faraday rotator, it does not require any external adjustment to work and shows very high immunity to external electromagnetic and mechanical interference. The configuration has been experimentally validated using electrical current values up to 580A. The experimental results also prove good sensitivity of the sensor allowing the measurement of small values of current down to 100 mA.

Keywords: Faraday effect, Fiber optic current sensor, Verdet constant, Sensor integration.

1. Introduction

Electrical current measurements, especially in power plants, still today remain a very challenging task. In order to satisfy, in an efficient way, the growing demand of electrical power, all the processes involved from the production to the transport and even often the final usage are getting a shifting up of the voltages, up to hundreds of kV. Classical methods to carry out electrical current measurements are usually based on Current Transformers (CTs). CTs must be not only adequately shielded against electromagnetic interference (EMI), but must also fulfil all the rigorous security standard in terms of insulation, requested in high voltage application. The complexity and the cost of CTs consequently increase exponentially. Fiber-Optic current Sensors (FOSs) could potentially be exploited in several high voltage applications where the electromagnetic immunity is a mandatory requirement [1,2]. Moreover, thanks to the intrinsic dielectric property of the optical fiber, they can guarantee a very high degree of insulation, at no additional cost in term of complexity of the sensor itself and also in term of production cost. Almost all the developed solutions rely on the magneto-optic Faraday effect. The Faraday effect describes the relation between light and magnetic field. The exposure of a magneto-optical medium to a magnetic field induces in it a non-reciprocal circular birefringence directly proportional to its magnitude [3, 4].

2. Sensor Configuration

The proposed sensor takes advantage of a new compact and pigtailed component that encloses a polarizing beam splitter/combiner directly attached to a 22.5° Faraday rotator. This component is employed in the configuration reported in Fig. 1. Its working principle relies on the basic property of the polarizing beam splitter (PBS), which divides the incident light into horizontal (H) and vertical (V) polarization states, transmitting H and reflecting V. In this configuration a low-coherence light source must be used in order to avoid additional noise due to the internal beating between the forward and the backward beams in the component. In addition, the component has been designed to work with unpolarized light as light source, so that it does not require the use of polarization maintaining fiber at its input. It is also self-aligned, hence increases the robustness of the configuration. The beam outgoing from the PBS gets a nonreciprocal rotation of 22.5°, thanks to the Faraday rotator, then it exits from the component by port 3, propagates in the fiber coil and it is reflected back by the Faraday rotator mirror (FRM). The light beam at the entrance of the component from port 3 has accumulated a SOP rotation equals to 112.5° with respect to the SOP of the light at the exit of the PBS. This is a key feature of the setup, because after the back propagation of the light in the 22.5° Faraday rotator the SOP of the light is properly rotated with respect to a PBS transmission axis of an angle α = 45° (that is $\alpha = \pi/4$ in radians), corresponding to the point of maximum sensitivity and linearity of the PBS transfer functions. The SOP of light after the back and forth propagation in the fiber coiled around the electrical conductor gets a polarization rotation by an angle [5]:

$$\vartheta(t) = 2VNi(t),, \qquad (1)$$

where V is the Verdet constant of the fiber, N is the number of spires in the coil and i is the current intensity. The total rotation of the SOP before hitting the PBS in the backwards direction is then $\alpha = \pi/4 + \vartheta(t)$ and the intensities of the beams exiting from the component are respectively:

$$I_1 = I_0 cos^2\left(\pi/4 + \vartheta(t)\right)$$
$$I_2 = I_0 sin^2\left(\pi/4 + \vartheta(t)\right)$$

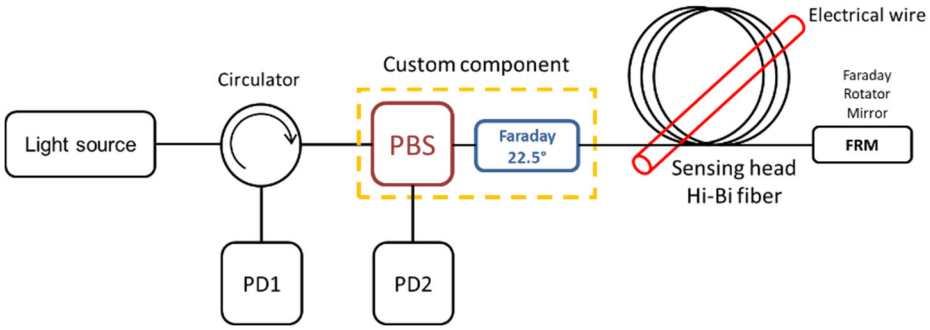

Fig. 1. Scheme of the polarimetric fiber optic current sensor.

The detection of both components of the light allows to obtain a signal fully independent from fluctuations of the optical power of the source and variation of the losses in the circuit. Calculating the ratio between the difference and the sum of the intensities of the two output components and applying the approximation for small value of ϑ, it is possible to obtain:

$$S_1 = \frac{I_1 - I_2}{I_1 + I_2} \approx \vartheta(t) \qquad (3)$$

The SOP of the light for detecting the electrical current in an efficient manner must remain as linear as possible during the propagation in the sensing coil. Residual and bending-induced linear birefringence tends to alter the SOP of the light in the coil. One of the most effective solutions for limiting the detrimental impact of birefringence is the use of a spun high birefringence (Hi-Bi) fiber [6]. Hi-Bi fibers, thanks to their particular spinning process, are able to preserve the entrance SOP of the light in the coil in absence of the magnetic field.

3. Experimental Results

The unpolarized and low-coherence light source employed in the experimental tests is the amplified spontaneous emission of an Erbium doped fiber amplifier at wavelength of 1550 nm. The sensing head consists in a coil of Hi-Bi fiber of 19 turns with 10 cm of diameter. The beams outgoing from port 1 and 2 of the component have been detected by two identical photodiodes, then the two signals were acquired and sampled by a National Instrument DAQ board and finally post-processed. The electrical current signal to be measured, flowing in a wire surrounded by the fiber coil, has been generated at the frequency of 50 Hz by a programmable AC power source. The electrical current is also monitored by a current clamp that generates a voltage proportional to the peak amplitude. A set of measurements have been carried out, aiming to evaluate the performance of the sensor for a current intensity, up to 580 A. In Fig. 2a are reported the measurements obtained by the clamp and the measurements obtained by the FOS, where the 50 Hz tone amplitude of the Fourier transform of the post-processed signals obtained by Eq. 3 is scaled to the current clamp values. The best model found that fits the FOS and the clamp values is the linear model. Fig. 2b shows the linear fitting curve and the corresponding experimental data, each point is the average of the value corresponding to a current step.

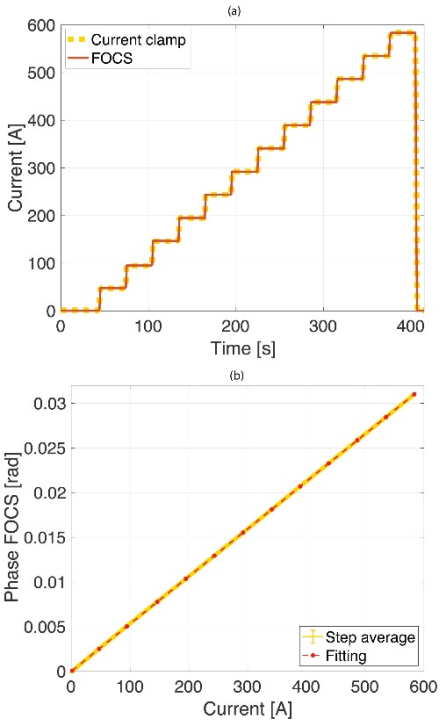

Fig. 2 (a) Electrical current measurement results by using the FOS and current clamp, (b) fitting curve between FOS and clamp measurements.

Another set of measurements have been carried out with the object to evaluate the goodness of the configuration for low values of current intensity. In this second set, the range of electrical current analyzed is between 0 and 3 A with a granularity of 300 mA.

In Fig. 3(a) has been summed up the measurements obtained by the FOS and they are compared with the values measured by the current clamp.

The standard deviation of the small noise fluctuations calculated by averaging the deviations obtained for all the steps is 0.034 A, leading to an accuracy of the sensor equal to about 0.1 A.

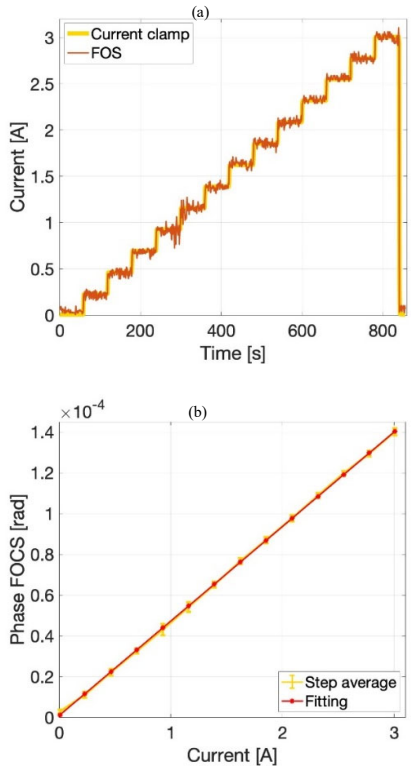

Fig. 3 (a) Fiber optic sensor (FOS) measurement in range 0-3 A scaled to the corresponding value measured by current clamp, (b) Fitting curve between FOS and current clamp measurements.

As in the previous set of measurements the values of the FOS are fitted to the electrical clamp values as reported in Fig. 3b. Even in this case the response of the configuration is perfectly linear.

4. Conclusions

In this work a novel configuration of a polarimetric FOS, with excellent performance for a wide range of electrical current values, has been presented. The proposed solution does not require components sensitive to the polarization, it is self-stabilized and the measurements are independent from the light source intensity. The experimental results have confirmed the linear response of the FOS to the electrical current, as expected from the theory. It has been also proven that, the it can measure small electrical current values, down to 100 mA.

Reference

[1]. Bohnert, Optical fiber sensors for the electric power industry, *Optics and Lasers in Engineering*, Vol. 43, 3-5, 2005, pp. 511–526.

[2]. Farnoosh Rahmatian, Abraham Ortega, Applications of Optical Current and Voltage Sensors in High-Voltage Systems, in *Proceedings of the IEEE/PES Transmission & Distribution Conference and Exposition: Latin America,* 2006, pp. 1-4.

[3]. A. Papp and H. Harms, Magnetooptical current transformer. 1: Principles, *Applied Optics*, Vol. 19, 22, 1980, pp. 3729–3734.

[4]. K. Bohnert, Fiber-Optic Current Sensor for Electrowinning of Metals, *Journal of Lightwave Technology*, Vol. 25, No. 11, 2007, pp. 3602-3609.

[5]. Yuefeng Qi et al., Novel Fiber Optic Current Transformer with New Phase Modulation Method, *Photonic Sensors*, Vol. 10, 2020, 275–282.

[6]. R. I. Laming et al., Electric current sensors employing spun highly birefringent optical fibers, *Journal of Lightwave Technology*, Vol. 7, 1989, pp. 2084–2094.

(005)

Detection of Trafficable Areas in Outdoors with a Downward Looking 2D LiDAR

A. Olivas and F. Torres
University of Alicante, Group of Automation, Robotics and Computer Vision, 03690, Alicante, Spain
E-mail: alejandro.olivas@ua.es, fernando.torres@ua.es

Abstract: Detecting and evading obstacles are essential components of mobile robots. In this paper, we use only a 2D Light Detection and Ranging (LiDAR) sensor to detect the trafficable areas in the terrain, analysing it. Therefore, the sensor was placed downward looking to detect obstacles with different heights and also potholes. Firstly, the detected points are segmented into lines, and a 3D map is generated with them. For classifying them into the ground, obstacles or potholes, different trajectories of the vehicle are generated, and depending on the height of the lines, the lines are classified. This process is done dynamically while the robot is moving for two reasons. The first one is to update the trafficable areas when there are dynamic obstacles. The second is to analyse the height variation during the trajectory to classify correctly sloping terrains. The experiments in simulated environments show that our method classifies successfully the areas.

Keywords: Mobile robots, LiDAR, Downward looking, Low-cost.

1. Introduction

The perception of the environment is a fundamental part of robotics. Robots can adapt to changes and be autonomous because they can detect and perceive these changes. This part is more important when the robot is in an unstructured environment because it has to detect unknowing objects.

Cameras have been used to perceive the environment and detect obstacles. Nowadays, there are many methods that use deep learning to detect obstacles. The obstacles can be classified using a convolutional trained neural network, so it can be identified the cars, pedestrians and other obstacles [1]. Other methods deal with obstacle detection in driving environments using unsupervised learning algorithms [2].

LiDARs are the other main type of sensor used to detect obstacles. Using the 2D LiDARs horizontally is the more common way to use them in mobile robots. They are used to generate 2D maps of the environment and to locate the robot by comparing the measures with the map. The occupancy grid maps [3] discretize the space in cells, which have a value that determines the probability of the cell being occupied. The state of each cell is estimated using a binary Bayes filter. This is an efficient algorithm for mapping assuming that the pose is known, and it is also robust against dynamic objects. Using the sensor in this way, it can only detect obstacles with the same height as the sensor or higher.

The 2D LiDARs can be placed downward looking, with the advantage to detect obstacles of lower height as well as potholes. Han *et al.* [3] present a method to divide the scanned points into segments searching consecutive points with a difference in height greater that a given threshold. From this division, obstacles can be detected. Pang *et al.* [4] extend this type of methods for sloping roads by calculating the height and the vector of the road surface, so it can effectively handle the changes in the road condition. Detecting the changes in the height of the road allows the correct identification the road surface on ramps and other passable slopes.

In our previous work [6], a 3D map of lines was made with a downward LiDAR and the lines were classified using their height. This classification works in structured indoor environments. However, the classification fails in terrains with slopes, and the method has problems detecting dynamic obstacles, that were saved in the 3D map, but they could not be reconsidered in future scans. In this paper, we present a classification that works also in unstructured outdoor environments and also a map that can handle dynamic objects.

2. Approach

In this research, the 2D LiDAR sensor is placed downward looking with some inclination since the objective is to detect obstacles or potholes in the ground. The data are represented in a 3D map where the origin of coordinates of the global axis is in the ground, just below the sensor at the start of the sensor. To obtain the points in the global coordinate system, the robot's position is needed. The problem of localization is considered resolved. In the used mobile robot, the localization was determined with the fusion of odometry and GPS.

The localization of the robot used in this research only returns three values: the position of the robot in x and y, and the direction of the robot θ. It was needed to approximate the value of z, which will be called height henceforth, to make a 3D map and classify the environment correctly. The nearest ground line to the actual position of the robot is used to estimate it as the mean between the previous height and the line's height. With this approximation instead of using

directly the line's height, the height is smoothed and there is less error in the estimation. However, there is still an accumulative error. This can cause problems when the robot navigates through explored areas. To solve this, the 3D map, which contains the detected lines, has a limited number of lines.

2.1. Line Detection

The point cloud detected in one measurement of the LiDAR will be segmented into lines, which will be used to determine what areas are trafficable. A point p_i belongs to a line if it satisfies two constraints:

$$|p_i^z - p_0^z| \leq \delta \quad (1)$$

$$\|p_i - p_{i-1}\| \leq d \quad (2)$$

The constraint (1) means that the point has to be in a threshold δ around the Z axis of the first point of the line. This is done because big changes in this axis mean the existence of an obstacle or pothole. The constraint (2) considers the distance between two consecutive points, because a big gap between them means that there is no information of that zone. The segmented lines with fewer points than n are removed to filter the number of little lines.

Then, the lines are refined because there are a lot of lines that were segmented because of the height difference with the first point. This happens for example in lateral walls. If the normalized vector from the first point to the last point of a line is equal to the normalized vector of the next line and to the vector from the first point of the first line to the last point of the second line, both lines are grouped into one line because they belong to the same straight. In Fig. 1, the result of the refinement can be observed. In this refinement, a slight error γ is allowed. The detected lines are added to the 3D map. As this map has a limited number of lines, the oldest lines are erased. Besides, before adding a new line, its nearest line is searched and if it is close enough, the old one is erased because they are considered the same line. Therefore, the map does not save the same line more than once.

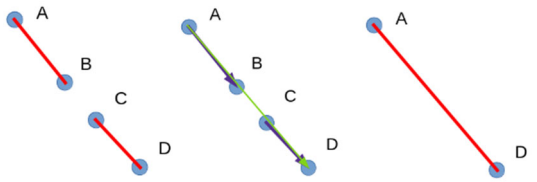

Fig. 1. Since the normalized vectors are sufficiently similar, the two lines have been joined into one.

2.1. Line Classification

The lines are classified dynamically while the robot is moving, determining where the robot can go and where not. For doing this, firstly some possible trajectories are generated to analyse if there are obstacles or potholes. In this research, it is used a mobile robot with Ackermann geometry, so the generated trajectories fit this type of vehicle. For each point of the trajectory, the lines of the map are analysed, determining the distance from the point to a line by resolving the equation (3).

$$\vec{p} + \alpha \cdot \vec{n} = \vec{f} + \beta \cdot \vec{v}\,, \quad (3)$$

where $\vec{p}$ is the point of the trajectory, $\vec{n}$ is the normalized vector obtained from the trajectory's direction, $\vec{f}$ is the first point of the line, $\vec{v}$ is the vector from the first point to the last one of the line, and α and β are the variables. The value of α is the distance between the line and the robot, and if β is between 0 and 1, it crosses the line. If vectors $\vec{n}$ and $\vec{v}$ are almost parallel, the normal vector of $\vec{n}$ is used to get a more realistic distance.

Using the value of β it can be obtained the height of the line in that part. If the height is in a threshold ζ around the height of the robot, the line is considered ground, otherwise an obstacle or pothole. The ground lines are taken into account only if β is between 0 and 1. However, the obstacle lines are lengthened by a distance equal to the width of the robot, so the value of β is between $-a$ and $1 + a$, which depends on the magnitude of $\vec{v}$.

The terrain may have slopes, so the z position is updated during the trajectory using the height of the nearest ground line, estimating the slope of the trajectory and analysing correctly the lines.

A 2D occupancy map is constructed using the classified lines. One region is considered untrafficable if there is an obstacle, but also if there are not enough ground lines, as in this case there may be a pothole. With this map, the robot can navigate avoiding obstacles and potholes and through environments with slopes like ramps. As it is updated while navigating, the dynamic obstacles are taken into account.

3. Experiments

The method was tested on a simulator, Gazebo, in environments with ramps and obstacles. Firstly, the parameters of the line segmentation and classification were tuned manually, and they are shown in Table 1. For the occupancy map, we set a resolution of 0.5 m, which means that the area of each cell is 0.5 m^2. This resolution was set considering the size of our robot, which is 1.08 m long and 1 m wide, and after checking that a smaller resolution did not improve notably the method despite of the increase in memory use. The maximum number of lines in the 3D map was configured as 200.

Firstly, we test our method in a ramp with an inclination of 10º and a pothole, shown in Fig. 2. The map generated after exploring it is shown in Fig. 3. The limits of the ramp are detected correctly except in a region at the top left of the image because the robot did not go near enough there to detect that it is untrafficable. The pothole is also detected correctly, and there are untrafficable cells near it because when

the robot is turning, the sensor has blind spots inside the radius of curvature.

Table 1. Parameters for line segmentation and classification.

Parameters	Description	Value
δ	Threshold in the Z axis to consider a point in a line.	0.05
d	Maximum distance between two consecutive points of line.	0.2
n	Minimum number of points in a line.	10
γ	Maximum allowed difference during the line refinement.	0.11
ζ	Threshold in the Z axis around the height to consider a line as ground.	0.2

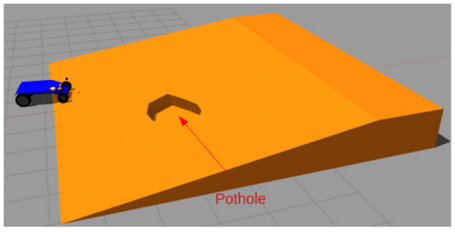

Fig. 2. Simulated sloping ground in Gazebo.

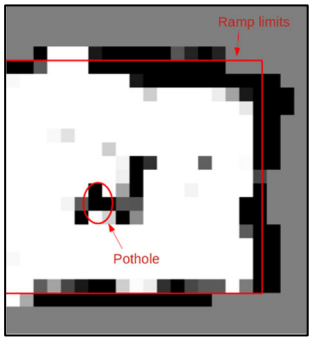

Fig. 3. Occupancy map of the ramp. White cells are trafficable, black are not and grey are unexplored.

Then, it has been tested in an environment with a dynamic obstacle, a pedestrian who is walking. Fig. 4 shows this simulation and the pedestrian path. The occupancy maps of two different moments are shown in Fig. 5, showing that our method can handle dynamic objects as it updates the map when the robot goes through an explored area.

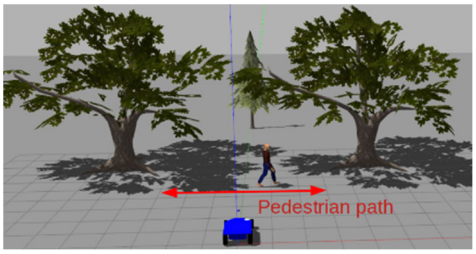

Fig. 4. Simulation of a dynamic object (pedestrian).

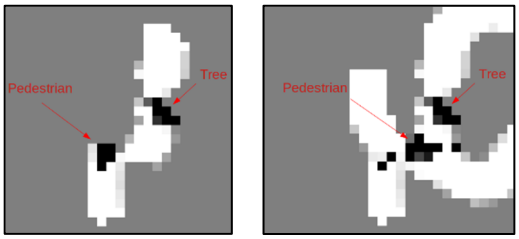

Fig. 5. Occupancy maps in two different moments. The pedestrian has another position and some cells of the previous position have been classified as trafficable.

4. Conclusions and Future Work

In this paper, we present a novel method to classify the environment in trafficable and untrafficable areas. It detects both obstacles and potholes in unstructured environments and the method is robust to the slopes in the terrain. This presents an advantage against past methods that have problems with sloping roads, don't take potholes into account or use more expensive sensors. The method is also robust against dynamic obstacles because it reconsiders the occupancy map when the robot navigates through explored areas.

This approach uses a 2D LiDAR and other sensors for the localization of the robot, such as encoders and GPS. However, the robot has no information for moving backwards, which is necessary for safety reasons. Nevertheless, adding such a sensor will continue to be more economic than using a 3D LiDAR sensor.

In future works, we have to test the method in the real robot to analyse the noise in the perception and localization, and how it impacts to our approach.

References

[1]. A. Dairi et al, Unsupervised obstacle detection in driving environments using deep-learning-based stereovision, *Robotics and Autonomous Systems*, Vol. 100, 2018, pp. 287-301.

[2]. G. Prabhakar et al, Obstacle detection and classification using deep learning for tracking in high-speed autonomous driving, in *Proceedings of the 2017 IEEE region 10 symposium (TENSYMP)*, 2017, pp. 1-6.

[3]. H. Moravec and A. E. Elfes, High resolution maps from wide angle sonar, in *Proceedings of the IEEE International Conference on Robotics and Automation,* 1985, pp. 116 - 121.

[4]. J. Han et al, Enhanced road boundary and obstacle detection using a downward-looking LIDAR sensor, *IEEE Transactions on Vehicular Technology*, Vol. 61, 2012, pp. 971-985.

[5]. C. Pang et al, Adaptive Obstacle Detection for Mobile Robots in Urban Environments Using Downward-Looking 2D LiDAR, *Sensors*, Vol. 18, 6, 2018, 1749.

[6]. A. Olivas González and F. Torres Medina, Detection and Classification of Obstacles Using a 2D LiDAR Sensor, in *Proceedings of the 5th International Conference on Advances in Sensors, Actuators, Metering and Sensing (ALLSENSORS' 2020)*, 2020, pp. 63-69.

(006)

Hardware Acceleration of Pulse Analysis using FPGAs in MicroTCA

C. Gonzalez [1], M. Ruiz [1], A. Carpeño [1], A. Pinas [1], D. Cano-Ott [2], J. Plaza [2], T. Martinez [2] and D. Villamarin [2]

[1] Universidad Politécnica de Madrid, Grupo de Instrumentación y Acústica Aplicada, Spain
[2] Ciemat, Spain
Tel.: +34 91 0678950, fax: +34 91 0678950
E-mail: c.gonzalezb@alumnos.upm.es

Summary: Real-time signal processing in large-scale scientific experiments requires specialized hardware with high computational capacity and speed. This paper describes the implementation of a digital pulse shape analysis (DPSA) system on an FPGA. The signals are acquired at 1 GS/s from a BC501A liquid scintillator. The algorithm consists of an FIR filter and a constant fraction discriminator (CFD) function to detect the pulses and estimate the time stamp at which each pulse occurs, a peak detection function to determine the number of pulses per signal and pileups, and finally, an energy calculation function to estimate the pulse energy. The proposed hardware architecture uses the JESD204B specification for high-speed ADCs on a XILINX FPGA device. The practical implementation is done with a MicroTCA system, including a NAMC-ZYNQ-FMC board with a Xilinx ZYNQ Ultrascale-MP SoC. The JESD204B physical and data link layers have been developed in Hardware Description Language (HDL), while the Xilinx High-Level Synthesis Language (HLS) has been used for the transport and application layers and processing blocks. This architecture achieves an analysis time of 53us per signal with an FPGA resource utilization of about 50 %.

Keywords: DPSA, JESD204B, HLS, Hardware acceleration.

1. Introduction

In particle physics and radiation detection, BC501A liquid scintillators are widely used as detectors to measure the energy and characteristics of particles and radiation sources [1] [2]. By harnessing the power of field-programmable gate arrays (FPGAs) and the hardware process acceleration techniques, digital pulse shape analysis (DPSA) [3] can be performed with reduced latencies, potentially enabling real-time application. However, the feasibility of realtime analysis is highly dependent on the available FPGA resources and the complexity of the algorithm used.

This paper proposes a hardware implementation for DPSA of signals from a BC501A liquid scintillator digitized at a rate of 1GS/s and 14-bit resolution as a real-time analysis system.

The proposed solution is based on a Micro Telecommunications Computing Architecture (MicroTCA) chassis [4] that provides physical, mechanical, electrical and thermal support for a NAMC-ZYNQ-FMC Advanced Mezzanine Card (AMC) [5]. NAMC-ZYNQ-FMC is a SoC-based AMC whose main component is a Xilinx ZYNQ Ultrascale+MP SoC [6]. In the SoC programming logic (PL) area, the JESD204B standard [7] is implemented to interface the digitizer and the DPSA application.

The JESD204 specification defines a serial interface that connects high-speed converters to logic devices such as FPGAs and ASICs. Analog Devices provides an open-source IP interface framework distributed under the GPL2 license to implement the JESD204 interface and the software to configure all the hardware elements [8]. The letter B in JESD204B refers to the second revision of the standard. The distribution of the hardware elements, operating system and DPSA application is shown in Fig. 1.

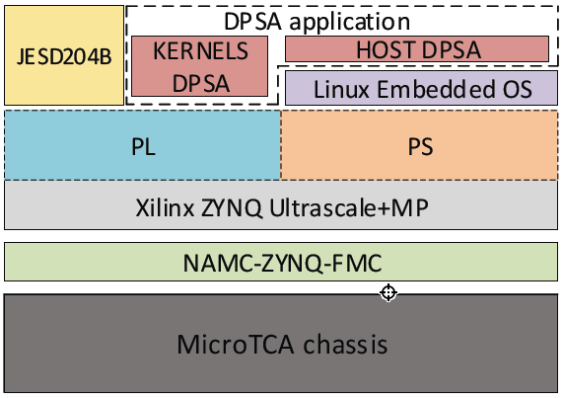

Fig. 1. Hardware elements, OS and DPSA application stack.

As described by Guerrero et al. in [3], the goal of the DPSA is to extract the parameters of physical relevance. In the case of the BC501A detector, the parameters are the time, amplitude, integrals over various time intervals, and the type of the incident particle. The DPSA application layer, located at the top of the stack, fulfills this objective. Within the Processing System (PS) of the Xilinx ZYNQ Ultrascale+MP SoC, a Linux Embedded System enables the execution of the DPSA application, which coordinates the execution of the kernels and reads the analysis results. The SoC PL area contains the hardware functions (kernels) that perform the signal analysis and achieve the goal of the DPSA.

2. Methodology

2.1. JESD204B Implementation

The JESD204B specification defines four layers based on functionality (Harris and Fan provide details in [9] and [10], respectively). The JESD204B implementation on the Xilinx Ultrascale+ MPSoC consists of the FPGA design implemented in the PL using Hardware Description Language (HDL) for the physical and data link layers and High-Level Synthesis (HLS) for the transport and application layers. An embedded Linux distribution running on the PS is used to configure the peripherals implemented in the PL and support the host software.

The solution avoids the use of a physical ADC to implement and validate a processing algorithm in the FPGA. A JESD204B interface emulates a DAC that generates 1GS/s and 14-bit resolution signals. The output of this interface is connected to another JESD204B interface that emulates the ADC (the JESD204B of the DAC is connected to the JESD204B of the ADC with an external loopback). The signals reproduced by the emulated DAC are stored in a file in the host system (coming from real captures of the experiment). These signals are sent from the host to the global memory accessible by the FPGA PL. Fig. 2 shows the DAC and ADC interfaces of the JESD204B connected by an external loopback, the implemented kernels on the PL, and the interactions of the PS and PL with the global memory.

The PL clock speed is 200MHz, while the acquisition rate is 1 Gs/s. This means that 5 samples are acquired per system clock cycle. To solve this problem, the JESD204B is implemented to send a line link 128-bit data frame per cycle to the DPSA. The data frame is coupled by the transport application layer of the JESD204B (RX kernel) so that the DPSA receives a constant sample stream per clock cycle. Fig. 3 shows the data stream that couples the difference between the data acquisition and processing clocks.

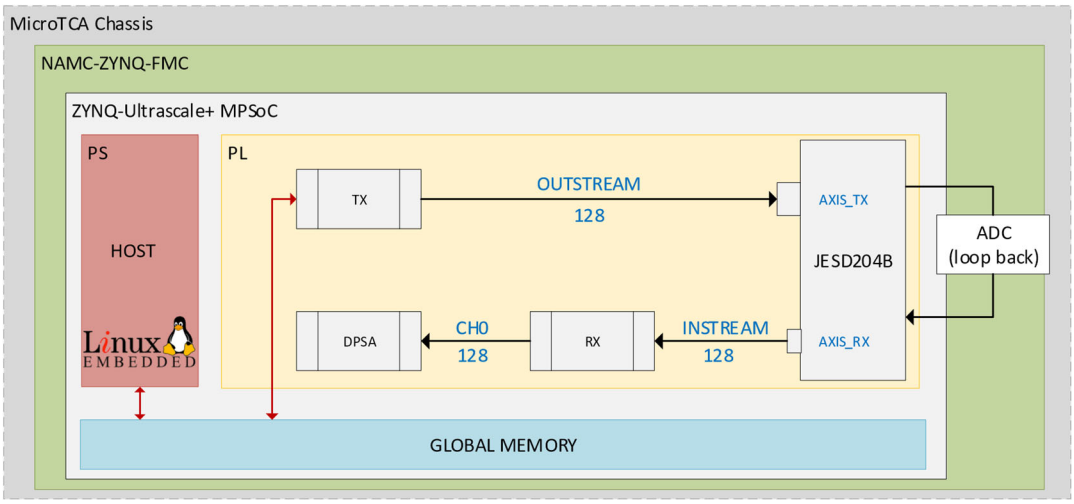

Fig. 2. ZYNQ-Ultrascale+ implementation. The PL implements the DPSA using the streaming data read with the JESD204B interface. An external loopback connects the signal generation with the data acquisition.

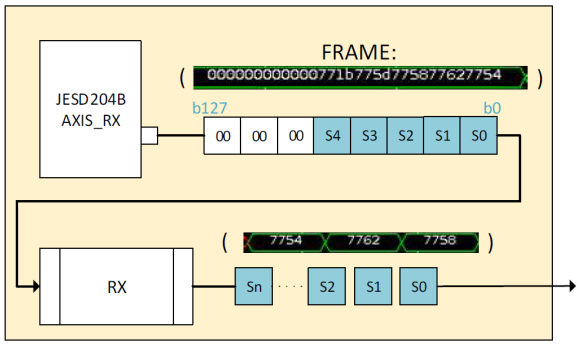

Fig. 3. Stream from 1 Gs/s ADC to 200MHz PL.

2.2. DPSA Application

To achieve the goal described by Guerro et al. in [3], a kernel called DPSA with three main functions is implemented in the FPGA in the PL area of the Xilinx Ultrascale+ MPSoC using HLS. These functions are designed to work with the pipeline technique.

In the first function (Compute RC & CFD process in Fig. 5), the signals are low-pass filtered by a 20tap FIR filter. This significantly increases the latency (it is necessary to perform 20 operations per sample), so the filter is not applied to the whole signal, but an area of interest that is found before filtering. The area of interest is threshold detected and starts n samples before the threshold is triggered (starting point). The filter parameters and the n value are set in the hardware configuration. If no other pulse is detected, the end point of the signal of interest is equal to the starting point plus a pre-set time interval to detect the energy. If another pulse is detected, the filter is applied to the entire signal from the starting point.

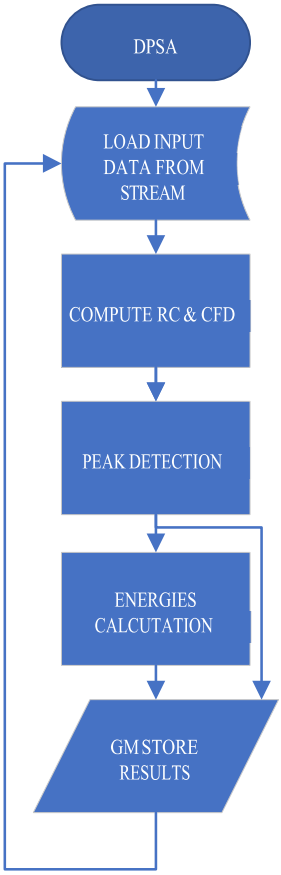

Fig. 4. DPSA application flowchart.

A Constant Factor of Discrimination (CFD) [11] is applied simultaneously as the FIR filter and only in the interest region of the signals. Thus, at the end of this function, a filtered signal and a CFD signal are streamed to the next function.

The second function detects the exact point where the peak occurs (Peak detection process in Fig. 5). This is the point where the filtered signal crosses the threshold and the CFD signal crosses the baseline. For the system to be considered reliable, it is necessary to interpolate to obtain the exact point where the CFD signal crosses the baseline. This point is the time at which the pulse occurs and must be stored as one of the results of the analysis. The function also determines the number of peaks per signal and whether there are pileups.

Finally, in a third function, the filtered signal is integrated over several time intervals and an array of energies is obtained (Energies Calculation process in Fig. 5).

In the PS area of the Xilinx Ultrascale+ MPSoC, the host software is implemented in C++, crosscompiled for an ARM architecture, and runs on an embedded Linux deployed with Petalinux. The functions of the host software are to: read signals from a file and write them to a buffer that the PL can access; coordinate the execution of application layer functions (kernels) on the PL; and finally, read the results stored by the kernels in global memory (GM).

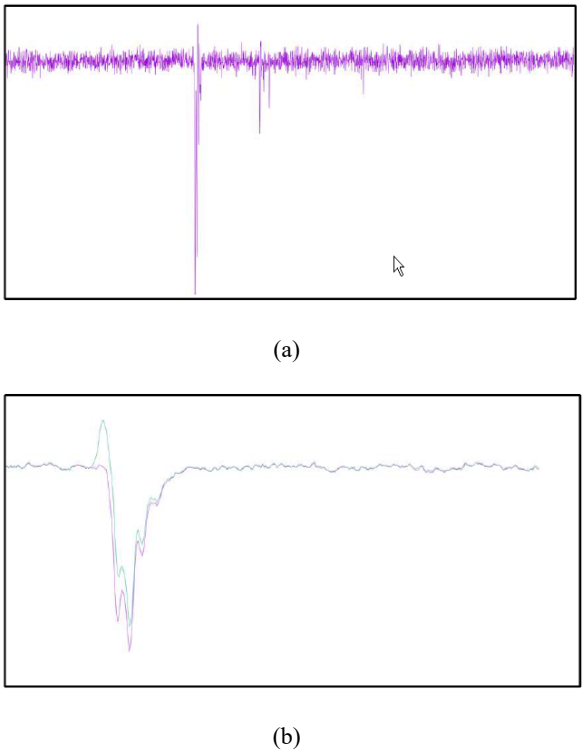

(a)

(b)

Fig. 4. A. Input signal and B. Filtered signal (purple) and CFD signal (light green).

2.3. Results Analysis

In order to determine the reliability and to obtain the performance characteristics of the system, an 8Gb database of signals was analyzed, showing similar results to an analysis implemented in C++, which is the starting point of this project. This is discussed in more detail in the Discussion section.

The analysis of execution times and FPGA resources used was performed with VIVADO tools.

3. Results

The result is a high-performance DPSA system that can be connected directly to a 1Gs/s via its JESD204B interface. Fig. 6 shows two screenshots taken from VIVADO analysis tool. Fig. 6 A. shows the percentage of FPGA resource utilization of the application layer and Fig. 6 B. the execution time of 53.476 us for analyzing a signal.

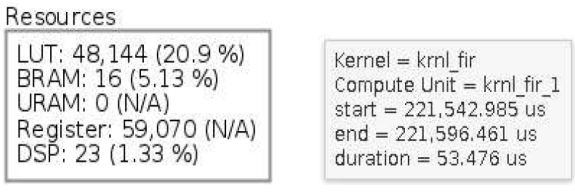

Fig. 6. A. Percentage of FPGA resource utilization. B. Application layer execution time.

In this paper, an MTCA-based high-speed data acquisition and processing system, including an AMC with an FPGA implementing a JESD204B interface, has been implemented. The pulse analysis application of a scintillator has been developed using hardware acceleration techniques based on HLS. The results show the feasibility of introducing this hardware implementation in data acquisition systems to obtain real-time results under certain experimental conditions. It is important to note that the baseline calculation is not implemented yet and will be added in a future revision. In order to compare the original DPSA implemented in C++ with this new implementation, the baseline used is the one available in the dataset obtained from real experiments with an AD14 digitizer (this DAQ device includes a specific firmware providing the baseline).

5. Conclusions

A high-performance embedded system to meet the DSPA goals has been implemented on a Xilinx ZYNQ Ultrascales+MP SoC supported by a MicroTCA architecture. As shown in Fig. 6, a typical analysis time is about 53us and the FPGA resources utilization of about 50 %.

Using the JESD204B interface to emulate the behavior of signal generation and data acquisition in conditions similar to the real experiment allows faster algorithm validation. The results in terms of execution time and latency allow us to explore the feasibility of integrating the solution on real experimental platforms, using tools that allow us to adapt the firmware of the acquisition devices.

The DPSA application is developed in HLS, which significantly reduces the development time.

References

[1]. Jianguo Quin, Caifeng Lai, Bangjiao Ye, Rong Liu, Xinwei Zhang, Li Jiang. Characterizations of BC501A and BC537 liquid scintillator detector, *Applied Radiation and Isotopes,* Vol. 104, 2015, pp. 15-24.

[2]. F. Arneodo, P. Benetti, A. Bettini, et al., Calibration of BC501A liquid scintillator cells with monochromatic neutron beams, *Nuclear Instruments and Methods in Physics Research Section A: Accelerators, Spectrometers, Detectors and Associated Equipment,* Vol. 418, Issues 2-3, 1998, pp. 285-299.

[3]. C. Guerrero, D. Canno-Ott, M. Fernández-Ordoñez, E. González-Romero, T. Martínez, D. Villamarín. Analysis of the BC501A neutron detector signals using the true pulse shape, *Nuclear Instruments and Methods in Physics Research Section A: Accelerators, Spectrometers, Detectors and Associated Equipment,* Vol. 597, Issues 2-3, 2008, pp. 212- 218.

[4]. Micro Telecommunications Computing Architecture Short Form Specification, *PICMG,* 2006.

[5]. NAT, NAT_AMC_ZYNQ_FMC Technical Reference Manual.

[6]. Xilinx, ZYNQ Ultrascale+ MPSoC, [Online], https://www.xilinx.com/products/silicondevices/ soc/zynq-ultrascalempsoc.html, Accessed 31 May 2023.

[7]. J. Harris, What is JESD204 and Why Should We Pay Attention to It, *Analog Devices*, 2019.

[8]. JESD204 Interface Framework (https://www.analog.com/en/designcenter/ evaluation-hardware-and-software/jesd204- interface-framework.html)

[9]. J. Harris, Understanding layers in the JESD204B specification: A high speed ADC perspective, *Analog Devices*, 2017.

[10]. H. Fan, Quickly Implement JESD204B on a Xilinx FPGA, *Analog Dialogue,* 49-02, 2015.

[11]. M. Beuzekom, Identifying fast hadrons with silicon detectors, Thesis, *University of Groningen*, 2006.

(007)

Advanced Polymer Materials for Real-time Sensing of Inflammation and Infection

M. Hrubý, H. Zhukouskaya and E. Tomšík
Institute of Macromolecular Chemistry CAS, Heyrovsky Sq. 2, 162 06 Prague 6, Czech Republic
Tel.: + 420 608 559 641 (mobile), +420 296 809 130 (office) fax: +420 296 809 410
E-mail: mhruby@centrum.cz

Summary: We describe new polymeric materials for use in an electrochemical multisensor, which will provide a potentiometric response upon contact with selected analytes, such as pH changes, presence of reactive oxygen species, free iron ions, etc., selectively detecting and distinguishing multiple biomarkers of bacterial and sterile pathologies in real time. The sensor electrodes also include a non-biofouling layer to minimize interferences. The target application of the new materials is the integrated potentiometric biosensor for early indication of the presence and the type of inflammation. They are to be used in devices for *in vitro* sensing of inflammation-related analytes in body fluids, such as synovial liquid, directly on-site in the operating room during the surgery. Alternatively, electrodes in such a sensor might be miniaturized and integrated into an implant with a wireless data transfer device with an external readout to allow *in situ* sensing without the necessity of invasive intervention.

Keywords: Polymer, Biosensor, Electrode, PEDOT, Polyoxazoline.

1. Introduction

Orthopedic surgery of the total hip and total knee arthroplasty are surgeries with the primary purpose of restoring joint function of persons affected by osteoarthritis. The growing life expectancy of the human population also increases the number of patients in need of such surgery, which can significantly improve one's quality of life. Unfortunately, orthopedic implants are highly susceptible to peri-implant sterile inflammation or microbial infections (prosthetic joint infections, PJI).

These complications, which manifest as pain, erythema, swelling and discharge from the wound site, require long hospitalizations and can lead to osteomyelitis, implant failure, sepsis, multiorgan dysfunction, amputation or even death.

Early detection of sterile/bacterial inflammation and its type is of key importance for successful therapeutic intervention. We describe new polymeric materials for use in an electrochemical biosensor simultaneously continuously measuring multiple inflammation/infection biomarkers. It will provide a set of potentiometric responses upon contact with selected analytes, such as pH changes, presence of reactive oxygen species, free iron ions etc. selectively detecting and distinguishing these biomarkers of bacterial and sterile infection in real time.

Such multisensor to be used in devices for *in vitro* sensing of inflammation-related analytes in body fluids, such as synovial liquid, directly on-site in the operating room during the surgery. Alternatively, electrodes in such a sensor might be miniaturized and directly integrated into an implant with a wireless data transfer device with an external readout to allow *in situ* sensing without the necessity of invasive intervention.

2. Results and Discussion

2.1. The pH-Responsive Sensoric Layer

The pH significantly decreases in the inflamed microenvironment and especially in the presence of bacteria that additionally lower the pH value by their metabolism [1].

Highly hydrophobic pH-sensing perfluorinated polyaniline thin films with a water contact angle of ca. 140° and low internal resistance properties were prepared through electrochemical polymerization. [2] Simultaneous possession of the water-repelling property and electron conductivity for superhydrophobic perfluorinated polyaniline leads to a unique polymer that is suitable as a solid contact in ion-selective electrodes for *in situ* monitoring of pH changes during early stages of inflammation and septic shock. The superhydrophobic properties should suppress interactions with interfering salts and proteins, and the sensitivity towards protons could be monitored by measuring the phase boundary potential, which depends on the H^+ concentration. The potentiometric measurements demonstrate a fast response with a slope of 44.4 ± 0.2 mV per unit pH. The presence of interfering ions and/or human serum albumin does not have any significant effect on the performance of the perfluorinated film. Moreover, it is demonstrated that the response of the perfluorinated film is reversible within the biomedically relevant pH range from 4.0 to 8.5, and stable over time.

2.2. The Reactive Oxygen Species – Responsive Sensoric Layer

Pathologically high concentrations of reactive oxygen species (ROS) in inflamed areas and in their vicinity are the key biomarkers of inflammation. Among the ROS, hydrogen peroxide (H_2O_2) is an eminent example. Its physiological concentrations in biological systems range from 1 to several hundred nM, whereas concentrations exceeding this range are associated with cell damage. Typical concentrations of H_2O_2 in an inflamed tissue are orders of magnitude higher.

We built a robust selective potentiometric sensor of reactive oxygen species (ROS) (Fig. 1) [3].

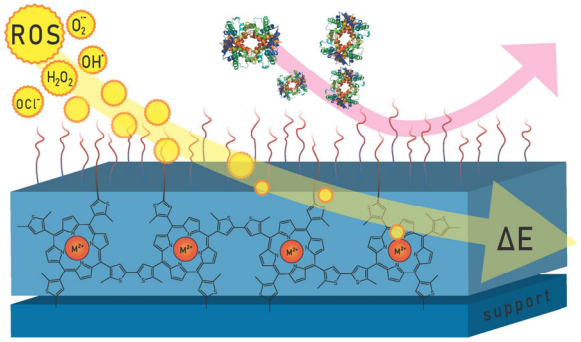

Fig. 1. Scheme of the ROS-sensing layer [3].

The sensor consists of a conductive polymer layer based on polythiophene with an incorporated porphyrin-metal complex that potentiometrically detects the presence of ROS. This sensor is covalently coated with a nonbiofouling layer of poly(2-methyl-2-oxazoline), which works as a biocompatibilizer but mainly prevents the sorption of proteins and other biomacromolecules naturally occurring in organisms, which could interfere with the ROS signal. We have shown that our potentiometric sensor shows a rapid response to hydrogen peroxide, does not experience interference with bovine serum albumin as a model serum protein when sensing ROS, is able to fully reversibly detect ROS with a linear response within a very wide range of biologically relevant concentrations and, most importantly, is able to distinguish between hydrogen peroxide and hypochlorite. We also performed a head-to-head comparison of two positional isomers of thienylated porphyrine for sensor applications and four different coordinated metals (Cu, Fe, Co and Mn, with Cu and especially Fe shown to be the most appropriate).

2.3. The Free Iron – Responsive Sensoric Layer

Very often the availability of iron is the limiting step of pathogenic bacterial infections. To suppress bacterial growth, organism actively strongly locally depletes free iron availability when an infection occurs.

We constructed a sensor for the determination of Fe^{2+} and/or Fe^{3+} ions [4] that consists of a polyaniline layer as an ion-to-electron transducer; on top of it, chelating molecules are deposited (which can selectively chelate specific ions) and protected with a non-biofouling poly(2-methyl-2-oxazoline)s layer. We have shown that our potentiometric sensing layers show a rapid response to the presence of Fe^{2+} or Fe^{3+} ions, do not experience interference with other ions (such as Cu^{2+}), and work in a biological environment in the presence of bovine serum albumin (as a model serum protein). The sensing layers detect free iron ions in the concentration range from 5 nM to 50 μM.

4. Conclusions

Our general "big picture" concept of the PJI detection is based on several (finally miniaturized) sensors and the presented partial sensors enable implementation of it into such a multisensor with a shared reference electrode. More detailed information can be found in the cited references [1-4].

Acknowledgements

The authors acknowledge financial support from the Czech Health Research Council (grant # NU20–06–00424) and from Czech Science Foundation (M.H., grant # 21–01090S).

References

[1]. E. Tomsik, K. Gunar, T. Krunclova, I. Ivanko, J. Trousil, J. Fojt, V. Hybasek, M. Daniel, J. Sepitka, T. Judl, D. Jahoda, M. Development of Smart Sensing Film with Nonbiofouling Properties for Potentiometric Detection of Local pH Changes Caused by Bacterial and Yeast Infections Around Orthopedic Implants, *Advanced Materials Interfaces*, Vol. 10, Issue 5, 2023, Article # 2201878, pp. 1-10.

[2]. E. Tomsik, P. Dallas, I. Sedenkova, J. Svoboda, M. Hruby. Electrochemical deposition of highly hydrophobic perfluorinated polyaniline film for biosensor applications, *RSC Advances*, Vol. 11, Issue 31, 2021, pp. 18852-18859.

[3]. T. Urbanek, I. Ivanko, J. Svoboda, E. Tomsik, M. Hruby, Selective potentiometric detection of reactive oxygen species (ROS) in biologically relevant concentrations by a modified metalized polyporphyrine sensing layer coated with nonbiofouling poly (2-alkyl-2oxazoline)s, *Sensors & Actuators: B. Chemical*, Vol. 363, 2022, Article # 131827, pp. 1-12.

[4]. R. Ismail, I. Sedenkova, Z. Cernochova, I. Romanenko, O. Pop-Georgievski, M. Hruby, E. Tomšík, Potentiometric Performance of Ion-Selective Electrodes Based on Polyaniline and Chelating Agents: Detection of Fe^{2+} or Fe^{3+} Ions, *Biosensors,* Vol. 12, 2022, Article # 446, pp. 1-14.

(010)

Software Defined Radio Based Concept for Extending Orthogonal Multi-tone Time Domain Reflectometry Method to Analyze Electrical Power Grids

A. Faschingbauer
Deggendorf Institute of Technology, Technology Campus Freyung
Grafenauer Str. 22, 94078 Freyung, Germany
Tel.: + 49855191764-22
E-mail: alexander.faschingbauer@th-deg.de

Summary: This paper presents a concept for extending Orthogonal Multi-tone Time Domain Reflectometry (OMTDR) method to a Multi-Domain Reflectometry System (MDRS). OMTDR is implemented onto Orthogonal Frequency-Division Multiplexing (OFDM) which enables parallel analysis of the meta data while data communication is running. The proposed MDRS generates/extracts meta data and analyses it using a multi-modal analysis approach. The goal is to evaluate an existing OMTDR approach, extend and apply it to a multi-branched complex power line network for detecting weak impedance changes.

Keywords: Reflectometry, Soft fault, Weak impedance changes.

1. Introduction

Electrical reflectometry methods are used in many areas like in the field of detecting defects or arcs in cables, detecting weak connections as well as using it indirectly in the context of structural health monitoring. The literature shows, that the accuracy of electrical reflectometry methods is steadily increasing, resulting in better defect localization (within few centimeter) and defect classification (e.g., weak impedance changes) [1]. OMTDR is one of the most promising approaches used for this purpose. It can be applied to communication lines (with useful signals) and power lines (DC or AC). If the System Under Test (SUT) already uses OFDM modulation, these signals can be directly used to analyse the underlying physical layer (e.g., copper wires). This makes OMTDR quite flexible and universal for different use cases. Several cable types and systems have been investigated. Unfortunately, most of them are at laboratory scale and with few exceptions not fully useable for real world problems. The presented concept addresses this problem. Therefore, the OMTDR method will be extended using metadata, generated from the data packets and all their representations themselves.

2. Related Work

Reflectometry is based on injecting test signals into a SUT and receiving a kind of echo back from the same system. A lot of electrical reflectometry methods exist. Table 1 depicts only some of them, especially for detecting soft faults. All methods can be sorted into two categories like detection of hard faults in wiring systems (short or open circuit) and detection of soft faults or soft/small/low impedance changes caused through damaged insulation, bent wires, moisture, or rust on contacts.

2.1. Coupling Methods

Electrical reflectometry requires an electrical signal coupling which can be realized differently. Table 2 gives a short overview about used coupling types, found in literature.

Table 1. List of electrical reflectometry methods.

Method	Description	Reference(s)
BTDR	Binary Time Domain Reflectometry	[2] [3]
(C)CTDR	(Continuous) Chaos Time Domain Reflectometry	[3] [4]
CTFDR	Cluster Time Frequency Domain Reflectometry	[5]
JTFDR	Joint Time Frequency Domain Reflectometry	[6]
OMTDR	Orthogonal Multi-tone Time Domain Reflectometry	[3]
SSTDR	Spread Spectrum Time Domain Reflectometry	[3] [7]
TDR	Time Domain Reflectometry	[8] [9]
TFDR	Time Frequency Domain Reflectometry	[3]
TRR	Time Reversal Reflectometry	[10]

Table 2. Coupling Methods.

Signal Coupling Method	Reference(s)
Direct	[3] [4] [5] [6] [8] [10]
Direct, Tuneable Resistors	[2] [3]
Direct, Capacitive, Inductive	[3] [7]
Inductive	[3]
Directional Coupling	[9] [11]

Direct coupling means that the in- and outputs of the reflectometer have an ohmic connection to the Cable under Test (CUT). In most cases the type of CUT is a coaxial or twisted pair cable. Tuneable resistors are used in combination with the Binary Time Domain Reflectometry (BTDR) method. Some reflectometers use a directional Bridge which separates the injected signal from the reflected signal with an attenuation factor. Also, capacitive or inductive coupling methods are used. These are more flexible, because they can be used with a wider range of different cable types.

2.2. Injected Signal

A very simple implementation of Time Domain Reflectometry (TDR) injects a voltage pulse with a specific duration [10] or a 1 ns gaussian pulse [5]. Also, other injected signals are possible like simple binary [2, 4] or even pseudo random signals [3]. Some articles describe a very detailed signal form e.g., 48 MHz square wave pseudo random signal [3, 7]. Some approaches use a Vector Network Analyzer (VNA) where the injected signal depends on the device itself [8].

2.3. Cable Types and Network Complexity

Literature shows research using different cable types. The range begins with wiring systems for data communication (twisted pair, coaxial cables) [9] and spans to power lines [3] which is a broad variety. Network complexity is another important aspect in presence of analyzing wiring networks. Complexity ranges from simple End-2-End connections to very complex multibranch networks which extend over a wide area [3].

2.4. Coexistence of Useful Signals

Some electrical reflectometry methods are applicable in systems where useful signals (ac/dc power, communication signals) are present. Table 3 gives a short overview, weather the method can handle useful signals or not.

Table 3. Methods with coexistence of useful signals and without.

Method	Seul Signal	Reference(s)
CTFDR	No	[5]
OMTDR	Yes	[3]
SSTDR	Yes	[3] [7]
TFDR	Yes	[3]
TRR	No	[10]

3. Concept

This concept extends OMTDR to a MDRS and applies it to detect soft faults in coaxial cables and power lines with connected devices. OMTDR is usually implemented onto OFDM. Data frames with payload are modulated onto multiple sub-carriers and transformed into the frequency domain using Inverse Fast Fourier Transformation (IFFT). This step typically creates I/Q-Samples, which are converted into electrical signals using a DAC. At this point the signal is ready for transmission. An OMTDR approach is presented in [12] using a Field Programmable Gate Array (FPGA) where transmitted samples before the DAC are directly compared with the received samples after the ADC in a digital manner. Also, some postprocessing steps are described [12]. This approach will be implemented using Software Defined Radio (SDR) technique (Python + GNU Radio + National Instruments Universal Software Radio Peripheral (USRP) X310). The proposed steps will also be adapted within this concept to verify the lab setup as well as the data analysis.

3.1. Laboratory Setup

Fig. 1 shows the laboratory setup, which consists of a SDR as interface between the software and hardware domain. There shall be two wiring options of SUT. Option 1 is a single transmission line (coaxial cable, type RG-58) with two different lengths (100 m or 500 m) and additionally four different termination types Z_t with

$$Z_t = \begin{cases} Z_L & = & 50\ \Omega \\ Z_0 & = & 0\ \Omega \\ Z_\infty & = & \infty\ \Omega \\ & [0, \infty[& \Omega \end{cases} \quad (1)$$

as match, short, open, or other defined impedance. Option 2 is a NYM type cable, used for power lines in the 230 V layer. This cable shall be used to create a power line network with several levels of network complexity. Also, some typical devices shall be connected to this multi-branched network to get a setup comparable to real world applications. Suitable coupling devices shall be selected and used for both options.

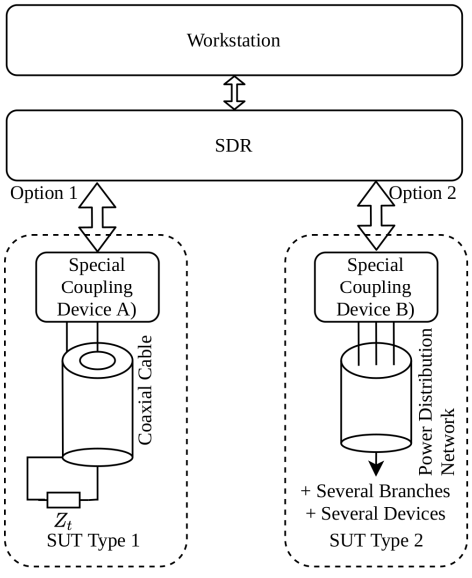

Fig. 1. Proposed Lab Setup.

3.2. Evaluation

The proposed lab setup with wiring option 1 is used to evaluate the communication system, the OMTDR method (hardware and software) as well as the extended methods. Therefore, an OFDM transmitter will be implemented, using GNURadio and existing building blocks. The OFDM receiver will be implemented in plain Python. This enables a simplified extraction of all kind of meta data required at any point of the signal processing chain. Later, the methods tested with wiring option 1, shall be applied to wiring option 2.

4. Extension of the OMTDR Method

Fig. 2 shows a simplified OFDM spectrum (dotted line). The spectrum consists typically of a defined number of sub- carriers with specified modulation type and purpose. These are depicted below the dotted line. Not every individual carrier is plotted. Instead, the number below the carriers show how many real carriers of the same type are present in the real spectrum at the shown position. Corresponding to the Fast Fourier Transformation (FFT) size, 64 subcarriers are placed. Therefore, each carrier can be computed into I/Q samples (time-domain) using the FFT or IFFT vice versa.

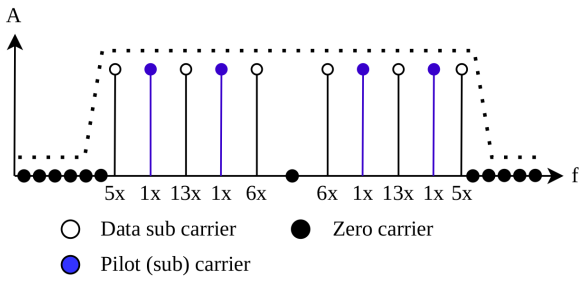

Fig. 2. Simplified OFDM frame in the frequency domain with subcarrier placement schema.

Fig. 3 shows a part of an OFDM packet in time-domain. At the beginning of each OFDM packet a cyclic prefix (CP), consisting of 16 I/Q samples is sent. This repeats until the end of a packet (EOP) is reached. Afterwards, two synchronization words, a packet header and several payload frames are sent, each separated by the CP. The parts between the CP blocks correspond to the time-domain representation of Fig. 2.

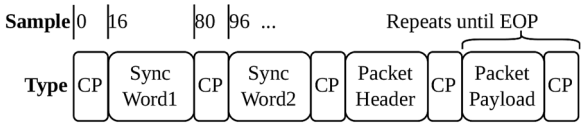

Fig. 3. OFDM datagram with frames, separated by the cyclic prefix.

Fig. 4 depicts the data processing chain. It is used to generate the raw files for later analysis. The Data Generator block is used to generate packets, containing a unique packet number. The packets are then stored in a binary format into a file. The OFDM Encoder block reads the binary packets from the foregoing file, arranges the binary data onto the subcarriers, places them together and produces I/Q samples, which are then stored in another file. The SDR Tx/Rx block reads the I/Q data and transfers it to the USRP where they are sent into the SUT. The received signal is a superposition of the transmitted signal and the response of the system. This signal is also saved to a file in I/Q representation. Now, the OFDM Decoder block detects the start of an OFDM packet, demodulates and decodes it and saves the data also into a file. In the Analysis block several methods are used to get additional information out of the data, saved in the files. The extraction of meta information from frequency (Fig. 2) and time domain (Fig. 3) is explained in the next parts.

5. Meta Data through Multi Domain Analysis

All analysis are grouped into domains. Each domain provides at least one meta data source. The meta data is generated during processing the pipeline in Fig. 4.

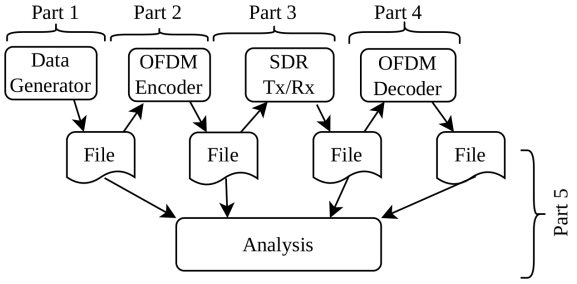

Fig. 4. Data generation and processing pipeline.

5.1. I/Q Domain

The first approach is to apply the OMTDR method using the I/Q samples of each transmitted and received packet directly like in [12]. Additionally, specially designed sequences for extracting parts of the signal could be used together with correlation.

5.2. Data or Packet Domain

Thus, the software OFDM receiver can detect the start of each packet in the receive stream file as well as in the transmit stream file. The number of packets sent, is well known. It must stay constant as long as not too many samples of a packet are damaged during propagation through the SUT. Additionally, all packets carry a unique packet number in their payload. Therefore, a packet drop can be detected. The received I/Q samples will be slightly changed through system noise and especially reflections of the system. Afterwards the corresponding transmit and receive

packets can be analyzed using the approach in [12] to get an insight of the SUT. Also, the total bit error rate (BER) of the whole packets as well as only of the pilot carriers and the relation between them could be considered.

5.3. Frame Domain

Each OFDM frame consists of a short sequence, which is used as a start of frame (SOF), a long sequence (used for correcting frequency drift) and several carriers, grouped into pilots and data carriers. In the case of the IEEE 802.11 standard, short and long sequence are standardized and therefore well-known [13, p. 3314, Table I-3]. Typically, the Schmidl & Cox synchronization technique is used to detect the short sequence and thus the SOF. It is assumed that other numeric calculations as well as machine learning approaches could be helpful to generate meta data out of these synchronization sequences.

5.4. Symbol Domain

Each OFDM symbol has several subcarriers. As visualized in Fig. 2, they can be grouped in zero carriers, data carriers and pilot carriers. The latter are typically used to estimate the transmission channel in communication systems. This information shall be considered as meta information source, too. The information, modulated onto the pilots is constant and it shall be used to track rapid time variations, which may be caused by the SUT. It is assumed that the time variation is a constant, but system specific value. The zero carriers may be used to estimate system typical noise. This could be interesting for SUT option 2, because there unshielded cables are used.

5.5. Frequency Domain

Also, the spectrum of the OFDM signal can be analyzed. Information like bandwidth, receive power or the signal to noise ratio (SNR) can be calculated and used as meta data further. Relation of amplitudes of subcarriers inside each OFDM symbol compared to the relation of amplitudes of subcarriers between all OFDM symbols in a Packet. Also, frequency components which have more power than in the original transmit signal can appear and therefore be used as meta information which may be system specific.

6. Expected Results

All of the proposed meta data may be used individually to get a specific fingerprint of the SUT. Moreover, the combination of two or more meta data sources using specific methods for combining them, could be a promising approach to detect small impedance changes.

7. Conclusion and Further Work

The presented concept shows an approach to extend the OMTDR method to a MDRS, using the underlying OFDM communication system. The main goal is to evaluate an existing OMTDR approach, extend and apply it to a multi-branched complex power line network for detecting weak impedance changes. Therefore, a multi-modal analysis is implemented. It is planned, to consider machine learning (ML) approaches later on. The proposed system is capable of generating the large amounts of training data required for ML approaches. The output of trained ML models may enable the detection of weak impedance changes, too.

Acknowledgements

This paper was written in the context of the SI-CM3S project, which is funded by the German Federal Ministry for Economic Affairs and Energy as part of the Central Innovation Program for SMEs (ZIM) on the basis of a resolution of the German Bundestag.

References

[1]. L. Incarbone, F. Auzanneau, W. Ben Hassen, and Y. Bonhomme, Embedded wire diagnosis sensor for intermittent fault location, in *Proceedings of the IEEE SENSORS,* Nov. 2014, pp. 562–565.

[2]. F. Auzanneau, Natural amplification of soft defects signatures in cables using binary time domain reflectometry, *IEEE Sensors Journal*, 21, 2, 2021, pp. 937 - 944.

[3]. C. M. Furse, M. Kafal, R. Razzaghi, and Y.-J. Shin, Fault Diagnosis for Electrical Systems and Power Networks: A Review, *IEEE Sensors Journal*, 21. 2. 2021, pp. 1–1.

[4]. F. Auzanneau, Binary time domain reflectometry: A simpler and more efficient way of diagnosing defects in wired networks, in *Proceedings of the IEEE AUTOTESTCON Conference,* Sep. 2018, pp. 1-8.

[5]. M. Franchet, N. Ravot, and O. Picon, Soft fault detection in cables using the cluster time-frequency domain reflectometry, *IEEE Electromagnetic Compatibility Magazine,* Vol. 2, No. 1, 2013, pp. 54–69.

[6]. S. Sallem and N. Ravot, Soft defects localization by signature magnification with selective windowing, in *Proceedings of the 2015 IEEE SENSORS Conference*, Nov. 2015, pp. 1–4.

[7]. E. Benoit, N. K. T. Jayakumar, S. Kingston, M. U. Saleh, M. Scarpulla, J. Harley, and C. Furse, Applicability of SSTDR Analysis of Complex Loads, in *Proceedings of the IEEE International Symposium on Antennas and Propagation and USNC-URSI Radio Science Meeting*, Jul. 2019, pp. 2087–2088.

[8]. M. Kafal, A. Cozza, and L. Pichon, Locating Multiple Soft Faults in Wire Networks Using an Alternative DORT Implementation, *Institute of Electrical and Electronics Engineers,* Tech. Rep. 10.1109/ TIM.2015.2498559, 2016.

[9]. Q. Shi and O. Kanoun, Application of iterative deconvolution for wire fault location via reflectometry, in *Proceedings of the International Symposium on Instrumentation Measurement, Sensor Network and*

Automation (IMSNA' 2012), Vol. 1, August 2012, pp. 102–106.

[10]. L. El Sahmarany, L. Berry, N. Ravot, F. Auzanneau, and P. Bonnet, Time Reversal for Soft Faults Diagnosis in Wire Networks, *Progress In Electromagnetics Research,* Vol. 31, 2013, pp. 45–58.

[11]. C. Gao, L. Wang, J. Mao, S. Hu, B. Zhang, and S. Yang, Non-Intrusive Cable Fault Diagnosis Based on Inductive Directional Coupling, *IEEE Transactions on Power Delivery,* Vol. 34, No. 4, August 2019, pp. 1684–1694.

[12]. W. Ben Hassen, F. Auzanneau, L. Incarbone, F. Peres, and A. P. Tchangani, Distributed Sensor Fusion for Wire Fault Location Using Sensor Clustering Strategy, *International Journal of Distributed Sensor Networks,* Vol. 11, No. 4, April 2015, p. 538643.

[13]. IEEE Std 802.11™-2016, IEEE Standard for Information technology, Telecommunications and information exchange between systems, Local and metropolitan area networks, Specific requirements, Part 11: Wireless LAN Medium Access Control, 2016.

(011)

Traffic Signaling and Cooperative Trajectories based on Visible Light Communication

M. A. Vieira [1,2], G. Galvão [1], M. Vieira [1,2,3] M. Véstias[1,4], P. Vieira[1,5] and P. Louro [1,2]
[1] ISEL-Polytechnic Institute of Lisbon, Portugal
[2] UNINOVA-CTS and LASI; Lisbon, Portugal
[3] NOVA School of Science and Technology, Lisbon, Portugal
[4] INESC-ID, IST, Un. de Lisboa, Lisbon, Portugal
[5] Instituto de Telecomunicações, *IST,* Lisbon, Portugal
E-mail: mv@isel.ipl.pt

Summary: Visible Light Communication (VLC) is a promising solution proposed for optimizing traffic signals and vehicle trajectories at urban intersections. This approach utilizes light communication between connected vehicles (CVs) and infrastructure to enable coordinated traffic interactions. By leveraging streetlamps, intersection signals, and headlights, VLC facilitates the transmission of information between CVs and the infrastructure. The system is designed to be flexible and adaptive, accommodating diverse traffic movements across multiple signal phases. To evaluate the effectiveness of VLC, simulations are conducted using the SUMO urban mobility simulator. These simulations generate traffic flows and incorporate VLC mechanisms and relative pose concepts for queueing, requesting, and responding to interactions. To dynamically control traffic flows and alleviate congestion during peak hours, a deep reinforcement learning algorithm is employed. This algorithm optimizes traffic by utilizing both Vehicle-to-Vehicle (V2V) and Vehicle-to-Infrastructure (V2I) communications. Comparisons are made between the traditional trajectory and signal optimization techniques. The results demonstrate the benefits of VLC in terms of throughput, delay, and the reduction of vehicle stops. In conclusion, VLC presents an integrated approach that harnesses light communication to optimize traffic signals and vehicle trajectories at urban intersections. Through simulations and comparisons, VLC proves its effectiveness in enhancing traffic efficiency and reducing congestion, offering promising insights for future urban traffic management systems.

Keywords: Visible light communication, Optical sensors, Cooperative traffic control, Connected vehicles, Deep reinforcement learning; SUMO simulation.

1. Introduction

In today's world, communication technology has become a subject of controversy due to the increasing overload of radio frequencies and the need for stable and consistent systems. As a potential solution to this challenge, Visible Light Communication (VLC) emerges by utilizing light-emitting diodes (LEDs) as light sources and photodiodes as photodetectors [1. By modulating visible light in time and frequency, VLC offers a promising alternative for communication technology [1]. Only light emitting diodes (LED) lamps can be used for the transmission of visible light [2]. This functionality has given rise to a novel communication technology, VLC, where LED luminaires can be used for high-speed data transfer [3]. VLC is an emerging technology [4] that enables data communication by modulating information on the intensity of the light emitted by LEDs. Increasingly, smart cities can become comfortable, quick, and safe places to travel. Technology has advanced to the point where even non-autonomous vehicles are equipped with sophisticated sensors and computers. That was the first step on the road to improve road safety.

The application of VLC goes beyond traditional communication methods and extends to intelligent traffic control systems. By implementing a real-time traffic control system, traffic flow can be significantly improved through effective resource management and information exchange. This study specifically focuses on utilizing Visible Light Communication as a means of transmitting information, providing guidance services, and delivering specific information to drivers. In the case of vehicular communications, the use of VLC is made easier because all vehicles, streetlights, and traffic lights are equipped with LEDs, using them for illumination. In this context, communication and localization are facilitated through the utilization of streetlamps, traffic signaling, and the headlights and taillights of vehicles. This approach allows for the simultaneous use of outdoor automotive lighting and infrastructure lighting to serve both illumination and communication purposes [5, 6].

We propose a cooperative I2V2V2I2V system that supports guidance services. This system employs an edge/fog-based architecture, which effectively manages the safe passage of vehicles through connected intersections. Vehicular Communication Systems are a type of network in which vehicles and roadside units are the communicating nodes, providing each other with information [7]. The main objective is to optimize traffic safety and efficiency on public roads through V2V and V2I communications [8-10]. Real-time traffic information is essential for optimizing traffic light duration. By monitoring the location, speed, and direction of nearby vehicles, significant improvements in traffic management can be achieved.

2. Connected Vehicles and VLC

The central aim is to enhance both safety and efficiency on public roads through the implementation of Vehicle-to-Vehicle (V2V) and Vehicle-to-Infrastructure (V2I) communications. This endeavor revolves around elevating situational awareness and curtailing traffic accidents. A key strategy involves utilizing real-time traffic information to inform dynamic adjustments in traffic light durations, ultimately optimizing traffic flow and minimizing potential hazards.

At the heart of this effort lies the integration of V2V and V2I communications. By harnessing the real-time data regarding the location, speed, and direction of nearby vehicles, a comprehensive and accurate understanding of the road environment is achieved. This real-time awareness enables informed decision-making, leading to substantial enhancements in traffic management. The envisioned outcome is a marked improvement in both the safety and efficiency of road usage, offering a promising path towards a smarter and more secure transportation landscape.

2.1. Intelligent Control System

To develop the intelligent control system model that facilitates safe vehicle management through intersections using V2V, V2I, and I2V communications, Reinforcement Learning (RL) concepts were used. RL is a training method based on rewarding desired behaviors and/or punishing undesired ones [11-13].

The simulations were agent-based and they have been carried out in a tool for Simulation of Urban MObility (SUMO) [14].

Fig. 1 illustrates the reinforcement learning loop, where the agent receives the current state of the environment (St) and learns from the feedback of the action taken (At) on the overall traffic flow. The agent's action directly affects the traffic light, which serves as the controller of the intersection. This iterative process allows the agent to learn from its actions and improve over time, avoiding negative situations and focusing on positive outcomes. The agent's experiences and actions are stored to train a model and enhance its decision-making capabilities [15]. The traffic lights in SUMO are controlled by the learning agent following its decisions, the overall flow of traffic is described, and the actions of the traffic lights control agent are rewarded. The reward (R_t), represent the accumulated total waiting time of all the cars in the intersection captured respectively at agentsteps $t-1$ and t. The objective of the IM is to minimize the total waiting time at each arm of the intersection. When a vehicle's speed drops below 0.1 m/s, a queue alert is triggered. The IM agent must explore new states while simultaneously maximizing its overall reward. To illustrate this concept, a dynamic phasing diagram and a state matrix based on the total accumulated time are provided.

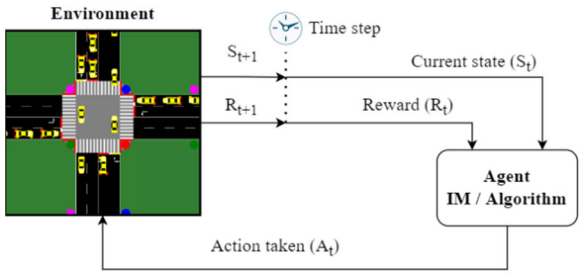

Fig. 1. Illustration of the reinforcement learning's loop of action-reward feedback.

2.2. Scenario, Environment and Architecture

In Fig. 2, a scenario with two traffic signal-controlled intersections is depicted. The scenario is designed with an orthogonal topology, organized into clusters of square unit cells. This layout helps define the structure and arrangement of the intersections within the scenario. Each transmitter, $X_{i,j}$, carries its own color, X, (Red, Green, Blue, Violet) as well as its horizontal and vertical ID position within the surrounding network (i,j) [16]. In the Proof of Concept (PoC), it was assumed that the crossroads are situated at the intersections of line 4 with column 3 and column 11.

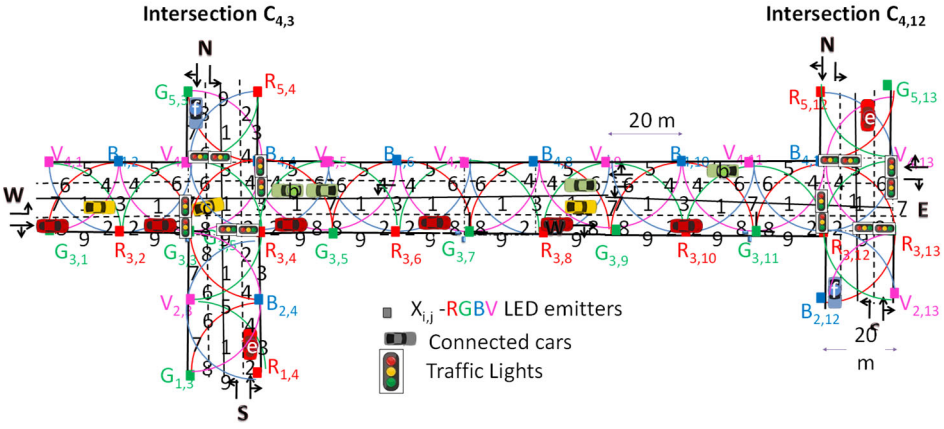

Fig. 2. Simulated scenario with the optical infrastructure.

In Fig. 2, there are two traffic signal-controlled intersections with four traffic flows. From the West, there are twenty red a_i vehicles with straight movement and four yellow c_i vehicles with left turn only. From the East, there are green *bi* vehicles with left turn only (thirteen straight and two left turn). From the South, there are six orange e_i vehicles, with two having a left-turn approach and four with straight movement. From the North direction, there are thirteen blue f_i vehicles, with nine going straight and four having a left turn at both intersections. The road request and response segments offer a binary choice between turning left/straight or turning right. The vehicles represent a percentage of the traffic flow, and their ordering in terms of priority is determined. The top three requests are a_1, b_1, and a_2, followed by b_2, a_3, and c_1. In the seventh, eighth, and ninth places are b_3, e_1, and a_4, respectively, followed by c_2 in the tenth place. The penultimate request is a_5, and the last one is f_1. Based on the assumptions, there are 540 cars approaching the intersection per hour, with 80 % of them coming from the east and west directions. Among these cars, it is assumed that 50% of them will make a left or right turn at the intersection, while the remaining 50 % will continue straight.

2.3. Visible Light Communication Link

A Vehicular Visible Light Communication system (V-VLC) is structured around a transmitter and a receiver connected via a wireless channel. The transmitter's role involves generating modulated light, often utilizing the ON-OFF-keying (OOK) amplitude modulation technique. Concurrently, the receiver detects fluctuations in the received light signal [17]. This dynamic system finds implementation in both the road infrastructure, manifesting as streetlights, and within the vehicles themselves, taking shape as headlights.

Within this ecosystem, the environment is meticulously defined, characterized by a cluster of square unit cells arranged in an orthogonal configuration. The cornerstone of this setup is the deployment of tetra-chromatic white light sources (WLEDs) positioned strategically at the corners of each unit cell. These light sources offer distinct data channels [18].

Functionally, the V-VLC system processes coded signals as inputs. These signals are transmitted by transmitters, which can take the form of streetlights or headlights. Their purpose ranges from vehicle identification (I2V), communication with traffic lights (V2I), to facilitating communication between vehicles (V2V). The encoded signals encapsulate not only the essential information about the transmitter's position within the network but also the steering angle (δ) imperative for guiding the driver's orientation along their trajectory.

To manage the seamless passage of vehicles through intersections, a sophisticated interplay of queue/request/response mechanisms and temporal/space-relative pose concepts are employed [19]. These mechanisms ensure efficient traffic management and orderly vehicular movement at crossroads.

The coded signals transmitted by the transmitters are subsequently received and decoded by a PIN-PIN photodetector. This photodetector boasts light filtering properties, ensuring the precision and accuracy of data reception, a pivotal aspect in maintaining the integrity of the communication process.

2.4. Architecture

Illustrated in Fig. 3 is the implementation of a hybrid structure seamlessly fusing mesh networking with cellular technology. At the crux of this configuration is the "mesh" controller, strategically positioned at streetlight installations. This controller assumes the critical role of a message-forwarding entity, orchestrating the efficient flow of information among vehicles operating within the mesh network. Its functionality closely resembles that of router nodes within a network framework.

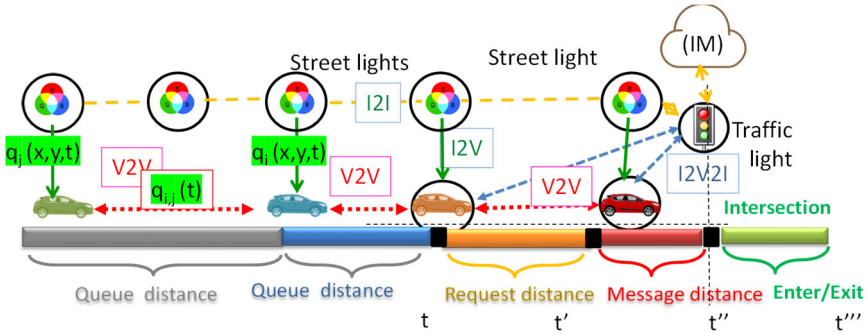

Fig. 3. VLC Edge Computing infrastructure.

Complementing the mesh controller is the hybrid controller, an innovative convergence of mesh and cellular capabilities. This hybrid entity performs a dual role: firstly, it functions as a border-router, skillfully bridging the mesh and cellular domains. Additionally, this hybrid controller serves as a catalyst for edge

computing functionalities, effectively extending the computational capacity of the network [20].

This architectural paradigm yields a host of functionalities. On one hand, it seamlessly supports edge computing capabilities, empowering the execution of computations closer to the data source. On the other hand, it accommodates device-to-cloud communication (I2IM), ushering in the potential for real-time data exchange between devices and cloud-based resources. Simultaneously, the architecture fosters peer-to-peer communication (I2I), facilitating direct information exchange among devices.

Embedded within this framework are computing platforms that hold a pivotal position. These platforms undertake the essential tasks of processing and interfacing with sensors and controllers. In essence, they form the dynamic hub where data is processed, transformed, and made available for further analysis or dissemination.

3. Intelligent Traffic Signal Control

3.1. Dynamic Traffic Phasing

In Fig. 4, a visual representation unfolds, elucidating the sequential progression of phases within the intersection. This orchestrated flow adheres to a structured cycle length comprising six distinct phases. Each of these phases is further intricately subdivided into 16 discrete time sequences or states, delineating a comprehensive temporal framework for the intersection's operation.

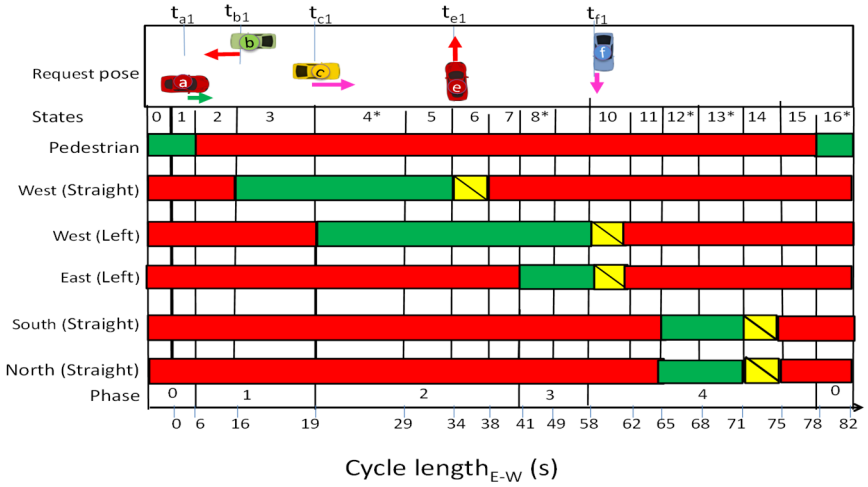

Fig. 4. Requested phasing of traffic flows. * Adaptive sequences.

An essential observation to highlight is that states designated with an asterisk (*) hold a dynamic quality, representing movable states that adapt in response to varying traffic demands within the cycle. Specifically, sequences marked with the numbers *"0"*, *"1"*, and *"16"* denote the exclusive pedestrian phase, signaling a dedicated time interval for pedestrian movement.

Furthermore, the synchronization of the cycle initiates with sequence *"1"*, marking the commencement of the orchestrated flow of phases. Within this cycle, phases one through four are each allocated sequence spanning from *"2"* to "*15*". These sequences within these phases play a pivotal role in meticulously regulating the traffic flow, ensuring a structured and efficient movement of vehicles through the intersection.

3.2. Adaptive V-VLC Traffic Control Evaluation

Using the application programming interface (API) provided by SUMO, it is possible to interface with external programs and interact with the simulation environment. SUMO provides various statistics related to the overall traffic flow and provides various outputs, such as diagrams illustrating the duration of each state or color of the traffic lights throughout the simulation. Based on the simulation scenario depicted in Fig. 2, a state diagram was generated using SUMO simulation. Fig. 5a and Fig. 5c show the phase diagrams for the two connected intersections, TL1 and TL2. The SUMO environment is illustrated in Fig. 5b.

The simulation scenario was adapted from a real-world environment in Lisbon [21], and it considers the presence of roads that impact the traffic flow at both intersections. These roads, referred to as the target road, have a dynamic influence on the traffic flow, and the impact of the historical traffic state from other roads on the target road is limited in time. Here, the E-W arm was considered as a target road. The transmission of traffic flow and traffic waves measures the time duration for which the traffic state of other roads affects the target road within the same period. As traffic continuously enters the system, the composition of the traffic flow on the target road undergoes changes over time. To improve the traffic flow conditions, a modification was made to the initially proposed phases (as shown in Fig. 4).

The modification involved an immediate transition from the pedestrian phase (Ph0) to the N>S phase (Ph4), followed by the remaining phases in both intersections. This change in phase order was found to enhance the traffic flow conditions in the simulation.

By adjusting the phase sequence and optimizing the traffic light control strategy based on the simulation results, it is possible to achieve improvements in traffic flow, reduce congestion, and enhance overall intersection performance. In Fig. 6, a comparison is presented between the queue (halting) and average speed observed every second in SUMO/VLC (Simulation of Urban MObility with Visible Light Communication) for a 130-second cycle. The simulation assumes a saturation flow of 2500 vehicles per hour.

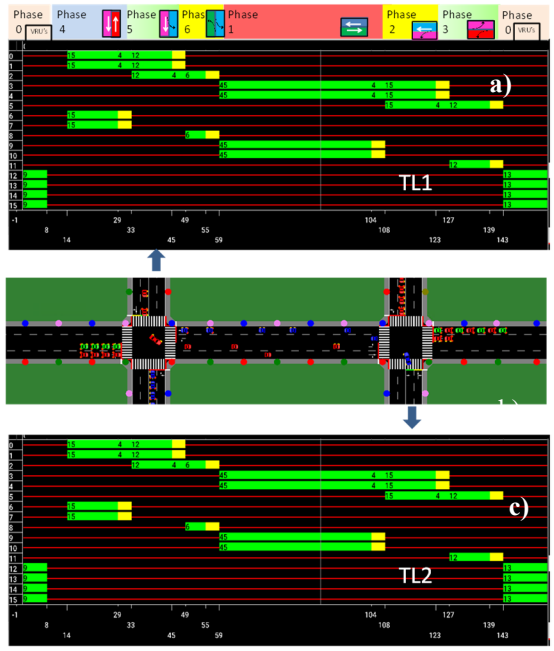

Fig. 5. State diagram resulting in two coordinated intersections (TL1 and TL2). On the top an insert of environment and the color phasing is inserted. At the midle the environment is draft.

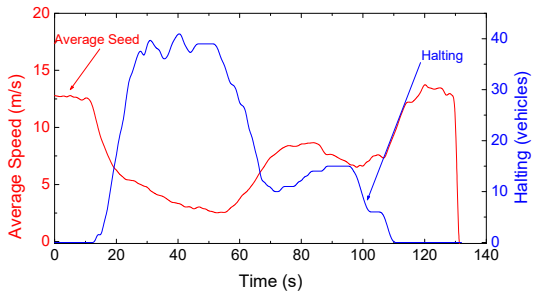

Fig. 6. Average speed and halting along a cycle.

The results demonstrate that on the regulated roads, there are typically no congested conditions occurring in each new cycle. The queue of vehicles in the first section of the demand acts as an integrator, meaning it accumulates vehicles and its length increases as vehicles enter the section. This becomes critical when the queue approaches the capacity of the link road. In the unsaturated regime, which assumes that all vehicles in the queue leave the target road by the end of the sampling time, the queue of vehicles is always zero. However, when the red light is activated, a maximum queue of vehicles is generated since all vehicles in the queue are held back. This analysis provides insights into the behavior of traffic flow and queue dynamics within the simulated environment. It demonstrates the impact of traffic lights and their timing on the accumulation and dispersal of vehicles at different sections of the road network. Fig. 7 represents the reward obtained, after the training, when the network was tested. The test was performed for the two intersections scenario with independent crossings. The results obtained from the experiment indicate that as the number of action steps increases, the cumulative rewards become more positive. This demonstrates that the agent learns to make better decisions over time during the test. The feasibility and benefits of creating a dynamic system that can adapt to specific traffic scenarios are evident in the results. Safety and privacy are crucial requirements for the V-VLC system.

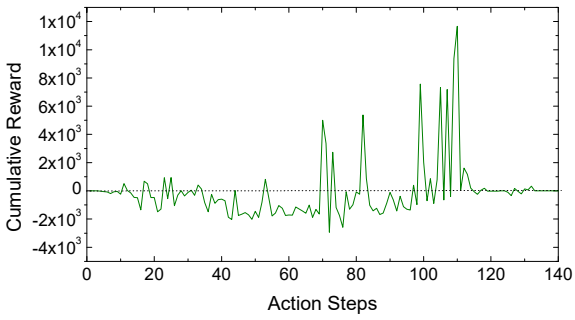

Fig. 7. Cumulative reward.

To bolster security, upcoming advancements should prioritize the enhancement of coding techniques to guarantee that exclusively authorized receivers can decipher secure request/response messages. These security measures extend deep into the fabric of the physical transmission process, particularly within the Line of Sight (LoS) channel. In this context, potential eavesdroppers are rendered passive observers, devoid of any access to transmitted information.

One promising avenue for augmenting security entails harnessing the positional data of streetlamps to deduce the flow of vehicular traffic. This innovative approach holds the potential to obviate the necessity for traditional certificates or passwords within the network. Instead, it paves the way for a paradigm shift toward statistical secrecy. By weaving this statistical approach into the security framework, the reliance on explicit authentication measures can be alleviated, while concurrently fortifying the layers of protection against unauthorized access.

In essence, the trajectory for fortifying security within the system rests upon refined coding techniques, the intrinsic security attributes of the LoS channel, and the intelligent utilization of positional information for traffic flow analysis. This approach promises to yield enhanced security measures, ushering in a future where secure communication flourishes within the framework of advanced vehicular systems.

4. Conclusions

V-VLC technology integration in connected cars offers significant improvements to urban traffic networks by integrating traffic signal control with driving behavior. This innovative system utilizes a queue/request/response approach for efficient intersection management while providing real-time monitoring of queues and messages. Through detailed data collection, V-VLC technology enables dynamic adjustments to traffic light phases and durations, leading to reduced travel times and minimized waiting for drivers. Furthermore, V-VLC enhances safety by directly monitoring crucial areas such as queue formation, ensuring a safer and more efficient traffic flow.

Acknowledgements

This research was funded (in part) by the Portuguese FCT program, Center of Technology and Systems (CTS) UIDB / 00066 / 2020 / UIDP / 00066 / 2020 and by IPL/2022 / POSEIDON_ISEL.

References

[1]. Zhaocheng Wang, Qi Wang, Wei Huang, Zhengyuan Xu, Wiley, Visible Light Communications: Modulation and Signal Processing, *Wiley-IEEE Press*, 2018.

[2]. Azevedo, I. L., Morgan, M.G., Morgan, F., The Transition to Solid-State Lighting, *Proceedings of the IEEE*, Vol. 97, No. 3, March, 2009, 481-510.

[3]. Schmid, S., Corbellini, G., Mangold, S., and Gross, T. R., An LED-to-LED Visible Light Communication system with software-based synchronization, in *Proceedings of the IEEE Globecom Workshops*, 2012, pp. 1264–1268.

[4]. Parth, H., Pathak, X., Pengfei, H. and Prasant, M.,Visible Light Communication, Networking and Sensing: Potential and Challenges, September 2015, IEEE Communications Surveys & Tutorials 17(4): Fourthquarter 2015, pp. 2047 – 2077, 2015.

[5]. Nawaz, T., Seminara, M., Caputo, S., Mucchi, L. and Catani, J., Low-latency VLC system with Fresnel receiver for I2V ITS applications, *J. Sensor Actuator Netw.,* Vol. 9, No. 3, Jul. 2020, p. 35.

[6]. Caputo, S., et al., Measurement-based VLC channel characterization for I2V communications in a real urban scenario, *Veh. Commun*., Vol. 28, Apr. 2021, Art. No. 100305.

[7]. Yousefi, S., Altman, E., El-Azouzi, R., and Fathy, M., Analytical Model for Connectivity in Vehicular Ad Hoc Networks, *IEEE Transactions on Vehicular Technology*, 57, 2008, pp. 3341-3356.

[8]. Elliott, D., Keen W., and Miao L., Recent advances in connected and automated vehicles, *Journal of Traffic and Transportation Engineering*, Vol. 6, Issue 2, pp.109-131, April 2019.

[9]. Jitendra, N., and Bajpai, Emerging vehicle technologies & the search for urban mobility solutions, Urban, *Planning and Transport Research*, 4, 1, 2016, pp.83-100.

[10]. Wang, N., Qiao, Y., Wang, W., Tang, S. and Shen, J. Visible Light Communication based Intelligent Traffic Light System: Designing and Implementation, in *Proceedings of the Asia Communications and Photonics Conference (ACP' 2018)*, 2018, pp. 1-3.

[11]. Iša, J., Kooij, J., Koppejan, R., and Kuijer, L., Reinforcement learning of traffic light controllers adapting to accidents, *Design and Organisation of Autonomous Systems*, 2006, pp. 1–14.

[12]. Forbes, J. R. N., Reinforcement learning for autonomous vehicles, *University of California*, Berkeley, 2002.

[13]. Liang, X., Du, X., Wang, G., and Han, Z., A Deep Reinforcement Learning Network for Traffic Light Cycle Control, *IEEE Transactions on Vehicular Technology,* Vol. 68, No. 2, Feb. 2019, pp. 1243-1253.

[14]. Alvarez Lopez, Pablo, at. al., Microscopic Traffic Simulation using SUMO, in *Proceedings of the 21st IEEE Intelligent Transportation Systems Conference, ITSC),* 2018, pp. 2575-2582.

[15]. Schepperle, H., Böhm, K., Agent-Based Traffic Control Using Auctions. In: Klusch, M., Hindriks, K.V., Papazoglou, M.P., Sterling, L. (eds), Cooperative Information Agents XI. CIA 2007. *Lecture Notes in Computer Science*, *Vol. 4676*. Springer, Berlin, 2007.

[16]. Vieira, M. A. et. al., Optical signal processing for a smart vehicle lighting system using a-SiCH technology, *Proc. SPIE,* 10231, Optical Sensors 2017, 102311L, 2017.

[17]. Vieira, M. A., Vieira, M., Louro, P., Vieira, P., Bi-directional communication between infrastructures and vehicles through visible light, in Proceedings of the Fourth International Conference on Applications of Optics and Photonics, Proc. SPIE 11207, 3 October 2019, 112070C.

[18]. Vieira, M. A., Vieira, M., Vieira, P. and Louro, P., Optical signal processing for a smart vehicle lighting system using a-SiCH technology, *Proc. SPIE 10231*, *Optical Sensors 2017*, 2017, 102311L.

[19]. Miucic, R. Connected Vehicles: Intelligent Transportation Systems, *Springer*, Cham, Switzerland, 2019.

[20]. Yousefpour, A. et al., All one needs to know about fog computing and related edge computing paradigms: A complete survey, *Journal of Systems Architecture*, Vol. 98, 2019, pp. 289-330.

[21]. Vieira, P., Vieira, M..A., Queluz, M. A, and Rodrigues, A., A Novel Vehicular Mobility Model for Wireless Networks, *Wireless Pers Commun*, 43, 2007, pp. 1689–1703.

(012)

Visible Light: An Identifier (ID) System for Building Guidance

M. Vieira [1,2,3], M. A. Vieira [1,2], P. Vieira [1,4] and P. Louro [1,2]
[1] ISEL-Polytechnic Institute of Lisbon, Portugal
[2] UNINOVA-CTS and LASI; Lisbon, Portugal
[3] NOVA School of Science and Technology, Lisbon, Portugal
[4]Instituto de Telecomunicações, *IST,* Lisbon, Portugal
E-mail: mv@isel.ipl.pt

Summary: This paper presents an approach that utilizes Visible Light Communication (VLC) to generate landmark route and alert instructions for supporting people's wayfinding activities. The system comprises ceiling luminaries serving as transmitters, which transmit map information, alerts, and path messages. Optical receivers collect this information in real time, providing users with the most optimal route to avoid congestion. Tetrachromatic identifier white sources are used for lighting and different data channels. The data is encoded, modulated, and converted into light signals. Mobile optical receivers capture data, determine their location, and read transmitted data simultaneously. Bidirectional communication allows users to interact with the received information. The system calculates the best route considering static or dynamic destinations, including buddy wayfinding services. Results show that the system enables self-location, travel direction deduction, and efficient navigation towards static or dynamic locations.

Keywords: Visible light communication, Geolocation, Indoor navigation, Bidirectional communication, Wayfinding, Optical sensors, Transmitter/receiver.

1. Introduction

In the realm of modern technology, visible light has emerged as an innovative and versatile tool for creating identification systems with a unique twist. The concept revolves around harnessing the power of light signals, carefully choreographed in timed sequences and divided into spatial beams, to serve as an Identifier (ID) system for building recognition. This groundbreaking approach leverages the capabilities of LED arrays, enabling bidirectional communication channels where light takes on the roles of both down-link and up-link channels.

The implications of this novel technology are vast and far-reaching. With its ability to encode information through modulated light signals, it finds applications in diverse domains such as positioning, navigation, security, and mission-critical services. This cutting-edge communication paradigm is known as Visible Light Communication (VLC), [1] a data transmission technology that seamlessly integrates into indoor environments, making use of existing LED lighting infrastructure with minimal modifications [2, 3]. VLC has become the development direction of the next generation communication network with its huge spectrum resources, high security, low cost, and so on [4, 5].

One of the standout features of this technology lies in its adaptability. By employing white polychromatic LEDs, a phenomenon known as Wavelength Division Multiplexing (WDM) comes into play, enabling the simultaneous transmission of multiple data streams at different wavelengths. This ingenious approach effectively increases the data transmission rate, allowing for more information to be conveyed within a given timeframe.

A pivotal aspect of this innovative system is the development of a WDM receiver that capitalizes on light-controlled filters. This receiver is designed to decode the intricate information carried by the multiplexed signals. Through the process of multiplexing, filtering, and decoding, the encoded signals are meticulously unraveled, resulting in the accurate recovery of the transmitted information [6, 7].

In summary, the convergence of visible light, LED arrays, and sophisticated data transmission techniques has birthed a revolutionary approach to identification and communication within building environments. As we delve deeper into the intricacies of this technology, we uncover its transformative potential to reshape various industries and propel us into an era of more efficient, secure, and intelligent systems.

In this paper, a VLC based guidance system to be used by mobile users inside large buildings is proposed. After the Introduction, in Section 2, a model for the system is proposed and the communication system described. In Section 3, the main experimental results are presented, downlink and uplink transmission is implemented and the best route to navigate calculated. In Section 4, the conclusions are drawn.

2. VLC System Model

The main goal is to specify the system conceptual design and define a set of use cases for a VLC based

guidance system to be used by mobile users inside large buildings.

2.1. VLC Emitter and Receiver Modules

The system model is structured around two primary modules: the transmitter and the receiver, illustrated in Fig. 1. The functionality of these modules is key to the successful operation of the technology.

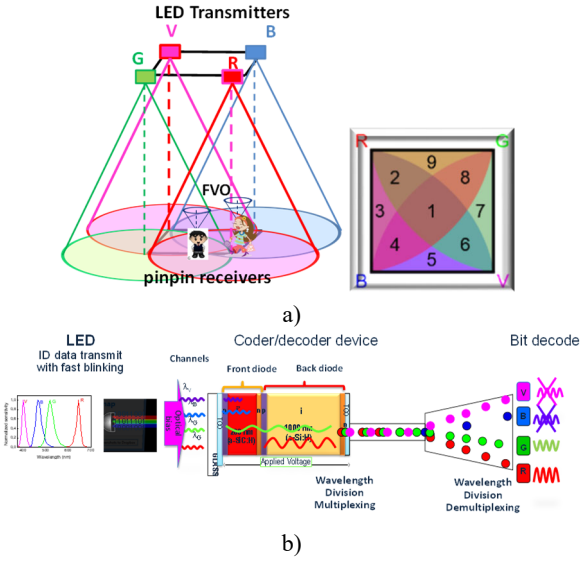

Fig. 1. a) Transmitters and receivers 3D relative positions and footprints in the square topology; b) Configuration and operation of the pin/pin receiver.

The first of these modules, the transmitter, assumes the crucial role of transforming data from the sender into an intermediary representation in the form of bytes. These bytes serve as an intermediate step before they are translated into light signals by the transmitter.

To realize both the communication and the building illumination, white light tetra-chromatic sources (WLEDs) are used providing a different data channel for each chip. The transmitter and receiver relative positions are displayed in Fig. 1a. Each luminaire is composed of four polychromatic WLEDs framed at the corners of a square. At each node, only one chip is modulated for data transmission (see Fig. 1a), the Red (R: 626 nm, 25 μW/cm^2), the Green (G: 530 nm, 46 μW/cm^2), the Blue (B: 470 nm, 60 μW/cm^2) or the Violet (V, 400 nm, 150 μW/cm^2). A fundamental difference between VLC and regular radio frequency (RF) communication is that VLC does not allow amplitude or phase modulation, and it must encode information by varying emitted light intensity. The LED can be dimmed (“off”) when transmitting data bit '0’ and at its maximum brightness ("on") when transmitting data bit '1'. This way, digital data is represented by the presence or absence of a carrier wave.

The conversion process involves taking the original data bit stream and feeding it into a modulator. This modulator employs an ON-OFF Keying (OOK) modulation scheme, which is a fundamental modulation technique widely used in communication systems. The essence of the OOK modulation lies in its binary nature. In this scheme, the presence of light signifies a binary "1" and its absence signifies a binary "0." By using this straightforward approach, the modulator effectively encodes the data onto the light signals. As the data bit stream varies, the modulator toggles the light emission on and off accordingly, translating the information into a sequence of light pulses.

Through this process, the transmitter converts the sender's data into light signals that will traverse the transmission medium. This methodology serves as the foundation for the subsequent stages of the communication process, as outlined in the system model.

The signal is propagating through the optical channel, and a VLC receiver, at the reception end of the communication link, is responsible to extract the data from the modulated light beam. In the receiving system, a MUX photodetector acts as an active filter for the visible spectrum. The integrated filter consists of a p-i'(a-SiC:H)-n/p-i(a-Si:H)-n heterostructure with low conductivity doped layers [10] as displayed in Fig. 1b. It transforms the light signal into an electrical signal that is subsequently decoded to extract the transmitted information. The obtained voltage is then processed, by using signal conditioning techniques (adaptive bandpass filtering and amplification, triggering and demultiplexing), until the data signal is reconstructed at the data processing unit (digital conversion, decoding and decision) [8] [9]. At last, the message will be output to the users. In order to receive information from several transmitters, the receiver must position itself so that the circles corresponding to the range of each transmitter overlap. This results in a multiplexed (MUX) signal that acts both as a positioning system and as a data transmitter. The grid sizes were chosen to avoid overlap in the receiver from adjacent grid points. The nine possible overlaps (#1-#9), defined as fingerprint regions are also pointed out for the unit square cell, in Fig. 1a.

2.2. Architecture and Geolocation

In VLC geotracking, geographic coordinates are generated to provide location information. However, the usefulness of this feature is further enhanced by using these coordinates to determine meaningful locations within a building and guide users through unfamiliar spaces or towards specific destinations, such as meeting rooms. To facilitate this process, VLC employs cells for positioning and a Central Manager (CM) that oversees and manages the entire system, including generating optimal routes. Introducing a paradigm-shifting concept, a mesh cellular hybrid structure is unveiled, offering an approach to network architecture. This groundbreaking framework takes shape in the form of Fig. 2, where the components and their interactions are vividly portrayed.

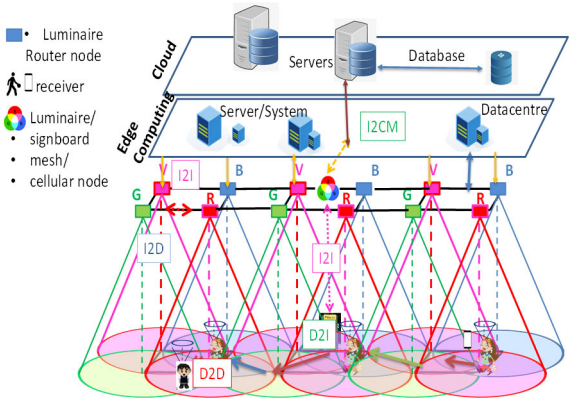

Fig. 2. Mesh and cellular hybrid architecture.

In addition to the establishment of secure pathways, the mesh network excels at enabling peer-to-peer communication, commonly known as I2I interactions. This architecture is designed to foster direct information exchange among devices, a process that assumes significance in a data-driven environment. The heart of this operation lies in the ability of each WLED (White Light Emitting Diode) to emit a unique Visible Light Communication (VLC) signal, essentially acting as a beacon of identification. Employing this beacon, the optical receiver adeptly calculates the user's trajectory, employing a specialized position algorithm. This calculated indoor route, denoted as q(x, y, z, δ, t), encapsulates critical spatial and temporal information, offering users insight into their movement within the indoor environment. A user moves from outdoor to indoor and requests assistance in finding the right track (D2I). They can customize their points of interest for wayfinding services. The requested information (I2D) is sent by the emitters, at the ceiling, to its receiver.

This architecture serves two purposes: enabling edge computing and device-to-cloud communication, and enabling peer-to-peer communication for information exchange. The culmination of this intricate network architecture is marked by the role of ceiling luminaires, which assume the mantle of routers or mesh/cellular nodes. Functioning as central hubs within this ecosystem, they engage in the vital task of disseminating messages (I2D) that encapsulate the calculated indoor route. Through their orchestrated efforts, users are provided with a tangible representation of their indoor trajectory, a testament to the architecture's capability to transform data into actionable insights.

3. Cooperative Guidance System

3.1. Communication Protocol, Coding/decoding Techniques

In the process of encoding the information, a modulation scheme known as On-Off Keying (OOK) was employed. This approach involves the toggling of the signal between two distinct states, representing binary values. Furthermore, the transmission was executed synchronously, adhering to a 64-bit data frame structure. This frame is partitioned into three primary segments: Sync, Navigation Data, and Payload. This breakdown is visually represented at the upper section of Fig. 4, and its essence is succinctly captured in the summarized form presented in Table 1.

Table 1. Frame structure.

Header	**Navigation Data**						**Payload**	
Synch	x	y	z	pin_1	pin_2	δ	Wayfinding data	Stop bit
5 bits (10101)	24 bits (4 bits per field)						34 bits (…….)	1 bit (0)
Frame length = 64 bits								

The header block stands as a synchronization mechanism, encompassing the bit sequence [10101]. This initial segment holds high importance, as it serves as a consistent marker repeated within each data frame. This repetition enables the receiver to accurately pinpoint the commencement of every frame. To achieve this, a standardized header bit sequence, specifically [10101], is concurrently applied to all emitters. This sequence is enacted in an alternating fashion between "on" and "off" states [10101].

Moving on to the second block, it accommodates the Identification (ID) data. This ID comprises 4+4+4 bits and conveys the geolocation information (x, y, z coordinates) of the emitters within the array. To encode these IDs, a 4-bit binary representation is adopted for decimal numbers. Notably, the z coordinate accounts for the floor number, which can be either positive or negative. To address this, the initial bit is employed to signify the sign of the floor number ("0" for positive, "1" for negative), with the remaining three bits encapsulating the numerical value of the coordinate.

In scenarios requiring bidirectional communication, user registration is necessitated. This process involves selecting a username (pin1) comprising four decimal numbers, with each number correspondingly linked to an RGBV channel. Additionally, should buddy friend services be sought, a 4-binary code for the meeting (pin2) must be provided.

The last segment, termed the δ block (steering angle δ), constitutes a 4-bit sequence. This component

completes the user's pose within the time frame q (x, y, δ, t). This pose is augmented with steering angle information, encompassing eight possible angles along the cardinal points. The significance of these angles, guiding the trajectory from a start point to the subsequent destination.

The codes assigned to both pin_2 and δ remain consistent across all channels. In scenarios where wayfinding services are unnecessary, these final three blocks assume a value of zero, thus furnishing the user solely with their own location information.

The third and concluding block is aptly labeled the "payload." This segment pertains to a sequence of bits that doesn't directly contribute to the navigation service. It encompasses miscellaneous data and concludes with a stop bit. To decode the information received via the photocurrent signal as captured by the photodetector, a crucial step is undertaken. This process relies on a calibration curve that has been pre-established to facilitate this mapping [10]. The calibration curve represents a sequence of bits meticulously designed to correspond to each conceivable decoding level. In essence, this calibration curve serves as a guide, aiding in the establishment of associations between photocurrent thresholds and specific bit sequences. In Fig. 3 a MUX/DEMUX signals of the calibrated cell is presented. In the same frame of time a random signal (Payload) is superimposed.

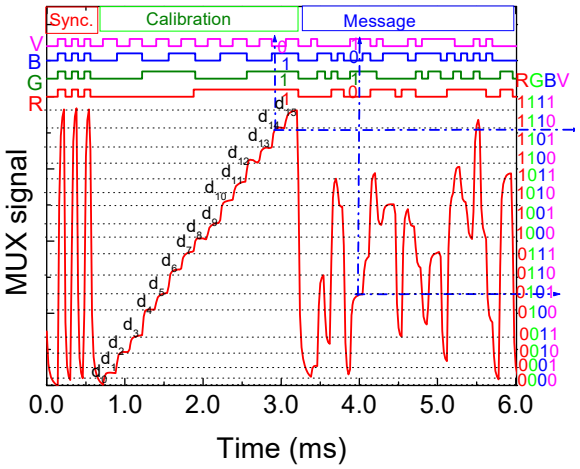

Fig. 3. MUX/DEMUX signals of the calibrated cell. In the same frame of time a random signal (Message) is superimposed.

This calibration curve leverages 16 distinct photocurrent thresholds. These thresholds correspond to bit sequences meticulously engineered to cover all sixteen permutations achievable from the four RGBV input channels (24 combinations). The brilliance of this approach lies in its simplicity: by juxtaposing the calibrated levels (d_0-d_{15}) with the assigned four-digit binary codes for each level, the decoding process becomes transparent and straightforward. This direct comparison illuminates the decoding pathway, rendering the message intelligible.

In Fig. 4 the MUX received signal and the decoding information that allows the VLC geotracking and navigation in successive instants (t_0, t_1, t_2) from user "7261" guiding him along his track is exemplified. The visualized cells, paths and the reference points (footprints) are also shown as inserts.

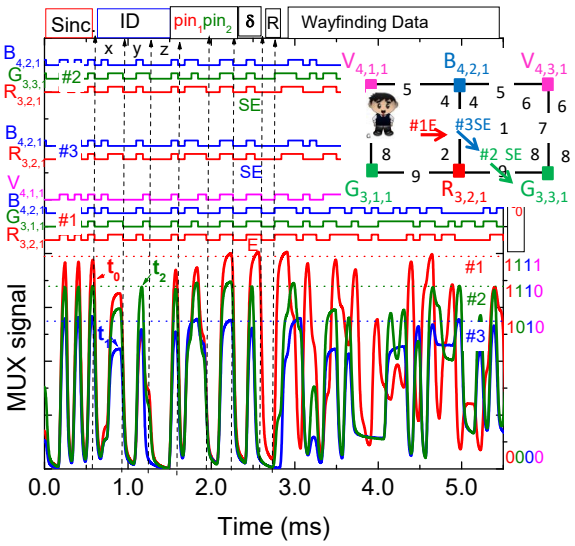

Fig. 4. Fine-grained indoor localization and navigation in successive instants. On the top the transmitted channels packets are decoded [R, G, B, V].

Here, the MUX received signal and the decoding information that allows the VLC geotracking and guidance in successive instants (t_0, t_1, t_2) from user "7261" guiding him along his track is exemplified. The visualized cells, paths, and the footprints are also shown as inserts. Data shows that at t_0 the network location of the received signals is $R_{3,2,1}$, $G_{3,1,1}$, $B_{4,2,1}$ and $V_{4,1,1}$, at t_1 the user receives the signal only from the $R_{3,2,1}$, $B_{4,2,1}$ nodes and at t_2 he was moved to the next cell since the node $G_{3,1,1}$ was added at the receiver. Hence, the mobile user "7261" begins his route into position #1 (t_0) and wants to be directed to his goal position, in the next cell (# 9). During the route the navigator is guided to E (code 3) and, at t_1, steers to SE (code 2), cross footprint #2 (t_3) and arrives to #9. The ceiling lamps (landmarks) spread over all the building and act as edge/fog nodes in the network, providing well-structured paths that maintain a navigator's orientation with respect to both the next landmark along the path and the distance to the eventual destination.

3.2. Multi-person Cooperative Localization and Guidance Services

In Fig. 5 the MUX synchronized signals received by two users that have requested guidance services, at different times, are displayed. In the top of the figure, the decoded information is shown and the simulated

scenario is inserted to guide the eyes. At the right hand the request/response information is inserted.

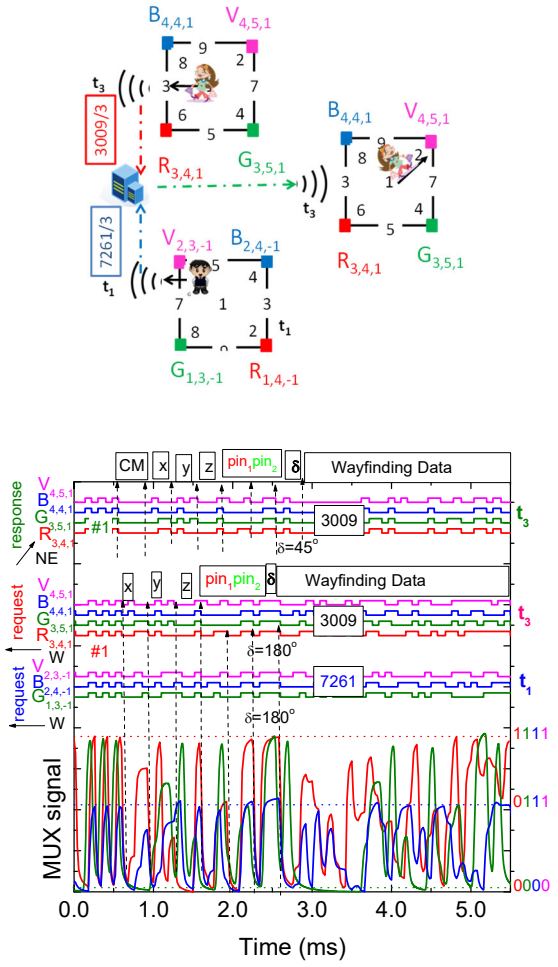

Fig. 5. MUX/DEMUX signals assigned requests from two users ("3009" and "7261") at different poses ($C_{4,4,1}$; #1W and $C_{2,3,-1}$; #6 W) and in successive instants (t_1 and t_3).

We have assumed that a user located at $C_{2,3,-1}$, arrived first (t_1), auto-identified as ($q_i(t_1)$, i="7261",) and informed the controller of his intention to find a friend for a previously scheduled meeting (code 3). A buddy list is then generated and will include all the users who have the same meeting code. User "3009" arrives later ($q_j(t_3)$), sends the alert notification ($C_{4,4,1}$; t_3) to be triggered when his friend is in his floor vicinity, level 1, identifies himself ("3009") and uses the same code (code 3), to track the best way to his meeting . The "request" message includes, beyond synchronism, the identification of the user ("3009"), its address and orientation, $q_i(t)$, ($C_{4,4,1}$, #1W) and the help requested (Wayfinding Data). Since a meet-up between users is expected, its code was inserted before the right track request. Upon receiving this request (t_3), the buddy finder service uses the location information from both devices to determine the proximity of their owners ($q_{ij}(t_3)$) and provides the best route to the meeting, avoiding crowded areas. In the "response", the block CM identifies the CM [0000] and the next blocks the cell address ($C_{4,4,1}$), the user (3009) for which the message is intended and finally the requested information: meeting code 3, orientation NE (code 4) and wayfinding instructions.

The outcomes of our study underscore the remarkable capabilities of VLC's dynamic LED-enhanced guidance system. This system not only furnishes users with precise and dependable route guidance but also empowers them to navigate effectively and engage in geotracking activities. As users traverse large building complexes, VLC technology offers a groundbreaking solution that steers them towards optimal routes while delivering continuous guidance throughout their journey.

The bidirectional communication prowess embedded within the system introduces a realm of possibilities for diverse services. Mission-critical applications can harness the inherent reliability and low-latency communication offered by the ID system. This reliability is particularly pertinent in scenarios requiring swift and trustworthy data exchange. Beyond this, the system's bidirectional communication capacities pave the way for an array of consumer-centric services. For instance, location-based advertisements can be intelligently deployed, personalized information can be seamlessly delivered, and indoor wayfinding functionalities can be fine-tuned to heighten user experiences within the building environment.

In essence, our research not only highlights the technical capabilities of the VLC-enabled guidance system but also envisions the transformative potential it holds for users within expansive indoor spaces. The system's dual nature, combining navigation and communication sets the stage for improved efficiency, enhanced experiences, and novel applications that redefine how individuals interact with and navigate through complex building structures.

4. Conclusions

This paper embarks on an exploration of the potential for Visible Light Communication (VLC) to revolutionize indoor navigation within vast building complexes. Tailored to the needs of mobile users, it introduces a novel guidance system that leverages the capabilities of VLC technology. Central to this system is a hybrid mesh cellular architecture, complemented by the establishment of an encompassing communication protocol tailored to multi-level scenarios.

The system acts as a steadfast navigational companion, seamlessly providing precise route guidance within complex indoor environments. The spectrum of functionalities includes navigation assistance, real-time route tracking, and reliable guidance for users in motion. The culmination of our experimental endeavors is reflected in global results, where the successful localization of mobile receivers coincides with the simultaneous transmission of data. A distinctive hallmark emerges in the form of a cooperative localization mechanism. As regions within

the environment become densely populated, this mechanism adeptly adapts by autonomously rescheduling localization tasks. This dynamic feature orchestrates the dissemination of guidance information and issues alerts, ensuring a responsive approach to dynamic environmental conditions.

Acknowledgements

This research was funded (in part) by the Portuguese FCT program, Center of Technology and Systems (CTS) UIDB / 00066 / 2020 / UIDP / 00066 / 2020 and by IPL/2022 / POSEIDON_ISEL.

References

[1]. Hassan, N. U., Naeem, A., Pasha, M. A. and Adoon, T. J. , Indoor Positioning Using Visible LED Lights: A Survey, *ACM Computing Surveys,* Vol. 48, 2015, pp. 1-32.

[2]. Tsonev, D., Chun, H., Rajbhandari, H., S., McKendry, J., Videv, S., Gu, E., Haji, M., Watson, Kelly, S. A., Faulkner, G., Dawson, M., Haas, H., and O'Brien, D., A 3-Gb/s single-LED OFDM-based wireless VLC link using a Gallium Nitride μLED, *IEEE Photon. Technol. Lett.*, 26, 7, 2014, pp. 637–640.

[3]. O'Brien, D.H., Minh, L., Zeng, L., Faulkner, G., Lee, K., Jung, D., Oh, Y., and Won, E. T., Indoor visible light communications: challenges and prospects, *Proc. SPIE 7091*, 2008*,* 709106.

[4]. Hassan, N. U., Naeem, A., Pasha, M. A., Jadoon, T., and Yuen, C., Indoor positioning using visible led lights: A survey, *ACM Comput. Surv*., Vol. 48, 2015, pp. 1–32.

[5]. Ozgur, E., Dinc, E., Akan, O. B., Communicate to illuminate: State-of-the-art and research challenges for visible light communications, *Physical Communication*, 17, 2015, pp. 72–85.

[6]. Vieira, M., Louro, P., Fernandes, M., Vieira, M. A., Fantoni, A. and Costa, J., Three Transducers Embedded into One Single SiC Photodetector: LSP Direct Image Sensor, Optical Amplifier and Demux Device, in Advances in Photodiodes, *InTech*, Chap. 19, 2011, pp. 403-425.

[7]. Vieira, M. A., Louro, P., Vieira, M., Fantoni, A. and A. Steiger-Garção, Light-activated amplification in Si-C tandem devices: A capacitive active filter model, *IEEE Sensor Journal*, 12, 6, 2012, pp. 1755-1762.

[8]. Vieira, M. Vieira, M. A., Louro, P., Vieira, P., Fantoni, A., Light-emitting diodes aided indoor localization using visible light communication technology, *Opt. Eng.* 57, 8, 2018, 087105.

[9]. Vieira, M. A., Vieira, M., Louro, P., Vieira, P., Bi-directional communication between infrastructures and vehicles through visible light, *Proc. SPIE 11207, Fourth International Conference on Applications of Optics and Photonics*, 3 October 2019, 112070C.

[10]. Vieira, M., Vieira, M. A., Louro, P., Fantoni, A., Vieira, P. Dynamic VLC navigation system in Crowded Buildings, *International Journal on Advances in Software,* 14, 3-4, 2021, pp. 141-150.

(015)

Classification of Sports Exercises and Repetition Counting based on Inertial Measurement Data

P. Krutz [1], M. Rehm [1], Z. Lang [1], M. Dix [1] and J. Patalas-Maliszewska [2]
[1] Chemnitz University of Technology, Institute for Machine Tools and Production Systems, Reichenhainer Strasse 70, 09126 Chemnitz, Germany
[2] University of Zielona Góra, Institute of Mechanical Engineering, 65-417 Zielona Gora, Poland
Tel.: +4937153134950
E-mail: pascal.krutz@mb.tu-chemnitz.de

Summary: Inertial measurement units (IMU) are often used in the field of Human Activity Recognition (HAR) and were also used in this work with the additional possibility of recording absolute positions by ultra-wideband measurement. Seven different sports exercises were recorded within the framework of a study, including 21 participants. After data preprocessing, artificial neural network structures were trained for exercise classification and an optimisation of the hyperparameters was carried out. The performance of the trained models was compared and validation accuracies of up to 91.6 % were achieved. Another focus was to implement an algorithm to count the correct completed repetitions independently of the type of activity. For this purpose, the distance within the samples presented in matrix form was calculated, which made it unnecessary to select characteristic signal variables specific to the exercise. Despite its comparatively simple structure, the implemented counting algorithm showed promising results, which could be further optimised by several post-processing routines.

Keywords: Inertial sensors, Human activity recognition, Repetition counting, Machine learning, Artificial neural networks.

1. Introduction

IMU sensors, in combination with broadband technologies and high-performance algorithms, offer great potential in the detection, monitoring and improvement of sports exercises. Especially in times of a lack of skilled workers and the demands resulting from the increasing individualisation of personal leisure time, digital therapy and training methods are needed for both the physiotherapy and fitness markets.

Typically, methods of supervised learning are predominantly used in the field of HAR. The most common approaches in the literature are those based on Support Vector Machine [1-3], followed by Naive Bayesian [4, 5] and k-Nearest Neigbour [6]. Less common are deep learning approaches using Convolutional Neural Networks (CNN) [7] and Long Short Term Memory (LSTM) Networks [8]. Unsupervised learning methods are the exception and have so far only been used to count the number of repetitions, for example in tennis strokes [9]. The work is based on preliminary work [10, 11] on supervised learning of three sports exercises, where high accuracy was achieved with both the classifiers and the neural networks used. The workflow included data acquisition and preprocessing, the training of AI models, the optimisation of model parameters and a final evaluation of model performance.

This study aims to choose, optimize and compare model structures and parameters for supervised learning using an extended database. The database consists of recordings of seven different sports activities performed by 21 participants. Another focus of this paper is the development of a universal counting algorithm suitable for counting repetitions of any sport activity.

2. Data Generation and Preprocessing

Within the study with 21 participants, 7 different exercises were completed at one sports device as successive sets. The execution of the different activities is shown in Fig. 1.

Fig. 1. Recorded exercises on the sports device, 1-support, 2-squats, 3-dips, 4-lunges, 5-pull ups, 6-sit ups, 7-pushups.

The exercises support, squats, dips, lunges, pull-ups, sit-ups and push-ups were recorded as continuous recordings with IMUs at the positions chest, hand and

foot. With a set sampling rate of 30 Hz the quantities linear axial accelerations, rotation rates, orientations (Euler angles, quaternions, magnetic flux densities), absolute pressure and the Cartesian position in space were captured. The time series were labelled during the recording process by switching the subjects between pause and activity intervals using a wearable device. In total, around 230 minutes of exercise data were recorded, divided into 24 exercise sets, which also included intervals of stretching and loosening exercises, labelled as pauses. Signal interruptions that occurred were linearly interpolated during data pre-processing and the time series of three IMUs were synchronised. The distribution of the generated motion data to the different classes is shown in Table 1. As can be seen from this, about half of the total amount of data belongs to the pause intervals. Despite the comparatively high volume of seemingly unnecessary data, it was fully utilized for model training in order to train the ability to distinguish between pause and active intervals.

Table 1. Distribution of classes in the used database.

class	lunges	dips	pull-ups	squats
# Samples	38997	22675	21736	32288
percentage [%]	9.39	5.46	5.23	7.77
class	**push-ups**	**pauses**	**sit-ups**	**support**
# Samples	21958	220290	32544	24816
percentage [%]	5.29	53.04	7.84	5.98

3. Training, Optimization and Compare of KNN

The supervised models were trained in Matlab R2022b. At first, the number of input variables was reduced to 36 by using only the linear accelerations, rotation rates, magnetometer data and Euler angles. Also the data were divided by segmentation in order to be able to process the time series as sequential data in Matlab. To ensure a diverse distribution of unbalanced data across the training and holdout validation sets, a segment length of 500 samples was chosen (corresponding to approximately 16 s of workout time). The ratio for the validation data holdout was set to 0.3. Consequently, 582 sequence blocks of training data and 249 blocks of validation data were generated. Subsequently, a LSTM- and a CNN-network were trained and an optimisation of the hyperparameters was carried out. The CNN network can be described as a temporal convolutional network (TCN), which consists of several CNN blocks connected in series. The time series are scanned in the form of a receptive field, the extent of which is influenced, for example, by the number of blocks. [12] The most accurate models are compared in Table 2 with the accuracies achieved and the training times required. The TCN could be trained more than three times as fast as the LSTM with slightly better accuracy.

Table 2. Comparison of the trained LSTM and TCN structures with the highest accuracies.

model	training time	accuracy		worst F1-score (class)
		training	validation	
LSTM	13 min 26 s	94.2	90.8	83.8 (pull-ups)
TCN	3 min 49 s	95.5	91.6	83.4 (pull-ups)

Fig. 2 shows the obtained confusion chart for validating the TCN. One possible reason for incorrect assignments after the optimisation of the hyperparameters can be justified with the applied methodology for labelling the data. In this study, the test persons independently initiate the beginning and end of an exercise interval by operating a wearable, implying that the activity ranges are not uniformly defined. This can be observed in the false positives and false negatives elements of the pause class, which contain significantly more samples than the other classes. However, this effect was already reduced by the implementation of a three-second countdown between the actuated switch-over point and the beginning of the exercise execution. However, deviations remain, especially in exercises where the starting position can only be assumed after the wearable has been activated (e.g. pull-ups and dips).

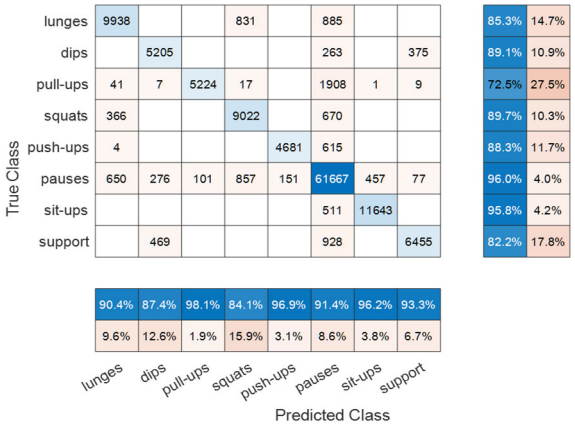

Fig. 2. Confusion matrix for applying the trained TCN on the validation data.

Furthermore, it must be taken into consideration that the subjects were largely unrestricted in their exercise execution. Different variations were tolerated, e.g. squats with stretched or bent arms and also simplified executions (e.g. pull-ups in inclined posture). Despite the fact that some exercises have a high degree of similarity (e.g. lunges/squats, dips/support), inter activity mismatch is limited. Fig. 3 shows the TCN model predictions for a section of the validation dataset. There are occasionally false assignments, which were filtered out by post-processing. In the smoothed prediction that is also shown, a sliding window of 50 samples was used to determine the dominant class in each window, which slightly improves the overall accuracy of the validation by additional 0.4 %.

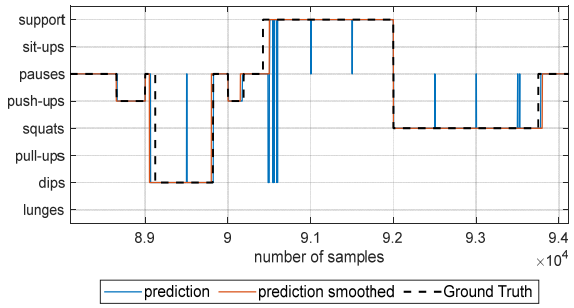

Fig. 3. Temporal course of the TCN model predictions for a segment of the validation data, comparing model prediction (non-smoothed/smoothed) and ground truth.

4. Repetition Counting

The execution of repetitive exercises is visible as a periodic progression of individual measured variables, which differ in type and curve progression depending on the respective type of exercise. In order to reduce the data load and to improve the generalisability of the implemented algorithms, the strategy was to use only variables that are independent of the orientation and position of the subjects. Therefore, only the values of the axial accelerations and rotation rates were considered. Consequently, 18 measurement variables were used to determine the number of completed repetitions. As the value ranges of the inertial measurement variables are widely distributed, symmetrical normalisation was applied to all variables in the interval [-1...+1].

In order to enable an evaluation of the counting algorithm without the influence of an upstream model for classification, the ground truth labels were used for the development of the counting algorithm. It is also important to mention that only the activity intervals in their chronological order from the recording were used as the data basis for the analysis. This order of data would also be present in a potential interconnection of model and counting algorithm, when the latter receives sequences of predictions by the classification model. Consequently, 24 sets in total were analysed in series by the counting algorithm.

The special requirement in this work was to find a parameter that shows an oscillating course for a variety of different sports exercises. Such an exercise-independent parameter can be calculated with the distance *Dis* between a pattern segment *A* and every segment *B* of the respective activity as described in equation (1) and (2). *A* and *B* are matrices with the dimension *m* x *n*, where *m* defines the number of samples, also called segment length and *n* the number of features for one segment.

$$C = A - B = \begin{bmatrix} a_{11} - b_{11} & \cdots & a_{1n} - b_{1n} \\ \vdots & \ddots & \vdots \\ a_{m1} - b_{m1} & \cdots & a_{mn} - b_{mn} \end{bmatrix}, (A, B \in \mathbb{R}^{m \times n}) \quad (1)$$

$$Dis(A,B) = \sum_{i=1,j=1}^{i=m,j=n} |c_{ij}| = \sum_{i=1,j=1}^{i=m,j=n} |a_{ij} - b_{ij}| \quad (2)$$

The pattern segment was selected in the centre of each exercise interval to avoid the influence of transition areas between other classes because, as previously mentioned, it was not possible to precisely define the start and end points of an exercise execution. After the segment length was set to 30 samples, the distances for all segments of an activity interval were calculated with a step size of one sample. The obtained distance values were smoothed by a moving average filter with a bandwidth of 15. Additionally, the median was calculated for each interval of smoothed distance values. The courses of unfiltered/filtered distances and the median values are presented in Fig. 4 for an exemplary execution of six pull-ups. The oscillating distance curves represent the number of completed repetitions. A characteristic attribute is that the distance increases significantly at the borders of an interval to be examined. In addition, the distance in the area of the pattern segment becomes zero. To count the repetitions, the number of intersections at the falling edge of smoothed distance values and the median were analyzed (red crosses in Fig. 4).

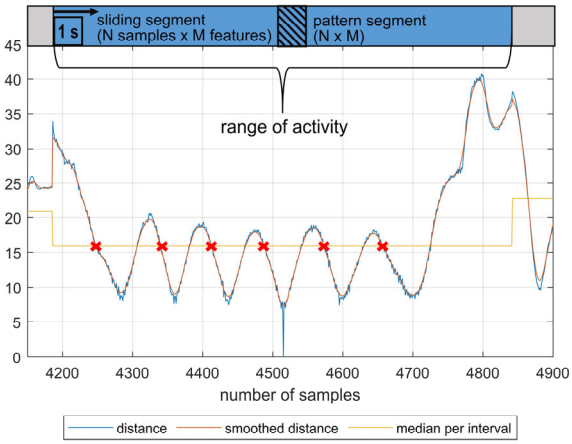

Fig. 4. Calculated distance values for the execution of six pull-ups, marking the counted intersections with the median at falling flank (N = 30, M = 18).

To evaluate the accuracy of the counting algorithm, the deviation rate and the class-wise deviation rate were used, described in (3) and (4). The deviation rate δ is signed and thus enables the assessment of whether too many or too few repetitons *Rc* have been counted in an exercise set. When determining the class-wise deviation rate δ_{class} for *n* records, the amounts of the individual deviation rates are calculated. All deviation rates are relativised by multiplying with the true number of repetitions *Rt*.

$$\delta = \frac{Rc - Rt}{Rt} \quad (3)$$

$$\delta_{class} = \frac{\sum_{i=1}^{i=n} Rt_i \cdot |\delta_i|}{\sum_{i=1}^{i=n} Rt_i} \quad (4)$$

In order to obtain a final value for the overall performance of the counting algorithm for a larger number of trials, δ_{SUM} was calculated with the weighted averaged of δ_{class}, considering the overall distribution of the m activity-classes and shown in equitation (5). There n_m is the number of samples of each activity-class and n_A the number of all activity-samples.

$$\delta_{SUM} = \frac{\sum_{i=1}^{i=m} \delta_{class} \cdot n_m}{n_A} \quad (5)$$

Table 3 shows the results of experiments for optimising the counting algorithm by varying the features and the segment length for distance calculation. First, the features were varied, using a segment length of 30 samples. The deviation rates listed (class-wise and weighted average) suggest that the accelerations (acc) have a significantly higher influence for successful repetition counting than the gyroscope data (gyro). The lowest δ_{SUM} was determined with a combination of rotation rates and accelerations and was therefore defined as the feature setting for the further investigations. The lower part of Table 3 shows the results of varying the segment length, i.e. the number of samples used to calculate the distance. It was varied in the range of 20 to 70 samples, with the best results obtained for the already used 30 samples and, with an additional minimal improvement of 0.7 % for δ_{SUM}, with 50 samples segment length.

For the detailed consideration of the class-wise delta, these two mentioned tests are considered (highlighted grey in Table 3). In both cases, the δ_{class} was most significant for the support class with 21.2 % and 23.9 % respectively. In contrast, the classes squats and sit-ups were the most reliably counted by far with δ_{class} between 2.3 % and 3 %.

Table 3. Results of optimisiation experiments, determine the deviation rates for the activities (1-support, 2-squats, 3-dips, 4-lunges, 5-pull ups, 6-sit ups, 7-push-ups) and the overall deviation.

	δ_{class} in %							δ_{SUM} in %
	1	2	3	4	5	6	7	
variable feature selection, segment length = 30								
acc + gyro	21.2	2.8	19.3	15.0	9.1	2.9	7.9	**10.8**
acc	18.6	8.3	14.6	13.4	7.5	5.2	9.0	10.9
gyro	38.3	3.9	34.8	58.1	28.6	11.7	10.7	27.5
variable segment length, features: acc + gyro								
20	19.7	4.4	21.5	23.5	12.1	7.3	9.0	14.0
40	23.9	3.0	19.3	14.2	8.5	2.6	7.3	10.8
50	23.9	3.0	15.9	12.4	9.6	2.3	7.3	**10.1**
60	23.1	3.0	16.7	12.4	14.6	2.6	7.9	10.8
70	26.1	2.8	19.3	13.7	14.6	3.5	9.0	12.0

In order to analyse possible causes for the partly very different values of δ_{class}, the deviations for each of the 24 recorded sets were considered for the upper, highlighted parameterisation in Table 3. Occurring δ with a modulus greater than 0.3 were examined in more detail. Typical scenarios for exceed and fall below the true number of repetitions were identified from different recordings and are presented below.

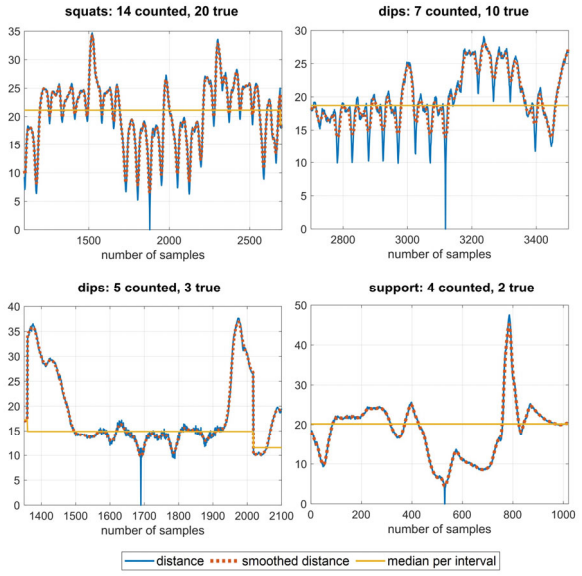

Fig. 5. Progressions of the distance values for incorrectly counted repetitions, top: lower deviation to the true number of repetitions ($\delta < 0$), bottom: exceeding true repetitions ($\delta > 0$); respective indication of the type of exercise with true and counted repetitions.

In Fig. 5 top left, the performance of squats is shown where the exercise execution was varied within the interval. As a result, the median is too high in the immediate vicinity of the pattern segment, so that there are no intersections with falling edges in this area. The upper right part of the figure is similar. Here, several repetitions of dips at the end of the interval were also no longer detected. In the lower part of Fig. 5, too few dips were recorded in the left example. Here the recognisable periodic progression of the distance values was comparatively short, which suggests only a short execution within the labelled active interval. In the fourth example (bottom right), the two completed repetitions of the support exercise cannot be identified in the progression. One interpretation is that the exercise was performed very irregularly, it is also possible that the test person was physically overloaded. Finally, it can be stated with regard to the evaluation of the faulty intervals that the implemented methodology is particularly susceptible to errors when exercises are performed irregularly. The observation that irregular execution is caused by physical overstress among the test subjects is supported by a dependable analysis of relatively simple exercises, like squats and sit-ups. A special status is occupied by the lunges, whose execution (step position of left and right foot alternately or identical for several repetitions) was

not exactly defined, which indicates that the sensor attached to only one foot does not contribute to a periodic progression of the distance values for all movements.

5. Discussion and Conclusion

In the presented work, a recorded data set with seven sports activities was examined. The first step was to classify the completed exercises using supervised machine learning methods. Two different network structures (LSTM and TCN) were trained and the hyperparameters of the models were iteratively optimised. The TCN model gave a good performance with 91.6 % validation accuracy using significantly shorter training times. One way to improve the accuracy of the prediction is by post-processing the labels produced during recording. This will enable a more accurate determination of the pure duration of the exercise, as it has been shown that the dominant percentage of misclassifications is caused by confusion of the break class with other activities. For further investigations, the interconnection of several classification levels would be another possible approach to further increase the model accuracy. For post-processing of the model predictions, a smoothing algorithm was applied that determined the dominant prediction class using a filter width of 50 samples. Although the overall accuracy of the prediction was only slightly improved to 0.4 %, the described procedure can optimise the user experience in possible applications for real-time recognition.

The second crucial aspect of the study involved developing a counting algorithm to track completed exercise repetitions. By calculating distance values for a pattern segment defined within an exercise interval, the number of repetitions could be made visible for all activities on the basis of this one parameter, which made the class-specific analysis of individual signal variables unnecessary. In order to finally determine the number of repetitions in an algorithmic way, the intersections of the distance values with the median of all distances of a single exercise phase were evaluated. For performance evaluation with different parameterisations (segment length, input features), the deviation rate was introduced. The implemented algorithm performed well when counting regular executions. The key advantage of the approach is its ability to load a new pattern segment as a reference for each new exercise interval, resulting in a highly robust algorithm capable of accommodating different people and their specific type of exercise execution. However, it is a precondition that the individual repetitions within an active exercise are performed very uniformly, which tends to lead to deviations in the case of conditionally demanding exercises. Furthermore, the calculated median of the distances was not always ideal, so that executions were not counted at all or even counted twice. Here, it would also be of interest for further research to develop a more robust processing method for irregular distance patterns.

Acknowledgements

This publication is funded by the Federal German Ministry for Economic Affairs and Climate Action.

References

[1]. S. Kautz et. al., Activity recognition in beach volleyball using a deep convolutional neural network, *Data Mining and Knowledge Discovery*, 2017, pp. 1–28.

[2]. Brock, H., Ohgi, Y., Assessing motion style errors in ski jumping using inertial sensor devices, *IEEE Sensors Journal*, 99, 2017, pp. 1–11.

[3]. Pernek, I. et.al., Recognizing the intensity of strength training exercises with wearable sensors, *Journal of Biomedical Informatics*, 58, 2015, pp. 145–155.

[4]. Connaghan, D. et. al., Multi-sensor classification of tennis strokes, *Sensors*, 2011, pp. 1437–1440.

[5]. Schuldhaus, D. et. al., Inertial sensor-based approach for shot/pass classification during a soccer match, in *Proceedings of the 21st ACM KDD Workshop on Large-Scale Sports Analytics*, Sydney, Australia, 2015, pp. 1–4.

[6]. Groh, B. H. et. al., Classification and visualization of skateboard tricks using wearable sensors, *Pervasive and Mobile Computing*, 40, 2017, pp. 42–55.

[7]. Jiao, L. et al., Multi-sensor Golf Swing Classification Using Deep CNN, in *Procedia Computer Science*, 129, 2018, pp. 59–65.

[8]. Rassem, A. et. al., Cross-country skiing gears classification using deep learning, *ArXiv Preprint* ArXiv:1706.08924, 2017.

[9]. Kos, M., Kramberger, I., A wearable device and system for movement and biometric data acquisition for sports applications, *IEEE Access*, 2017, pp. 6411–6420.

[10]. Patalas-Maliszewska, J. et. al., Inertial Sensor-Based Sport Activity Advisory System Using Machine Learning Algorithms, *Sensors*, 23, 3, 2023, 1137.

[11]. Pajak, I. et. al., Sports activity recognition with UWB and inertial sensors using deep learning approach, in *Proceedings of the IEEE International Conference on Fuzzy Systems (FUZZ-IEEE' 2022)*, 2022, pp. 1-8.

[12]. Mathworks: Sequence-to-Sequence Classification Using 1-D Convolutions, https://de.mathworks.com /help/deeplearning/ug/sequence-to-sequence-classification-using-1-d-convolutions.html, 19.07.2023.

(016)

Difference in Sensor Placement Position of Insole-type Pressure Transducers

Y. Uchida [1], T. Funayama [2], E. Ohkubo [1] and Y. Kogure [3]
[1] Dept. of Life Science, Teikyo University of Science, Adachi-ku, 120-0045 Tokyo, Japan
[2] Dept. of Occupational Therapy, Teikyo University of Science, Uenohara-shi, 409-0193 Yamanashi, Japan
[3] Professor Emeritus, Teikyo University of Science, Adachi-ku, 120-0045 Tokyo, Japan
Tel.: + 81369101010, fax: + 81369103800
E-mail: uchida@ntu.ac.jp

Summary: A system aimed at detecting changes in physical condition is proposed in this study. To reduce costs, the number of pressure sensors is limited to four. The system evaluates the changes in the load applied to each sensor on the insoles. Commercially available insoles are classified into S, M, and L sizes and are cut to fit the shoe size. Consequently, sensors are not always attached to the appropriate position on the insole, and substantial variations are expected to occur because of misalignment. We found that the output characteristics differed significantly depending on the position of the toe sensor. In particular, the toe length varies considerably among individuals, and it is important to adjust the sensor position to suit each individual. The peak value of the sensor output and the steepest slope value at the subsequent decrease emerged as promising feature values. The incorporation of machine learning into the output results, including other sensor positions, is expected to yield more accurate data.

Keywords: Insole, Pressure sensors, Health condition, Arduino nano, Bluetooth, Decision tree, Machine learning.

1. Introduction

Rapid aging is a global problem [1] that is expected to become a major societal concern not only in Europe but also in Asia [2]. The number of caregivers for the elderly is expected to increase due to the declining birth rate, and the number of caregivers for each elderly person is expected to decrease, resulting in the elderly being cared for by the elderly. Among the primary concerns in caring for the elderly is that they may become bedridden owing to fractures caused by falls.

Many studies have employed images and sensors to prevent falls [3-7]. Insole sensors, which are commercially available and relatively easy to use, are often used to prevent falls because the gait state is greatly influenced by physical conditions. While these commercial insole sensors were mainly developed for athletes, they have attracted considerable interest for their relevance to lower limb dynamics, crucial not only for runners but also for people of all ages. Furthermore, there is a growing interest in gait analysis within rehabilitation centers and facilities dedicated to the elderly.

We previously reported a sensor that is used as a reference when determining movement limitation states using data from the insole sensor pressure distribution [8-10]. The e-rubber smart insole, known as FEELSOLE®, was available in three sizes (S, M, and L) with 2 cm increments. In this case, the output of the toes seemed low, which raised the question of whether it was important to accurately determine the sensor position. Because the tip of each toe has a short bone, a slight difference in the sensor ground position may affect the output. There are diseases and disorders for which information from the toe portion of the insole is important, including hammertoe, a condition in which the toes are bent.

Therefore, we fabricated a device in which the pressure sensor was fixed to the shoe insole with tape to allow the sensor position to change arbitrarily. Using this insole, the pressure changes during walking were examined by changing the position of the toe sensor, and the effects of different sensor positions were investigated.

The research was approved by the Ethics Committee of Teikyo University of Science.

2. Experimental

The pressure distribution screen of a commercially available smart insole shows the pressure applied to the sensor in different colors. In an initial experiment to determine the optimal sensor position, the sensor was placed as shown in Fig. 1(a) using an INTERLINK FSR-402 sensor to obtain the foot pressure distribution for comparison with the simplified display. The sensor was affixed to four locations: 15 mm from the toe, 60 mm from the inside and outside of the foot, and 20 mm from the heel. The side with the affixed sensor faced downwards. As the experiment progressed, as shown in Fig. 1(b), measurements were obtained by changing the sensor placement position to 80 and 90 mm for the inner and outer sensor positions, respectively. This adjustment aimed to achieve a more accurate distribution of foot pressure. As shown in Fig. 2, the system uses an Arduino Nano to convert analog signals from the sensors into digital format and sends them to a PC via Bluetooth using a Microchip SDB with PIC24FJ64GB004. The received signals were

processed by a program created by processing, and the files were saved. For comparison, the smart insole FEELSOLE® was used on top of the fabricated insoles. Because of the cushioning effect of the smart insole, the output of the homemade insole sensor was approximately 0.5V lower. A 9V battery was used for this prototype owing to the unavailability of a polymer battery charger during the prototype phase due to supply shortage. A homemade insole sensor was attached to the right foot for measurement. Sandals were used instead of shoes, primarily because patients in Japanese hospitals prefer sandals owing to their ease of removal and wear. Moreover, this choice facilitates easy wiring of sensor signals to the Arduino Nano and Microchip SBDBT attached to the top of the footwear.

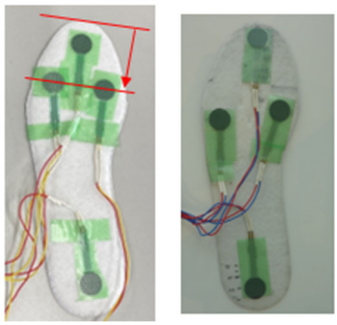

(a) (b)

Fig. 1. Sensor position.

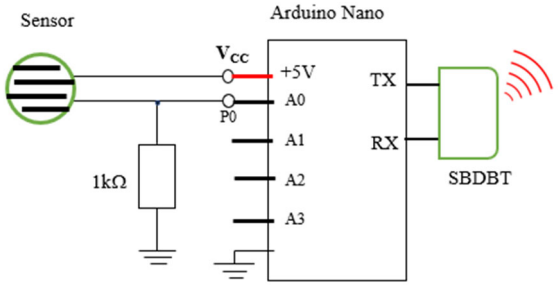

Fig. 2. Measurement system.

During the measurement, the participant walked for approximately 30 or 60 s, with and without motion restriction on the right knee joint using a supporter, for a distance of approximately 3 m. A video was captured from the front for separate analysis. While walking, the participant repeatedly performed U-turns and straight turns. The position of the sensor was varied from the tip of the insole to examine the relationship between the sensor position and the presence or absence of motion restriction in the right knee joint. At 70 mm, the sensor position was lower than that of the inside and outside sensors, as shown in the photograph in Fig. 1(a).

The participant was a male in his 60s. Exercise restriction was simulated using a supporter in the knee area.

3. Results

3.1. Output Waveforms from a Self-made Insole Sensor

With the sensor positioned 15 mm from the tip of the insole, the measurement results during walking with and without motion restriction are shown in Figs. 3 (a) and (b), respectively. The position of the peak was different in each cycle, and the output voltage was lower in some cycles. In the absence of motion restriction, the signal decreased with time.

Assuming that the low-output state below 50 % of the peak value corresponded to the state at the U-turn, we compared the difference between the peak (maximum value) and the minimum value among four consecutive values in the interval up to the low-output value before the first U-turn. The interval was used as a break in this case. The difference tended to be larger under these limitations.

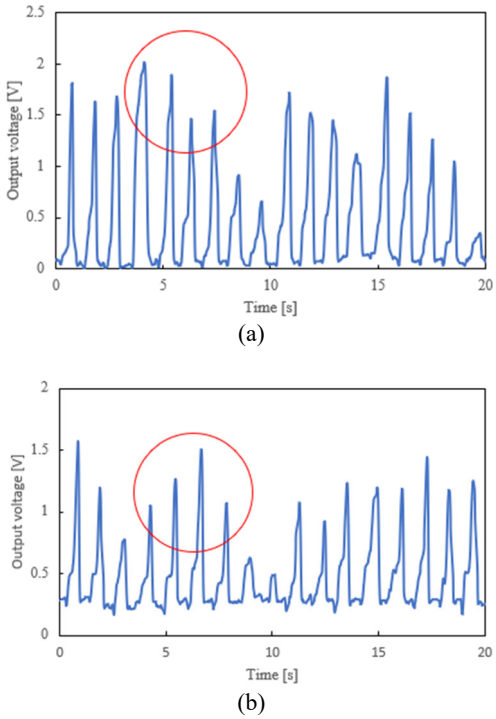

Fig.3. Measurement results during walking without (a), and with motion restriction (b).

3.2. Comparison of Average Output Voltages and the Difference between Maximum and Minimum Output Voltages

The sensor position from the toe was varied from 15 mm to 70 mm. Fig. 4 illustrates two characteristic examples: the average of the four sensor output voltages and the difference between the maximum and minimum output voltages. In the figure, Toe represents the case without motion limitation, ToeR represents the case with motion limitation, and labels marked as dif represent the maximum and minimum voltage differences.

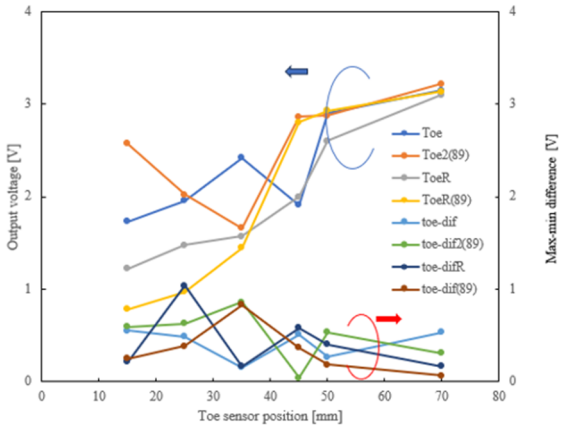

Fig. 4. Average of four sensor output voltages and the difference between maximum and minimum voltages.

When the sensor position of the toe was changed without motion restriction, different results were obtained. The output was such that the characteristics shifted to the left, except for the area close to the tip, but the output voltage at a distance closer to the tip increased. The trend of the difference between the maximum and minimum values did not change significantly with or without motion limitation, or with different measurements.

3.3. Change in Peak Value with no Motion Limitation by Self-made Device

A decrease in the output voltage was observed with the passage of measurement time when the toe sensor position was changed. The time variation of the peak value when the toe sensor position was changed is shown in Fig. 5. The horizontal axis represents the point evaluated as the peak, and not the time, owing to the nature of the evaluation software. The peak points correspond to the measurement time, and at 50 mm, the values are almost stable, except for the U-turn point.

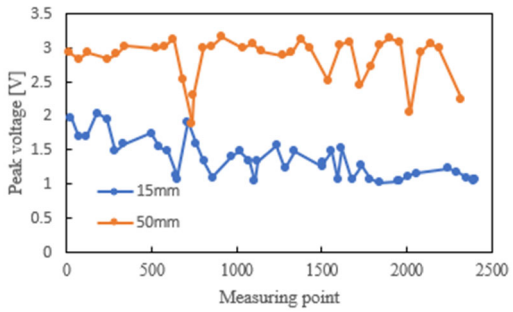

Fig. 5. Change in peak value with no motion limitation by self-made device.

3.4. Output from Smart Insole

The output from the smart sensor was obtained for confirmation because the output from the self-made insole sensor decreased with time. The results are shown in Fig. 6. The unit of output from the smart insole was N. Because the sensor position of the smart insole did not change, slight variations in amplitude were observed while the period remained relatively constant. This differed from the observed output pattern of the self-made insole sensor.

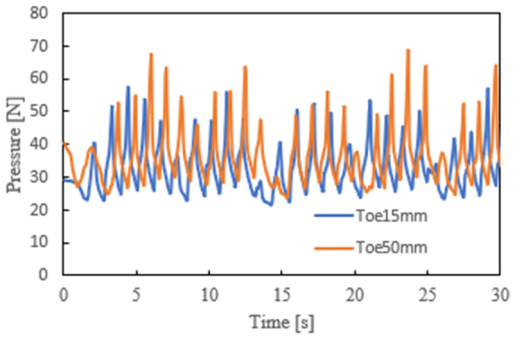

Fig. 6. Output of the smart insole sensor when the position of the self-made sensor was changed.

3.5. Classification using a Decision Tree

As reported in SEIA' 2022 and our previous paper, the set of peak values and the steepest slope values in the decreasing portion after the peak reflect the participant's characteristics. Based on this idea, we attempted classification using a decision tree with the output from the sensor at the toe portion and the maximum slope in the decreasing portion after the peak. The results are shown in Fig. 7. The restricted and unrestricted data are circled in red and black, respectively. It is evident that the two regions can be classified.

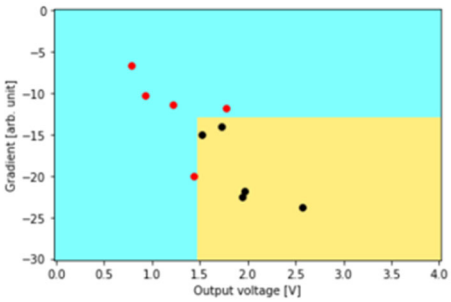

Fig. 7. Classification using a decision tree.

4. Discussion

4.1. Sensor Position and Motion Limitation

Up to a sensor position of approximately 35 mm, the output voltage was larger when no restriction was applied than when a restriction was applied, probably because of the smaller kick of the foot during walking when restricted and the foot was flat with the right foot landing evenly. The toes of the subjects were located 40 mm from the base of the toes to the tips of the feet.

Therefore, the toe sensor was closer to the medial and lateral sensors at a position of 45 mm or more, such that the output was almost the same, regardless of the limitation. This supports the case where the output data from the sensors on the toe side vary considerably depending on the sensor position around the base of the toes. In contrast, minimal changes are observed when the toes are closer to the center of the foot. In addition, the range between the maximum and minimum values increased when there was a restriction because the landing of the foot at each time during walking varied.

4.2. Comparison of Two Types of Insole Sensors

In this experiment, the choice of sandals allowed easy shifting of the insole, leading to frequent changes in the position of the sensor. This is believed to be the case in this study. This highlights the importance of therapists ensuring the sensor is accurately fixed to the desired position to increase the reproducibility of the experiment.

4.3. Consideration of Classification Methods

Although the number of experiments conducted was small, we successfully demonstrated that decision-tree classification based on the set of peak values and the steepest slope value in the decreasing portion after the peak could be used to classify the data into two groups. However, the boundary area does not differ significantly. Thus, it is necessary to increase the amount of data and consider a classification method such as a support vector machine.

5. Conclusions

It is desirable to consider the sensor position corresponding to the participant's characteristics so that the therapist can obtain the desired data using an insole sensor. However, owing to cost constraints, it is important to select features that consider variations in sensor positions. We found that one candidate is the slope that indicates a decrease after the peak value, which we have proposed.

Acknowledgments

This work was supported by JSPS KAKENHI, Grant Numbers JP20K11924 and JP23K11207.

References

[1]. J. D. Sciubba, Population Aging as a Global Issue, *Oxford Research Encyclopedia of International Studies*, Oxford, UK, 2020.

[2]. T. Jayawardhana, S. Anuththara, T. Nimnadi, R. Karadaanaarachchi, R. Jayathilaka, and K. Galappaththi, Asian Ageing: The relationship between the elderly population and economic growth in the Asian context, *PLOS ONE*, 18, 4, 2023, e0284895.

[3]. M. M. Alam, and E. B. Hamida, Surveying Wearable Human Assistive Technology for Life and Safety Critical Applications: Standards, Challenges and Opportunities, *Sensors*, 2014, 14, pp. 9153-9209.

[4]. X. Qian, H. Cheng, D. Chen, Q. Liu, H. Chen, H. Jiang, and M-C. Huang, The Smart Insole: A Pilot Study of Fall Detection, *BODYNTES*, 2019, LNICST 297, pp. 37-49.

[5]. S. Subramaniam, S. Majumder, A. I. Faisal, and M. J. Deen, Insole-Based systems for Health Monitoring: current Solutions and Research Challenges, *Sensors*, 2022, 22, 438.

[6]. S. Usmani, A. Saboor, M. Haris, M. A. Khan and H. Park, Latest Research Trends in Fall Detection and Prevention Using Machine Learning: A systematic Review, *Sensors,* 2021, 21, 2021, 5134.

[7]. Y. Uchida, T. Funayama, Hori, M. Yuge, N. Shinozuka and Y. Kogure, Possibility of Detecting Changes in Health Conditions using an Improved 2D Array Sensor System, *Sensors & Transducers*, Vol. 259, Issue 5, 2022, pp. 29-36.

[8]. T. Funayama, Y. Uchida, and Y. Kogure, Assessment of Walking Condition Using Pressure Sensors in the Floor Mat, in *Proceedings of the Eleventh International Conference on Global Health Challenges GLOBAL HEALTH 2022*, Valencia, Spain, November 15, 2022, 70023.

[9]. T. Funayama, Y. Uchida, and Y. Kogure, Detection of motion restriction with smart insoles, *Sensors & Transducers*, Vol. 259, Issue 5, 2022, pp. 61-68.

[10]. T. Funayama, Y. Uchida and Y. Kogure, Step Measurement Using a Household Floor Mat and Shoe Sensors, *International J. of Advances in Life Science*, Vol. 15, No. 1&2, 2023, pp. 33-34.

(017)

Electrochemical Determination of Cd^{2+}, Pb^{2+}, Cu^{2+} and Zn^{2+} in Liquids using Modified Titanium Dioxide

Vorobets V. S., Fomanyuk S. S., Medyk I. A., Kolbasov G. Ya., Karpenko S. V.
Vernadsky Institute of General and Inorganic Chemistry of the NAS of Ukraine, Department of electrochemistry and photoelectrochemistry of non-metallic systems, 32/34 Acad. Palladin Str., 03142 Kyiv, Ukraine
Tel.: + 380442252280
E-mail: vorobetsvs@i.ua

Summary: Nanocrystalline Ce- or Y-modified titanium dioxide thin films electrodes were used to determine the concentration of Pb^{2+}, Cd^{2+}, Cu^{2+}, Zn^{2+} ions in liquids by anodic stripping voltammetry (ASV) and stripping photoelectrochemical (SP) methods. In both cases well-defined signals for studied heavy metal ions (HMIs) were obtained. The optimal conditions to determine the concentration of studied HMIs by ASV method have been chosen. It is determined that the magnitude of analytical signal of Cd, Pb, Cu, Zn depends linearly on its concentration, thus Ce-TiO_2 and Y-TiO_2 electrodes can be used as indicator electrodes for determination of studied HMIs by ASV method. The prospects of using the SP method to determine the cadmium, lead and copper content in liquid media are shown. The sensitivity of SP method to Pb^{2+} was 0.01 mg·L^{-1}, to Cu^{2+} – 0.1 mg·L^{-1}, to Cd^{2+} –0.01 mg·L^{-1}.

Keywords: Stripping voltammetry, Stripping photoelectrochemical method, Modified TiO_2 electrodes, Heavy metals.

1. Introduction

The global nature of modern environmental problems requires constant monitoring of toxic substances in the environment. Heavy metal ions (HMIs), such as lead, mercury, cadmium, zinc, copper, manganese, etc., are the most challenging pollutant entering natural and anthropogenic environments. They pose a major risk to human health due to their toxicity, resistance to biodegradation and the ability to accumulate in tissues, causing a number of diseases. On the other hand, such metals as iron, copper, zinc, molybdenum participate in biological processes and in certain quantities are recognized as necessary trace elements for the functioning of plants, animals and humans. Therefore, the development of sensitive methods for determining the residual amounts of heavy metals in waters is an urgent task. To effectively address this issue, robust, sensitive, and selective electrochemical sensing techniques are required to enable the rapid detection of hazardous contaminants.

One of these methods is stripping voltammetry (SV) [1], based on the ability of elements accumulated on the working electrode from the analyzed solution to dissolve electrochemically at a certain potential characteristic of each element. The registered maximum current of an element depends on the concentration of this element. The process of accumulation on the working electrode takes place at a certain electrolysis potential for a given time. The process of electrochemical dissolution of the reduction products from the electrode surface and the registration of analytical signals (in the form of peaks) on the voltammogram is carried out at a certain voltage. As active electrodes in SV mercury electrodes [2], mercury-film [3], electrodes based on carbon materials [4], and others [5, 6] are usually used. The disadvantage of most techniques [3-6] is the complexity of manufacturing the applied electrodes. This, as well as the toxicity of mercury used in the manufacture of electrodes or in measurements by adding a solution of Hg(II) ions to the background electrolyte [5], requires the search for new non-toxic, chemical inert materials with stable properties.

This work presents the results of using anodic stripping voltammetry (ASV) and stripping photoelectrochemical (SP) method for determining the concentration of HMIs (Pb^{2+}, Cd^{2+}, Cu^{2+}, Zn^{2+}) in liquids using new electrode materials based on nanocrystalline Ce- or Y-doped titanium dioxide.

2. Experimental

2.1. Preparation of thin-film Ce/Y-TiO_2 electrodes

Nanoscale titanium dioxide was synthesized by the sol-gel method from titanium (IV) tetraisopropoxide using Triton X-100 as a pore agent, as reported in our previous work [7].

2.2. Electrochemical Measurements

The electrochemical measurements was performed under potentiodynamic conditions using a PC-based electrochemical setup which had the following characteristics: measured currents $2\cdot10^{-9}$– $1\cdot10^{-1}$ A, potential scan rate 0.01–50 mV/s, working electrode potential range –4 to + 4 V. Platinum was used as a counter electrode, Ce-TiO_2 and Y-TiO_2 films on Ti substrate as working electrode, Ag/AgCl as reference electrode. The measurements were made in 0.1 M hydrochloric acid, 0.35 M formic acid and acetate buffer (pH=5.0).

2.3. Photoelectrochemical (PEC) Measurements

The PEC measurement was performed using an PGSTAT Elins P-8S. Platinum served as the counter electrode, while Ce-TiO_2 and Y-TiO_2 films were employed as the working electrode on a titanium substrate. As the reference electrode was used Ag/AgCl. The PEC study was carried out in 0.1 M KI solutions. The spectral dependences of photocurrent quantum yield of modified TiO_2 films were measured in a quartz cell on a setup, which included an MDR–2 monochromator and the light source was a DKSSh–500 xenon lamp with stabilized discharge current.

3. Results and Discussion

3.1. Determination of Cadmium, Lead, Copper and Zinc by ASV Method

Cadmium, lead, copper and zinc were determined by the ASV method that involves three main steps:

1. Deposition (electroconcentrating): In this step, the Pb^{2+}, Cd^{2+}, Cu^{2+}, Zn^{2+} ions are electrochemically deposited onto the surface of the working electrode. The deposition is performed by applying a negative potential to the working electrode in the presence of the HMIs (Pb^{2+}, Cd^{2+}, Cu^{2+}, Zn^{2+}), causing them to be reduced and deposited onto the electrode surface.

2. Stripping (electrodissolution): After deposition, the potential of the working electrode is scanned in the positive direction, causing the deposited heavy metal ions to be oxidized and stripped from the electrode surface. The resulting current is proportional to the concentration of HMIs that were deposited on the electrode surface during the electroconcentrating step.

3. Analysis: By measuring the current produced during the stripping step, the concentration of HMIs in the original sample can be quantified using a calibration curve generated from standard solutions of known Pb^{2+}, Cd^{2+}, Cu^{2+}, Zn^{2+} concentrations.

Solutions of 0.1 M hydrochloric acid, 0.35 M formic acid and acetate buffer (pH=5.0) were used as background electrolytes. The solutions were stirred during the preliminary electroconcentrating at potential of –(1000–1600) mV (vs silver-chloride reference electrode) for 60–240 s and then the potential was scanned from -1600 mV to +200 mV. It is determined that the magnitude of analytical signal of HMIs in studied electrolytes depends linearly on the ion concentration of each studied heavy metal ions, thus Ce-TiO_2 and Y-TiO_2 electrodes can be used as indicator electrodes for determination of these HMIs by ASV method.

Fig. 1 shows the ASV response to Pb(II) over the metal ion concentration range from 0.1 to 5.1 mg·L^{-1} in solution 0.1 M HCl used as background solution. The Pb(II) peak is clearly seen at about -0.45 V, the linearization equation in 0.1 M HCl as background solution is i/mA = -0.02 + 0.52 C/mg·L^{-1}, with a correlation coefficient of 0.992 (Fig. 2, curve 2), the sensitivity for electrochemical analysis of Pb(II) is 0.52 mA mg·L^{-1}.

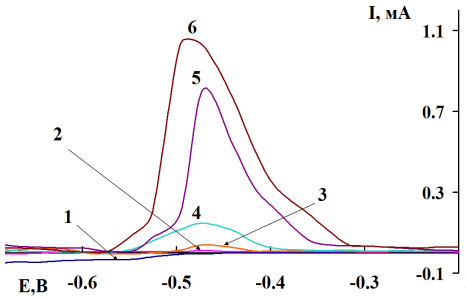

Fig. 1. Polarization curves on Y-TiO_2 electrodes in acetate buffer (pH=5.0) containing: 1 – background solution; 2–0.1; 3–0.6; 4– 1.6; 5–3.1; 6–5.1 mg/L of Pb(II) ions. Ee -1.4V, te - 120 s.

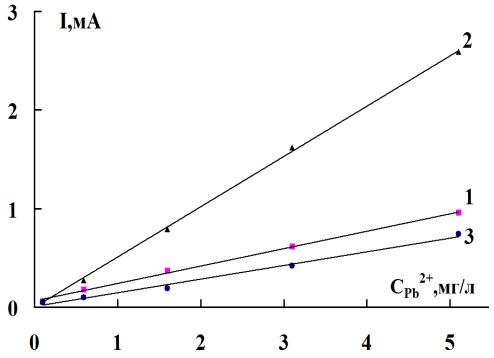

Fig. 2. Dependence of the analytical signal magnitude of Pb on its concentration in: 1-acetate buffer; 2-0.1 M HCl; 3-0.35M formic acid.

In other solutions (acetate buffer (pH = 5.0) and 0.35M formic acid) used as a background electrolyte, the magnitude of the analytical signal of Pb also linearly depends on the Pb(II) ion concentration, however, the sensitivity to Pb in these solutions is much lower than in 0.1M HCl solution (Fig. 2, curves 1 and 3).

The ASV responses to Cd(II) over the concentration range from 0.001 to 2.0 mg·L^{-1} are shown in Fig. 3. The Cd (II) peak is visible at about -0.7±0.05 V. The linearization equation in acetate buffer (pH = 5.0) as background solution is i/mA = -0.04 + 0.26 C/mg·L^{-1}, with a correlation coefficient of 0.996 (Fig. 4, curve 1), the sensitivity for electrochemical analysis of Cd (II) is 0.26 mA mg/L. In solution of 0.35M formic acid used as a background electrolyte, the magnitude of the analytical signal of Cd also linearly depends on the Cd (II) ion concentration, however, the sensitivity to Cd in this solution is lower than in acetate buffer (Fig. 4, curves 2).

It was found that ASV responses to Cu(II) and Zn(II) over the concentration range of 0.1 to 5.1 mg·L^{-1}.in acetate buffer with pH = 5.0 are

observed at -0,3±0,05 V for Cu(II) and -0,9±0,05 V for Zn(II), and the magnitude of the analytical signals of Cu and Zn also linearly depend on the Cu(II) and Zn(II) ion concentration.

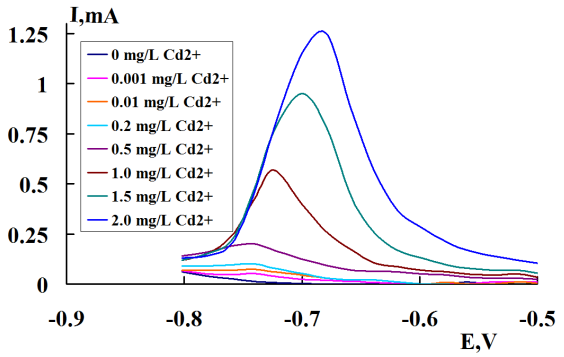

Fig. 3. Voltammetry of cadmium on 1%Ce-TiO_2 electrodes in acetate buffer (pH = 5.0) containing Cd(II) ions: 1- 0; 2- 0.001; 3- 0.01; 4- 0.5; 5- 1.0; 6- 1.5; 7- 2 mg/L ions Ee = -1.5 V, t_e = 180 c.

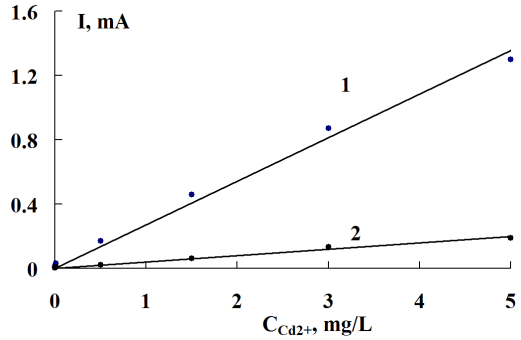

Fig. 4. Effect of the nature of the electrolyte on the concentration dependence of Cd^{2+}: 1-acetate buffer with pH = 5.0; 2- 0.35 M formic acid.

The use of titanium dioxide electrodes modified with rare earth elements as working electrodes also allows simultaneously determination of the concentration of heavy metals in their mixture in liquids without removing oxygen (unlike mercury, amalgam, carbon and other electrodes that are commonly used for analysis by this method). As shown in Fig. 5, concentrations of heavy metal ions (Pb(II), Cd(II), Cu(II), Zn(II)) and O_2 were simultaneously detected under similar conditions. The results show that the detection (individual or simultaneous) of the four considered heavy metal ions and O_2 results in well-separated stripping peaks, respectively observed at -0.45 V, -0.7 V, -0.3 V, -0.9 V and -0.55 V. It is thus easy to distinguish the four heavy metal ions and oxygen from the potential of the stripping peak with our modified electrodes.

Optimal conditions for the determination of lead, cadmium, copper and zinc in liquids by the stripping voltammetry are presented in Table 1.

It was found that the sensitivity of the ASV method to Pb^{2+} was 0.05 mg·L^{-1}, to Cu^{2+} – 0.1 mg·L^{-1}, to Zn^{2+}– 0.1 mg·L^{-1}, to Cd^{2+} –0.1 mg·L^{-1}.

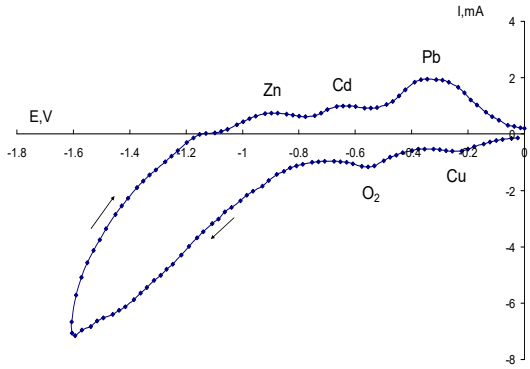

Fig. 5 Voltammograms at 2 % Y-TiO_2 electrodes in acetate buffer (pH = 5.0) with a content of Me ions (Me = Cu, Pb, Cd, Zn) of 2 mg/L; Ee = -1.4 V, t_e = 120 c.

Table 1. Optimal conditions for the determination of heavy metals by ASV

Me	Film	E_e, V	t_e, s	E_{as}, V
Cd	Ce-TiO_2. Y-TiO_2	-1.5	180	-0.7±0.05
Pb	Ce-TiO_2. Y-TiO_2	-1.4	120	-0.45±0.05
Cu	Ce-TiO_2. Y-TiO_2	-1.0	120	-0.3±0.05
Zn	Ce-TiO_2. Y-TiO_2	-1.4	240	-0.9±0.05

Note. E_e - electroconcentrating potential, t_e- time of electroconcentrating, E_{as}-analytical signal potential

3.2. Determination of Cadmium, Lead and Copper Concentration by SP Method

The stripping photoelectrochemical method consists in preliminary electrochemical concentration of heavy metals on electrodes in the form of metals or metal oxides, followed by measurement of their photoelectrochemical response (photocurrent or voltage drop) and comparing it before and after concentration in different parts of the spectral rang. Analysis of the spectral characteristics of the photocurrent at different concentrations of Pb^{2+}, Cd^{2+}, Cu^{2+} (Figs. 6 and 7) showed that the concentrating of metal products of heavy metal ions on the TiO_2 electrodes leads to a decrease in the photoresponse in the spectral range of 250-350 nm, which corresponds to light absorption by the TiO_2 film, even with small amounts of HMIs.

At the same time, the photoresponse signal correlates with the concentration of heavy metal ions. This is reflected by straight -line graphs of the dependence of quantum yield on the logarithm of concentration, as shown in Fig. 8 and Fig. 9.

The sensitivity of SP method to Pb^{2+} was 0.01 mg·L^{-1}, to Cu^{2+} – 0.1 mg·L^{-1}, to Cd^{2+} –0.01 mg·L^{-1}.

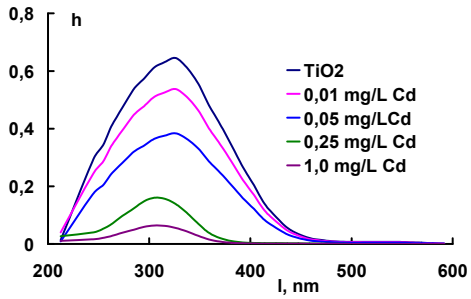

Fig. 6. Spectra of photocurrent quantum yield of titanium oxide films at different concentrations of cadmium in acetate buffer.

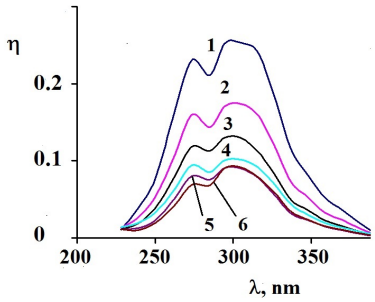

Fig. 7 Photocurrent quantum yield spectra of titanium dioxide films at different copper concentrations in acetate buffer: 1- 0; 2- 2.0; 3- 3.0; 4- 4.0; 5- 5.0; 6- 6.0 mg/L of Cu(II) ions.

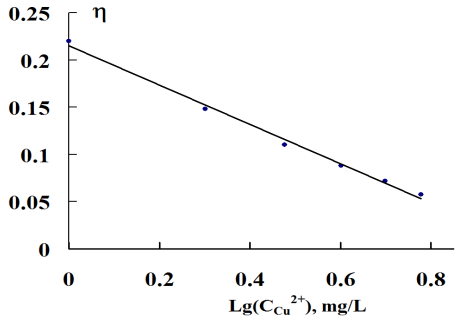

Fig. 8 Plot of the dependence of the photocurrent quantum yield on the concentration of copper ions in acetate buffer.

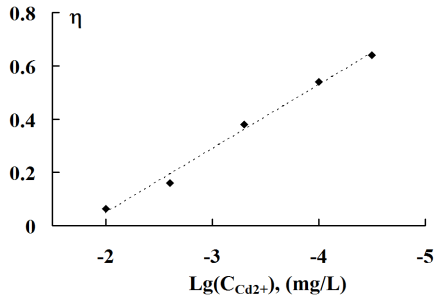

Fig. 9 Dependence of photocurrent quantum yield on the logarithm of cadmium ion concentration, C, in acetate buffer.

4. Conclusions

1. New electrode materials containing films of nanodispersed titanium dioxide modified with rare-earth elements (Y, Ce), have been synthesized. The materials characterized by high sensitivity and selectivity in determining the concentration of heavy metals (Pb, Cd Cu, Zn) and oxygen in liquids,.

2. Combined methods of express analysis of liquids for the content of small concentrations of heavy metals (Pb, Cd, Cu, Zn) based on a combination of stripping voltammetry and stripping photoelectrochemical method have been developed.

3. Sensor systems for joint determination of oxygen and heavy metals (lead, cadmium, copper, zinc) in liquids have been developed.

References

[1]. J. S. Paulo, R. Stradiotto Nelson, Simultaneous determination of trace amounts of zinc, lead and copper in rum by anodic stripping voltammetry, *Talanta*, Vol. 44, 1997, pp. 185-188.

[2]. C. Fernandez-Bobes, M. T. Fernandez-Abedul et. al., Anodic stripping voltammetry of heavy metals using a hanging mercury drop electrode in a flow system, *Electroanalysis*, Vol. 10, Issue 10, 1998, pp. 701-706.

[3]. Metrohm, Determination of cadmium and lead by anodic stripping voltammetry at mercury film electrode, *Application Bulletin 241/2 e*, p. 14. https://www.metrohm.com/ru-ru/applications/AB-241

[4]. M. Rievaj, P. Tomčik, M. Čerňanska et. al., Trace determination of lead in environmental and biological samples by anodic stripping voltammetry on carbon paste electrode, *Chem. Anal.,* Vol. 53, Issue 5, 2008, pp. 717-723.

[5]. K. C. Armstrong, C. E. Tatum, R. N. Dansby-Sparks et. al., Individual and simultaneous determination of lead, cadmium, and zinc by anodic stripping voltammetry at a bismuth bulk electrode, *Talanta*, Vol. 82, Issue 2, 2010, pp. 675-680.

[6]. L. Jing, G. Shaojun, Z. Yueming, W. Erkang, High-sensitivity determination of lead and cadmium based on the Nafion-graphene composite film, *Anal. Chim. Acta*, Vol. 649, Issue 2, 2009, pp. 196-201.

[7]. V. S. Vorobets, G. Ya. Kolbasov, I. A. Medyk et. al., Synthesis, Photo- and Electrocatalytic Properties of Nanostructured Y-TiO_2 Films, *Surf. Eng. Appl. Electrochem.* Vol. 57, Issue 5, 2021, pp. 535–541.

(018)

Near-Field Microwave Probe Technique for Local Broadband Characterization of Nanocomposite Materials

H. Bakli [1] and M. Makhlouf [2]
[1] Laboratory of Electronics and Electrical Systems Engineering, BP 48 Cherchell, 42006, Tipaza, Algeria
[2] Laboratory of Combustion, Detonation and Ballistic, BP 48 Cherchell, 42006, Tipaza, Algeria
Tel.: + 213670261014
E-mail: baklih@yahoo.com

Summary: Local characterization and determination of small dielectric and conductivity contrasts of PVC/Graphene/Fe_2O_3 nanocomposites using near-field microwave probe technique is investigated in this paper. The proposed method presents a lot of advantages such as simplicity, low coast, broadband operation and high sensitivity. An electrical model is proposed to represent the probe-sample interaction and an inverse procedure based on one-port calibration model is used to relate the measured reflection coefficient to the local properties of the material under test. Permittivity and conductivity of PVC/Graphene/Fe_2O_3 nanocomposites are experimentally determined at different test frequencies at a wide band frequency.

Keywords: Near-field microwave probe, PVC/Graphene/Fe_2O_3 composites, Graphene, Calibration model, Conductivity, Dielectric permittivity.

1. Introduction

Recently, conductive polymer composites find large-scale applications as anti-static materials in printed electronics, supercapacitors, organic solar cells, biosensors, flexible transparent displays, etc [1, 2]. These materials are produced by combining reinforcing charges with a matrix system such as polymer. This combination of charges and polymer provides characteristics superior to either of the materials alone and are increasingly being used as replacements for relatively heavy metallic materials. In addition, conductive composites are highly interesting for electromagnetic shielding applications. In fact, the rapid development of electronic gadgets, commercial, biological, military and defence systems create electromagnetic (EM) noise known as EM pollution. EM pollution causes human health diseases and worsens the functioning of electronic equipment and their durability [3, 4]. So, it has therefore become essential to develop and characterize composite materials.

Near-field microwave probe technique (NFMP) has become a powerful tool for super resolution imaging and local characterization of various materials such as dielectrics, semiconductors and metals [5-12]. This high resolution can be achieved thanks to the use of near-field probes witch present very small size [8-10]. Nevertheless, these probes exhibit high input impedance resulting in a poor accuracy of measurement by using standard 50 Ω measurement equipment such as conventional vector network analyzer (VNA). To overcome this problem, these probes have been associated to resonators to match the probe high impedance to the impedance of the microwave measuring instrument. However, the use of resonators limits severely the frequency band of operation. Moreover, resonators exhibit a high unloaded quality factor that fails in the presence of the material under test. Consequently, the local broad-band electromagnetic characterization of new materials such as composites materials with high sensitivity and accuracy remains a challenge.

In this work, a simple and inexpensive technique is proposed for the local determination of small Dielectric and conductivity contrasts of conductive nanocomposites. The working principle is based on the association of a near field probe and a vector network analyzer. The idea is to exploit the probe's own resonant frequencies. In fact, at these frequencies, the levels of the reflection coefficient magnitude are around 0, which can ensure high measurement sensitivity and therefore characterization over a wide frequency band.

Thus, in section 2, to better understand the electromagnetic interaction between the microwave probe and the material under test, the electrical field distribution is simulated by using HFSS™ from Ansys. A lumped element model is also developed to represent the sample-probe interaction. The sample preparation protocol is described in section 3. In section 4, the experimental set-up and results are provided to validate the proposed approach. As a demonstration different PVC/Graphene/Fe_2O_3 nanocomposites have been characterized in a large band of frequency.

2. Probe-sample Interaction

2.1. Simulation of the Probe-sample Interaction

To study the probe-sample interaction, the distribution of electrical field around the probe tip, is simulated using HFSSTM at the test frequency 2.45 GHz. As shown in Fig. 1, which represents the

distribution of the electrical filed when no material is considered (probe in air), the electrical field is well confined around the probe apex.

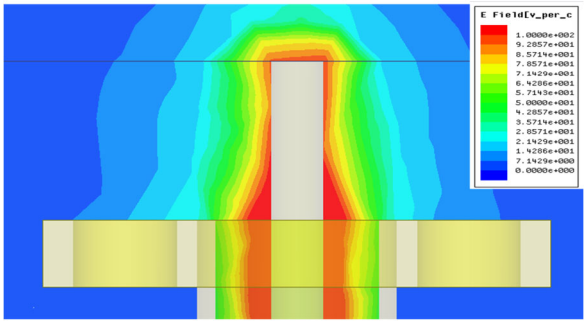

Fig. 1. HFSS™ simulation of electric field at the cross-section along the probe when the tip is in air (f=2.45 GHz).

From these results, we can conclude that high resolution and thus local characterization can be achieved by using this probe.

2.2. RLC Model

Because of the small size of the probe tip in comparison with the wavelength (near-field region), the probe–sample interaction can be represented by a lumped element network in the quasi-static approximation and thus Z_t can be calculated as the impedance of the whole RLC network (Fig. 2)

$$Z_t^{-1} = \left(\frac{1}{j\omega C_c} + Z_s\right)^{-1} + j\omega C_{str}\,, \qquad (1)$$

where C_c is the coupling capacitance, Z_s is the sample near-field impedance represented with the bulk sample capacitance C_s, inductance L_s and resistance R_s. The capacitance between the sample and the outer conductor of the coaxial probe C_{out} can be ignored, since $C_{out} >> C_c$. The capacitance between the tip and the outer conductor of the open-ended coaxial probe is represented by the parasitic stray capacitance C_{str}. When the tip-sample separation is much smaller than the tip size ($h << D$), the influence of C_{str} can be neglected [11]. Thus, the lumped element model of such a probe–sample interaction can be simplified as a coupling capacitance C_c in series with the sample impedance Z_S.

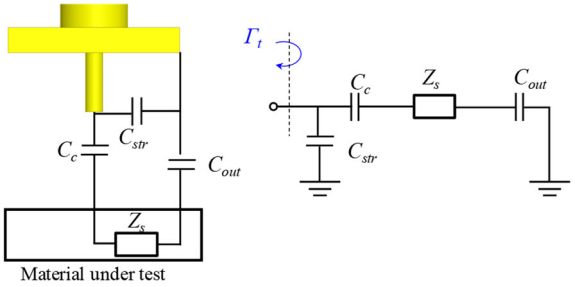

Fig. 2. Lumped element model of tip-sample interaction.

3. Sample Preparation

3.1. Hydrothermal Grafting of Iron Oxide Fe_2O_3 onto Graphene

Due to the obvious existence of nucleation and homogeneous grain development, hydrothermal synthesis has been chosen because it was proven to be more favourable than other techniques. In general, hydrothermal synthesis is a method for crystallizing materials from an aqueous solution by controlling thermodynamic variables such as temperature, pressure, and concentration. The reactions are usually carried out in a metal autoclave with a chemically inert and thermally stable Teflon container.

An aqueous solution of ferric chloride (11.26g Fe_2Cl_3, $6H_2O$ in 100 ml H_2O) has been first prepared and agitate for 3 hours and 30 minutes until a homogeneous solution is achieved. Graphene solution has been then added to the first solution gradually. The used graphene was fabricated by electrochemical exfoliation process from graphite of electrical storage devices and treated by microwave irradiation for 15 seconds [6].

After that, a concentrated aqueous solution of NaOH is slowly added to the previous solution (drop by drop) while stirring until the pH is around 10.96. The resulting solution is vigorously agitated for 30 minutes before being placed in an autoclave for three hours of hydrothermal treatment at 180°C.

3.2. Elaboration of PVC/Graphene/Fe_2O_3 Nanocomposites

We start by mixing the Graphene/Fe_2O_3 solution with the DBS (Dibutyl Sebacate), then sonicating it for 30 minutes to scatter the graphene and prevent agglomeration. Finally, we add the PVC. The mixture is heated for 1 hour at 155 °C.

A series of nanocomposites were constructed to explore the influence of fillers on the characteristics of PVC, and the compositions developed are summarized in the Table 1.

4. Experimental Results

4.1. Open-ended Coaxial Probe Measurement

PVC/Graphene/Fe_2O_3 nanocomposite samples have been first characterized using open-ended coaxial probe. This technique consists to place an open-ended coaxial transmission line in contact with a sample so that the electrical fields around the end of the probe will interact with the sample under test. A VNA is then used to measure changes in the reflection coefficient affected by the electromagnetic properties of the sample, referenced to the connector plane.

In Fig. 3, we represent the different magnitude spectra of the reflection coefficient for the different PVC/Graphene/Fe_2O_3 composite materials measured by using an open-ended probe.

Table 1. Composition of nanocomposites materials.

PVC/Graphene/Fe_2O_3 Composition	PVC %	DBS %	G %	Fe_2O_3 %
3 % Fe_2O_3	45 %	52 %	0 %	3 %
3 % Graphene	45 %	52 %	3 %	0 %
5 % Graphene	45 %	50 %	5 %	0 %
5%Graphene3%Fe_2O_3	45 %	47 %	5 %	3 %

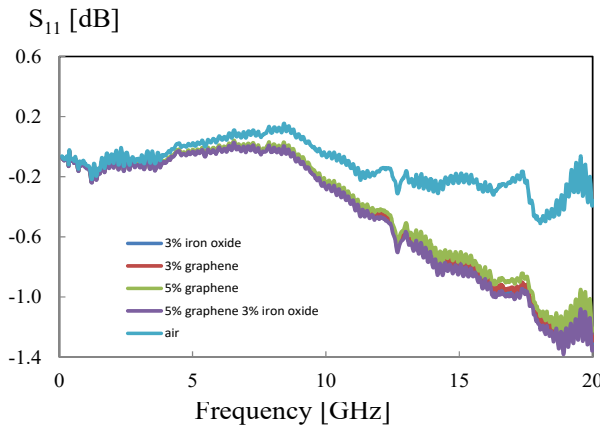

Fig. 3. Measured magnitude spectra of the reflection coefficient for air and PVC/Graphene/Fe_2O_3 nanocomposite materials using open-ended coaxial probe.

From this graph, it can be noted that it is very difficult to distinguish between different composite materials, and thus it can be concluded that measuring small contrasts in permittivity and conductivity of nanocomposite materials using this technique is not possible.

4.2. NFMP Measurement

In Fig. 4, we present the experimental set-up based on the association of a near-field probe that consists of a commercial coaxial connector (RoHS Multicamp SMA Square Flange Jack Receptacle, 50Ω), with a central conductor which lengthens to form a tip with a diameter of 1.3 mm as well as a vector network analyzer (Keysight PNA 5222A).

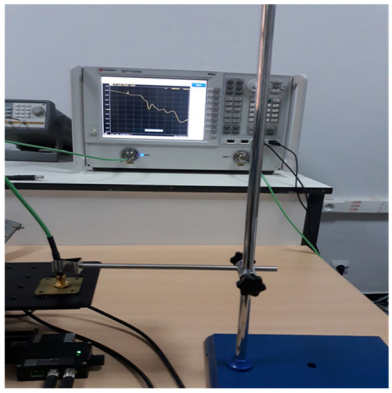

Fig. 4. Experimental set-up.

In Fig. 5, we represent the different magnitude spectra of the reflection coefficient for the different PVC/Graphene/Fe_2O_3 composite materials.

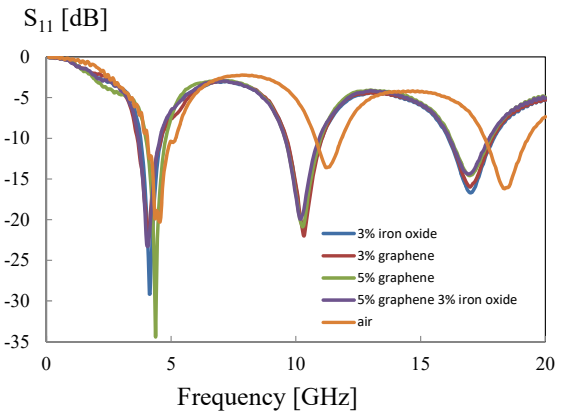

Fig. 5. Measured magnitude spectra of the reflection coefficient for air and PVC/Graphene/Fe_2O_3 nanocomposite materials.

This graph shows that the following tree resonance frequencies can be investigated: around 4, 11 and 18.5 GHz, and that the composite materials are well differentiated by means of reflection coefficient magnitude.

In Fig. 6, we represent the different magnitude spectra of the reflection coefficient for the different PVC/Graphene/Fe_2O_3 composite materials around a third resonance frequency of 18.5 GHz.

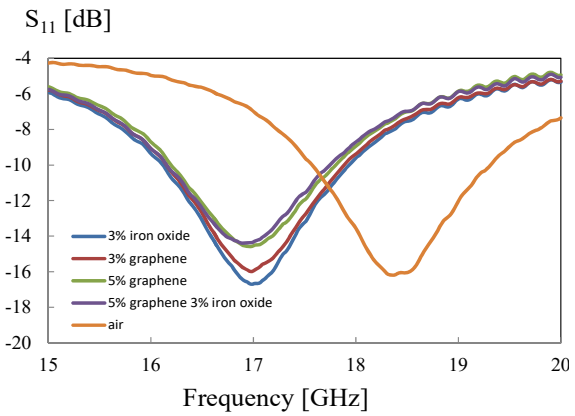

Fig. 6. Measured magnitude spectra of the reflection coefficient for air and PVC/Graphene/Fe_2O_3 nanocomposite materials around 18.5 GHz.

From this graph, one can note that when concentrations of graphene and/or iron oxide increase, the resonant frequency shifts and the magnitude of the reflection coefficient increases. In fact, when the concentration of nanoparticles increases, the particles' interaction within the matrix increases. The average polarization correlated with a cluster of particles is more robust than an individual particle due to improved composite inclusion dimensions and thus greater interfacial area.

This results in a higher average polarization and, hence, a larger contribution to the dielectric properties and conductivity.

5. Conclusions

The PVC/Graphene/Fe_2O_3 nanocomposites have been characterized using a near-field microwave probe technique. An electrical model based on lumped elements was proposed to represent the probe-sample interaction. A calibration model will be developed and presented in the final version of this article to retrieve the materials' electromagnetic properties from the measured reflection coefficient. The conductivity and permittivity of these materials will be determined at different test frequencies in a large band of frequency.

References

[1]. H. Pang, L. Xu, D. X. Yan, and Z. M. Li, Conductive polymer composites with segregated structures, *Progress in Polymer Science*, Vol. 39, Issue 11, 2014, pp. 1908–1933.

[2]. G. Mook, R. Lange, and O. Koeser, Non-destructive characterization of carbon-fiber-reinforced plastics by means of eddy-currents, *Composites Science and Technology,* Vol. 61, Issue 6, 2001, pp. 865–873.

[3]. V. Shukla, Review of electromagnetic interference shielding materials fabricated by iron ingredients, *Nanoscale Advances,* Vol. 1, Issue 5, 2019, pp. 1640–1671.

[4]. A. Tamburrano, D. Desideri, A. Maschio, and M. Sabrina Sarto, Coaxial waveguide methods for shielding effectiveness measurement of planar materials up to 18 GHz, *IEEE Transactions on Electromagnetic Compatibility,* Vol. 56, Issue 6, 2014, pp. 1386–1395.

[5]. A. Tselev, N. V. Lavrik, I. Vlassiouk, D. P. Briggs, M. Rutgers, R. Proksch, and S. V. Kalinin, Near-field microwave scanning probe imaging of conductivity inhomogeneities in CVD graphene, *Nanotechnology,* Vol. 23, Issue 38, 2012, p. 385706.

[6]. H. Bakli, M. Moualhi, and M. Makhlouf, High-sensitivity electrical properties measurement of graphene-based composites using interferometric near-field microwave technique, *Measurement Science and Technology,* Vol. 33, Issue 4, 2022, p. 045012.

[7]. D. E. Steinhauer, C. P. Vlahacos, F. C. Wellstood, S. M. Anlage, C. Canedy, R. Ramesh, A. Stanishevsky, and J. Melngailis, Quantitative imaging of dielectric permittivity and tunability with a near-field scanning microwave microscope, *Review of Scientific Instruments,* Vol. 71, Issue 7, 2000, pp. 2751–2758.

[8]. M. Farina, D. Mencarelli, A. Di Donato, G. Venanzoni, and A. Morini, Calibration protocol for broadband near-field microwave microscopy, *IEEE Transactions on Microwave Theory and Techniques,* Vol. 59, Issue 10, 2011, pp. 2769–2776.

[9]. A. Imtiaz and S. M. Anlage, Effect of tip geometry on contrast and spatial resolution of the Near-Field Microwave Microscope, *Journal of Applied Physics,* Vol. 100, Issue 4, 2006, p. 044304.

[10]. R. A. Kleismit, M. K. Kazimierczuk, and G. Kozlowski, Sensitivity and resolution of Evanescent Microwave Microscope, *IEEE Transactions on Microwave Theory and Techniques,* Vol. 54, Issue 2, 2006, pp. 639–647.

[11]. S. M. Anlage, V. V. Talanov, and A. R. Schwartz, Principles of near-field microwave microscopy scanning probe microscopy: electrical and electromechanical phenomena at the nanoscale, Scanning Probe Microscopy, Vol. 1, S. Kalinin and A. Gruverman (Eds.), *Springer Sci*, New York, 2007, pp. 215–253.

[12]. C. Gao, F. Duewer, and X.-D. Xiang, Quantitative microwave evanescent microscopy, *Applied Physics Letters,* Vol. 75, Issue 19, 1999, pp. 3005–3007.

(020)

Comparison of the Depth Accuracy of a Plenoptic Camera and a Stereo Camera System in Spatially Tracking Single Refuse-derived Fuel Particles in a Drop Shaft

M. Zhang [1], R. Streier [2], M. Vogelbacher [1], S. Wirtz [2], V. Scherer [2] and J. Matthes [1]
[1] Karlsruhe Institute of Technology, Institute for Automation and Applied Informatics,
Hermann-von-Helmholtz-Platz 1, 76344 Eggenstein-Leopoldshafen, Germany
[2] Ruhr-University Bochum, Department of Energy Plant Technology,
Universitätstr. 150, 44801, Bochum, Germany
Tel.: + 49 721 608-24919, fax: + 49 721 608-22602
E-mail: miao.zhang@kit.edu

Abstract: With the development of depth cameras in the last decades, several cameras are able to acquire 3D information of the captured scenes, such as plenoptic camera and stereo camera system. Because of the differences in principle and construction of various depth cameras, different cameras own particular advantages and disadvantages. Therefore, a comprehensive and detailed comparison of different cameras is essential to select the right camera for the application. Our research compared the depth accuracy and stability of a stereo camera system and a plenoptic camera by monitoring the settling processes of various refuse-derived fuel particles in a drop shaft. The particles are detected at first using detection approaches, and the particle detections are subsequently associated in accordance with data association algorithms. The spatial particle trajectories are obtained by the tracking-by-detection approach, based on which the performances of the cameras are evaluated.

Keywords: 3D Measurement, Plenoptic camera, Stereo camera system, Particle tracking-by-detection, Comparison of 3D sensors.

1. Introduction

The knowledge of 3D measurements is of significant importance in various applications, for instance, object localization and tracking. To achieve the 3D localization of objects, a 3D sensor is quite essential. With the development of measurement techniques, more and more sensors are able to acquire 3D information concerning captured scenes, such as the time-of-flight (ToF) camera [1], the structured light camera [2], the stereo camera system [3], and the plenoptic camera [4]. Given the multiple potential options for 3D cameras, selecting an appropriate solution based on using the environment is of interest to a range of research communities. For instance, in [5], the consumer depth camera Microsoft Kinect with a novel depth imaging technique is compared to the state-of-the-art continuous wave amplitude modulation ToF cameras by a set of experimental setups for the purpose of evaluating the respective merits and drawbacks of the cameras. Further, Chiu *et al.* [6] compared 3D reconstruction results based on data collected by two different types of depth cameras (ToF and stereoscopic cameras) and commercial 3D scanning systems to determine the selection of the depth camera concerning the applications.

As indicated by the review of the related works, the ToF camera, the structured light camera, and the stereo camera system have been widely researched regarding their availabilities of providing depth information. Notwithstanding, the research on plenoptic cameras based on the plenoptic function is still scarce, so there is insufficient information concerning comparison with other depth cameras. In addition, since the plenoptic camera has been developed in recent decades, several issues concerning the plenoptic camera remain problematic, *e.g.*, incomplete corresponding data processing techniques and custom imaging hardware [7].

This study contributes to comparing a plenoptic camera and a stereo camera system in spatially tracking single refuse-derived fuel (RDF) particles in a drop shaft. These two camera systems were selected in accordance with use case addressed (experimental setup, depth, resolution, etc.) and are compared primarily in terms of depth accuracy. Moreover, the structured light camera and the ToF camera are basically not adequate for observing small particles (such as RDF particles), and therefore, only the stereo camera system and plenoptic camera are considered. First, the two cameras measure the depth of objects distributed equidistantly in the drop shaft. Subsequently, the motions of four RDF fractions in the drop shaft, *viz.*, wood chips, PE-granule, paper shred, and confetti, are photographed separately. The captured images are then used to derive the 3D trajectory of each RDF particle by image processing techniques according to the tracking-by-detection principle. By comparing the 3D trajectories from the same object, the performances of cameras can be evaluated.

This paper is structured as follows: in section 2, the experimental setup is illustrated. Section 3 briefly demonstrates the applied image processing approaches to detect and track particles. In section 4, the

corresponding results are discussed. Section 5 concludes the paper.

2. Experimental Setup

Single RDF particles are transported to the upper part of the drop shaft and then fall through a tube into the drop shaft, as shown in Fig. 1. As a consequence of the extra distance provided by the tube, the particles are accelerated to their terminal velocities before the recording starts. In order to achieve a high contrast of the illuminated particle to the background, the inner wall of the drop shaft is painted black. With 18 LED modules, the lighting system, located at the top inlet of the drop shaft, is able to offer a total luminous flux of 104,400 lm. Furthermore, a drawer with tilted panels is installed at the bottom of the drop shaft, which ensures one particle within a certain capture period. As schematically depicted in Fig. 1, the total distance between the top edge of the drawer and the location of the cameras is 4.8 m. While the plenoptic camera was fixed directly above the drop shaft, the two stereo cameras were mounted on each side above of the drop shaft. Table 1 lists the technical parameters of the utilized stereo camera system and the plenoptic camera.

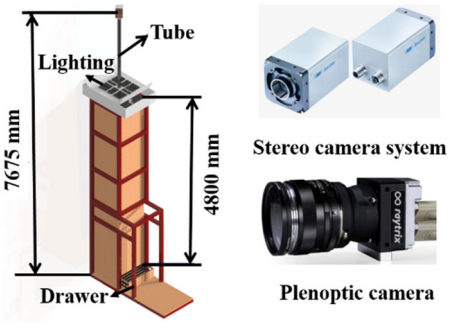

Fig. 1. Schematic of the drop shaft (left) and the utilized two depth camera systems (right).

The stereo camera system was calibrated with a checkerboard in accordance with the calibration method recommended in [8]. Additionally, the intrinsic and extrinsic parameters entailed for the subsequent stereo rectification were also determined. Meanwhile, the plenoptic camera was calibrated based on the principles demonstrated in [9].

Table 1. Technical details of 3D cameras utilized in the study.

	Stereo camera	Plenoptic camera
Manufacturer	Baumer	Raytrix
Model	VLXT-28 M.I	R12
Principles of depth measurement	Stereoscopic camera	Light-field technique
Image resolution	1920 ×1464 px	2048 × 1536 px
Max. frame rate	500 fps	330 fps

RDF contains a broad range of fractions, and four representative fractions, namely wood chips, confetti, paper shreds, and polyethylene (PE) granules, as shown in Figure 2 were selected for the particular experiment. The particles' actual sizes can be roughly estimated according to the 1 cm scale at the bottom right of the figure. Additionally, Table 2 lists the 3D dimensions of the fuel fractions. In the following, the paper presents the comparison of the depth cameras concerning the experiments with the depicted four fractions.

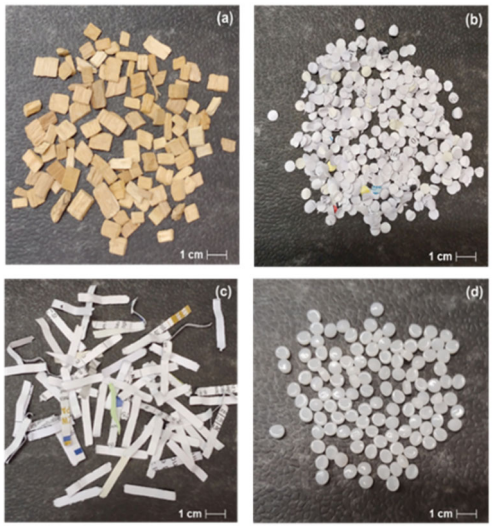

Fig. 2. Various RDF fractions applied in the experiments. (a) Wood chips. (b) Confetti. (c) Paper shreds. (d) PE granules. [10]

Table 2. Physical properties of the experimented RDF fractions

Fraction	Form	Length (mm)	Width (mm)	Thickness (mm)
Wood chips	Cuboid	5-10	4-7	1
Confetti	Round flake	6	6	0.104
Paper shred	Long flake	25-35	6	0.104
PE granule	Round plate	4	4	2

3. Image Processing Approaches

The spatial trajectory of each single RDF particle is derived based on the principle of tracking-by-detection, which identifies objects at first and associates the detections into trajectories afterward. Since the measurements refer to single particle tracking-by-detection, the detection and tracking process are relatively uncomplicated. The particles are identified by virtue of binarization and then associated temporally. The available image processing approaches for multiple particle tracking-by-detection

using the plenoptic camera are presented in [11], which include a novel combined detection method and a data association approach using a linear Kalman filter with the 2.5D global nearest neighbor approach. The same image processing procedure can also be used on the stereo camera system. Notwithstanding, as a consequence of the higher depth accuracy provided by the stereo camera system, the processing might be refined accordingly.

4. Results and Discussion

First, in order to obtain an initial estimate of the accuracy of the two cameras, both cameras measured the distance to a calibration object simultaneously, where the object was placed at six different depth positions. For each captured image, plenty of pixels belonging to the object can be captured. Hereby, we recognize a mean depth as the representing depth of the object. Fig. 3 shows the depths of the calibration object with different ground truth depths measured by both camera systems, where 200 measured depth points of each ground truth depth are selected and displayed in the figure. Additionally, Fig. 4 presents the comparison result by a boxplot to point out the measured median distance and its corresponding distribution over time. The zero point is defined as the upper edge of the drop shaft scaffold, which is 4.8 m to the bottom. As revealed by the figure, the stereo camera system delivers median measured distances smaller than the ground truth values, whereas the plenoptic camera system measures the distances that are first smaller and then larger than the true values. Moreover, the measurement deviation of the stereo camera system tends to increase as the measurement distance increases. Comparatively, the measurement error of the plenoptic camera decreases at first, roughly minimized at around 3 m to 4 m, and then boosts. Compared to 4 m, where the median measurement deviates from the ground truth value by only 48 mm, the error at 4.8 m reaches 470 mm. Overall, the stereo camera shows superior stability and accuracy in measuring the distance of non-moving objects compared to the plenoptic camera.

In addition to comparing the differences between the two depth cameras in measuring fixed calibration objects, the cameras are also compared for measuring continuously varying depths of the calibration object, as schematically depicted in Fig. 5. The varying distance is measured five times, and the resulting five trajectories are shown in the figure. Generally, the distance changes measured by the two cameras are comparable. As revealed in Fig. 5, the measurements of the plenoptic camera are accompanied by more significant fluctuations, especially at the beginning and the end. Since the drop shaft is 4.8 m high, the trajectory should end up fluctuating slightly at 4.8 m. Therefore, we can deduce a larger measured value of the plenoptic camera at 4.8 m, which indicates an agreement with the statement provided in Fig. 4.

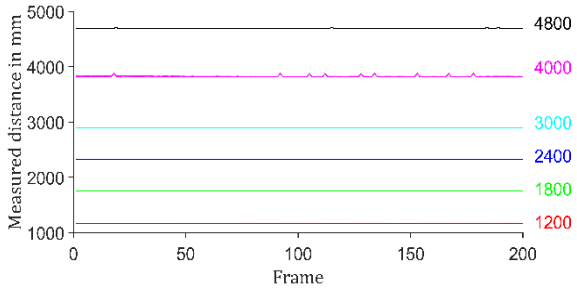

(a) Stereo camera system

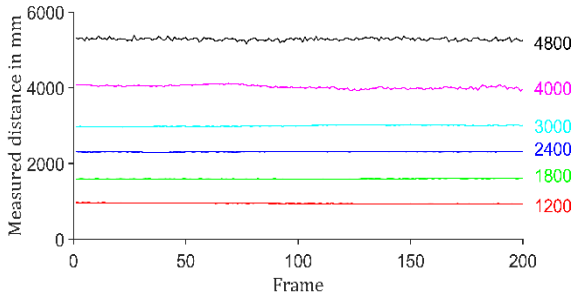

(b) Plenoptic camera system

Fig. 3. Measured depth of the calibration object with different ground truth depths. The horizontal coordinate is the frame number, and the vertical coordinate represents the measured distance.

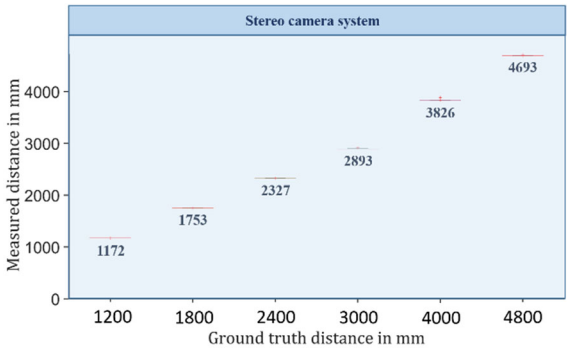

(a)

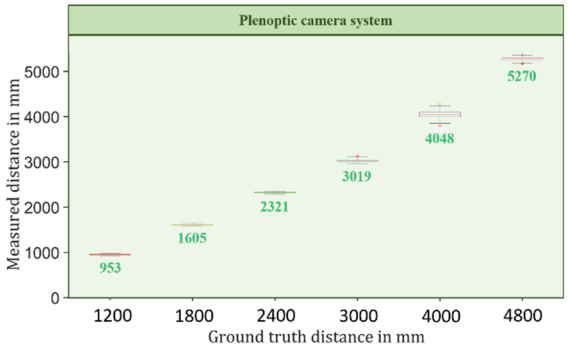

(b)

Fig. 4. Boxplot of measured depth. The horizontal coordinate is the actual distance of the object, and the vertical coordinate represents the measured distance. (a) Measured distance of the stereo camera system. The S refers to the stereo camera, and the blue number is the median of the measured value. (b) Measured distance of the plenoptic camera system. The P stands for the measured value of the plenoptic camera, and the green number is the corresponding temporal median.

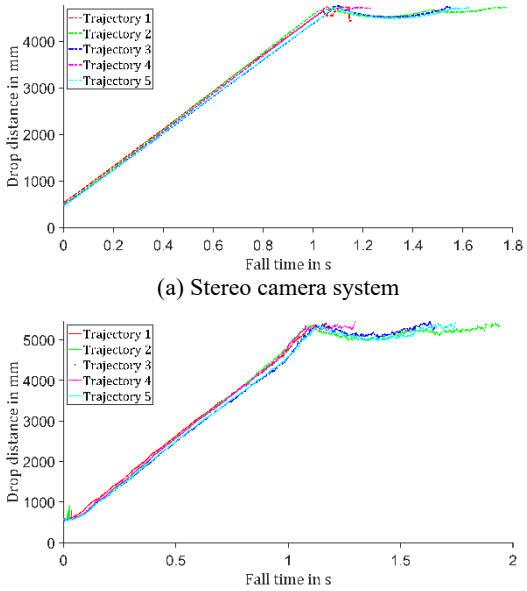

(a) Stereo camera system

(b) Plenoptic camera system

Fig. 5. Measured continuously increasing drop distance with relation to fall time. The horizontal coordinate is the fall time, and the vertical coordinate represents the drop distance.

As a result of completing the comparison of measuring the distance of fixed objects and continuously increasing distances, an initial impression of the accuracy of the two cameras is obtained. Thereafter, the trajectories of various RDF particles derived by the two cameras are also compared. For each fraction, ten particles were dropped, detected, and tracked. For clarity, only one trajectory of each fraction is presented in Fig. 6.

Because the two cameras were triggered asynchronously and their captured ranges differed, time differences exist between the captured corresponding trajectories. In order to achieve a visual comparison of the trajectories' similarities, the trajectories captured by the plenoptic camera are delayed by a certain amount of time. For the purpose of determining the time, the average value of the first ten captured depths by the plenoptic camera is computed. Subsequently, the depth value that is closest to the average value on the captured trajectory belonging to the stereo camera system is searched, and the corresponding time is the delay time. Apparently, the plenoptic camera provides a longer measured depth range, especially when tracking smaller particles such as confetti and plastics. As far as stability is concerned, the fluctuations of the trajectories with respect to all fractions provided by the plenoptic camera are much more substantial than those of the stereo camera system, as also revealed in the previous experiments. The measurement fluctuations of the plenoptic camera are more considerable than the stereo camera system for measuring both stationary and moving objects. Moreover, the fluctuations of measuring small objects are even more significant, which is not conducive to object tracking. Although the trajectories provided by the stereo camera system fluctuate more slightly, small particles can be detected and tracked longer by the plenoptic camera.

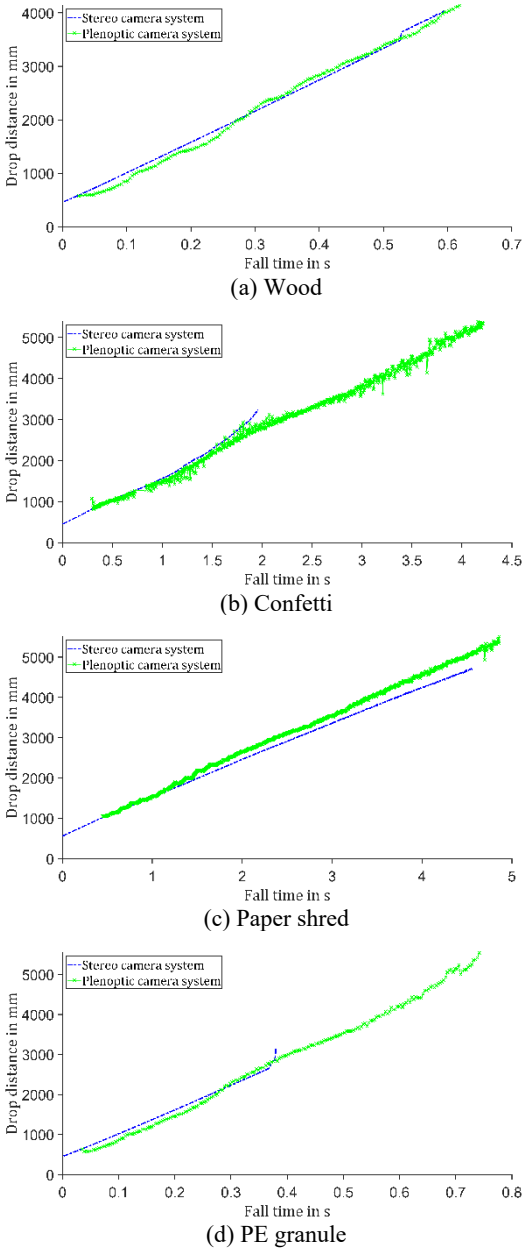

(a) Wood

(b) Confetti

(c) Paper shred

(d) PE granule

Fig. 6. Examples of drop distance with relation to fall time of various particle fractions. The horizontal coordinate is the fall time, and the vertical coordinate represents the drop distance.

In addition, the point-based similarity of the resulting trajectories of each particle is computed according to dynamic time warping [12], which aims to find the warping path between two trajectories with the smallest warping cost. Dynamic time warping can compute the similarity of two time series (*e.g.*, the time-depth trajectory), especially for time series with different lengths and frame rates. Dynamic time warping warps and distorts the time series automatically (*i.e.*, localized scaling on the time axis)

so that the two signals are as consistent as possible to obtain the maximum similarity. Supposing two time series Q and C with respective lengths n and m, the value of the i^{th} frame from Q is denoted as q_i and the value of the j^{th} frame from C as c_j afterward. To align these two series, a matrix of the dimension n×m is constructed with matrix elements (i, j) denoting the Euclidean distance between the two points q_i and c_j. The smaller the distance, the higher the similarity. Dynamic time warping finds the minimum of the sum of the Euclidean distances and recognizes the sum as the warping cost. The dynamic time warping takes the time shift into consideration and is thus superior to simply computing the Euclidean distance between the corresponding trajectories. Fig. 7 gives an example of the distance between two trajectories (obtained signals) using dynamic time warping. The figure above depicts the originally measured distances of the two cameras, and the bottom figure presents the comparison of the distances using dynamic time warping. The outcome of the comparison is the sum of the Euclidean distances between corresponding points.

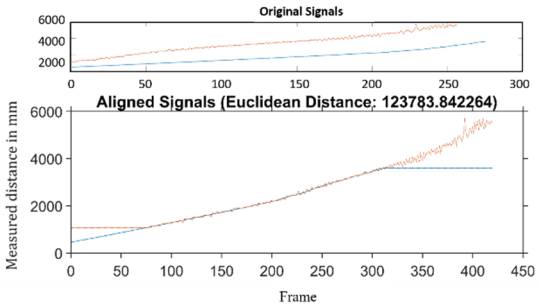

Fig. 7. Schematic of the point-based similarity utilizing dynamic time warping. The horizontal coordinate is the captured frame, and the vertical coordinate represents the measured drop distance.

Table 3 illustrates the computed median distances of the fractions in accordance with dynamic time warping. The bottom row of Table 3 indicates the distance normalized by the number of frames. As presented in Fig. 7, the trajectory is automatically patched according to the initial or termination value after the shifting to ensure the same length, which gives rise to more considerable distances. Therefore, the larger the time difference between the two trajectories, the further the resulting distance will be. As shown in Table 3, wood chip has shorter matching distance as a consequence of its regular and rapid movement. Compared to woos chip, confetti and paper shred have a larger windward area and greater wind resistance. As a result, their falling motions tend to be more irregular and slower, leading to longer trajectory distances. This can also be indicated by the trajectory instances in Fig. 6. Although PE also triggers regular movement, the difference existing in the captured range of the two cameras results in a large standardized warping distance.

Table 3. Median distances of the fractions in mm using dynamic time warping.

Fraction	Wood chips	Confetti	Paper shred	PE granule
Distance	101212	420171	644593	159781
Standardized distance	241.55	325.32	323.21	491.20

5. Conclusions

The study compared two different 3D cameras, *viz.*, a stereo camera system and a plenoptic camera, preliminarily with respect to their depth accuracy and stability in measuring the depth of fixed calibration objects, continuously varying depths, and tracking various single RDF fractions in a drop shaft. Concerning measuring the depth of fixed objects, the two cameras are able to provide comparable depth accuracy. The accuracy of the stereo camera decreases with increasing distance, whereas the measurement deviation of the plenoptic camera is nonlinear, which decreases at first and then rises. Additionally, the plenoptic camera measures the depth with the presence of a considerable variation, which shows a negative impact on the tracking process. The same statement can also be deduced when measuring the continuously varying depths. Generally, the two cameras deliver falling distances with a high agreement between each other. Nevertheless, the depth stability provided by the stereo camera is superior. When comparing the cameras in tracking fuel particles, the point-based matching distance using dynamic time warping is introduced to illustrate the similarity between the measured depth trajectories. The distances of the fractions with regular and rapid motions, *e.g.,* wood chips and PE granules, are significantly shorter than those with long-time motions. Furthermore, with the plenotpic camera, the small particles are longer visible. Hence, we can infer a longer observation of the small particles with the plenoptic camera.

To conclude, the stereo camera system and the plenoptic camera could provide comparable depth accuracy. In this regard, the stereo camera system shows a slight advantage. However, the measurement stability of the stereo camera system is far superior to the plenoptic camera. Since the measured depth of the plenoptic camera is accompanied by considerable fluctuations, their impacts on further tracking processes can not be ignored. In several cases, more sophisticated tracking approaches or post-processing are essential to deal with the depth fluctuations caused by the plenoptic camera. On condition that the issues caused by fluctuations can be tackled, the plenoptic camera can replace the stereo camera system in situations, where the stereo camera system can not be applied, such as only one opening is available.

Acknowledgements

This study is supported by AiF-German Federation of Industrial Research Associations (No. 20410N).

References

[1]. T. Ringbeck, M. Albrecht, J. Frey, M. Grothof, H. Heß, H. Kraft, T. Möller, J. Mosen, and B. Schink, Time- of-Flight 3D camera for autonomous navigation and industrial automation, in *Proceedings of the 11th international : an event of the Association for Sensor Technology, AMA (R. Lerch, ed.)'*, Nürnberg, Germany, Mai 2003.

[2]. V. L. Tran and H. Lin, A structured light RGB-D camera system for accurate depth measurement, *International Journal of Optics*, Vol. 2018, 8659847.

[3]. R. Orozco, C. Loscos, I. Martin, and A. Artusi, Chapter 4 - multiview HDR video sequence generation, High Dynamic Range Video, F. Dufaux, P. Le Callet, R. K. Mantiuk, and M. Mrak, eds. *Academic Press*, Cambridge, MA, USA, 2016.

[4]. R. Ng, Digital light field photography, PhD thesis, *Stanford University*, 2006.

[5]. B. Langmann, K. Hartmann, and O. Loffeld, Depth camera technology comparison and performance evaluation, in *Proceedings of the 1st International Conference on Pattern Recognition Applications and Methods*, *SciTePress - Science and Technology Publications*, 2012.

[6]. C.-Y. Chiu, M. Thelwell, T. Senior, S. Choppin, J. Hart and J. Wheat, Comparison of depth cameras for threedimensional reconstruction in medicine, in *Proceedings of the Institution of Mechanical Engineers, Part H: Journal of Engineering in Medicine,* Vol. 233, Jun 2019, pp. 938–947.

[7]. E. M. Hall, B. S. Thurow, and D. R. Guildenbecher, Comparison of three-dimensional particle tracking and sizing using plenoptic imaging and digital in-line holography, *Appl. Opt.,* Vol. 55, Aug. 2016, pp. 6410–6420.

[8]. Z. Zhang, A flexible new technique for camera calibration, *IEEE Transactions on three-dimensional Pattern Analysis and Machine Intelligence,* 22, 11, 2000, pp. 1330-1334.

[9]. C. Heinze, S. Spyropoulos, S. Hussmann, and C. Perwass, Automated robust metric calibration algorithm for multifocus plenoptic cameras, *IEEE Transactions on Instrumentation and Measurement,* 65, 5, 2016, pp. 1197-1205.

[10]. M. Zhang, M. Vogelbacher, K. Aleksandrov, H.-J. Gehrmann, D. Stapf, R. Streier, S. Wirtz, V. Scherer, and J. Matthes, A Novel Plenoptic Camera-Based Measurement System for the Investigation into Flight and Combustion Behavior of Refuse-Derived Fuel Particles, *ACS Omega,* 8, 19, 2023, pp. 16700–16712.

[11]. M. Zhang, M. Vogelbacher, V. Hagenmeyer, K. Aleksandrov, H.-J. Gehrmann and J. Matthes, 3-D refuse-derived fuel particle tracking-by-detection using a plenoptic camera system, *IEEE Transactions on Instrumentation and Measurement,* 71, 2022, pp. 1-15.

[12]. Paliwal, K. K., Anant Agarwal, and Sarvajit S. Sinha. A Modification over Sakoe and Chiba's Dynamic Time Warping Algorithm for Isolated Word Recognition, *Signal Processing,* Vol. 4, 1982, pp. 329–333.

(021)

Impact of Solvent on Ammonia Detection Performance of Polyaniline-based Sensors

S. Vassaux, N. Redon, E. A. da Silva and C. Duc
Center for Energy and Environment, IMT Nord Europe, Institut Mines-Télécom,
University of Lille, F-59000 Lille, France
Tel.: + 33327712222
E-mail: sabine.vassaux@imt-nord-europe.fr; nathalie.redon@imt-nord-europe.fr;
edilene.dasilva@imt-nord-europe.fr; caroline.duc@imt-nord-europe.fr

Summary: Ammonia constitutes a polluting gas in atmosphere. Chemiresistive sensors based on the polyaniline (PAni) can be used to monitor it. In this technology, the doped PAni is dispersed in a solvent like m-cresol, n-methyl-2-pyrrolidone or dichloroacetic acid, as reported in the literature. However, these solvents cause environmental and toxicity issues. This study aims to identify a safer solvent for PAni formulation displaying efficient gas sensing performances. Several alternative organic solvents were selected and tested in the formulation of PAni doped with camphorsulfonic acid (CSA). PAni-films morphology was characterized using SEM. Sensing performances of those materials formulated with various solvents have been evaluated at different ammonia concentrations. Results show that the solvent influences the surface morphology of PAni/CSA films, suggesting different specific surface areas. Then, the sensitivity of the sensors to ammonia response is impacted by the solvent. The role of the active layer morphology on the sensing performance is highlighted.

Keywords: Chemiresistive sensors, Ammonia detection, Polyaniline-based sensors, Sustainable formulation.

1. Introduction

Ammonia is a polluting gas, which at high concentrations, can cause human illnesses by inhalation [1]. Hence, ammonia monitoring is crucial in several industrial and agricultural applications. To measure ammonia in real-time, many sensing methods exist such as optical, acoustic method or solid-state sensing technologies [1]. Among these latter, the chemiresistive devices based on conductive polymers and more specifically based on polyaniline (PAni), display the advantages to be easily customized, to have a good processability and to work at room temperature [2]. To manufacture polyaniline-based sensors, the polymer needs to be dispersed in a solvent. Up to now, most popular solvents identified to disperse the insoluble doped polyaniline were m-cresol [3], dichloroacetic acid [4] or chloroform. These solvents raise environmental and toxicity issues. To reach a sustainable fabrication of polyaniline-based sensors, safer solvents must be found. Therefore, the objective of this study is to identify safer solvents to disperse conductive polyaniline, without impacting drastically its sensing performance. The influence of the solvent on properties of Polyaniline films will be studied.

2. Materials and Methods

2.1. Materials

Polyaniline-emeraldine (Mw = 65000 g mol^{-1}) and (+)-Camphor-10-sulfonic acid (CSA), chosen as the doping agent were provided by Sigma Aldrich. They were mixed together to obtain a doping rate of 50 %. The powder mix was then meticulously incorporated in four different solvents: dichloroacetic acid (DCAA), acetic acid (AA) and ethanol (E), selected given the same carbon number on their chain, and Toluene (T) chosen due to its aromatic structure, which is similar to the one of m-cresol. The resulting solutions stayed under stirring at 700 rpm for 5 days and then were sonicated for 1 hour. Four "PAni/CSA/solvent" solutions were obtained. The solutions concentrations were comprised between 20 and 30 g/L. The sensor fabrication was carried out through drop-cast technique: 1 to 2.5 µL of the solutions were deposited onto gold interdigitated electrodes on a polyimide flexible substrate. The sensors were dried on a hotplate at 100 °C for one night, and during 7 days at 100 °C in an oven under vacuum.

2.2. Methods

The morphology of the PAni films was observed using Scanning Electron Microscopy at a voltage of 10 kV and a magnification size of 1000. Ammonia detection performance was evaluated at different concentrations (from 50 to 2000 ppb), at a constant temperature (20.4 °C) and a constant relative humidity of 51 %, as a relative humidity of (50 ± 5) % corresponds to the recommended ideal atmosphere relative humidity to test specimens [5].

Relative responses of all sensors were calculated as a function of the resistance under clean air (R_0) and real-time resistance (R) as followed:

$$Relative\ Response = \frac{R-R_0}{R_0} \times 100 \qquad (1)$$

The relative response according to ammonia concentration measured in the exposure chamber was plotted and the sensitivity, corresponding to the slope of the linear regression, was obtained.

3. Results

Fig. 1 shows great morphology variability among PAni/CSA films formulated in the presence of different solvents. Uniform and smooth films are obtained using PAni within dichloroacetic acid (DCAA), while a more porous polymer film is observed for PAni films formulated with acetic acid (AA). Needle-shaped particles result from the toluene evaporation on the polymer film (T), while large aggregated structures are obtained after ethanol (E) evaporation.

Then, the influence of the solvent on ability of PAni/CSA sensors to detect ammonia was studied. Fig. 2 shows that all sensors are sensitive to ammonia and present the commonly observed behavior of PAni-based sensors, characterized by an increasing relative response with the ammonia concentration [1]. Moreover, independently of the solvent, the sensors present good reversibility characterized by a relative response around 17 ± 5% of their initial value after 30 minutes of desorption under clean air. An interesting point is that the sensitivity of the sensors is drastically impacted by the solvent. The sensitivity of DCAA, AA, T and E samples are 5.86, 39.82, 74.34 and 87.28 (%/ppm), respectively. Those variations can be mainly attributed to the difference of specific surface area (Fig. 1). Indeed, given the morphology of the samples, the specific surface area of E an T samples should be well higher than the one of AA and DCAA samples. A higher specific surface area is known to facilitate the interaction of ammonia vapor with the PAni film [6] and to lead to enhanced performance, as it was suggested by Tanghy [2]. Finally, in this study, the PAni sensor formulated with ethanol displays the best performances with the highest sensitivity and the best reversibility.

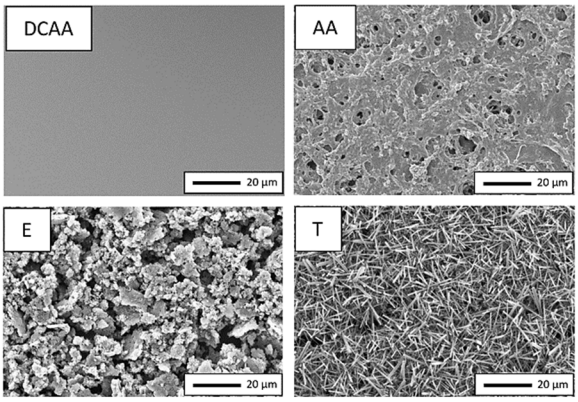

Fig. 1. SEM images of PAni films deposited on a Polyimide substrate for solutions DCAA, AA, E and T.

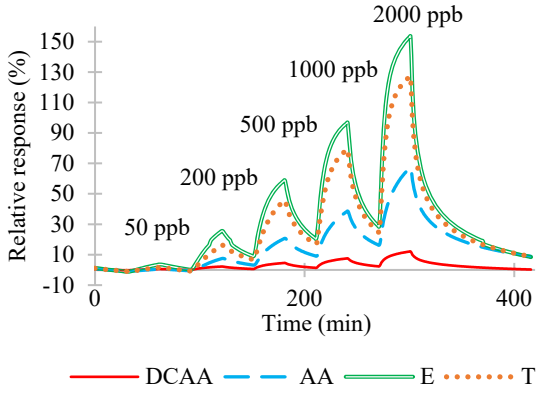

Fig. 2. Response toward ammonia concentration from 0 to 2000 ppb of PAni/CSA sensors from solutions DCAA, AA, E and T (51 % RH and 20.4 °C).

4. Conclusions

The solvent used to disperse the doped polyaniline has a great influence on the morphology and sensing performance to ammonia of PAni-based films. The microstructure and hypothetically the corresponding specific surface area of the PAni film leads to a better sensitivity to ammonia, without impacting drastically the reversibility of the sensor. Ethanol seems to be a promising alternative as a safer solvent to keep the efficient sensing capability to ammonia of PAni films.

Acknowledgements

Authors are thankful to IMT Nord Europe for the financial support and Groupe TERA.

References

[1]. D. Kwak, Y. Lei, et R. Maric, Ammonia gas sensors: A comprehensive review, *Talanta*, Vol. 204, 2019, pp. 713-730.

[2]. N. R. Tanguy, M. Thompson, et N. Yan, A review on advances in application of polyaniline for ammonia detection, *Sensors and Actuators B: Chemical*, Vol. 257, 2018, p. 1044-1064.

[3]. T. Vikki *et al.*, Molecular Recognition Solvents for Electrically Conductive Polyaniline, *Macromolecules*, Vol. 29, No. 8, 1996, p. 2945-2953.

[4]. T. E. Olinga, J. Fraysse, J. P. Travers, A. Dufresne, et A. Pron, Highly Conducting and Solution-Processable Polyaniline Obtained via Protonation with a New Sulfonic Acid Containing Plasticizing Functional Groups, *Macromolecules*, Vol. 33, No. 6, 2000, pp. 2107-2113.

[5]. International Organisation for Standardization, International Standard ISO 554-1976 (E) : Standard atmospheres for conditioning and/or testing-Specifications, 1976.

[6]. Z. Pang, E. Yildirim, M. A. Pasquinelli, et Q. Wei, Ammonia Sensing Performance of Polyaniline-Coated Polyamide 6 NaNofibers, *ACS Omega*, Vol. 6, No. 13, 2021, p. 8950-8957.

(023)

Feasibility of Gait Change Detection using Smart Footwears

T. Funayama [1], Y. Uchida [2], Y. Kogure [3], D. Souma [4] and R. Kimura [5]
[1] Faculty of Medical Sciences, Teikyo University of Science, Uenohara-shi, Ymanashi, Japan
[2] Faculty of Life & Environmental Sciences, Teikyo University of Science, Adachi-ku, Tokyo, Japan
[3] Professor Emeritus, Teikyo university of Science, Adachi-ku, Japan
[4] Department of Rehabilitation, Isogo Central Hospital, Yokohama-shi, Kanagawa, Japan
[5] Department of Rehabilitation, Seirei Yokohama Hospital, Yokohama-shi, Kanagawa, Japan
Tel.: + 81554634411, fax: + 81554636944
E-mail: funayama@ntu.ac.jp

Summary: This study focused on the potential of utilizing pressure sensors and accelerometers in the field of rehabilitation. Wearable devices have evolved significantly in recent years. By harnessing these technological devices, the progress of patients undergoing rehabilitation can be monitored and analyzed. Assessments of the soles and walking can potentially be used for understanding health status, extending beyond mere gait analysis to a heightened capacity for discerning one's health status. Rehabilitation robots that not only assist with physical strength but also repetitively guide desirable movements potentially produce sustained effects, even after their use is discontinued. Therefore, we examined walking before wearing a robot, during robot-assisted walking, and after wearing the robot, using smart insoles and acceleration measurements. The results suggest that smart insoles attached to shoes and accelerometers could potentially detect changes in gait.

Keywords: Smart insole, Accelerometer, Activity measurement, Gait change detection.

1. Introduction

Wearable devices capable of measuring activities, which have rapidly gained popularity in recent years, can also be used for the rehabilitation of daily activities [1–2]. For this purpose, the equipment should be beneficial, easy to operate, easy to wear, convenient, and practical for older people and those with disabilities who have health challenges. Furthermore, it is crucial that healthcare professionals and caregivers understand and utilize the data effectively. A plethora of data can be acquired from digital devices. However, the more abundant the collected data, the more complex and challenging it becomes to comprehend its underlying implications. Furthermore, a higher number of sensors is often correlated with increased costs and device operation complexity. Walking speed is sometimes referred to as the “sixth vital sign” and can provide insights into the body's state beyond just locomotion [3]. In recent years, research on smart insoles has increased [4–11]. We used a smart insole with pressure sensors placed in four parts of the sole and an attached accelerometer worn on the shoe to compare data before, during, and after walking using a gait-assisting robot.

We report the potential of smart insoles and accelerometers to detect changes in walking through robot-assisted rehabilitation. This study was approved by the Human Research Ethics Committee of the Teikyo University of Science.

2. Experiment Method

2.1. Devices

We used a wireless smart insole (FEELSOLE®) that had pressure sensors. It allows for measurements in four parts (toe, heel, inside, and outside) of each foot, making a total of eight parts. The insoles must be calibrated before use. Calibration was performed four times: with no pressure and no feet in the shoes, standing on both feet, and standing on one foot on each side. The sampling frequency was set to 50 Hz. Using ORPHE ANALYTICS, data was stored on the cloud and downloaded in the CSV format.

An ORPHE CORE® accelerometer was used. The data were uploaded to the cloud using the ORPHE ANALYTICS application, and data upload was confirmed by downloading the data in the CSV format. The sampling frequency was set to 200 Hz. We used two triaxial accelerometers, one for each leg, making a total of two devices. The assessments were conducted by attaching the devices to the outer side of each shoe, one on each foot. Data from both smart insoles and accelerometers were synchronized using ORPHE ANALYTICS. The robot used in this study was the Orthobot®, which is commonly used for walking and gait rehabilitation. When attached to a long-leg brace, the robot steers the lower limbs in favorable movement patterns. The placement of the sensors is depicted in Fig. 1, and the scene of the robot equipped for walking is showed in Fig. 2.

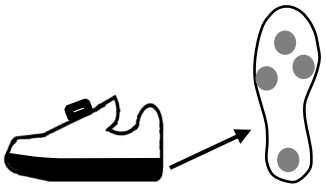

Fig. 1. Insole sensors and accelerometers.

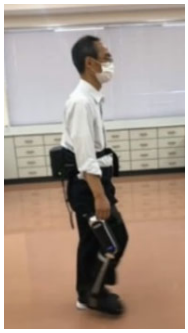

Fig. 2. Walking with robot.

2.2 Measurement and Analysis

We measured pre-usage walking, walking while wearing the robot, and post-usage walking using smart insoles with built-in pressure sensors, shoes fitted with accelerometer sensors. The subject performed three walking trials for approximately 20 seconds each while wearing the walking-assist robot. The analysis used data from the third trial. Gait analysis after use was conducted twice: once at five minutes and again at twelve minutes of robot use. The 1000th to 6000th data points were analyzed, excluding the periods immediately after the start and just before the end of the study.

Peak values were identified from the insole data, representing the points of highest sensor force application for the four parts–heel, toe, inside, and outside–during a single foot-ground contact. The subsequent decrease in the sensor values after each peak was calculated to determine the rate of decrease. The peak values were detected using the find_peaks function from the Python library, SciPy. The threshold for peak determination was set at 50 % of the maximum value for each trial for the heel, toe, inside, and outside parts. The rate of decrease indicates a decline in the value following the peak and was calculated by determining the difference in the weighted averages of adjacent data points. In other words, the difference between the weighted averages of the x and x+1 data points was computed. The weighted average was obtained using five values (the target value and two values each before and after) and calculated as follows: Due to the significant influence of the central region, the percentages were calculated by assigning 40 % to the target value of the waveform, 20 % to the values before and after one peak, and 10 % to the values before and after two peaks. The maximum rate of decrease after each peak was determined, and then, due to multiple foot-ground contacts within a single walk, the mean of the maximum decrease rates for that walk was calculated. The mean maximum decrease rates were compared across different parts of the sole, including the heel, toe, inside, and outside of the foot. The weighted average difference after the peaks extracted using find_peaks had positive values sometimes; however, only negative values were utilized in the calculations.

The data from the accelerometer were examined by calculating the absolute value in each case and taking the square root of the sum of the squares of the values in the X, Y, and Z axes. The subject was a man in his 60 s who wore the robot on his right leg.

3. Results

3.1 Insole and Accelerometer Data

An example of the data obtained from the insole and accelerometer is shown in Fig. 3. The data from the insole are represented on the Y-axis on the left, whereas the data from the accelerometer are represented on the Y-axis on the right.

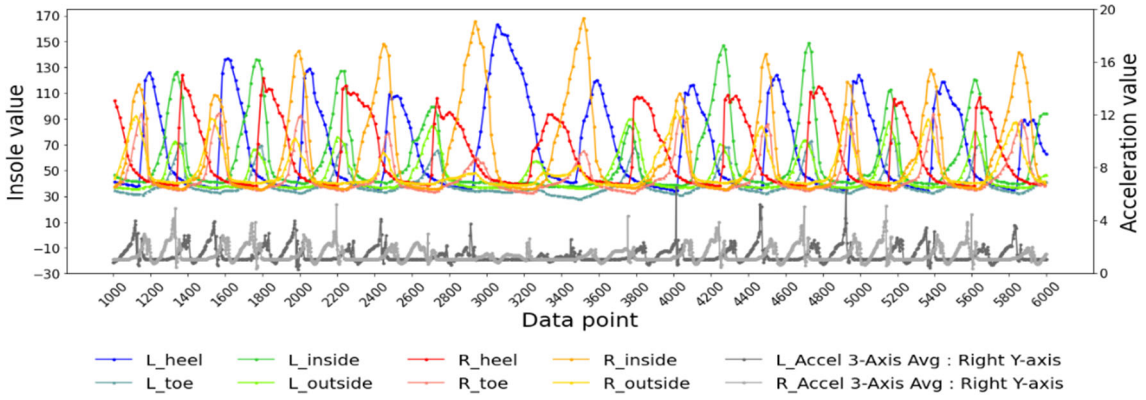

Fig. 3. Insole and acceleration data.

The acceleration only represents the value obtained by taking the square root of the sum of the squares of the values in the three axes (X, Y, and Z axes). Each color corresponds to a specific area: blue for the left heel, light blue for the left toe, green for the left inside, yellow-green for the left outside, red for the right heel, pink for the right toe, orange for the right inside, yellow for the right outside. Additionally, left acceleration is depicted in dark gray, and right acceleration is depicted in light gray. “L” and “R” in

all figures and tables represent “Left” and “Right,” respectively. The data from both the left and right insoles as well as the accelerometers are synchronized.

3.2. Peak Values of the Insoles

Table 1 presents the mean peak values for the four parts of the left and right insoles. Twelve minutes after the robot was removed, a decrease was observed in the outside region, whereas the values from the heel and inside regions increased.

Table 1. Mean of peak values.

	Before	During	5 min after	12 min after
L_heel	118.4	132.4	119.0	122.6
L_toe	70.2	68.2	72.0	72.2
L_inside	122.4	135.7	138.3	133.5
L_outside	75.9	63.5	65.3	73.0
R_heel	108.4	98.8	114.0	129.8
R_toe	85.4	37.5	82.2	79.5
R_inside	135.3	126.3	148.1	152.2
R_outside	79.5	37.8	71.2	65.7

3.3. Rate of Decrease

An example of the post-peak maximum decrease rates is shown in Fig. 4. These data are from the right insole prior to robot usage. Because the decrease rates were expressed as absolute values, higher values indicated greater decrease rates, suggesting swift shifts in the center of gravity.

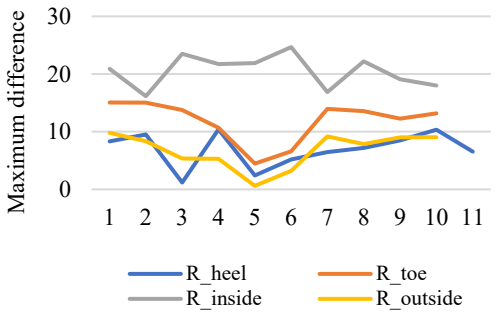

Fig. 4. Post-peak decrease rate (right foot).

Peaks were automatically calculated using the find_peaks function in Python with the threshold set at 50 % of the maximum value. Consequently, the number of peaks extracted may vary in different regions of the insole. The X-axis in Fig. 4 represents the number of peaks. Figs. 5 and 6 show the mean absolute maximum post-peak decrease rates for each walking instance. Larger values indicate greater rates of decrease, signifying rapid shifts in the center of gravity. These effects were detected not only in the right foot where the robot was attached but also in the left foot. The most significant differences in the rate of decrease were in the inside of both the left and right feet, and the effects were discernible up to twelve minutes after robot removal.

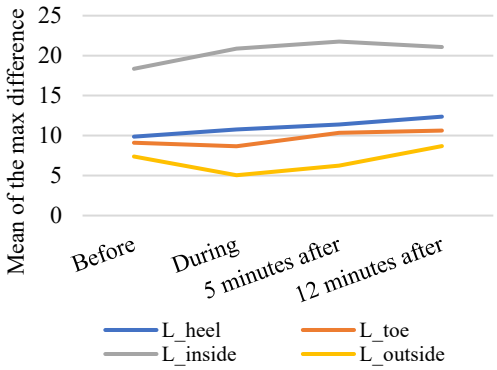

Fig. 5. Post-peak decrease rate (left foot).

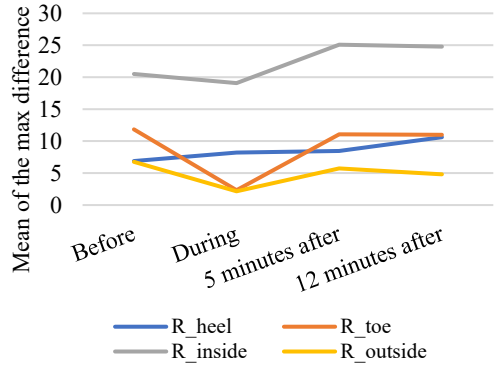

Fig. 6. Post-peak decrease rate (right foot).

3.4. Accelerometer Data

Accelerometer data were compared based on the mean of the absolute values. As shown in Fig. 7, the square root of the sum of the squares of the values for the three axes increased after robot-assisted walking, suggesting an overall acceleration of leg movement. Acceleration in the X- and Y axes increased during walking in both the during-robot- and post-robot-assisted walking phases compared with before robot-assisted walking, whereas it decreased in the Z-axis during robot-assisted walking and twelve minutes later. This may indicate a potential to capture changes in walking patterns. Furthermore, examining the standard deviation (refer to Table 2), it was observed that even in this result, the maximum was achieved at five minutes after robot-assisted walking, and the value increased significantly twelve minutes thereafter.

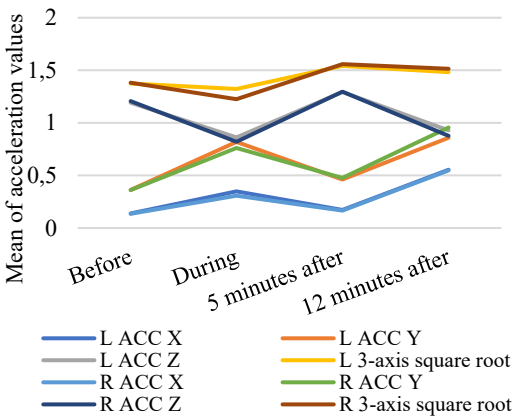

Fig. 7. Acceleration data.

Table 2. Standard deviations of the accelerometer data.

	Left	Right
Before	0.605	0.591
During	0.589	0.491
5 minutes after	0.877	0.903
12 minutes after	0.865	0.832

4. Discussion

After robot-assisted walking, there was a tendency for the peak values to increase at the heel and inside part of the foot. Moreover, the inside part exhibited a significant maximum decrease rate after the peak, indicating rapid weight transfer. Accelerometer data revealed differences in the speed and movement direction after robot-assisted walking. This suggests the possibility of an increased stride length or greater leg swing. The effects of robot-assisted walking influenced both the right foot, to which the robot was attached, and the left foot, based on data from both insole and acceleration measurements. Therefore, assessing its effects using either the insole or accelerometer alone is possible.

5. Conclusions

Changes were detected in both the insole and accelerometer before and after robot-assisted walking sessions. Data collected twelve minutes after robot removal also varied. The insoles and accelerometer sensors attached to the shoes have the potential to detect changes in walking patterns. In the future, provided that the use of sensors becomes more accessible in the field of rehabilitation, they may contribute to assessing the effectiveness of rehabilitation training and determining how much of the effect of rehabilitation persists after its completion.

Acknowledgements

This study was supported by JSPS KAKENHI, Grant Number JP23K11207.

References

[1]. S. Raghav, S. Mani, A. Anand, S. Pathak, A. Singh, G. Kandasamy, M. Kumar, Role of Sensor-Based Insole as a Rehabilitation Tool in Improving Walking among the Patients with Lower Limb Arthroplasty: A Systematic Review, *Intelligent Systems and Smart Infrastructure: Proceedings of ICISSI 2022*, 2023, 38.

[2]. B. Marques, J. McIntosh, A. Valera, and A. Gaddam, Innovative and assistive eHealth technologies for smart therapeutic and rehabilitation outdoor spaces for the elderly demographic, *Multimodal Technologies and Interaction*, 4, 4, 2020, 76.

[3]. A. Middleton, G. D. Fulk, M. W. Beets, T. M. Herter, S. L. Fritz, Self-selected walking speed is predictive of daily ambulatory activity in older adults, *Journal of Aging and Physical Activity*, Vol. 24, Issue 2, 2016, pp. 214 -222.

[4]. T. Funayama, Y. Uchida, Y. Kogure, Detection of motion restriction with smart insoles, *Sensors & Transducers,* Vol. 259, Issue 5, 2022, pp. 61-68.

[5]. T. W. Seo, J. Y. Lee, B. H. Lee, The reliability test of a smart insole for gait analysis in stroke patients, *Korean Physical Therapy Science*, Vol. 29, No.1, 2021, pp. 30-40.

[6]. S. Saidani, R. Haddad, R. Bouallegue, R. Shubair, A New Proposal of a Smart Insole for the Monitoring of Elderly Patients, in *Proceedings of the 35th International Conference on Advanced Information Networking and Applications*, Toronto, Canada, 12-14 May 2021, Vol. 2, pp. 273-284.

[7]. E. M. Macdonald, B. M. Perrin, L. Cleel, M. I. C. Kingsley, Podiatrist-Delivered Health Coaching to Facilitate the Use of a Smart Insole to Support Foot Health Monitoring in People with Diabetes-Related Peripheral Neuropathy, *Sensors*, Vol. 21, Issue 12, 2021, 3984.

[8]. S. Subramaniam, S. Majumder, A I. Faisal, M J. Deen, Insole-Based Systems for Health Monitoring: Current Solutions and Research Challenges, *Sensors*, 2022, Vol 22, Issue 2, 438.

[9]. S. Kim, S. Park, S. Lee, S. H. Seo, H. S. Kim, Y. Cha, et al., Assessing physical abilities of sarcopenia patients using gait analysis and smart insole for development of digital biomarker, *Scientific Reports*, Vol. 13, Issue 1, 2023, 10602.

[10]. V. Tsakanikas, A. Ntanis, G. Rigas, C. Androutsos, D. Boucharas, N. Tachos, et al., Evaluating gait impairment in Parkinson's disease from instrumented insole and IMU sensor data, *Sensors*, Vol. 23, Issue 8, 2023, 3902.

[11]. T. Funayama, Y. Uchida, and Y. Kogure, Step Measurement Using a Household Floor Mat and Shoe Sensors, *International Journal on Advances in Life Sciences,* Vol. 15, No. 1 & 2, Issue 5, 2023, pp. 33-43.

(024)

Exploring the Hidden Complexity: Approximate Entropy and Sample Entropy Analysis in Pulse Oximetry of Female Athletes

A. M. Cabanas [1], D. Catalán [1], N. Sáez [1], C. Flores [1], and P. Martín-Escudero [2]
[1] Departamento de Física, Universidad de Tarapacá, Arica, 1010069, Chile
[2] Medical School of Sport Medicine, Faculty of Medicine, Universidad Complutense de Madrid, Madrid, 28040, Spain
E-mail: acabanas@academicos.uta.cl

Summary: In recent years, the use of Approximate Entropy (ApEn) and Sample Entropy (SampEn) to quantify the complexity of time-series data in the medical and sports fields has attracted significant attention. These methods have been employed across various biomedical signals, such as heart rate, to evaluate physiological changes or conditions. This study aims to examine the application of ApEn and SampEn to temporal series of pulse oximetry and heart frequencies collected from a cohort of female athletes. Through a comparative analysis, we highlight the differences between ApEn and SampEn in representing the regularity and unpredictability of these physiological signals. Additionally, we delve into the relationship between these entropy measures and the athletes' maximal oxygen consumption ($VO_{2,max}$). Preliminary findings suggest that while both entropy measures provide valuable insights into the athletes' physiological complexities, SampEn emerges as a more consistent and dependable metric, especially for shorter data sets. Furthermore, we've uncovered pivotal insights regarding the relationship between fitness levels and entropy measures, suggesting the potential of these metrics as predictors or indicators of both athletic performance and cardiovascular health. This study emphasizes the importance of entropy-based metrics in sports physiology and sets the stage for more specialized interventions for athletes using monitoring devices.

Keywords: Pulse oximeter, Approximate entropy, Sample entropy, $VO_{2,max}$, Women's response to exercise.

1. Introduction

In recent years, there has been escalating interest in understanding the factors that influence the physiological response of women to exercise, particularly the variations in oxygen saturation. Research has shown that women tend to exhibit an early decrease in oxygen saturation during maximal exercise, experiencing this at lower oxygen intakes compared to men. Some theories postulate that active, healthy women might encounter exercise-induced arterial hypoxia due to anatomical differences in lung capacity and structure, potentially affecting oxygen diffusion. However, more recent studies suggest that the oxygen desaturation observed in women is the primary limiting factor in achieving peak maximum oxygen uptake ($VO_{2,max}$) levels, rather than mere lung size or capacity [1].

The advent of wearable sensors, which continuously monitor physiological variables like heart rate (HR) and oxygen saturation using photoplethysmography (PPG), offers a promising avenue to understand exercise effects and to tailor training interventions. Pulse oximetry, a non-invasive optical technique, has emerged as a vital tool for studying oxygenation during physical exertion, enabling continuous tracking of changes in peripheral oxygen saturation. Although pulse oximetry has limitations [2], investigating oxygen saturation variations through wearable devices like pulse oximeters can significantly augment our comprehension of physiological responses to exercise. This understanding can then be leveraged to personalize training interventions and optimize performance monitoring.

Emerging evidence points to the intricate patterns of variability in SpO2 signals as a treasure trove of insights into respiratory control and the perception of breathlessness during hypoxic conditions [3]. Fluctuations in SpO_2 are correlated with breathlessness perception and reflect the exchange of information with other respiratory variables [4].

The assessment of dynamical system regularity is a prominent subject in the fields of science and engineering. Indeed, the ability to discern levels of complexity within biological data sets has become increasingly important. This measurement has diverse applications, such as analyzing medical health conditions [5,6], identifying anomalies in real-time network dynamics [7] and predicting earthquakes [8]. Various statistical and mathematical approaches have been developed to quantify complexity within time series data. These methods encompass the Kolmogorov complexity measure [9], the C1/C2 complexity measure [9], and entropy [10].

This growing understanding of physiological time-series data complexity has paved the way for various statistical metrics. In this context, Approximate Entropy (ApEn) and Sample Entropy (SampEn) have gained prominence in recent times [11,12]. These measures, originally developed to quantify the regularity and complexity of time-series data, have

found extensive applications in the biomedical realm, helping discern patterns and irregularities in various physiological signals [11, 12].

Pulse oximetry and heart rate data, pivotal indicators of cardiovascular and respiratory health, offer a myriad of insights ripe for entropy-based analysis. In the realm of athletic performance, these physiological indicators are invaluable. They not only reflect an athlete's health but also offer a lens into performance potential and resilience [1]. Female athletes, given their distinct physiological dynamics, represent a fascinating demographic for such investigations, demanding tailored methodologies for analysis and interpretation [1].

Central to athletic performance, especially in endurance sports, is the measure of $VO_{2,max}$ — the maximal oxygen consumption. This parameter essentially represents an individual's capacity to transport and utilize oxygen during incremental exercise, often correlated with cardiovascular fitness and aerobic endurance [11]. The relationship between $VO_{2,max}$ max and entropy measures of pulse oximetry and heart frequencies can provide profound insights into the intricacies of female athletic performance [12].

While both ApEn and SampEn aim to quantify the unpredictability of fluctuations in a time series, they are not without their nuances. ApEn has been observed to have certain biases, especially with shorter data sets, which can render its results unreliable [13]. SampEn, developed as an improvement over ApEn, addresses some of these limitations, offering more consistency and reliability, especially with short data sets [13].

This article delves into the nuances of ApEn and SampEn as applied to time-series data from pulse oximetry and heart rates of female athletes. Our objective is to offer a statistically robust and consistent metric of system complexity, elucidate the distinctions between these entropy measures, and explore their interplay with $VO_{2,max.}$

2. Methods

Entropy, a foundational thermodynamics concept that gauges disorder within a closed system, holds significance in nonlinear dynamical systems for assessing complexity. It proves valuable for scrutinizing time series due to its unconstrained approach to probability distribution [14]. Shannon entropy (ShEn) and conditional entropy (ConEn) serve as fundamental metrics to measure information quantity and generation rate, respectively [5]. These underpin other entropy gauges developed to evaluate time series intricacies. In this framework, entropy provides researchers the ability to quantify complexity within relatively short data sets based on meaningful experimental comparisons to control groups.

Pincus introduced the widely employed approximate entropy (ApEn) metric as a measure of regularity to quantify levels of complexity within a time series [14]. It measures system complexity akin to entropy and is better suited for analyzing clinical cardiovascular and other time series data. Another entropy measure, sample entropy (SampEn), was established by Richman and Moorman [16]. SampEn aligns more closely with theoretical expectations than ApEn across various conditions [16]. This enhanced accuracy makes SampEn valuable for analyzing experimental clinical cardiovascular and other biological time series data.

In our research, we extracted time-series data pertaining to pulse oximetry and heart rate from a group of twenty-seven physically active and healthy female participants. These athletes underwent an incremental exercise test using a treadmill ergometer. Data from ergospirometry was meticulously recorded on protocol sheets, which were later transferred to anonymized databases. We then employed Approximate Entropy (ApEn) and Sample Entropy (SampEn) methods to evaluate the complexity and regularity of these time-series datasets.

2.1. Entropy-Based Regularity Assessment of Time Series Data

To quantify the regularity and complexity of our time-series data, we employed two entropy-based metrics: Approximate Entropy (ApEn) and Sample Entropy (SampEn).

ApEn measures the unpredictability of fluctuations in a time-series dataset. Introduced by Pincus [17,18], it's been applied in various biomedical contexts for its ability to handle short and noisy data. ApEn is robust to noise, works for both stochastic and deterministic processes, and produces non-negative values indicating complexity.

Given a time-series data of length N $u(i), u(2), \dots, u(N)$, the following steps outline its computation:

1. Fix parameters: m (pattern length) and r (similarity criterion).
2. Form N-m+1 vectors of length m from the time series $\mathbf{x}_m(i)$. The distances between them is: $d[x(i), x(j)] = max_k(|u(i+k) - u(j+k)|$ with $0 \leq k \leq m-1$
3. For each vector, count the number of vectors that are similar to it within a tolerance r. $C_i^m(r)$=(number of $j \leq N-m+1$ such that $d[x(i), x(j)] \leq r)/(N-m+1)$.
4. Compute the regularity measure for patterns of length m as:
$$\varphi^m(r) = \frac{1}{N-m+1} \sum_{i=1}^{N-m+1} log C_i^m(r) \quad (1)$$
5. The statical estimator of the ApEn(m,r,N) is then defined as:
$$ApEn(m,r,N)(u) = \varphi^m(r) - \varphi^{m+1}(r) \quad (2)$$

On the other hand, SampEn is a refinement of ApEn, designed to be less dependent on time series length and more consistent [16]. SampEn addresses some of the biases and inconsistencies of ApEn. Indeed, its calculation excludes self-matches, making it a more unbiased estimator of system complexity. Given the same time series, the computation involves:

1. Similar to the steps in ApEn, begin with a time series of length N and construct vectors.
2. However, in counting the number of matches, do not include self-matches (i.e., exclude the case j=i).
3. Define regularity measures for sequences of length m as:

$$B^m(r) = \frac{1}{N-m}\sum_{i=1}^{N-m} C_i^m(r)$$

and

$$A^m(r) = \frac{1}{N-m-1}\sum_{i=1}^{N-m-1} C_i^{m+1}(r)$$

4. Compute SampEn(m,r,N)(u) as:

$$SampEn(m,r,N) = -ln\frac{A^m(r)}{B^m(r)}$$

In summary, both ApEn and SampEn measure the regularity or unpredictability of time-series data, with SampEn being refined to exclude self-matches. This distinction in the counting method results in SampEn generally producing more consistent and reliable results than ApEn.

To investigate the influence of parameters on entropy calculations, time series data was analyzed using various combinations for ApEn and SampEn. The parameters were "m" (length of data for comparison) with values of 1, 2, and 3, "r" (sensitivity criterion) set at 0.1, 0.15, 0.20, and 0.25 times the standard deviation of the whole time series. "N" (data length) represents the total count of steps in the series. In this context, "m" indicates the number of steps compared in a sequence, while "r" denotes the acceptable variance in step lengths. For example, with m=2, two steps are compared, and with r=0.2, step lengths are considered similar if they vary within 20% of the series' overall standard deviation. Let us remark that a practical approach is to define the tolerance as r=0.2SD, where SD represents the standard deviation of the dataset. This facilitates comparisons between datasets with varying amplitudes. For the purposes of this study, every time series was normalized to yield an SD of 1.

3. Results

Table 1 summarizes the clinical variables of N (the 27 participants in the study). The values presented are averages, accompanied by their respective standard deviations to provide an understanding of the variability within the data.

The temporal evolution of the oxygen saturation SpO_2 and the HR obtained from the ECG signal for two athletes is depicted in Fig. 1. The blue lines correspond to the SpO_2 temporal series while the red and pink lines correspond to the HR dataset in bmp [1]. The continuous line correspond to an athlete with a good physical fitness condition ($VO_{2,max}$=45.7 ml/(kg·min)). The dash-dotted lines correspond to a dark-skinned athlete with an excellent physical fitness condition ($VO_{2,max}$=50.9 ml/(kg·min)).

Table 1. Clinical characteristic of the participants.

Subjects: 27	$\bar{X} \pm SD$
Age (years)	22.96 ± 6.19
Size (cm)	163.81 ± 6.90
Weight (kg)	57.24 ± 6.70
BMI (kg/m^2)	21.31 ± 1.98
HR_{max} (bmp)	189.81 ± 8.54
$VO_{2,max}$(ml/(kg·min))	48.90 ± 7.62

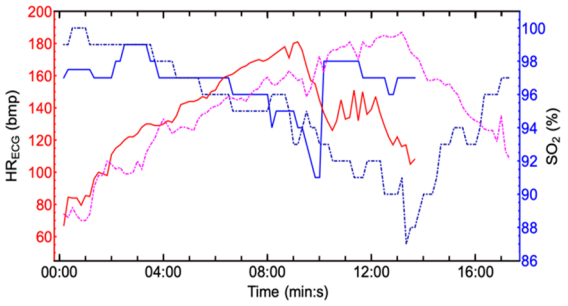

Fig. 1. Temporal evolution of SpO_2 and HR time series for two different athletes [1].

Fluctuations have the potential to convey valuable insights into the overall health and functioning of the respiratory system. The impact of modifying "m" (embedding dimension) and "r" (threshold) on Approximate Entropy (ApEn) and Sample Entropy (SampEn) was explored for both HR and SpO_2 time series.

Fig. 2 depicts values of SampEn and ApEn for heart rate (HR, represented in red colors) and pulse oximetry (SpO_2, represented in blue colors) across three panels, each corresponding to an athlete with varying fitness levels based on their $VO_{2,max}$ values. Panel a) corresponds to an athlete with medium condition ($VO_{2,max}$ <40). In this case, for both HR and SpO_2, the ApEn and SampEn values seem relatively constant across different values of "r" for the different values of "m". This consistency suggests that, for athletes with medium fitness levels, increasing the dimensionality (increasing "m") doesn't significantly change the entropy estimates across various threshold values ("r"). Since lower entropy values indicate more regularity and less complexity, this suggests that athletes with medium fitness levels may have more predictable and regular physiological response.

Panel b) corresponds to an athlete with good condition (40<$VO_{2,max}$ <50). We observe that the values of ApEn and SampEn are higher than panel a) but slightly lower than panel c). This increase in entropy values suggests that as fitness levels improve, the physiological responses exhibit more complexity. This could be due to the cardiovascular and respiratory systems' adaptability, as they become better trained to handle varying physical challenges.

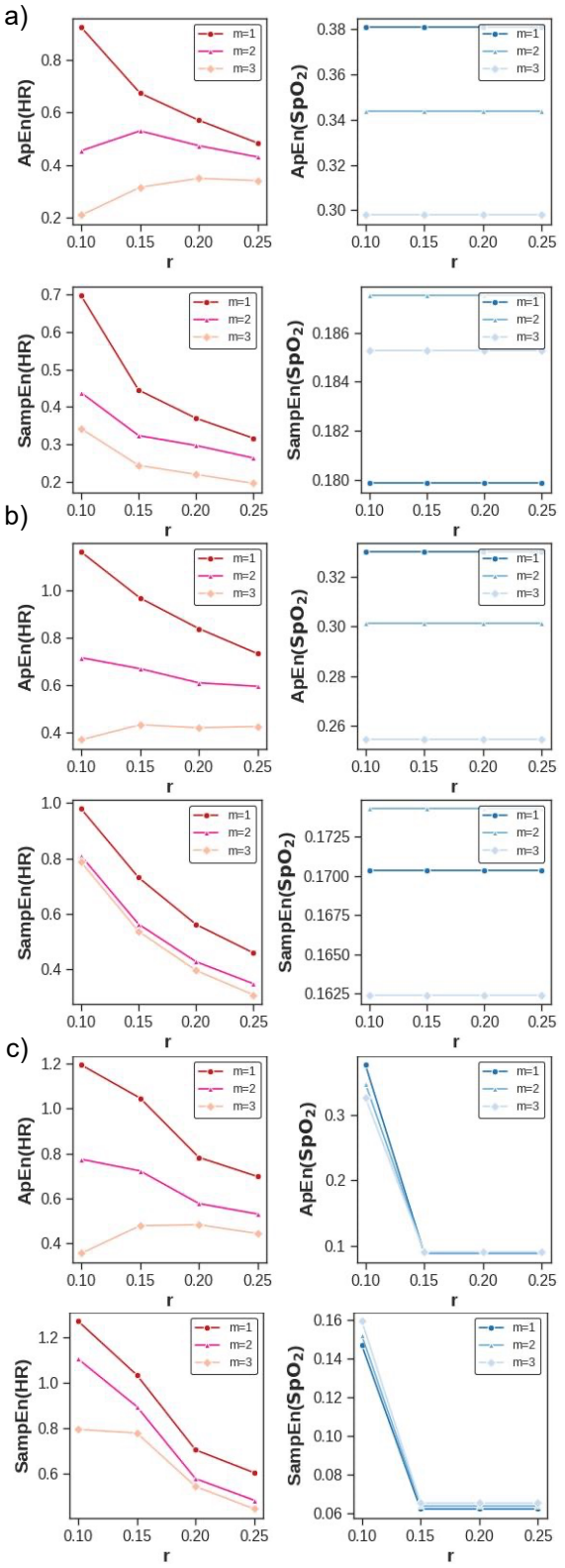

Fig. 2. ApEn and SampEn for three athletes with a) medium, b) good and c) excellent condition.

Besides, for both HR and SpO2, the ApEn and SampEn values seem relatively constant across different values of "r" for the different values of "m". This also suggests that, for athletes with medium fitness levels, increasing the dimensionality doesn't significantly change the entropy estimates across various threshold values (r). Lastly, panel c) shows ApEn and SampEn for an athlete with excellent condition ($VO_{2,max}$>50). There's a noticeable variability in ApEn and SampEn values across different r values, especially for m=2. This variability could be indicative of the more complex physiological adaptations and responses in athletes with superior fitness levels. Their cardiovascular system might be more adaptable and capable of dynamic responses to different physiological challenges.

Across the panels, SampEn values seem consistently lower than ApEn values for both HR and SpO_2. ApEn can be biased, especially for short datasets, as it counts self-matches, leading to higher values. In contrast, SampEn eliminates this bias by excluding self-matches, often resulting in lower values [14, 16].

When examining the complexity and regularity of physiological time series using Approximate Entropy (ApEn) and Sample Entropy (SampEn), the choice of parameters "m" and "r" is crucial. In our case, the choice of m=2 and r=0.2 is supported by both empirical and theoretical considerations. As shown in Fig. 2 when m=2, the entropies provide a stable measure across different conditions and subjects. Besides, using m=2 is computationally efficient, especially for longer time series. As the embedding dimension increases, the computational demands rise exponentially. The choice of r=0.2 is based on the idea of examining patterns that deviate by 20 % of the standard deviation of the time series. This value is a common choice in many studies and provides a balance between sensitivity and specificity.

The choice of m=2 and r=0.2 is also consistent with many previous studies on physiological time series. It provides a balance between sensitivity, reliability, computational efficiency, and discriminative power. Furthermore, this consistency allows for better comparability across studies and condition.

Fig. 3 displays the values of ApEn and SampEn for the specific choices of m=2 and r=0.2. Each dot represents an individual athlete's entropy values. A clear trend is observed: as the fitness condition of the athletes improves, there's an increase in the values of both ApEn and SampEn. This upward trend signifies that as athletes achieve higher fitness levels, their physiological responses become more complex and less predictable, echoing the intricacies of a well-trained cardiovascular system.

Additionally, we observe a higher degree of dispersion in the entropy values among athletes with excellent fitness conditions. This increased dispersion may indicate that while all these athletes are at a high fitness level, the intricacies of their physiological responses vary more widely. Such variance could be attributed to multiple factors, including specific training regimens, genetic factors, or other physiological aspects that contribute to an athlete's overall performance and adaptability.

Table 2 presents a detailed comparison of Approximate Entropy (ApEn) and Sample Entropy (SampEn) values as a function of the fitness conditions

of the athletes. The values are presented as averages ($\bar{X}$) alongside their respective standard deviations (SD), providing insights into both the central tendency and variability of the entropy measures. Athletes with medium fitness levels have an average ApEn of 0.57 for heart rate (HR), with a standard deviation of 0.13. This suggests a moderate level of complexity in their heart rate patterns. For pulse oximetry (SpO_2), the average ApEn is higher at 0.96 with a broader spread (SD=0.49), indicating greater unpredictability in oxygen saturation levels for this group. The average SampEn for HR is 0.33 with an SD of 0.08, indicating a lower complexity compared to ApEn. The average SampEn for SpO_2 is 0.19, with an SD of 0.04, reflecting a more regular and predictable oxygen saturation pattern than its ApEn counterpart.

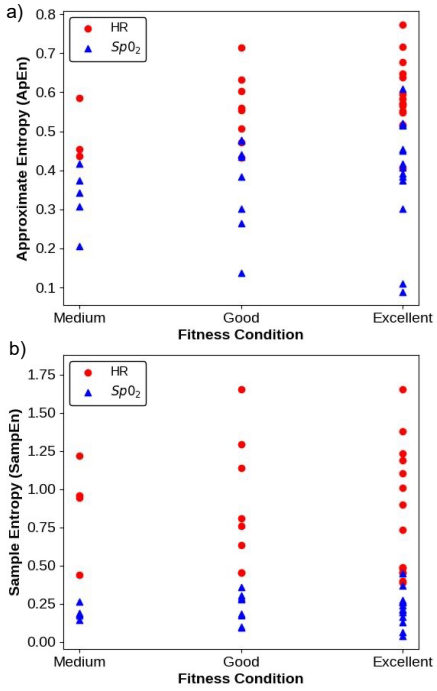

Fig. 3. a) ApEn and b) SampEn for m=2 and r=0. The blue dots correspond to the HR data, while the red triangles correspond to the SpO_2 data.

Table 2. Approximate Entropy and Sample Entropy average and SD ($\bar{X} \pm SD$) as a function of the fitness condition of the athelets.

Fitness Condition	ApEn ($\bar{X} \pm SD$)		SampEn ($\bar{X} \pm SD$)	
	HR	SpO_2	HR	SpO_2
Medium	0.57 ± 0.13	0.96±0.49	0.33 ± 0.08	0.19 ± 0.04
Good	0.56 ± 0.09	0.90 ± 0.43	0.36 ± 0.12	0.22 ± 0.10
Excellent	0.60 ± 0.09	0.85 ± 0.42	0.40 ± 0.15	0.22 ± 0.11

Furthermore, athletes in good condition show an ApEn of 0.56 (SD = 0.09) for HR, almost similar to the medium fitness group. Their SpO_2 ApEn is slightly lower than the medium group at 0.90 with an SD of 0.43. The SampEn for HR increases to 0.36 with an SD of 0.12. The SpO_2 SampEn average is 0.22 with an SD of 0.10, showing a slight increase in complexity compared to the medium fitness group.

Lastly, athletes with excellent fitness have an average ApEn of 0.60 for HR with an SD of 0.09, marking the highest complexity among the groups. Their SpO_2 ApEn is 0.85 with an SD of 0.42, slightly lower than the good fitness group. The SampEn for HR is at its highest for this group, averaging 0.40 with an SD of 0.15. The SpO_2 SampEn remains consistent with the good fitness group, averaging 0.22, but with a slightly higher SD of 0.11.

In essence, the table underscores the nuanced physiological differences that manifest across varying levels of athlete fitness, captured effectively through entropy measures. The data also reveals a greater variability (as seen from the SD values) in entropy measures, especially in the excellent fitness group. This might suggest that while these athletes are all highly fit, there's a diversity in their physiological responses.

4. Conclusions

The primary focus of this article was to explore the utility of Approximate Entropy (ApEn) and Sample Entropy (SampEn) as regularity statistics for female athletes during incremental exercise. Our results not only underscore the potential of entropy measures as diagnostic tools but also illuminate the subtle physiological differences evident as athletes approach peak fitness levels.

Athletes possessing medium to good fitness levels display stable ApEn and SampEn values, signifying a uniform and predictable physiological response. Conversely, athletes at the pinnacle of fitness exhibit greater variability in entropy measures, indicative of intricate physiological adaptations and a highly adaptable cardiovascular system.

A notable observation was the consistent bias in ApEn, which consistently produced higher values compared to SampEn. This disparity originates from the inclusion of self-matches in ApEn calculations. Thus, SampEn emerges as a more reliable measure, particularly for shorter datasets. It's crucial for researchers to account for this bias when employing entropy measures for analysis. Our study sheds light on the intricacies of physiological time series, with entropy values offering a window into the complexity and regularity of physiological responses. This paves the way for a deeper comprehension of an athlete's adaptability and overall health. Integrating easily computable ApEn and SampEn metrics into monitoring devices has the potential to revolutionize personalized training interventions. Additionally, the broad application of these metrics across diverse research fields promises new avenues for analytical exploration. Work in this direction is in progress.

Acknowledgements

A.M.C., D.C., N.S. and P.M-E. thanks support from ANID Project SA22I0178. A.M.C thank support from ANID Project SA77210039.

References

[1]. P. Martín-Escudero, A. M. Cabanas, M. Fuentes-Ferrer, M. Galindo-Canales. Oxygen Saturation Behavior by Pulse Oximetry in Female Athletes: Breaking Myths, *Biosensors.* Vol. 10, Issue 11, 2021 pp. 1-19 .

[2]. Division of Industry and Consumer Education (DICE). United States Food and Drug Administration. FDA. Pulse Oximeter Accuracy and Limitations: FDA Safety Communication. 2021.

[3]. Y. Jiang, J. T. Costello, T. B. Williams, N. Panyapiean, A. S. Bhogal, M. J. Tipton, et al., A network physiology approach to oxygen saturation variability during normobaric hypoxia, *Experimental Physiology,* Vol. 1, Issue 106, 2021, pp. 151-9.

[4]. A. L. Holder, A. Wong, The Big Consequences of Small Discrepancies: Why Racial Differences in Pulse Oximetry Errors Matter, *Critical Care Medicine,* Vol. 2, Issue 50 2022, pp. 335-337.

[5]. H. Azami, J. Escudero, Amplitude and Fluctuation Based Dispersion Entropy, *Entropy*, Vol. 20, 2018, 210.

[6]. B. Yan, S. He, K. Sun, Design of a network permutation entropy and its applications for chaotic time series and EEG signals, *Entropy*, Vol. 21, 9, 2019, 849.

[7]. S. E. Benkabou, K. Benabdeslem, B. Canitia Unsupervised outlier detection for time series by entropy and dynamic time warping, *Knowledge and Information System,* Vol. 54, 2018, pp. 463-486.

[8]. A. Ramírez-Rojas, L. Telesca, F. Angulo-Brown, Entropy of geoelectrical time series in the natural time domain, *Natural Hazards and Earth System Sciences,* Vol. 11, 2011, pp. 219-225.

[9]. Y. Li, Y. Fan, Complexity measure applied to the analysis EEC signals, in *Proceedings of the 27th Annual IEEE Conference on Engineering in Medicine and Biology, Shanghai*, China, 1–4 September 2005; pp. 4610–4613.

[10]. L. Zunino, F. Olivares, F. Scholkmann, O. A. Rosso, Permutation entropy based time series analysis: Equalities in the input signal can lead to false conclusions, *Physics Letters, Section A: General, Atomic and Solid State Physics*, Vol. 381, 2017, pp. 1883-1892.

[11]. A. Delgado-Bonal, A. Marshak, Approximate entropy and sample entropy: A comprehensive tutorial, *Entropy,* Vol. 21, 6, 2019, 541.

[12]. M. Spedding, R. Marvaud, A. Marck, Q. Delarochelambert, J. F. Toussaint, Aging, VO2 max, entropy, and COVID-19, *Indian Journal of Pharmacology*, 54, 2022, pp. 58-62.

[13]. J.M. Yentes, N. Hunt, K.K. Schmid, J.P. Kaipust, D. McGrath, N. Stergiou, The appropriate use of approximate entropy and sample entropy with short data sets, *Annals of Biomedical Engineering,* Vol. 2, Issue 41, 2013, pp. 349-365.

[14]. S. M. Pincus, Approximate entropy as a measure of system complexity, *Proceedings of the National Academy of Sciences,* Vol. 6, Issue 88, 1991, pp. 2297–301.

[15]. J. W. Liou, P. S. Wang, Y. T. Wu, S. K. Lee, S. D. Chang, M. Liou, ECG Approximate Entropy in the Elderly during Cycling Exercise, *Sensors*, Vol. 14, 2022, 22.

[16]. J. S. Richman, J.R. Moorman. Physiological time-series analysis using approximate entropy and sample entropy maturity in premature infants Physiological time-series analysis using approximate entropy and sample entropy, *American Journal of Physiology Heart and Circulatory Physiology*, Vol. 278, 2000, pp. H2039-H2049.

[17]. S. Pincus, and W. Huang, Approximate entropy - statistical properties and applications, *Communications in Statistics - Theory and Methods,* Vol. 21, 1992, pp. 3061-3077.

[18]. S. Pincus, Approximate entropy (ApEn) as a complexity measure, *Chaos,* Vol. 5, Issue 31, 1995, pp. 110–117.

(025)

Development of a Smart Irrigation System for Apple Fields using a LoRaWAN Network

R. Mendicino, S. Tritini, A. Mejia-Aguilar and R. Monsorno
Center for Sensing Solutions, Eurac Research, Via A. Volta, 13/A, Bolzano, Italy
Tel.: +39 0471 055395
E-mail: roberto.mendicino@eurac.edu

Summary: Smart irrigation systems used in agriculture are becoming increasingly important due to the optimization and management of resources, especially water. Recent climate change events have caused water shortages in many areas, making it critical to improve irrigation efficiency in agriculture for sustainable agricultural production. We provide a smart irrigation method to enhance irrigation efficiency, by means of a multi-platform approach, combining a wireless sensor network (WSN) of soil moisture and a phenocam to monitor plant stress. The developed system consists of three main hardware elements: a LoRaWAN gateway that collects data from the sensor nodes and, thanks to its internet connectivity, allows the second component, a phenocam, to collect RGB and infrared photos; and, as the last component, the sensor nodes that are distributed in the field and measure the soil moisture at different positions and depths. In addition to the hardware, a large software component is part of the system, with databases, dashboards for displaying data in real-time, and analysis tools.

Keywords: Agriculture smart sensors, LoRaWAN network, Soil moisture sensors, Phenocam.

1. Introduction

The United Nations Convention to Combat Desertification (UNCCD) reported that drought affected at least 1.5 billion people and cost US$125 billion globally. Forecasts estimate that by 2050, droughts may affect over three-quarters of the world's population [1]. In this scenario, systems that monitor and optimize the use of water are very important. Novel sensors, comprising of smart sensors, are able to take decisions, including different communication protocols, optimize power consumption, and keep good resolution and accuracy, and have been introduced in the agriculture domain for some decades. In parallel, the capacity to adapt existing sensing methods to new applications is opening new opportunities to understand vegetation dynamics, especially in agriculture. Phenology cameras, or phenocams, investigate interactions between growth, phenology, and harvest traits [2].

We propose a system easy to replicate, scale up, to be efficient, and economically affordable, working for different farming crops, cost-effective to implement, and open to integrating different type of sensors.

LoRaWAN has already been used in many Internet of Things (IoT) applications for the agriculture domain because of its large communication range, battery life, high network capacity, and cost-effectiveness, which, compared to other solutions, allows for a better cost-effectiveness ratio [2][3]. Starting from a commercial LoRaWAN gateway, a series of additional circuits and modifications have been made in order to efficiently integrate the phenocam. Phenocam has shown to be a good technology for field phenotyping, as it investigates interactions between growth, phenology, and harvest traits [4]. A custom node has also been developed, with an emphasis on the power budget. The nodes have been installed in an apple orchard at Laimburg (Bolzano), inside the project LIDO (Laimburg Integrated Digital Orchard) [5], and data collection immediately began.

2. Design of the System

Fig. 1 shows the hardware and software architecture of the proposed system, which is composed of: LoRaWAN gateway with the integration of phenocam (mod. NetCam SC H264), IoT nodes with custom electronics to minimize power consumption, LoRaWAN network server, database and visualization tools and soil moisture and temperature sensor.

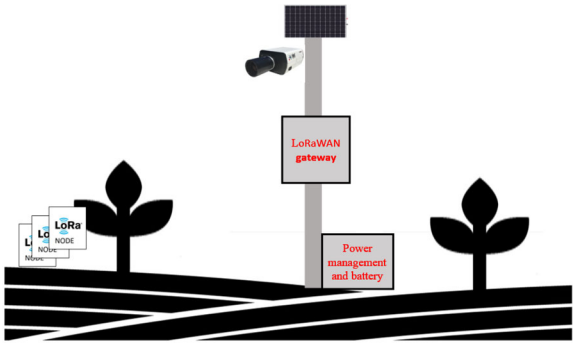

Fig. 1. Schematic of the hardware components that compose the system.

The integration of the LoRaWAN gateway with phenocam has been achieved by adding a commercial voltage regulator circuitry inside the gateway for the correct power supply of both devices and a relay to switch on the camera when required.

The communication between the camera and gateway is guaranteed by Ethernet connectivity, and the relay is activated by using an internal pin of the motherboard that, after much reverse engineering, has been found to be controllable by software. A custom software for the gateway has been developed that allows the camera to be switched on, wait for connectivity, and download the picture directly to the phenocam API.

The camera has been installed at a height of approximately 3 meters and pointing to the north to avoid unwanted light scattering, on the same pole where the photoelectric panel and battery pack have been installed.

The IoT nodes use a Pycom Lopy4 as their main microcontroller, which has an integrated LoRaWAN communication module, an ADC 16 Bit that acquires data from the sensors via I2C communication, and a custom circuit that generates the correct power supply for the sensors and microcontroller.

Additionally, the LTC6995-2 component switches the system on every 30 minutes for 30 seconds (the time necessary to acquire and send the new data) and reduces the power consumption to 300µW during sleep mode. A battery of 3100mAh and a 78×100 mm^2 panel, along with its circuit, are assembled to complete the node.

Fig. 2a shows the block diagram of the system. Since the ADC module has only four inputs and each node needs to collect data from three soil moisture sensors and three temperature sensors, the number of channels is not enough.

Therefore, since the temperature is less important in this application, it has been decided to use the internal ADC of the Pycom Lopy4 for two measured temperatures. It is based on Espressif Systems ESP32, in which the ADC has a higher noise level compared to the dedicated module.

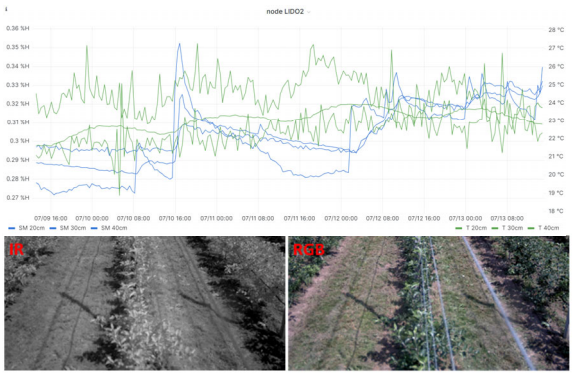

Fig. 3. In the top part the sensor node data (temp. & soil moisture) and in the bottom part an example of the phenocam images (RGB and IR).

This choice will be reflected in the results, where it is possible to note that the noise level is higher for the temperature acquired by the Pycom Lopy4 ADC.

Soil moisture and temperature sensors have been integrated to measure both moisture and temperature. Moisture measurement uses the principle of frequency-domain sensors (FDR), which measure the dielectric constant of the soil in order to measure the volume of soil moisture content.

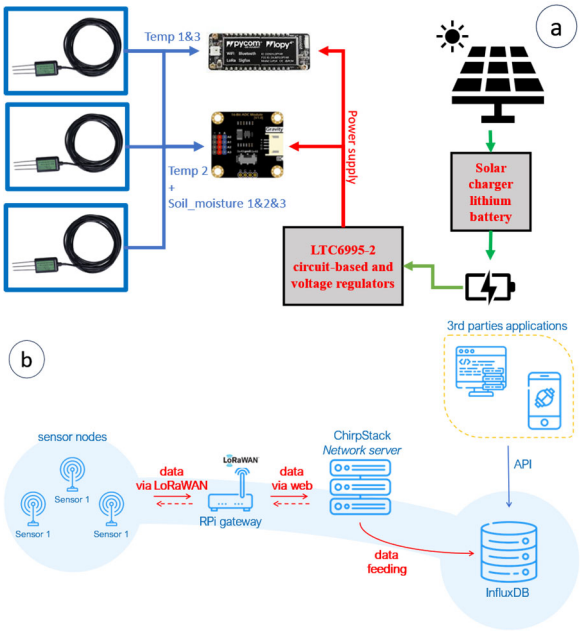

Fig. 2. a) Block scheme of the sensor node, b) architecture of the back-end system.

The output is linear in the range 0-2 V for volumetric moisture content 0-100 % of soil moisture and 0-2 V for the temperature -40 C to 80 C.

The sensors have been installed at different depths between 20-40cm to map the temperatures and soil moisture in dependence on position and depth.

The LoRaWAN network server has been chosen to be ChirpStack, a platform that allows the registration of many LoRaWAN devices in a network. Moreover, it is possible to create the applications that help to collect the data coming from the devices, and to monitor all packets passing through the network. Via its interface a decoding script has been configured to receive the data coming from the registered devices and converts it into the correct format before sending it to the API to be stored in the database (Fig. 2b).

The system is configured to use an API that links the network server with the database to save all the incoming data. A timeseries-based (NoSQL) database, called InfluxDB, is used to store the devices' timeseries. The data are displayed on a public dashboard developed using the Grafana platform [6].

3. Preliminary Results

Fig. 3 shows the dashboard with the related information of soil moisture over time and the pictures obtained by phenocam.

The data collection of the soil moisture has a cadence of 30 minutes.

Due to the analog nature of the circuitry for the power management of the node, the information is not synchronous.

Conversely, the acquisition of the phenocam is one image per hour from 7:00 AM to 5:00 PM.

Although the data is currently displayed on the dashboard as row data and saved in the database. It is important to note that the noise became apparent in the data acquired by the Pycom Lopy4 microcontroller. This is evident in the graph of the temperature, where the two temperatures acquired directly by the microcontroller are much noisier than the others acquired by the ADC board.

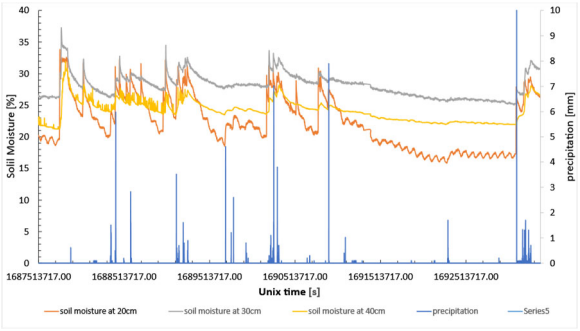

Fig. 4. The trend of soil moisture at different depths (20, 30 and 40cm) and the precipitation data collected by the Laimburg weather station.

Fig. 4 shows the trend of soil moisture at the three different depths of 20, 30 and 40cm and the precipitation data collected by an official weather station. Specifically, the weather station in Laimburg (Bolzano) is used, which belongs to the network of weather stations installed and maintained by the Provincia Autonoma di Bolzano [7]. The station collects several parameters such as: air temperature, air humidity, precipitation, solar radiation, wind speed and direction, atmospheric pressure, and sunshine hours per day. The data collected is organized in daily averages or in single values taken every 5 minutes. In this case, the parameter of precipitation has been used to compare the soil humidity.

In order to facilitate the synchronization of the data acquired by the sensors and the official weather station, the time has been reported as Unix time.

Soil moisture peaks mainly correspond to the events of precipitation given by the rain. Since this data corresponds to the summer season, other peaks are present due to artificial irrigation.

The level of soil moisture sited at 40cm is more stable compared to the others, in particular with the one sited at only 20 cm.

If we observe the data, it is possible to note a few hours of difference in the maximum peak, this is due to the time required by the water to penetrate to higher depths.

Since this season has been characterized by abundant rains throughout the summer, the soil moisture data does not show any significant lack of water or suffering in the plants.

The derived products from the phenocam are:

• Red, Green, and Blue channels (RGB), which are useful for checking the field condition (orchard management);

• Near Infrared channel (NIR) to observe details that are not in the visible range;

• NDVI, the most standard and well-studied index (-1 unhealthy, +1 healthy) calculated with the formula NDVI = (NIR – Red) / (NIR + Red);

• reCI, used to have an estimation of the response to chlorophyll content in leaves nourished by nitrogen, calculated with the formula ReCI = (NIR / RED) – 1;

• GNDVI, similar to NDVI but using the green channel of RGB, calculated with the formula GNDVI = (NIR – Green) / (NIR + Green).

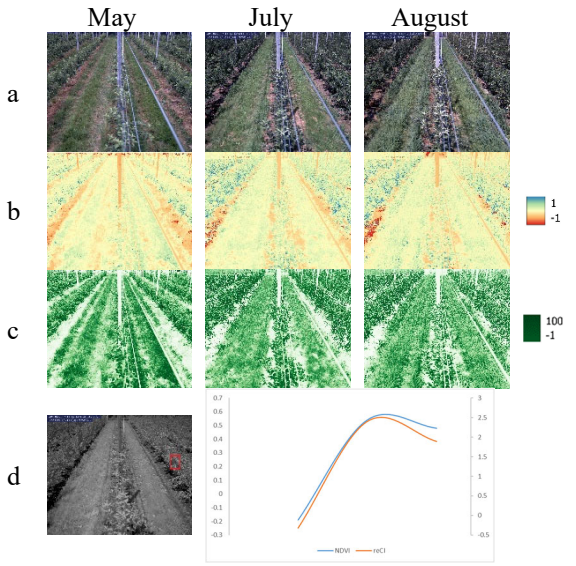

Fig. 5. (a) RGB, (b) NDVI, (c) reCI and (d) NIR products. (d) Time series for an area of interest (red square).

Fig. 5 shows the capacity of our proposed method to integrate raster information. From the management perspective, the RGB product seems to be in accordance with the vegetation period. However, NDVI and reCI show a decrease during August. More likely it was an intervention in the orchard (pruning) to reduce the vigor of the plant (green biomass) while the fruits consume more available nutrients resulting in increasing the volume of them.

4. Conclusions

This work intends to present a smart system for monitoring soil moisture in an apple field using a multi-sensor approach, by means of soil moisture/temperature WSN integrated by phenocams monitoring system and integrating data coming from the nearest meteorological stations. The intention is to observe local variability at the level of the trees due to different soil conditions, water and nutrient assimilation, as well individual conditions of stress.

The system has been running smoothly since installation (May 2023) and the data collected is being analyzed by the agronomist. The results of the analysis will be used to inform future decisions about the crop.

References

[1]. The United Nations world water development report 2021 (https://www.unesco.org/reports/wwdr/2021/en)

[2]. P. Fraga-Lamas, M. Celaya-Echarri, L. Azpilicueta, P. Lopez-Iturri, F. Falcone, T. M. Fernández-Caramés, Design and empirical validation of a LoRaWAN IoT smart irrigation system. *MDPI Proceedings*, Vol. 42, No. 1, 2019, p. 62.

[3]. M. Usmonov, F. Gregoretti, Design and implementation of a LoRa based wireless control for drip irrigation systems, in *Proceedings of the 2nd International Conference on Robotics and Automation Engineering (ICRAE' 2017*), 2017, pp. 248-253.

[4]. H. Aasen, N. Kirchgessner, A. Walter, F. Liebisch, PhenoCams for field phenotyping: using very high temporal resolution digital repeated photography to investigate interactions of growth, phenology, and harvest traits, *Frontiers in Plant Science,* 11, 2020, 593.

[5]. LIDO - Laimburg Integrated Digital Orchard (https://lido.laimburg.it/it/)

[6]. Soil moisture - Eurac Research - LIDO, dashboard Grafana (https://cssprocapi01.eurac.edu/grafana/public-dashboards/e07f4785e8bb42d5897a6ae8f2a35cdd?orgId=1)

[7]. Provincia Autonoma di Bolzano – Alto Adige, Meteo Alto Adige, Stazione meteo Laimburg (https://meteo.provincia.bz.it/stazioni-meteo-valle.asp?stat_stid=1261)

(026)

The use of Azure Cloud Tools for Monitoring Indoor Air Quality

L. C. Eduardo [1], C.R.S. Alexandre [2] and A. S. F. Tercio [3]
[1] Universidade Estadual Paulista - UNESP, Engineering College - Ilha Solteira, São Paulo, Brazil
E-mail: eduardo.cruz23@etec.sp.gov.br
[2] Universidade Estadual Paulista - UNESP, Engineering College - Ilha Solteira, São Paulo, Brazil
E-mail: alexandre.cr.silva@unesp.br
[3] Federal University of Catalan - UFCat, Department of Computing, Catalão, Goiás, Brazil
E-mail: tercioas@ufcat.edu.br

Summary: Monitoring air quality in indoor collective environments is important for well-being and health care. This paper presents an indoor air quality monitoring system using ESP8266 and sensors DHT22, MICS6814, and GP2Y1014AU0F. The monitoring, storage, and processing of data are done using Azure IoT Hub, IoT Central, Blob Storage, and Power BI cloud services. The main objective is to monitor air quality through the Internet using as many cloud services as possible, facilitating data visualization and eliminating the need for hardware infrastructure for data storage, availability, and processing. Tests were conducted in an indoor environment, reading data such as temperature, humidity, CO, NH_3, and NO_2. These data can be viewed via IoT Central, stored as objects and CSV files in Blob Storage, and represented in graphs through Power BI.

Keywords: Monitoring; Indoor air quality; Internet of Things; Cloud computing; Web application.

1. Introduction

Changes in air quality due to human activities can cause various health problems, making it necessary to monitor air quality in enclosed environments. Many papers related to air quality have been developed based on the Internet of Things (IoT), as discussed in [1-3].

This paper presents an air quality monitoring system using the ESP8266 microcontroller and sensors DHT22, MICS6814, and GP2Y1014AU0F.

The collected data is sent to the cloud using Azure IoT Hub, stored in Blob Storage, and manipulated by IoT Central and Power BI services.

2. Methodology

This project uses the ESP8266 microcontroller connected to the internet by WiFi to read and send sensors data to the Azure IoT Hub cloud using the MQTT (Message Queuing Telemetry Transport) protocol.

The ESP8266 acts as an MQTT publisher [4], authenticating with the Azure cloud service using libraries provided by the cloud service itself. The microcontroller provides the necessary information, such as the service subscription, the ID of the device connected to the IoT Hub, and the connection key provided by Azure.

The IoT Hub service acts as the MQTT broker, collecting the received messages and forwarding them to the IoT Central service, which acts as the MQTT subscriber and also allows for data visualization through the internet [5].

For storage and visualization of raw data, the Blob Storage service is used, which stores the data in two containers: one with the data formatted as objects and another containing the data in CSV (Comma-Separated Values) spreadsheet format. Fig. 01 illustrates the structure and connections between the project's elements.

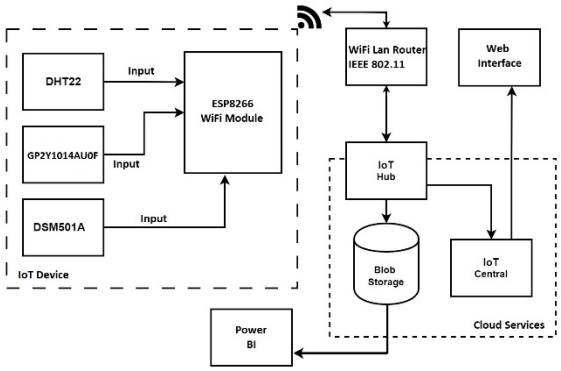

Fig. 1. Complete structure of the project with the connections between its elements.

The data stored in the Blob Storage service can be accessed by other systems within the Azure service through HTTP (Hypertext Transfer Protocol) or HTTPS (Hypertext Transfer Protocol Secure) requests, as well as externally through APIs (Application Programming Interfaces) [6].

3. Results

For this paper, the IoT device was deployed in a home office residential environment from June 12th to June 16th, 2023. The environment is ventilated by a fan and is used by only one person.

The data can be viewed almost in real-time through IoT Central using any personal device with internet access.

The data stored in a container in the Blob Storage service as a CSV file is read by the Microsoft Power BI app, allowing for the creation of charts for each data

point. Table 1 presents the organized data read from the CSV file.

In Fig. 2, the charts generated by the Power BI app related to temperature and humidity are presented.

Table 1. Data stored in a CSV file by the Blob Storage service.

		CO	NH_3	NO_2	PM 10	PM 2.5	Temperature °C	Humidity
12/06/2023	Min	1	0	3	11	2	18	40
	Máx	1	0	6	18	6	31	55
13/06/2023	Min	0	0	2	6	3	16	41
	Máx	1	0	6	14	6	26	63
14/06/2023	Min	0	0	4	9	4	13	50
	Máx	1	0	9	11	6	19	71
15/06/2023	Min	1	0	4	5	5	12	55
	Máx	1	0	8	10	5	16	73
16/06/2023	Min	1	0	6	6	2	12	50
	Máx	3	0	9	10	6	22	75

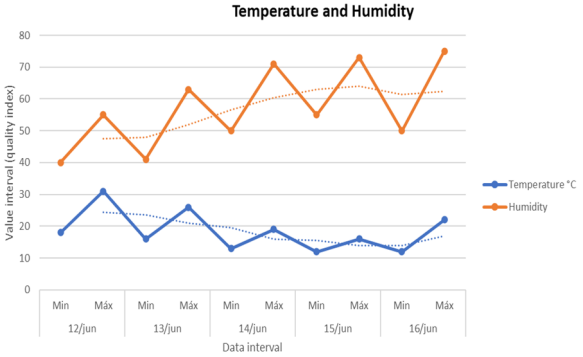

Fig. 2. Graph with collected data on temperature and humidity.

To access the data stored in the CSV file in the Blob Storage service through the Power BI tool, you simply need to provide the access key provided by the cloud service and add it as a data source within Power BI.

This key is available in the container information of the Blob through the URL (Uniform Resource Locator) access parameter, just copy the access URL and add it to Power BI in the data source options. [6].

Fig. 3 shows the charts generated by the Power BI app using the data stored in the CSV file related to gases CO, NO_2, NH_3, and suspended particulate matter levels in the air.

4. Conclusions

This paper presented an IoT system for reading telemetry data collected by sensors interconnected through the ESP8266, using Azure cloud services for storage and monitoring of indoor air quality.

The cloud services facilitated the creation of the user interface for data visualization and storage, as well as communication with the Power BI app, used for data analysis. The main challenge encountered was selecting the cloud services that met the project's requirements.

For future implementations, the IoT Edge cloud service could be added for remote triggering of air quality control devices such as air conditioners, fans, or other equipment installed in the environment.

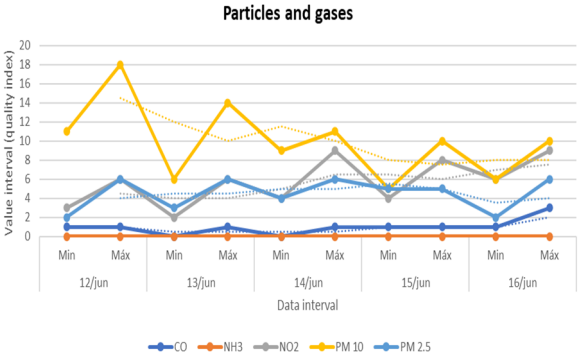

Fig. 3. Data collected on particles and gases.

Acknowledgements

This paper was partially funded by the Coordenação de Aperfeiçoamento de Pessoal de Nível Superior - Brasil (CAPES) - funding code 001. The 2nd author has a PET sholarship.

References

[1]. D. Wall, P. McCullagh, I. Cleland e R. Bond, Development of an Internet of Things solution to monitor and analyse indoor air quality, *Internet Things,* Vol. 14, June 2021, p. 100392.

[2]. R. Mumtaz et al., Internet of Things (IoT) Based Indoor Air Quality Sensing and Predictive Analytic—A COVID-19 Perspective, *Electronics*, Vol. 10, No. 2, January 2021, p. 184.

[3]. W. A. P. Ferreira, Rede neural ARTMAP Fuzzy implementada em hardware aplicada na previsão da qualidade do ar em ambiente interno, dissertação de doutorado, *UNESP - Universidade Estadual Paulista*, Ilha Solteira, 2021.

[4]. Microsoft Learn (https://learn.microsoft.com/pt-br/azure/iot/iot-mqtt-connect-to-iot-hub)002E

[5]. HiveMQ (https://www.hivemq.com/blog/mqtt-essentials-part2-publish-subscribe/).

[6]. Microsoft (https://learn.microsoft.com/pt-br/azure/storage/blobs/storage-blobs-overview).

(028)

Visible Light Communication for Indoors Automated Guidance Vehicles

P. Louro [1,2], M. Vieira [1,2,3] and M. A. Vieira [1,2]
[1] ISEL-Polytechnic Institute of Lisbon, Portugal
[2] UNINOVA-CTS and LASI; Lisbon, Portugal
[3] NOVA School of Science and Technology, Lisbon, Portugal
E-mail: paula.louro@isel.pt

Summary: The advent of devices with wireless communication capabilities has generated increased interest in indoor navigation. Several wireless technologies have been proposed for indoor location, as the traditional Global Positioning System has a poor performance in a closed space. This research proposes the use of an indoor localization system based on Visible Light Communication (VLC) to support guidance and operational tasks of Autonomous Guided Vehicles (AVG). The research is focused on the development of the guidance VLC system, transmission of control data information and decoding techniques. Trichromatic white LEDs are used as transmitters and photodiodes with selective spectral sensitivity are used as receivers. The downlink channel establishes an infrastructure-to-vehicle link (I2V) and provides position information to the vehicle. The decoding strategy is based on accurate calibration of the output signal. Characterization of the transmitters and receivers, description of the coding schemes and the use of different modulations will be discussed.

Keywords: Visible light communication, Autonomous guides vehicle, Indoor positioning, Guidance, OOK, Manchester.

1. Introduction

Automated guidance vehicles (AGV) are mobile robots powered by electricity that operate independently. The navigation of the AGV can follow a fixed route or a free ranging route. Several technologies can be used to provide guidance to the AGVs [1], ranging from magnetic, optical or radio based technologies. Visible Light Communication (VLC) is an optical wireless communication technology operating in the visible range of the spectrum, that provides several advantages, such as, license-free spectrum, high-speed, immunity to electromagnetic radiation and security, among others [2]. As it can be used in localization applications, in this paper we propose the use of an AGV guidance system based on Visible Light Communication (VLC) able to provide information on the current position of the vehicle and enable it to navigate autonomously. VLC [3].

This system uses white tetrachromatic LEDs operating as optical signal transmitter's and a:SiC:H pinpin heterostructure as receivers [4-6]. These photodetector devices exhibit active filtering, amplification, and selective sensitivity [7, 8] in the visible range. Different visible wavelength signals are encoded in the same optical transmission path, so the device multiplexes the different optical channels, performs filtering processes (amplification, switching, and wavelength conversion), and outputs a multiplexed signal [9, 10]. The modulated signal transmitted by each emitter can be recovered by decoding this signal [11, 12]. For a reliable calibration curve, each photocurrent level must be accurately regulated [13, 14]. To decode the multiplexed signal, we will use On-Off keying modulation and Manchester codes [15]. This system is intended for indoor positioning and guidance of autonomous guided vehicles (AGV) used to transfer materials from pickup places to drop off places [16] inside an automated warehouse. The system attends bidirectional communication with links Infrastructure-to-Vehicle (I2V) and Vehicle-to-Infrastructure (V2I). The link I2V provides an indoor localization information inside the warehouse enabling navigation services [17]. Operational information for operation inside the warehouse is also transmitted to the AGVs. The links V2I and V2V provide cooperation services to enhance system performance [18, 19].

The indoor localization system involves optical wireless communication, computer-based algorithms, smart sensor and optical sources network, which constitutes a transdisciplinary approach framed in cyber-physical systems.

2. VLC System Description

The VLC transmitter uses commercial RGB LEDs provide three different wavelengths, centered on the red, green, and blue bands (620 nm, 530 nm and 470 nm) with standard linewidths (ranging from 24 nm to 38 nm), high luminous intensity (in the range from 340 mcd up to 980 mcd) and wide half intensity angle (120 º). Along the indoors space, LED bulbs provide simultaneous lighting and communication, defining navigation cells (Fig. 1a).

The VLC receiver used in the VLC system is a photodiode composed of a pinpin heterostructure based on a-SiC:H/a-Si:H. It exhibits active filtering and amplification properties and a selective sensitivity, as its design was tailored to address a wavelength sensitive device in the visible spectrum (Fig. 1 b).

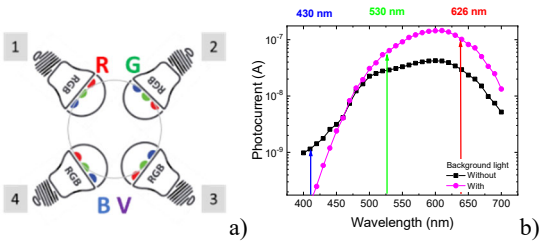

Fig. 1. a) VLC transmitters; b) spectral sensitivity of the VLC revceiver.

In this photodiode, two a-Si:H pins are mounted on top of one a-SiC:H pin, which allows the device to be used over the full visible spectrum. The device is operated under reverse bias to improve collection efficiency. Steady state optical bias using short visible wavelength (400 nm) is used to improve amplification of the longer wavelengths and attenuation of the short ones.

Specific data codes are needed to define the communication link and the type of message to be transmitted. The structure used for coding the information transmitted by the I2V channel with a word of 64 bits.

Data transmission demands the use of a specific modulation scheme. Here we will use both OOK and Manchester. A comparative evaluation between both modulations will be discussed. OOK assigns different levels of amplitude to each of the data bits we wish to modulate, with a bit time duration of bit. Manchester assigns both levels to each bit, one per bit time duration bit, but it is the transitions from on to off ("on-off") or off to on ("off-on") that distinguish between '0' and '1' data bits.

In the test scenario used in this work the AGVs can move in a linear warehouse configuration with racks on either side of the aisle for picking up materials, as displayed in Fig. 2. A matrix notation that specifies the row and column of the navigation cells is used to number the cells. The AGV at the initial position (position 1) is directed to move to an intermediate position (position 2) and then to the destination (position 3).

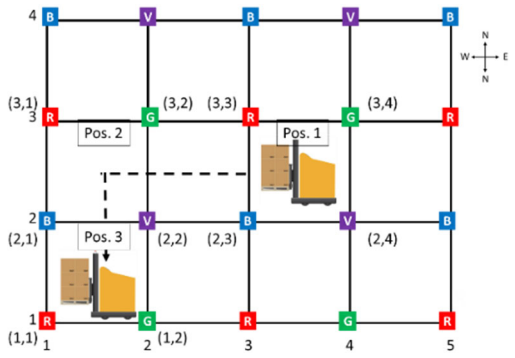

Fig. 2. Layout of the warehouse space including VLC transmitters and AGV successive positions (initial, intermediate and destination).

3. VLC System Description

Specific data codes are needed to define the communication link and the type of message to be transmitted. In every channel, it was used synchronous transmission based on a data frame of fixed length. Synchronization of the frames can be enabled using different approaches. The SoT is placed at the beginning of the frame and the EoT at the end. Then a TYPE block with 4 bits is used to define the type of message (0000 in request/acknowledge mode, 0011 in standard/update mode). The complete structure of the data frame has the format displayed in Fig. 3.

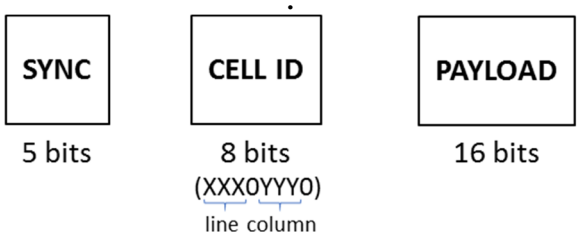

Fig. 3. Data frame structure of the VLC communication channel.

The block labelled GEO-LOCATION (16 bits) identifies the cell and footprint. The cell identification is coded as XXX0YYY0, where XXX addresses the line and YYY the column of the cell. The footprint is produced by coding the R and B emitters with four bits set to 1 and four bits set to 0, while the R' and B' emitters are coded with two bits set to 1 and two bits set to 0, and then two bits set to 1 and two bits set to 0. The 36 bits MESSAGE block addresses specific instructions transmitted to the user and dependent on the type of communication mode.

4. Modulations Comparison

In Fig. 4 it is displayed the photocurrent signal measured inside footprint #1 (region covered by the four optical signals RGBV) a position 2 using the OOK and Manchester modulations.

The output resultant signal acquired by the receiver device shows different levels of photocurrent that can be assigned to the correspondent optical excitation. As the device exhibits capacitive effects, the photocurrent level exhibits a rising or falling slope, dependent whether the transition occurs from a lower to an upper level, or vice-versa. Consequently, this effect becomes more evident when two or more adjacent bits have the same state. As OOK modulation simply uses '0's or '1's for bit states, the signal is likely to contain many adjacent symbols ('1s' or '0s') which reinforce this effect.

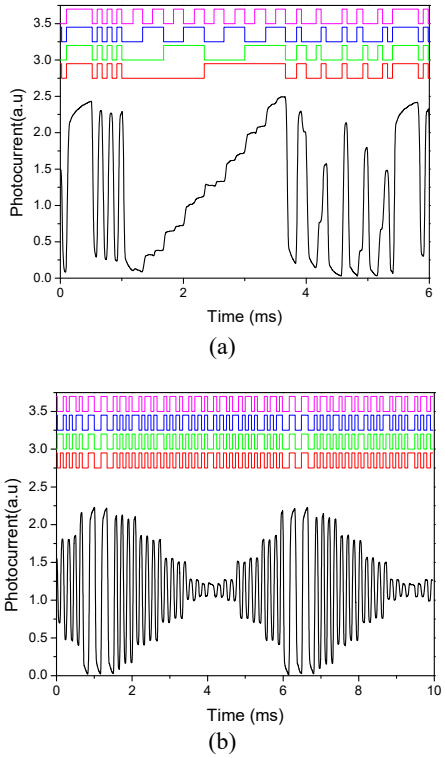

Fig. 4. Transmitted data message at the intermediate position (2) using the modulation: a) OOK; b) Manchester.

4. Conclusions

The proposed application focuses on the use of VLC based system to support the guidance of AGV. The physical layer of the communication system was fully characterized, from transmitters and receivers to the propagation channel modelling and data coding. Two modulation techniques, OOK and Manchester, were used to infer bit decoding performance. As the multiplexed signal results from multiple optical channels, its waveform is complex. It is necessary to use decoding techniques to determine the correct bits transmitted by each optical channel. Improvements to the decoding technique include parity check error control.

Acknowledgements

This research was funded by UIDB / 00066 / 2020 / UIDP / 00066 / 2020 and by IPL/2022 / POSEIDON_ISEL.

References

[1]. Durrant-Whyte, H., Rye, D., Nebot, E., Localization of Autonomous Guided Vehicles. In: Giralt, G., Hirzinger, G. (eds), Robotics Research, *Springer*, London, 1996.

[2]. Pathak, P. H.; Feng, X.; Hu, P.; Mohapatra, P. Visible Light Communication, Networking, and Sensing: A Survey, Potential and Challenges, *IEEE Communications Surveys Tutorials*, 17, 2015, pp. 2047–2077.

[3]. Paula Louro, Manuela Vieira, Manuel A. Vieira, Bidirectional visible light communication, *Opt. Eng.* 59, 12, 2020, 127109.

[4]. M. Vieira, M. Fernandes, J. Martins, P. Louro, A. Maçarico, R. Schwarz, and M. Schubert, Improved Resolution in a p-i-n Image Sensor by Changing the Structure of the Doped Layers, Amorphous and Heterogeneous Silicon Thin Films-2000, *Mat. Res. Soc. Symp. Proc.,* S. Francisco, April 24-28 USA, Vol. 609, 2000.

[5]. M. A. Vieira, M. Vieira, V. Silva, P. Louro, Optical signal processing for indoor positioning using a-SiCH technology, *Proc. SPIE 9891, Silicon Photonics and Photonic Integrated Circuits V,* 98911Z, May 13, 2016.

[6]. P. Louro, M. Vieira, M. Fernandes, J. Costa, M. A. Vieira, J. Caeiro, N. Neves, M. Barata, Optical demultiplexer based on an a-SiC:H voltage controlled device, *Phys. Status Solidi C*, 7, No. 3–4, 2010, pp. 1188– 1191.

[7]. P. Louro, V. Silva, I. Rodrigues, M. A. Vieira, M. Vieira, Transmission of Signals Using White LEDs for VLC Applications, *Materials Today: Proceedings,* 3, 3, 2016, pp. 780–787.

[8]. M. A. Vieira, M. Vieira, P. Louro, V. Silva, A. S. Garção, Photodetector with integrated optical thin film filters, *Journal of Physics: Conference Series,* 421, 2013, 01201, http://iopscience.iop.org/1742-6596/421/1/012011/.

[9]. M. Vieira, M. A. Vieira, P. Louro, MUX/DEMUX SiC receiver for visible light communications, *Microsystem Technology*, Vol. 28, 2022, pp. 1587–1592.

[10]. Louro, P., Silva, V., Vieira, M. A., Vieira, M., Viability of the use of an a-SiC:H multilayer device in a domestic VLC application, *Phys. Status Solidi C,* 11, No. 11–12, 2014, pp. 1703–1706.

[11]. P. Louro, M. Vieira, M. A. Vieira, Geolocalization and navigation by visible light communication to address automated logistics control, *Opt. Eng.,* 61, 1, 2022, 016104.

[12]. P. Louro, J. Costa, M. Vieira, M. A. Vieira, Y. Vygranenko, Use of VLC for indoors navigation with RGB LEDs and a-SiC:H photodetector, *Proc. of SPIE, Vol. 10231, Optical Sensors,* 2017, 102310F-2.

[13]. M. Vieira, M. A. Vieira, P. Louro and P. Vieira, Geolocation and Wayfinding Services Using Visible Light Communication, *Sensors & Transducer*s, Vol. 245, Issue 6, October 2020, pp. 49-56.

[14]. M. Vieira, M. Fernandes, P. Louro, A. Fantoni, Y. Vygranenko, G. Lavareda, C. Nunes de Carvalho, Image and color sensitive detector based on double p-i-n/p-i-n a-SiC:H photodiode, *Mat. Res. Soc. Symp. Proc.,* Vol. 862, 2005, A13.48.

[15]. M. A Vieira, M. Vieira, P. Louro, L. Mateus, P. Vieira, Indoor positioning system using a WDM device based on a-SiC:H technology, *Journal of Luminescence,* 191, 2017, pp. 135-138.

[16]. Faiza Gul, Syed Sahal Nazli Alhady, Wan Rahiman, A review of controller approach for autonomous guided vehicle system, *Indonesian Journal of Electrical Engineering and Computer Science*, Vol. 20, No. 1, October 2020, pp. 552-562.

[17]. M. A. Vieira, M. Vieira, P. Louro, P. Vieira, Redesign of the trajectory within a complex intersection for

visible light communication ready connected cars, *Opt. Eng.* 59, 39, 2020, 097104.

[18]. M. A. Vieira, M. Vieira, P. Vieira, P. Louro, Vehicle-to-vehicle and infrastructure-to-vehicle communication in the visible range, *Sensors & Transducers* 218, 12, 2017, pp. 40-48.

[19]. M. A. Vieira, M. Vieira, P. Vieira, P. Louro, Optical signal processing for a smart vehicle lighting system using a-SiCH technology, *Optical Sensors,* 10231, 2017, 102311L.

(029)

Wind Estimation via UAV Parameters and Artificial Intelligence related to Ultrasonic Anemometer Measurements

Michael Kurz [1], Federico Mothes [2], Markus Kreuzer [3] and Alexander Knoll [4]
[1 2 3] Munich University of Applied Sciences, Lothstr. 64, 80335 Munich, Germany
Tel.: +4915781711447
E-mail: Michael.kurz@hm.edu

Summary: With rapid advances in the unmanned aerial vehicle (UAV) field and their ever-growing popularity especially in a wide range of civilian and commercial applications, UAV operations in urban areas become inevitable. Still, low-level flight missions in urban landscape pose a significant challenge not the least because of turbulences. Therefore, it is necessary for UAVs to receive information about present or upcoming turbulences in close-up range early enough, to reduce the risk of critical situations such as crash. Currently, extensive methods are established to measure wind conditions. They range from flow sensors to ultrasonic anemometers that mark the state-of-the-art. The wind-sensors are either fixed to one location, which leads to a spatial limited measurement coverage, or when mounted on a flying device, influence the flight dynamics due to bulky appearance. In this paper, a novel approach for UAVs to estimate the 3D/2D wind vector via artificial neural networks from an ultrasonic anemometer and simulated respectively real UAV quadcopter parameter is presented. The research question to be addressed is whether the artificial intelligence approach can complement or even replace costly wind measurements sensors.

Keywords: UAV, Wind speed and orientation estimation, Ultrasonic anemometer, Artificial neural network, Urban air environment, Quadcopter.

1. Introduction

A new era of transportation is on the horizon and therefore UAV's are more and more likely to be integrated in the civil sector as transportation system. So far, there is no uniform legislation and integration concepts for the infrastructure are still under development [1]. By then, major requirements must be fulfilled regarding social factors, system factors, aircraft factors and safety-related factors [2]. Especially the safety-factor plays a major role when it comes to the acceptance by the public to be used as transportation system.

Due to the structure and the flight dynamics, UAVs are more likely to feel the presence of external disturbance than other aircrafts. Therefore, strategies and intelligent algorithms must be developed, to fulfill all safety related requirements and increase reliability.

One of those external disturbances is the wind, which greatly affects UAVs compared to other aircraft and is characterized by sudden change in speed and direction [3]. Therefore, a key challenge in the use of UAVs as transportation systems is to measure and estimate the surrounding wind in urban areas, to develop algorithms and flight-plan strategies to keep the UAV stabilized during the flight and avoid "turbulent" areas to prevent major catastrophes [4]. Estimating such wind disturbances and using this data to develop flight strategies or inform flight controls and other traffic partners can improve safety in general.

To verify this approach and to answer the question, if artificial neural networks can complement or supplant wind sensors, an additional UAV mounted with an external ultrasonic anemometer serves as benchmark system. Also, measurement data generated from the ultrasonic anemometer is used as training data for the neural network.

This paper proceeds as follow. As reminder of this disquisition, we first describe the external ultrasonic anemometer (Section II). In Section III, the preliminary information about the UAV Mathematical Model. Section IV presents the wind vector estimation method using artificial neural networks. Section V Conclusions.

2. Ultrasonic Anemometer

Wind estimation with UAVs is not a new research field to the science community and has been conducted with many different methods/approaches. Generally, those approaches can be classified in two categories:

- indirect methods, that measure the response of the UAV to external disturbance and determine the required characteristics of the wind directly from internal control sensors,
- or direct methods, that use external wind sensors deployed on the UAV.

Wind estimation with the ultrasonic anemometer belongs to the direct approach. In addition to conventional anemometers, is the ultrasonic anemometer capable to measure the wind speed in 3-dimensional direction according to the UAV's heading [5].

In this paper, an ultrasonic anemometer is deployed on a UAV as seen in Fig. 1.

Those scenarios do not replicate real life scenarios of UAVs; therefore, this paper presents a realistic 3D/2D urban area wind vector estimation technique

based on the spikes of the UAVs flight dynamic parameters caused by wind via neural networks.

Fig. 1. Quadcopter with a deployed Ultrasonic-Anemometer [5]

3. UAV Mathematical Model

Considering the quadcopter to be symmetrical consisting of a 6 DOF rigid body, the dynamics (translation and rotation) can be derived by Newton-Euler formalism. For describing the dynamics, an Earth fixed frame I and a Body fixed frame B in the center of gravity (cog) of the UAV is specified (see Fig. 2) [6]. Using the chain rule for a rotation body frame, the law of motions becomes:

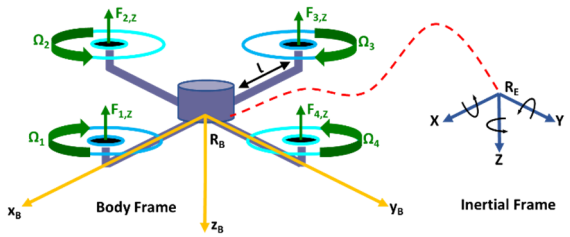

Fig. 2. Quadrocopter model.

Translation

Newton's second law $I_{3\times3}m\dot{V}^B + \omega \times mV^B = f^B$ (1)

Rotation

Euler's rotation equation $I\dot{\omega}^B + \omega^B \times I\omega^B = \tau^B$ (2)

$\boldsymbol{I_{3\times3}}$ - describes the identity matrix of the UAV, $\boldsymbol{m \in R}$ is the total mass of the UAV, $\dot{\boldsymbol{V}}^{\boldsymbol{B}} = [\boldsymbol{u}, \boldsymbol{v}, \boldsymbol{w}]$ - is the linear acceleration, $\boldsymbol{\omega^B} = [\boldsymbol{p}\ \boldsymbol{q}\ \boldsymbol{r}]$ - is the angular acceleration and $\boldsymbol{I \in R}$ - is the moment of inertia. $\boldsymbol{F^B} \in \boldsymbol{R^3}$ - are the propulsion forces and $\boldsymbol{\tau^B} \in \boldsymbol{R^3}$ - respectively the propulsion moment that act on the UAV, all with respect to the body-fixed frame B.

Equations of Motion

As a result, the complete dynamic model governing the UAVs motion and can therefore be used as input for neural networks is as follows:

$$\begin{bmatrix}\dot{u}\\ \dot{v}\\ \dot{w}\end{bmatrix} = \begin{bmatrix}rv - qw\\ pw - ru\\ qu - pv\end{bmatrix} + \begin{bmatrix}-gsin\theta\\ gcos\theta sin\phi\\ gcos\theta cos\phi\end{bmatrix} + \frac{1}{m}\begin{bmatrix}0\\ 0\\ F_T\end{bmatrix} + \frac{1}{m}\begin{bmatrix}F_{Dx}\\ F_{Dy}\\ F_{Dz}\end{bmatrix} \quad (3)$$

$$\begin{bmatrix}\dot{p}\\ \dot{q}\\ \dot{r}\end{bmatrix} = \begin{bmatrix}\frac{I_{yy}-I_{zz}}{I_{zz}}qr\\ \frac{I_{zz}-I_{xx}}{I_{yy}}pr\\ \frac{I_{xx}-I_{yy}}{I_{zz}}pq\end{bmatrix} + \begin{bmatrix}\frac{1}{I_{xx}}\tau_\phi\\ \frac{1}{I_{yy}}\tau_\theta\\ \frac{1}{I_{zz}}\tau_\psi\end{bmatrix} + \begin{bmatrix}-\frac{1}{I_{xx}}J_r\dot{\theta}\Omega_r\\ \frac{1}{I_{yy}}J_r\dot{\phi}\Omega_r\\ 0\end{bmatrix} \quad (4)$$

4. Turbulence Vector Estimation Using Neural Networks

In general, an artificial neural network is a computing system modeled in the image of the brain. It consists out of many neurons, which receive, process, and transmit signals to each other [7].

Regarding this paper, wind data generated by the ultrasonic anemometer (benchmark system) in addition to the UAVs flight dynamic and control parameter, obtained by the simulated and real UAV model, shall serve as network input for the NN-training. Target is to estimate specified wind speed and direction acting on the UAV's body in order to comply or eliminate additional wind sensory devices.

5. Technical Description

Wind speed and directions measurements in the field with ultrasonic anemometers are conducted according to typical coverage path planning for UAVs in urban environments [8].

Therefore, the UAV follows dedicated waypoints in a fixed manner, to measure wind profile characterized as turbulences. The waypoints are always located on the lee side (downwind side) of buildings with the height of at least 15 m.

Regarding the estimation process with the LSTM, the ultrasonic anemometers shall serve as benchmark but also as reference system that provides the wind data for training and estimation process of the LSTM network.

The LSTM itself will be trained on the measured wind data in at least 1 dimension at first, with a frequency of 35 Hz, but also with UAV parameters such as position drift, tilt angles and rates, rotational speed of the rotors as well as velocity and acceleration of the drone itself. Measured wind data and simulation frequency are adapted to each other. The hyper parameter such as activation function, layer, batch size or input parameter of the LSTM are constantly adjusted, to increase accuracy of estimation compared to the ultrasonic anemometer.

6. Conclusion

By means of a reproducible wind estimation with artificial intelligence related to ultrasonic anemometers but also state of the art wind estimation sensors in general, a basis for AI-wind estimations via LSTM is created. In comparison with measurement data obtained

from the ultrasonic anemometer, a reliable wind estimation especially in urban areas can be achieved. Especially in the case of urban air traffic, real time wind estimations without bulky and costly sensor devices will increase affordability of UAVs used as air taxis for provider and user, also safety factors related to control and accidents,

The main contributions of this work are:

- Increase safety related factors regarding the flight dynamics of the UAV by omit bulky sensors
- Circumvention the need of specialized tools
- Provide a cost-effective alternative for sampling wind speed and direction

The ultrasonic anemometer measurement system mounted on a UAV as well as the developed LSTM-algorithm results will be presented.

References

[1]. A. Bauranov and J. Rakas, Designing airspace for urban air mobility: A review of concepts and approaches, *Progress in Aerospace Sciences,* Vol. 125, 2021, p. 100726.

[2]. Q. Long, J. Ma, F. Jiang, and C. J. Webster, Demand analysis in urban air mobility: A literature review, *J Air Transp. Manag,* Vol. 112, 2023, p. 102436.

[3]. B. H. Wang, D. B. Wang, Z. A. Ali, B. Ting and H. Wang, An overview of various kinds of wind effects on unmanned aerial vehicle, *Measurement and Control*, Vol. 52, No. 7–8, 2019, pp. 731–739.

[4]. P. Abichandani, D. Lobo, G. Ford, D. Bucci, and M. Kam, Wind measurement and simulation techniques in multi-rotor small unmanned aerial vehicles, *IEEE Access,* Vol. 8, 2020, pp. 54910–54927.

[5]. W. Thielicke, W. Hübert, U. Müller, M. Eggert, and P. Wilhelm, Towards accurate and practical drone-based wind measurements with an ultrasonic anemometer, *Atmos Meas Tech,* Vol. 14, No. 2, 2021, pp. 1303–1318.

[6]. G. P. Falconí, J. Angelov, and F. Holzapfel, Hexacopter outdoor flight test results using adaptive control allocation subject to an unknown complete loss of one propeller, in *Proceedings of the 3rd IEEE Conference on Control and Fault-Tolerant Systems (SysTol' 2016),* 2016, pp. 373–380.

[7]. E. Akgün and M. Demir, Modeling course achievements of elementary education teacher candidates with artificial neural networks, International *Journal of Assessment Tools in Education,* Vol. 5, No. 3, 2018, pp. 491–509.

[8]. A. Majeed, S. O. Hwang, A Multi-Objective Coverage Path Planning Algorithm for UAVs to Cover Spatially Distributed Regions in Urban Environments, *Aerospace*, Vol. 8, No. 11, 2021, pp. 343-377.

.

(030)

Digital Twin-based Models of Human Activities, Localization, and Energy Consumption of WBAN Network using IMU Sensors

Noureddine Boujnah [1], Rafika Brahmi [2] and Ridha Ejbali [3]
[1] engCORE center, Carlow Institute, SETU, Ireland
[2,3] Research Team in Intelligent Machine (RTIM), University of Gabes, Tunisia
E-mail: noureddine.boujnah@setu.ie, rafikabrahmi47@gmail.com, ridha_ejbali@ieee.org

Summary: Wireless Body Area Network (WBAN) is a network of sensors collecting data from the human body such as temperature, blood pressure, heart and brain activity, and many other human physiological variables. Inertial Motion Unit (IMU) sensors collect acceleration and angular speed data to predict human motion and activities and assist WBAN energy consumption and positioning. This paper provides the theoretical framework of a WBAN network equipped with IMU sensors to be integrated into a digital twin. A digital twin is a digital replica of the human and his environment consisting of models and data and responsible for decision-making. This paper highlights the IMU data's possible usage in the digital twin framework. Due to the limited capability of the body network controller (BNC), a digital twin can monitor and assist WBAN networks.

The functionalities of the digital twin developed in this work are human activities prediction, positioning, and power consumption efficiency model in the WBAN network. Features will use available networks and sensor parameters, initial position conditions to build the theoretical model, propose a strategy for power consumption and recognize the human activity using the data-based model. The outputs of this paper are positioning and energy efficiency theoretical models and a data-based HAR model elaboration.

Keywords: Inertial motion unit, Wireless body area network, Digital twins, positioning, Signal to noise ratio, Energy efficiency.

1. Introduction

Wireless Body Access Network (WBAN) is a small-scale wireless network attached to the human body and dedicated to healthcare monitoring and wellbeing applications. It consists of tiny sensor nodes attached to the body, measuring physiological signals such as blood pressure, glucose, temperature, cerebral signal, and motion [1]. The collected data are processed and encapsulated into small packets and sent to the body network controller, the body network controller (BNC), which is placed in a central position in the body, and performs additional tasks such as data compression, aggregation, and transmission. This paper highlights the role of the IMU sensor (Inertial Motion Unit) in the WBAN network and the modeling of the digital twin.

The digital twin is an intelligent copy of the cyber-physical world with advanced capabilities such as prediction and decision-making [2].

This paper proposes three main functionalities of a healthcare digital twin using kinetic data collected by IMU sensors for human action recognition, positioning, and energy consumption reduction. We present the training and testing results of HAR classification using LSTM (Long Short-Term Memory). And provide the theoretical framework for positioning sensors and energy consumption WBAN. Fig. 1 describes our approach in this paper.

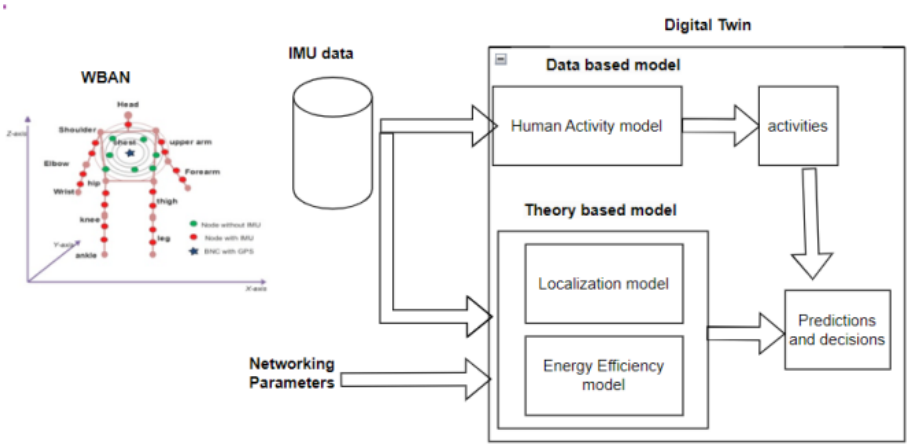

Fig. 1 The digital twin receives IMU data containing accelerations and angular speed. The digital twin comprises data-driven activity recognition models and a theory-based prediction model.

The digital twin will assist the WBAN network in modeling human activities using collected data and simulating the nodes' position and energy consumption.

The remainder of this paper will be organized as follows: we refer to some previous works in the second section, in the third section, we describe the position model using accelerometer and gyroscope data, we define the metric used to assess energy efficiency and propose a path selection algorithm for transmitted data in section four. Section five will be dedicated to modeling Human Action using realistic data collected using IMUs. Finally, section six concludes our paper.

2. Related Works

Several research works were carried out to highlight the role of collected data using sensors in wireless networks [3]. Inertial sensors (Inertial Measurement Unit) are used jointly with the camera to describe accurate 3D human motion in [4], in [5] authors model the body posture in conjunction with transmission mode using a stochastic approach to reduce energy consumption under link capacity constraint. Recent work on [6] showcases the possibilities of applying a digital twin for indoor healthcare using WBAN and associated sensors and highlights possible deployments and improvements.

Localization using wireless technologies was used to determine transmission nodes, using theory-based and data-driving techniques to improve accuracy. However, it requires convenient theoretical models and a large amount of data samples; related works on localization can be found in [7] and [8], where authors propose jointly the theoretical and machine learning approaches to find the appropriate model for macro localization.

3. Sensor Position Model

In this paper, we assume each node is equipped with an IMU sensor, and collected data can be stored temporally and transmitted opportunistically. Data collected by accelerometer sensor generates 3X1 time series vectors $\vec{a}(t)$ measured in m/s^2, the output of gyroscope is a 3X1 vector describing the angular speed of the sensor(rad/s) around three axis: Two axis (Gx) and (Gy) defining the plane parallel to the ground and one vertical axis (Gz), G is virtual point at the human body with the simplest motion. The current position, with respect to a fixed reference frame, can be approximated using the relationship between the sensor's position of node l, sensor's speed, acceleration $\overrightarrow{a_l}$ and rotational parameters retrieved from IMU:

$$\overrightarrow{X_l}(t_{n+1}) = \overrightarrow{X_l}(t_n) + h\overrightarrow{V_l}(t_n) + \frac{h^2}{2} R_\theta(\theta_l(t_n))R_\varphi(\varphi_l(t_n))R_\psi(\psi_l(t_n))\overrightarrow{a_l}(t_n) \quad (1)$$

where

t_n: discrete time,

h=t_{n+1}-t_n,

$\overrightarrow{V_l}$: Speed of sensor l approximated as:

$$\overrightarrow{V_l}(t_{n+1}) = \overrightarrow{V_l}(t_n) + hR_\theta(\theta_i(t_n))R_\varphi(\varphi_i(t_n))R_\psi(\psi_i(t_n))\overrightarrow{a_l}(t_n)$$

The 3 rotational matrices, R_θ, R_φ and R_ψ are given by:

$$R_\theta(\theta_l(t_n)) = \begin{pmatrix} \cos(\theta_l(t_n)) & \sin(\theta_l(t_n)) & 0 \\ -\sin(\theta_l(t_n)) & \cos(\theta_l(t_n)) & 0 \\ 0 & 0 & 1 \end{pmatrix}$$

$$R_\varphi(\varphi_l(t_n)) = \begin{pmatrix} 1 & 0 & 0 \\ 0 & \cos(\varphi_l(t_n)) & \sin(\varphi_l(t_n)) \\ 0 & -\sin(\varphi_l(t_n)) & \cos(\varphi_l(t_n)) \end{pmatrix}$$

$$R_\psi(\psi_l(t_n)) = \begin{pmatrix} \cos(\psi_l(t_n)) & 0 & \sin(\psi_l(t_n)) \\ 0 & 1 & 0 \\ -\sin(\psi_l(t_n)) & 0 & \cos(\psi_l(t_n)) \end{pmatrix}$$

θ_i, φ_i and ψ_i are the rotational angles (Euler's angles) around (Gz), (Gx) and (Gy), respectively, and linked to gyroscope instantaneous output as:

$$\begin{cases} \theta_i(t_n) = \theta_i(t_{n-1}) + h\dot{\theta}_i(t_n) \\ \varphi_i(t_n) = \varphi_i(t_{n-1}) + h\dot{\varphi}_i(t_n) \\ \psi_i(t_n) = \psi_i(t_{n-1}) + h\dot{\psi}_i(t_n) \end{cases} \quad (2)$$

$\dot{\theta}_l$, $\dot{\varphi}_l$ and $\dot{\psi}_l$ are the 3 angular speeds collected by the gyroscope, the gyroscope measures the angular speed. Moreover, we need to add further assumptions regarding the rotation order, because R_θ, R_φ and R_ψ does not commute with respect to the matrix product. To determine the right order selection, we need to add more conditions. The acceleration $\overrightarrow{a_l}(t_n)$ is expressed in Eq.1 using the IMU frame at time t_{n-1}, the acceleration and speed can be calculated iteratively using angular speeds and initial conditions. The mathematical model at the digital twin can be further improved and simulated taking into consideration that product $R_\theta(\theta_l)R_\varphi(\varphi_l)R_\psi(\psi_l)$ is not commutative.

We can express the instantaneous distance between the sensor and BNC as function of transmitter and receiver antenna parameters such as transmitted power, received power and antenna gains.

4. Energy Reduction

4.1 Determination of Communication Path

In this section we define the criteria used in this paper to establish a link between a node and the BNC with maximized energy efficiency, algorithm used for instantaneous path determination is distance based, and get as input the distance matrix $D(t_n) = (d_{ij})$ whos elements are given by:

$$d_{ij}(t_n) = \left\| X_i(t_n) - X_j(t_n) \right\| \quad (3)$$

The path selection is performed by minimizing and updating the following cost function:

$$g(X) = \|X - X_{BNC}(t_n)\|^2 + \|X - X_0(t_n)\|^{-2} \quad (4)$$

$g(X)$ is iteratively minimized when a selected node is far from the transmitting one and near to BNC under the following constraint: $\|X_i(t_n) - X\| < \boldsymbol{r}$, **with** X_i is the position of the i[th] selected node, $X_0(t_n)$ is the position of transmitting node and $X_{BNC}(t_n)$ is the position of BNC , r is the node's transmission range, r depends on the WBAN technologies, the propagation environment, the sensitivity at the receiver, and technical requirements for the network. If $\|X_0(t_n) - X_{BNC}(t_n)\| < r$ then no need for relays.

The following algorithm for path selection, to be implemented in the digital twin, is used for path selection:

Algorithm (communication path selection)

0- Path initialization
1- Find $X_{i_{new}} = \min_X g(X)$
Under constraint: $\|X_i(t_n) - X\| < r$
2- $i \leftarrow i_{new}$
3- path=[path, $Node_{i_{new}}$*]*
4- if $Node_{inew} \neq BNC$ *then, Find the next relay node else End*

The operation of path selection will be performed at digital twin level and decision will be communicated to BNC, positions and distances are determined using collected information from IMUs, the digital twin transmits to BNC the selected path and finally BNC inform all WBAN nodes about the decision. Discussion about communication procedures and message exchanges between DT and BNC will be planned for future works.

4.2. Energy Efficiency

Studying energy consumption in WBAN can help increase battery life, basics models for energy consumption and evaluation metrics were proposed in [9], this paper highlights all possible sources for energy dissipation in a WBAN. In this paper we correlate the WBAN energy consumption with digital twin models to propose fast actions and decisions to reduce energy usage. Each node of WBAN can be located within a dynamic range of the BNC, the star topology approach, where all nodes transmit to BNC has several drawbacks including high power usage, interferences, and packet loss. Nodes relaying will be used to reduce power usage and improve quality of service. The communication path consists of the transmitting node, relays and the BNC node. The role of the relay node is to receive and forward amplified signal to the next node in the path. In this section, we aim at maximizing the energy efficiency at the digital twin given by the formula:

$$ee = \frac{log2(1+SNR(path))}{E(path)} \quad (5)$$

where $SNR(path)$ is the total Signal-to-Noise Ratio between the transmitter and the destination node (BNC node), can be formulated using the SNR's cascade rule, and it can be formulated as:

$$SNR(path) = \frac{\alpha^N \mu^{N-1} \prod_{i=1}^{N} d_i^{-2}}{1+\sum_{l=1}^{N} (\alpha\mu)^{N-l+1} \prod_{j=l}^{N} d_j^{-2}} \frac{P_t}{W_B K T} \quad (6)$$

And, $E(path)$ is the total energy, dissipated by nodes, per communication path and given by:

$$E(path) = NE_0 + E_{BNC} + E_{TA} \quad (7)$$

with,

$$E_{TA} = \left(1 + \frac{\mu-1}{\mu} \sum_{l=1}^{N} (\alpha\mu)^l \prod_{j=l}^{l-1} d_j^{-2}\right) \frac{P_t}{\rho} \quad (8)$$

where N is the number of nodes per link(one node transmitting and N-1 relaying) ,W_B is the system bandwidth, K is the Boltzmann constant, T the temperature in Kelvin, ρ stands for the link data rate expressed in bit/s, $\alpha = \left(\frac{c}{4\pi f_c}\right)^2$, c is the speed of light in a vacuum, f_c is the operating central frequency and μ the amplification ratio of the node's power amplifier(PA), P_t is the transmitted power at the antenna, $E_b = \frac{P_t}{\rho}$ is the energy per transmitted bit. Distances between nodes are determined using position estimation. The optimization variable are P_t and μ, E_0 is the energy used for sensing and data processing per node and E_{BNC} the energy consumed at BNC and E_{TA} the total energy for signal transmission and amplification, it depends on sampling frequency and the amount of data to be processed. Power amplifier gain, frequencies and transmitted power information can be found in [10].

5. Activity Recognition

5.1 Methodology

The digital twin encompasses both theoretical models for localization, path selection and energy consumption and data driven techniques for human action recognition based on IMU data collected.

In our study, we address the problem of human activity recognition (HAR) by using deep neural network models based on long-term memory layers (LSTM). The time series data collected by IMU sensors are pre-processed and segmented into sampled shapes at regular intervals and used to train and test LSTM models. We explored different LSTM architectures, with variable number of layers, to identify the most accurate and robust model for human activity recognition. The selected LSTM architecture will be implemented on the Edge for real-time activity recognition, and then integrated into a digital twinning framework. Fig. 2 illustrates the various steps of the proposed method.

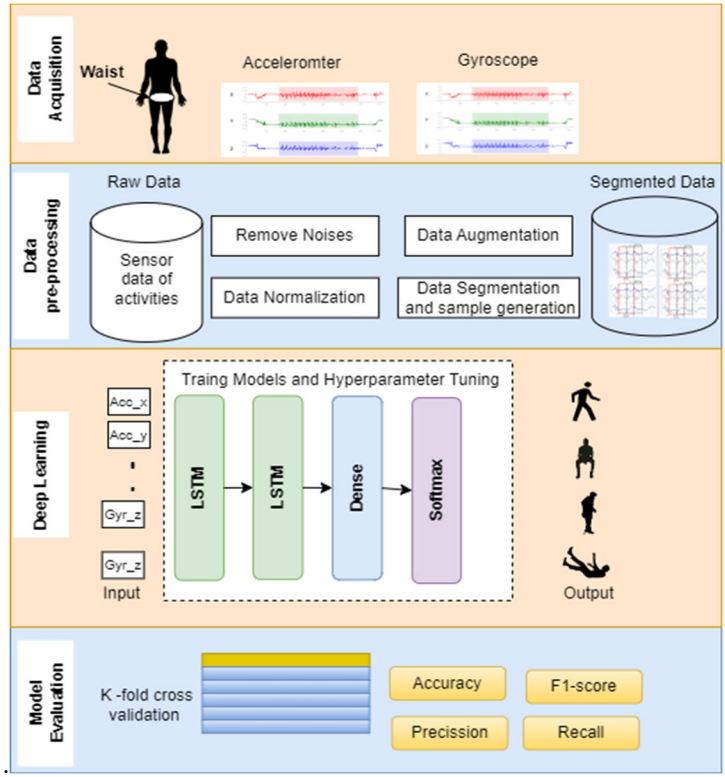

Fig. 2. The Human Activity Recognition (HAR) Sensor Framework consists of four steps: (a) Data collection using smartphones, (b) Preprocessing the raw data, (c) deep learning models for HAR (d) Evaluate each model using K-fold cross validation.

5.2. Data Collection and Preprocessing:

The dataset was collected from a group of 4 people, with heights ranging from 1.54 to 1.78 meters. The IMU data was collected using smartphones fixed to the waist of each participant. Each person performs repeatedly one of the following activities: standing, walking, sitting and falling. The minimum number of repetitions is 7 for each activity. Each activity was performed for duration of 6 seconds, and data were recorded at a sampling rate of 100 Hz. The data collection process was simplified using the Physics Toolbox Smartphone application, a flexible tool for recording sensor data. All collected data was then transferred to the PC, where it was stored as a CSV file for further pre-processing and analysis. The number of samples of each activity is presented in Fig. 3. After the collection of the IMU data, a variety of pre-processing techniques were performed to the dataset before feeding it into the deep learning models. Preprocessing includes the following steps [8]:

a- Applying 5-point moving average filters for all samples to smooth and de-noise the signal.
b- Global normalization using the maximum and minimum values of the recordings to maintain the magnitude information of each activity.
c- Increase of the number of epochs by using sliding window overlap. In this work, a sliding window size of 120 with 50% overlap was used.
d- Data segmentation: the dataset used is split into 70 % for training and 30% for model testing.

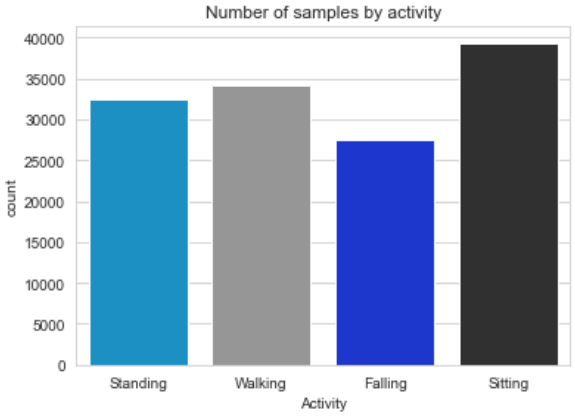

Fig. 3. Label distribution.

5.3. Deep Learning Models for HAR

In this work, we used and trained four deep learning models with LSTM architecture, as presented in Fig. 4. Each model consists of LSTM cells, a fully connected layer, and a decision layer offering 4 potential classes.

The LSTM models are trained with a learning rate of 0.0009, a batch size of 1024 and Adam optimzer. We use Python 3.9 with TensorFlow and Keras libraries to build models.

The following metrics are used to evaluate the classification performance of various LSTM architectures:

- Accuracy = $\frac{TP+TN}{TP+TN+FP+FN}$
- Precision = $\frac{TP}{TP+FP}$
- Recall = $\frac{TP}{TP+FN}$
- f1-score =2 .$\frac{precision*recall}{precision+recall}$
- The Confusion matrix (CM): CM plots the true labels horizontally and the predicted labels vertically.

TP: True Positive, TN: True Negative, FP: False Positive, FN: False Negative.

5.4. Results

The results of the experiments are discussed in this section. The LSTM networks trained on our dataset were evaluated using the cross-validation protocol [8]. Fig. 5 illustrates a graph comparing the accuracy before and after applying the cross-validation to predict human activity. Details on accuracy, precision, recall, and F1-score for various LSTM models in Table 1. and Table 2.

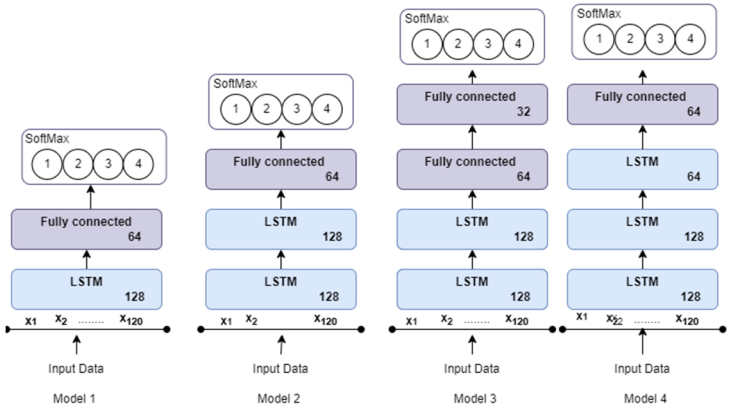

Fig. 4. Deep Learning model Structures - Model 1: LSTM-1L, Model 2: LSTM-2L, Model 3: LSTM-2L2, and Model 4: LSTM-3L.

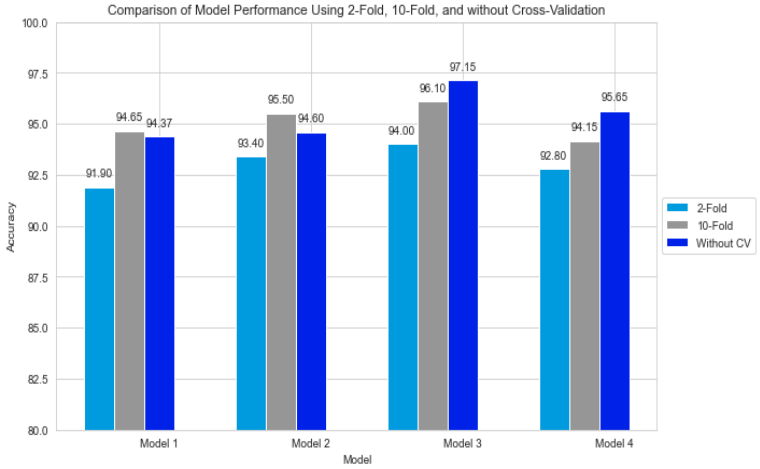

Fig. 5 Accuracy comparison for LSTM models with and without cross-validation for activity prediction.

Table 1. Performance metrics of LSTM networks used in the experiment by 2-fold cross validation protocol.

Architecture	Avg. Accuracy (%)	Avg. Precision (%)	Avg. Recall (%)	Avg. F1 score (%)
Model 1	91.90	92.12	91.87	91.85
Model 2	93.40	93.47	92.87	93.02
Model3	94.00	93.80	93.79	93.73
Model 4	92.80	92.78	92.34	92.53

Table 2. Performance metrics of LSTM networks used in the experiment by 10-fold cross validation protocol.

Architecture	Avg. Accuracy (%)	Avg. Precision (%)	Avg. Recall (%)	Avg. F1 score (%)
Model 1	94.65	94.49	94.52	94.75
Model 2	95.50	95.23	95.16	95.19
Model 3	96.10	96.08	96.04	96.03
Model 4	94.15	93.94	93.89	93.87

According to results from Table 1, Table 2 and Fig. 5 the proposed model 3 achieves an accuracy equal to 97.15 % without cross validation and Precision 94 % and 96.10 % using 2-fold and 10-fold cross validation.

CMs in Fig. 6 indicate that the model achieves an accuracy of 87.86 % for the class" falling" for 2-fold cross validation and 91.43 % for 10-fold cross validation. However, misclassification still exists, particularly for "sitting" and "falling" classes and requires more significant data.

Fig. 7 is a plot of the accuracy as function of number of epochs for LSTM model-3 for training and test. Accuracy shows a stable behavior after epoch 120 with a value higher than 90 %.

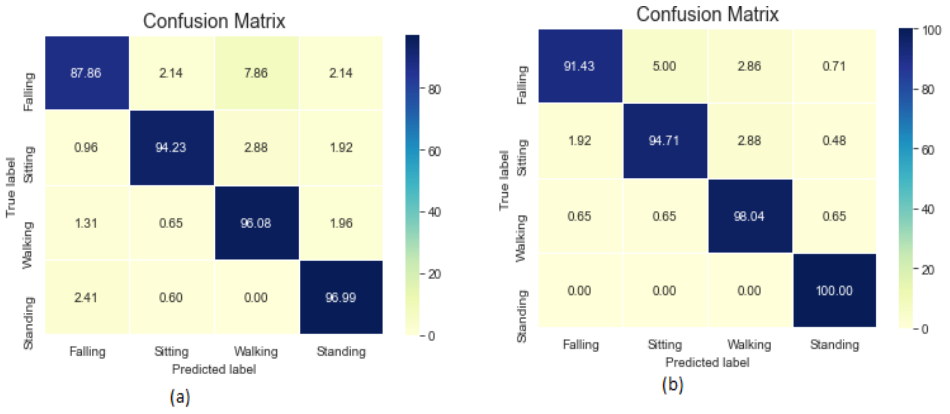

Fig. 6. Normalized Confusion Matrix of model 3 for 2-Fold Cross Validation (a) and 10–fold cross validation (b).

Fig. 7. Training and test of LSTM models 3 for 4 classes HAR and associated accuracy.

6. Conclusions

In this short paper, we propose theory based and data based models in the framework of digital twin and WBAN. First, we present the theoretical models of positioning of WBAN sensors and a technique to assess energy consumption using networking parameters and collected data from IMU sensors. Moreover, a data driven model is proposed using IMU realistic data. an LSTM models were used for Human Activity Recognition (HAR).

This work will be further improved in the future to include simulators for human action, data security and integration of next generation 6G techniques.

References

[1]. Reichman, A, Takada, J., Body Communications, in Pervasive Mobile and Ambient Wireless Communications, Roberto Verdone and Alberto Zanella (eds.), *Springer*, London, UK, 2012.

[2]. S. Mihai et al., Digital Twins: A Survey on Enabling Technologies, Challenges, Trends and Future Prospects, *IEEE Communications Surveys & Tutorials,* Vol. 24, No. 4, 2022, pp. 2255-2291.

[3]. Zhang, C., Patras, P., Haddadi, H., Deep Learning in Mobile and Wireless Networking: A Survey. *IEEE Communications Surveys Tutorials,* 21, 3, 2019, pp. 2224 – 2287.

[4]. Li, C., Yu, L., & Fei, S., Real-Time 3D Motion Tracking and Reconstruction System Using Camera and IMU Sensors, *IEEE Sensors Journal*, 19, 15, 2019, pp. 6460 - 6466.

[5]. Noureddine Boujnah, Fedia Mars Energy saving in WBAN networks under rate constraints, in *Proceedings of the 4th International Conference on Control Engineering and Information Technology (CEIT'2016),* Hammamet, Tunisia, 2016, pp. 1-4.

[6]. Cai, J., Chen, J., Hu, Y. et al., Digital twin for healthy indoor environment: A vision for the post-pandemic era, *Front. Eng. Manag.*, 10, 2023, pp. 300–318.

[7]. N. Boujnah and P. Korbel, Crowdsourcing based terminal positioning using linear and non-linear interpolation techniques, in *Proceedings of the Advances in Wireless and Optical Communications Conference (RTUWO' 2016),* Riga, Latvia, 2016, pp. 101-106.

[8]. R. Brahmi, N. Boujnah, G. Ben Abdennour and R. Ejbali, Social Distancing elaboration for indoor environment using machine learning techniques, in *Proceedings of the International Wireless Communications and Mobile Computing Conference (IWCMC' 2022),* Dubrovnik, Croatia, 2022, pp. 1022-1027.

[9]. Bilandi, N., Verma, H. K. & Dhir, R., Performance and evaluation of energy optimization techniques for wireless body area networks, *Beni-Suef Univ J Basic Appl Sci*, 9, 2020, 38.

[10]. N. G. El-Feky, D. M. Ellaithy, M. H. Fedawy, Ultra-wideband CMOS power amplifier for wireless body area network applications: a review, *International Journal of Electrical and Computer Engineering (IJECE)*, Vol.13, No. 3, June 2023 , pp. 2618-2631.

(031)

Sensing the Mechanical Properties of AlN Thin Films using Micromechanical Membranes

Aditya [1], T. Sommer [1,2], M. Althammer [3,1] and M. Poot [1,2,4]
[1] Department of Physics, TUM School of Natural Science, TU Munich, 85748 Garching, Germany
[2] Munich Center for Quantum Science and Technology (MCQST), 80799 Munich, Germany
[3]Walther-Meißner-Institut, Bayerische Akademie der Wissenschaften, 85748 Garching, Germany
[4]Institute for Advanced Study, Technical University of Munich, 85748 Garching, Germany
E-mail: menno.poot@tum.de

Summary: The current interest in quantum technologies calls for the development of novel materials and hybrid structures. Understanding the mechanical properties of a material can be a challenge, especially at the nanoscale. We use the eigenfrequencies of in-house fabricated silicon nitride membranes to extract the stress in a film that is deposited on top. The high stress results in sharp resonances that can be located precisely so that the mechanical properties of the top layer can be determined accurately. We highlight this approach using aluminum nitride – an important material for on-chip quantum optics and optomechanics - grown onto the micromechanical membranes. The detection is done optomechanically by exciting the modes using a piezo actuation and detecting the vibrations in the reflected laser light. For this, different lasers are at our disposal. The resonances of a wide variety of highly stressed membranes are measured. The frequencies follow the expected inverse length dependence of a stressed membrane and depend on the thickness of the top layer. Using finite-element simulations, the stress in the bilayer is determined. A cross-over between compressive and tensile stress is observed as a function of the AlN thickness.

Keywords: Optomechanics, Film stress, Aluminum nitride (AlN), MEMS, Silicon nitride (SiN), Bilayer membrane.

1. Introduction

Micromechanical membranes provide an important platform for a wide variety of optomechanical experiments. This can range from scanning force microscopy [1], to study cavity optomechanical backaction [2], the observation of hybridization of degenerate eigenmodes [3], topological energy transfer [4], all the way to radiative heat transfer mediated via Casimir fluctuations [5]. Another important aspect of these very thin membranes is that they can be used to sense materials that are placed on top [6]. This provides an interesting route to measuring the mechanical properties of a variety of materials that can be deposited or grown on top of existing high-stress silicon nitride (SiN) membranes.

We make membranes with and without the second layer on top and measure their eigenmodes. The dimensions of our membranes can be varied by design and typical sizes are 10 s to 100 s of um in width and length. The thickness is determined by the SiN film thickness and is typically 100s of nm [3]. We illustrate that we can determine the stress in an aluminum nitride (AlN) layer grown on top of a suspended SiN membrane. AlN is an important material for the emerging field of quantum technologies, especially when photonic integrated circuits with nonlinear optics or optomechanics are involved [7-9].

2. Samples and Setup

The membranes are made on chips that consist of a 330 nm thick SiN layer on top of a 3.3 um thick silicon oxide (SiOx) layer. Underneath these two layers is the silicon carrier. The stoichiometric SiN is grown commercially using LPCVD and has a tensile stress of about 1100 MPa. Release holes are defined using electron-beam or optical lithography followed by reactive ion etching. The number of holes and their distance set the size of the membrane. A layout of a typical chip can be seen in Fig. 1. Holes in the SiN layer expose the underlying oxide and by immersing the chip into buffered hydrofluoric acid (BHF), the exposed SiOx is etched isotropically, resulting in circularly expanding drums originating at the etch holes. The etching is continued until these “drums” are no longer supported by “pillars”, thus forming a suspended SiN membrane. The finite selectivity of BHF between SiN and SiOx results in slightly taped profiles of the SiN. This is also visible in optical reflection maps.

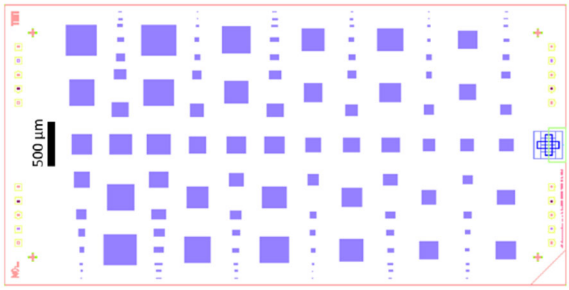

Fig. 1. Layout for a 6 × 10 mm chip with 120 membranes of different sizes indicated in blue.

Next, AlN is grown on top using DC magnetron sputtering as detailed in Ref. [10]. Using X-ray diffraction, it is confirmed that the film is of good crystalline quality and has a c-axis orientation. It is known from literature that the growth process and the final thickness influence the stress in the AlN [11]. It is thus important to have a quick and reliable method to determine the stress in the deposited film and in the resulting bi-layer membrane.

The chips are glued onto a piezo element for actuation and mounted in a vacuum chamber as shown in Fig. 2.

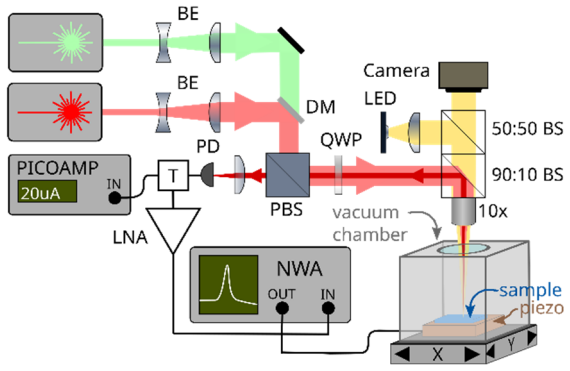

Fig. 2. Schematic of the measurement setup. Two different lasers can be used for measuring the driven response of the bilayer membranes that are mounted on a piezo actuator and placed in the vacuum chamber. For clarity, the green laser light path is not shown in full. Adapted from Ref. [3].

In short, a red HeNe laser (633 nm, Mellers Griot) is focused onto one of the membranes – or any other mechanical resonator - and the reflected light is collected on a high-speed photodetector (Newport 818-BB-21). Since the reflection depends on the distance between the membrane and the highly reflecting Si, this provides a sensitive way to measure the local displacement of the membrane and can also be used to map the eigenmodes [3]. The driven response is measured using a network analyzer (HP 4396A). Typically, first overview scans are done and then zooms of the resonances are taken at higher resolution. From the resonance peaks, the eigenfrequencies and quality factors are obtained by fitting a harmonic oscillator (or Duffing) response to the data. This procedure is repeated semi-automatically for the different membranes on each chip. Then the next chip with a different AlN thickness is inserted and measured again, resulting in large datasets that are processed using Matlab scripts. Using these, the responses can be viewed, fitted, and the fit results can be studied as function of the membrane parameters. Fig. 3 shows a selection of four membranes with identical size on the four different chips. The peaks correspond to the fundamental (i.e., the (1,1) mode [3]) out of plane eigenmodes. A clear dependence on the AlN thickness can be seen: the thicker the AlN, the lower the resonance frequency. Here it is noted that in the overviews, the driving power is relatively high and that the peaks appear somewhat distorted, but care is taken to have zooms with enough resolution and lower excitation so that the frequencies can be determined precisely.

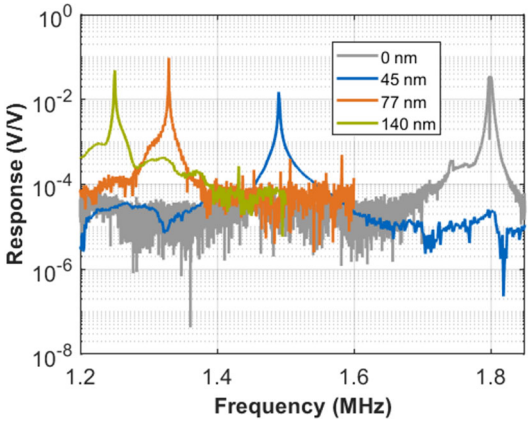

Fig. 3. Driven response near the fundamental eigenfrequency for the nominally-same membrane on different chips with different AlN thicknesses. The AlN layer clearly shifts the resonances to lower frequencies.

The readout always works well for SiN-only membranes, but for bilayer membranes with different AlN thicknesses it is - unlikely but still - possible that the derivative of the reflectivity w.r.t. the displacement vanishes. Hence, alternatively a green (532 nm; OneFive Katana) and even a violet laser (405 nm, not shown) can be used to sense the motion. Fig. 4 compares reflectivity maps for two laser wavelengths and chips with different AlN thicknesses. The differences in contrast between the membrane and support are clearly visible. The different lasers (see Fig. 2) allow selection of the best color for the optomechanical readout.

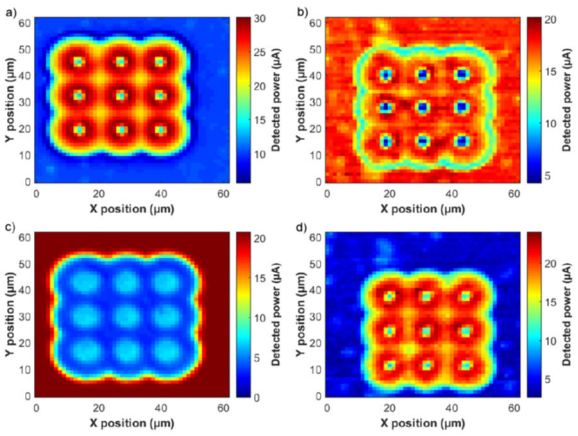

Fig. 4 Reflectivity maps for a 3x3 membrane. The top (bottom) row is taken at 633 (532) nm. The left (right) column has 77 (140) nm of AlN grown onto the suspended silicon nitride membrane.

3. Resonance Frequencies

The driven response is measured for all 480 membranes (120 membranes with varying size per chip as shown in Fig. 1, 4 chips with different thicknesses t_{AlN}). The fundamental eigenfrequencies of the same membrane on four different chips were plotted in Fig. 3; from zooms the exact resonance frequency is determined and this is plotted against the size of the membrane in Fig. 5. The strongly varying frequency with membrane size L_{eff} makes it beneficial to convert the frequency to the speed of sound, which – for an idealized membrane - equals the square root of the thickness-weighted sum of the stress and mass density of the bilayer. With the known properties of the SiN layer, the stress in the AlN film can be extracted. In practice, the membrane shape is affected by the hydrofluoric acid release, resulting in a slightly more complex geometry. For the required precision, bandstructure calculations using finite element simulations are used to connect the speed of sound to the material properties, in particular the thickness dependence of the stress in the AlN thin film.

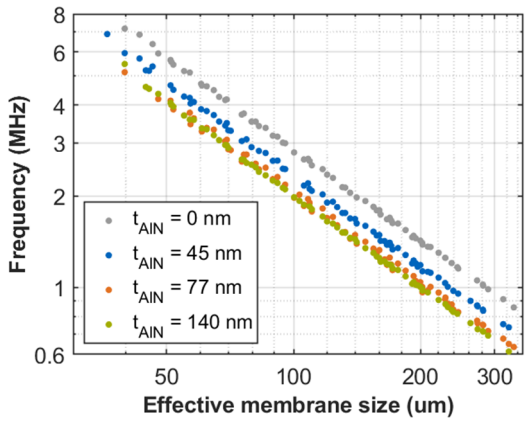

Fig. 5. Fundamental resonance frequency for membranes of different size with different amounts of AlN on top. The slope of -1 in this log-log plot indicates that $f \propto 1/L_{eff}$ i.e. that the membranes are stress dominated.

4. Thickness Dependence of the AlN Film Stress

The data in Fig. 3 and 5 shows a clear dependence on the AlN thickness. This is on one hand due to the additional mass, and on the other hand due to a difference between the stress in SiN and AlN. The latter is extracted using finite-element simulations. Interestingly, Fig. 6 shows that the stress transitions from compressive to tensile. We believe that this is due to the complex growth of AlN on SiN [7] and a finer sweep of the film thickness will be done to study this in more detail.

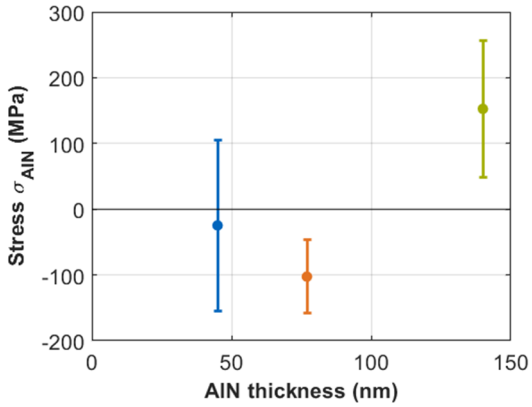

Fig. 6. Extracted stress in the AlN film σ_{AlN} vs the thickness t_{AlN}.

5. Conclusions and Outlook

As proof of principle, we have used our SiN micromechanical membranes to determine the stress in AlN thin films that were grown on top. Although here we focused on AlN, our method is not limited to this material, as in principle any (semi-) transparent material may be sensed. With slight changes to the optical setup (specifically: heterodyne detection), even that requirement may be lifted in the future. The method is thus applicable to any transparent or reflecting thin film that can be grown onto our suspended SiN membranes.

Acknowledgements

We thank P. Soubelet for discussion, J. Röwe for initial measurements, D. Hoch and J. Röwe for assistance with nanofabrication, and M. Müller for growth of the AlN. Funding: DFG EXC-2111-390814868 and TUM-IAS (DFG & EU FP7 291763).

References

[1]. D. Hälg, T. Gisler, Y. Tsaturyan, L. Catalini, U. Grob, M.-D. Krass, M. Héritier, H. Mattiat, A.-K. Thamm, R. Schirhagl, E. C. Langman, A. Schliesser, C. L. Degen, and A. Eichler, Membrane-based scanning force microscopy, *Physical Review Applied,* Vol. 15, 2021, L021001.

[2]. J. D. Thompson, B. M. Zwickl, A. M. Jayich, F. Marquardt, S. M. Girvin and J. G. E. Harris, Strong dispersive coupling of a high-finesse cavity to a micromechanical membrane, *Nature,* Vol. 452, 2008, pp. 72-75.

[3]. D. Hoch, K.-J. Haas, L. Moller, T. Sommer, P. Soubelet, J. J. Finley and M. Poot, Efficient Optomechanical Mode-Shape Mapping of Micromechanical Devices, *Micromachines,* Vol 12, 2021, 880.

[4]. H. Xu, D. Mason, L. Jiang, and J. G. E. Harris, Topological energy transfer in an optomechanical

system with exceptional points, *Nature,* Vol. 537, 2016, pp. 80–83.

[5]. K. Y. Fong, H.-K. Li, R. Zhao, S. Yang, Y. Wang, and X. Zhang, Phonon heat transfer across a vacuum through quantum fluctuations, *Nature,* Vol. 576, 2019, pp. 243–247.

[6]. P.-L. Yu, T. P. Purdy, and C. A. Regal, Control of material damping in high-Q membrane microresonators, *Physical Review Letters,* 108, 2012, 083603.

[7]. G. Terrasanta, T. Sommer, M. Müller, M. Althammer, R. Gross, and M. Poot, Aluminum nitride integration on silicon nitride photonic circuits: a hybrid approach towards on-chip nonlinear optics, *Optics Express,* Vol. 30, 2022, pp. 8537–8549.

[8]. X. Liu, A. W. Bruch, and H. X. Tang, Aluminum nitride photonic integrated circuits: from piezo-optomechanics to nonlinear optics, *Advances in Optics and Photonics,* Vol. 15, 2023, pp. 236–317.

[9]. L. Fan, C.-L. Zou, M. Poot, R. Cheng, X. Guo, X. Han, and H. X. Tang, Integrated optomechanical single-photon frequency shifter, *Nature Photonics,* 10, 2016, pp. 766–770.

[10]. G. Terrasanta, M. Müller, T. Sommer, S. Geprägs, R. Gross, M. Althammer, and M. Poot, Growth of Aluminum Nitride on a Silicon Nitride Substrate for Hybrid Photonic Circuits, *Materials for Quantum Technology*, Vol. 1, 2021, 021002.

[11]. L. Xie, H. Zhang, X. Xie, E. Wang, X. Lin, Y. Song, G. Liu, and G. Chen, Structure and optical properties of AlN crystals grown by metal nitride vapor phase epitaxy with different V/III ratios, *ACS Omega,* Vol. 7, 2022, pp. 23497–23502.

(032)

Video Stream Processing for an Autonomous Tunnel Drainage Rover

A. L. Giordano [1], T. Schachinger [2], V. Micic Batka [2] and B. G. Zagar [1,3]
[1] Montanuniversität Leoben, Chair of Electrical Engineering, 8700 Leoben, Austria
[2] ÖBB Infrastruktur, 1020 Vienna, Austria
[3] Johannes Kepler University Linz, 4040 Linz, Austria
E-mail: alessandro-leone.giordano@stud.unileoben.ac.at

Summary: Drainage pipes in tunnels are very complicated to service but still need rather frequent inspections in order to detect the initiation of deposited scales stemming from carbonate that tends to precipitate when the pH-value of the mountain water rises with the release of gaseous carbon dioxide CO_2 due to a decreasing water pressure. Drainages allow to design tunnels without resistance to ground water pressure. We present a camera-based optical sensor, developed for an autonomous operating tunnel drainage rover, that is able to detect and quantify deposited calcite constricting more or less severely the free cross section the drainage rover needs to safely navigate the pipe. The pipe's cross section is imaged via an area-scan camera at a frame rate adopted to the rover's speed so that at least every 50 mm of movement a frame is acquired. The presented image processing software is segmenting and classifying each frame into the pipe's wall, the pipe's free lumen, eventually existing water, and calcite.

Keywords: Tunnel drainage inspection, Autonomous tunnel rover, Optical sensor, Digital image processing, Calcite deposit detection.

1. Introduction

In Austria – like in other middle European countries – railway and motorway tunnels are a very important part of the national infrastructure. Depending on many boundary conditions, there are various design possibilities for these tunnels. One of the most important factors for the design of the tunnel structure is its position in relation to the groundwater level. If the tunnel is below the water table, in many cases the water pressure has to be relieved by drainages. Particularly in mountainous areas with overburdens of more than several hundred meters, this is the only way the tunnel structures can be technically build. Within the tunnel structure, there are drainages. These drainages usually have a diameter of 160 to 250 mm. They are made of thermoplastics. Polypropylene is used in current construction projects because of its good mechanical properties.

In a great number of the tunnels, precipitations consisting of calcium carbonate occur inside the drainages [1]. This is either due to the calcium content of the ground water or especially due to the dissolution of portlandite of the cement bearing support elements used in tunneling works. These precipitations are called “scales”. They can grow slowly (several centimeters thickness over years) or very quickly (several centimeters thickness during several weeks) and have different mechanical properties. If the drainages are clogged due to these scales, the water pressure in the surrounding of the tunnel structure increases. As a result, either the tunnel structure may suffer damage or water seeps into the tunnel. Both cases lead to a reduced availability of the tunnel for railway operation.

Currently, the total length of Austrian Railways’ (ÖBB) tunnels is about 254 km, with about 445 km of drainages. With the completion of major projects Brenner Base Tunnel, Koralm Tunnel, Semmering Base Tunnel und Granitztal Tunnel, a total of about 1,081 km of drainages will have to be maintained in ÖBB tunnels [2]. In this paper we report on the development of an inspection rover which can operate without influence on the railway traffic and automatically navigate through the rather constricted drainage pipes, thereby recording the calcite scales, the water table and measure environmental conditions, like temperature, the pH-value, and the conductivity of the runoff water within the pipe, all as functions of the position along the pipe. Fig. 1, top shows the CAD model of the tunnel rover, where the frontal green structure is the video camera to record a continuous video stream. Fig. 1, bottom shows a photo of the realized fully functional rover’s prototype still produced by 3D printing.

2. Autonomous Navigation Software

Since servicing areas within the drainage are spaced between 333 m and up to 500 m at most, the rover needs to be given the capability to autonomously advance through the drainage system and thereby avoiding any obstacles, like thicker than navigable calcite scales, etc.

It was decided to use a computer vision approach to provide it these capabilities, although tactile sensors operating like rodent whiskers, or ultrasonic Time-of-Flight sensors like employed by bats were initially also considered as options. The latter were dropped in favor of the image processing scheme since drainage run-off renders them unsuitable most of the time.

The developed image processing software needs to look ahead some limited distance, identify any obstacles there might be (most of the time it simply

will be calcite deposits), determine the free cross section of the pipe and indicate to the rover's drive to either advance normally, stop to allow for finer resolution image processing aimed at ultimately deciding whether the rover will be able to pass the obstacle, or, to conclude returning back is the only viable option. Although software meeting these requirements are known to exist for autonomous vehicles already [3], transferring these algorithms into the less general environment of a drainage pipe and running them on the very limited processing power available at the rover's processing unit is not a straightforward endeavor.

Besides, the software needs to annotate any acquired cross section with flags indicating the severeness of the constriction, its position along the track, and all analogue measurements, like temperature, pH value, conductivity, etc.

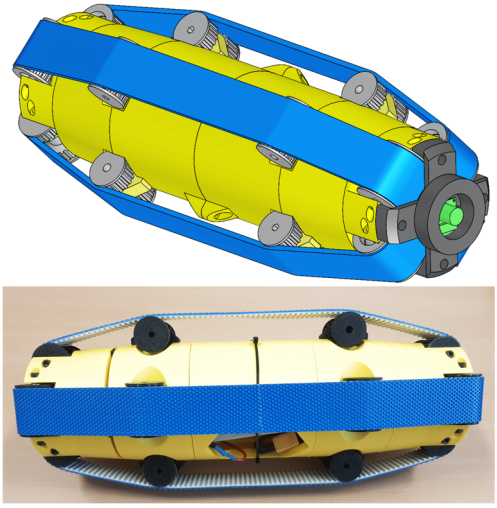

Fig. 1. Top, CAD view of the rover, with the forward-looking camera indicated in green. Bottom, the realised 3D printed prototype.

3. Processing of the Video Stream

The drainage rover has a size of approximately 500 mm length and an overall diameter of 180 mm. It is equipped, besides other measurement hardware, with a miniaturised forward-looking RGB video-camera (see Fig. 1, top in green) with a resolution of 720 by 576 pixels. The optics has a focal length, which given the camera's physical size offers a strong wide angle imaging capability but gives rather strongly distorted images (barrel distortion), that needs to be equalised for correct geometrical measurements [4]. The rover is designed to autonomously inspect a few kilometres of pipe between automatically recharging its batteries. During inspection the task of the rover's image processing is to identify and record calcite deposits, their mass and, ideally, cross-sectional distribution. Due to the rather limited processing power of the rover's power saving image and signal processing hardware designing an efficient and effective code is crucial.

Video frames are acquired at the standard rate of 25 frames per second. The rover is advancing at around 1 m/s, thus each frame covers approximately 4 cm. The scene illumination is achieved by a white light LED offset from the camera's axis by 2 cm and illuminating under a beam angle of 160 ° with a half value angle of 120 °. The LED's intensity is set such as to bring the exposure time down to approximately 5 ms thus keeping image blur in check. To ensure a sufficiently dense video inspection, each frame of the recording taken by the rover's frontal camera is read in and processed further.

Since calcite deposits can distinctively/visually be separated from the drainage pipe, as they appear in different colour schemes (Fig. 2, left), a colour segmentation approach is examined. By creating colour-based masks the frame is segmented into a binary image depicting preferably only calcite while the drainage pipe itself is blackened out. Converting the incoming frame's colours to their complementary form as seen in Fig. 2 on the right simplifies adjusting the image's RGB settings to achieve an enhanced contrast. As the segmentation is colour-based and the changes in contrast are detected by the gradient operators, increasing the contrast is a vital step for a more accurate segmentation [5].

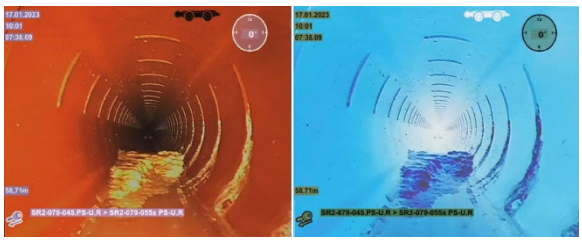

Fig. 2. Left, original input frame. Right, frame with complementary colour and enhanced contrast.

The original input image as well as the one with an enhanced contrast are both in RGB colour space. Even though a segmentation based on this very colour space is possible, due to the irregular lighting conditions inside the pipe, converting the image to the L*a*b* colour space [6] resulted in a much better segmentation. Implementing thresholds for the three L*a*b* parameters, that were optimised using 3 video sequences, and further using them to create and apply the mask m_1 (Eqn. 1), outputs a binary black and white image.

$$m_1(i,j) = \begin{cases} 1, & 0.000 \le L \le 62.645 \\ 1, & -8.652 \le a \le 34.864 \quad i = 0,1,\cdots,760 \\ 1, & -63.300 \le b \le 2.616 \quad j = 0,1,\cdots,576 \\ 0, & \text{Otherwise} \end{cases} \tag{1}$$

Given areas that do not correspond with the adjusted thresholds will therefore not be shown and are blackened out whereas the pixels that are in the adjusted thresholds' range, preferably only calcite, remain visible and are whitened out (Fig. 3, right).

Due to wide angle imaging, there is a higher than usual dynamic range in exposure the processing has to take care of. In particular, problems arise for over-exposed parts of the image, especially areas close to the rover and slots wherefrom the drainage water enters, where colour that is defined by the ratio of the a* and b* parameters, tend towards appearing washed-out white and are hence not masked out as seen in Fig. 3 on the right.

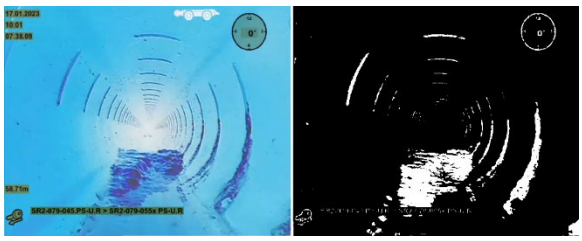

Fig. 3. Left, complementary image. Right, m_1 to mask out background.

To improve the image segmentation following the error-prone first mask m_1, a second mask m_2 is implemented and applied to restrict the region of interest (ROI). This is achieved by autonomously cutting off and hence blackening out extensive bordering regions (Eqn. 2) to only keep the rectangular centre of the image as seen in Fig. 4 on the right to be considered further.

$$m_2(i,j) = \begin{cases} 0, & 0 \le i \le 170 \\ 0, & 808 \le i \le 888 \\ 0, & 0 \le j \le 200 \\ 0, & 902 \le j \le 1102 \end{cases} \tag{2}$$

There are indeed other methods to define an ROI adjusted for each frame, for instance by implementing a circular Hough transform to detect circular structures [7, 8]. Yet, due to its numerical complexity of $O(N^3)$ of the circular Hough Transformation [9] it's use is prohibitive for the hardware given and is therefore not adapted to operate during the online inspection of the drainage pipe as it does not allow to recognise calcite deposits in real-time.

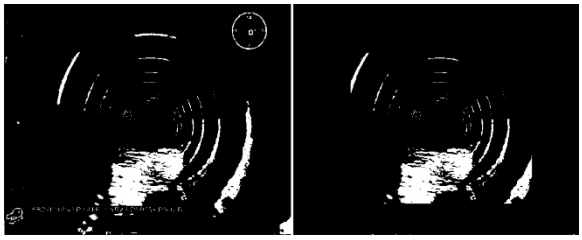

Fig. 4. Left, m_1. Right, m_2 to define the ROI.

Due to the irregular lighting conditions and other environmental parameters, for instance drainage water inside the pipe reflecting strongly, certain areas are masked out even though they, indeed, are calcite structures. Since the aim is to also quantify the calcite deposit's mass, we are also interested to identify and measure the convex hull [10] of the calcite layer. Holes within a mask are unphysical and thus filled using the morphological filling operation [11], 12] to showcase the entirety of the detected calcite scale as seen in Fig. 5 on the right. To increase both the specificity and the sensitivity of the detector as to also avoid mistakenly whitened drainage slots, a morphological hit-or-miss operator [13] matched to the shape of these slots is implemented, which, if found in the binary image, removes structures corresponding to these very shapes. Even though this method is efficient to successfully mask out the drainage slots, it mistakenly masks out actual calcite regions as well wherefore the proper sizing of the implemented shape is crucial.

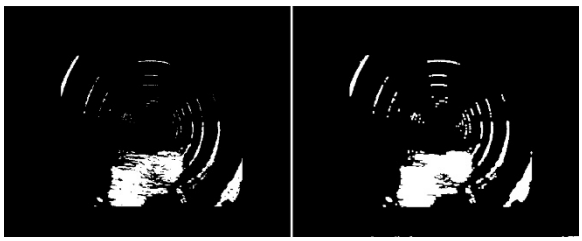

Fig. 5. Left, m_2. Right, image with filled holes by the morphological filling operation.

Subsequently to aid the rover's navigation, the sizes of calcite obstacles need to be classified as impassable or traversable. This is done by constricting the cross section by the bounding box' outlines and checking for sufficient clearance. A singular bounding box is a numeric array with 4 entries [x, y, width, height], x and y define the upper left corner [14].

To process more than just one bounding box within each frame (see Fig. 6), every potential bounding box surrounding whitened sections in the current frame is added to a data structure. To now classify the calcite scales by size, the height and width parameters of each bounding box are taken from the data structure and multiplied to receive the bounding box' area a_i which is then added to a one-dimensional array A (Eqn. 3). If a_i exceeds a defined minimum size (here set to 1000 pixels), the rectangle will be depicted in the final image, if not, this box' entry will be removed from A. In Eqn. 3 the elements of A; a_1, a_2, … are the determined areas of bounding boxes, n is the total number of detected bounding boxes before extracting the ones that are smaller than the defined minimum size.

$$A = \begin{pmatrix} a_1 \\ a_2 \\ \cdots \\ a_n \end{pmatrix} \tag{3}$$

$$a_i = \{\ 0, \quad a_i \le 1000 \quad i = 1, 2, \cdots, n$$

Now, only calcite structures that exceed the size limit defined by the rectangle's minimum area (here 1000 pixels or more) are shown being surrounded by a bounding box as depicted in Fig. 7 on the left.

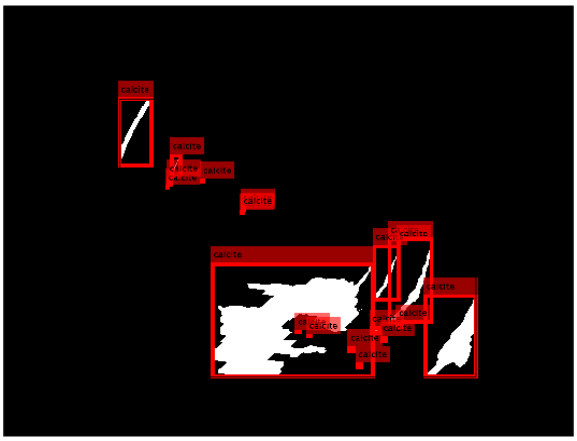

Fig. 6. Image including all bounding boxes still without classification.

Further information like current location or estimated size can be added to the bounding box' description. If the calcite scale ahead of the rover evokes a risk of getting stuck, the video processor can send a halt signal to the rover's drive via Controller-Area-Network-Bus (CAN-Bus) which will cause a hold and possibly a reversal to the previous docking station to reconsider action. After further inspection the decision of proceeding as usual and driving onwards or initiating backtracking can be made.

On the left in Fig. 7, the final result, the binary image including the bounding box surrounding a white pixel field is depicted. Since it is not possible to differentiate the white pixels by their distance to the rover as the used video-camera only supports 2D imaging, the binary image is not a reliable source to define the calcite deposit's volume and can therefore only be used to estimate coarsely the volume. This issue might be improved by using a Time-of-Flight camera which essentially can depict a 3D image and is consequently helpful to determine the calcite volumes, too [15]. To make the output image more identifiable, the binary image is invisibly layered underneath the original input frame, while the bounding boxes are still visible. Hence, as seen in Fig. 7 on the right, the written output frame now essentially shows the incoming image including an appropriate bounding box correctly indicating a calcite scale.

As depicted in Fig. 7 on the left, during the rover's inspection tour inside the drainage pipe, calcite deposits ahead the rover can occur. In case the deposits reach a size that might risk the rover's safe continuation of its inspection, a backtracking firmware is integrated. The aim of the backtracking module is to firstly secure the rover from possible obstacles and to secondly offer a more sufficient analysis of the calcite deposit ahead to then indicate whether or not backtracking is the only viable option. To decide whether a deposit is potentially unsafe to cross or not, the area of the bounding box surrounding the frontal calcite deposit is defined, as they provide a sufficient estimate of the calcite deposit's size. Once a bounding box's area exceeds the chosen size of risk (here 6000 pixels), a signal can be sent via CAN-Bus to the rover which then executes a code to stop. To analyse the given calcite deposit more precisely, the rover then backtracks for a defined distance (some cm) and a height detecting module operating on m_2 seen in Fig. 4 is started. Firstly, all occurring white pixels are counted to determine the calcite's cross-sectional area to additionally estimate the calcite deposit's volume.

Fig. 7. Right, binary image including bounding box. Left, output image indicating calcite deposit with bounding box.

To further define the space between the drainage pipe's ceiling and the calcite deposit to essentially determine if the rover can pass safely, the drainage slots which are falsely indicated to be calcite and are therefore depicted in the binary image are utilised. Since the binary image only consists of two values, 0 for black and 1 for white, the image's matrix is filtered row by row to find the first and therefore highest in elevation occurring white pixel in the frame. This very pixel is part of a drainage slot and is hence associated with the pipe's ceiling. Once found, this very column is filtered to discover an accumulation of white pixels which indicates a calcite deposit. Subtracting the column's value of the highest pixel by the one of the lowest essentially results in the passing height. This module executes a more precise analysation of the calcite deposit and can therefore better determine whether backtracking is viable or continuing onwards is safe without getting stuck. As the matrix analysation to determine the passing height is time costly and exceeds the given processing power, this module is not a reliable source to determine calcite structures in time during the rover's driving.

4. Conclusions and Outlook

High calcium concentrations in drainage water can cause drainage pipes used for tunnelling systems to accumulate calcite deposits which, if not handled in time, increase in size. Once a calcite deposit reaches a certain size, the drainage system is at risk of clogging and hence can negatively affect tunnelling operations. A rover is implemented to autonomously navigate through the drainage pipes while recording calcite deposits as well as other environmental parameters of interest. To successfully recognise calcite deposits along the drainage pipe, an online image processing system

is implemented on the incoming video stream from the camera positioned on the rover's front. We can demonstrate successful autonomous operation of the rover based on a rather simple and thus power saving image processing protocol, that aims at detecting obstacles ahead of the rover's current position. Since these obstacles are scale deposits a colour processing scheme proved sufficient as is shown with some major intermediate steps in Fig. 8.

Future work will be directed towards using Time-of-Flight camera's capabilities to more precisely measure not only the free cross section of the pipe but also the total volume of scales ahead of the rover's position.

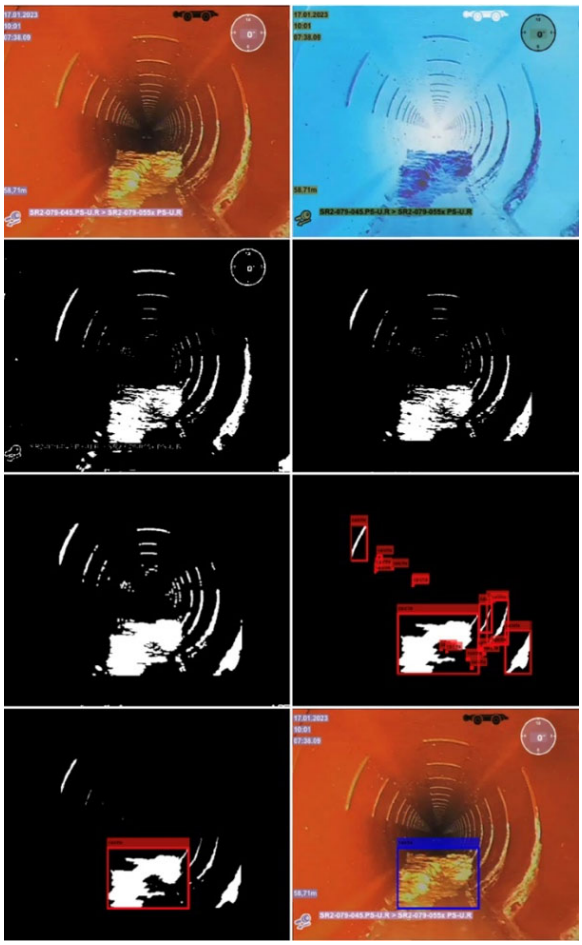

Fig. 8. From top left to bottom right, single frame of the continuous video stream, inverted to complementary colours, created L*a*b*-segmented binary image, define ROI, delineate image and fill holes, implement bounding boxes and classify bounding boxes by size.

Acknowledgements

The authors gratefully acknowledge the partial financial support for the work presented within the framework of the EU Horizon 2020 Programme under grant GA 101012456, Programme In2Track3 / Shift2-Rail - CFM.IP3-01-2020 Innovation Action, and ÖBB - Infrastruktur, Vienna.

References

[1]. Stefanie Eichinger, Assessment and formation mechanisms of scale deposits in tunnels of the ÖBB-Infrastruktur AG – A subproject of the Task Force Drainage, *Geomechanics and Tunneling*, 13.3, 2020, pp. 273–285.

[2]. Tobias Schachinger et al., Current research by ÖBB Infrastruktur AG on scale monitoring without track closures, *Geomechanics and Tunnelling,* 11.3, 2018, pp. 277–285.

[3]. Christoph Stiller, Promises and Challenges of Automated Vehicles, plenary lecture, in R. Moreno-Díaz, F. Pichler, A. Quesada-Arencibia, editors, in *Proceedings of the 17th International Conference on Computer Aided Systems Theory (EUROCAST' 2019),* Las Palmas de Gran Canaria, Spain, February 17 - 22, 2019, Springer Notes in Computer Science Book , 2020, 12013.

[4]. Jean-Yves Bouguet, Camera Calibration Toolbox for Matlab (1.0), *CaltechDATA*, 2022.

[5]. The MathWorks, Image Processing Toolbox™ User's Guide, Designing and Implementing Linear Filters for Image Data - Contrast Enhancement Techniques, 2023, pp. 8-69–1-72, URL: https://de.mathworks.com/help/pdf_doc/images/images_ug.pdf (28. 8. 2023).

[6]. Steven Bleicher, Contemporary Color: Theory and Use, 3rd edition, *Taylor & Francis Ltd*, 2023.

[7]. Mark David Jenkins, Tom Buggy, Gordon Morison, An imaging system for visual inspection and structural condition monitoring of railway tunnels, in *Proceedings of the IEEE Workshop on Environmental, Energy, and Structural Monitoring Systems (EESMS),* Milan, Italy, Jul. 24 - 25 2017.

[8]. L. Attard, C. J. Debono, G. Valentino, M. Di Castro, Vision-Based Tunnel Lining Health Monitoring via Bi-Temporal Image Comparison and Decision-Level Fusion of Change Maps, *Sensors*, 21, 2021, 4040.

[9]. Yonghong Xie, Qiang Ji, A new efficient ellipse detection method, in *Proceedings of the International Conference on Pattern Recognition,* 2002.

[10]. David Avis, David Bremner, Raimund Seidel, How good are convex hull algorithms?, *Computational Geometry,* 7, 5–6, 1997, pp. 265–301.

[11]. The MathWorks, Image Processing Toolbox™ User's Guide, Code Generation for Image Processing Toolbox Functions - Generate Code for Object Detection, 2023, pp. 21-5–21-21, URL: https://de.mathworks.com/help/pdf_doc/images/images_ug.pdf (28. 8. 2023).

[12]. Pierre Soille, Morphological Image Analysis; Principles and Applications, *Springer*, 2nd edition, 2003.

[13]. Anil K. Jain, Fundamentals of Digital Image Processing, *Pearson*, 2015.

[14]. MathWorks, https://de.mathworks.com/help/vision/ref/bboxwarp.html#d124e195212 (28.8.2023).

[15]. Infineon Technologies AG, REAL3™ image sensor family, 3D depth sensing based on Time-of-Flight, 2015, URL: https://www.infineon.com/dgdl/Infineon-REAL3+Image+Sensor+Family-PB-v01_00-EN.PDF?fileId=5546d462518ffd850151a0afc2302a58 (28. 8. 2023).

(033)

An IoT Communication Platform for Interactive Buildings Energy Management System

L. Mihet-Popa
Østfold University College, Department of Engineering, Kobberslagerstredet 5, 1671 Fredrikstad; Norway
Tel.: + 4792271353
E-mail: lucian.mihet@hiof.no

Abstract: More than 40 % of the world's energy is used in buildings, from which 50 % of energy is wasted because of non-existing or inefficient building energy management system (BEMS). By using a BEMS energy consumers are more connected, better controlled, monitored and managed, and the smart building has emerged. This paper deals with development of an IoT communication platform for building energy management systems. This is done by using an edge/cloud-computing architecture based on communication modules and service providers. We propose an IoT platform based cloud-computing which is able to monitor the power consumption and thermal battery storage functionalities from a local solar production in real-time. The platform will be part of an innovative and integrated BEMS approach that aims at achieving a highly efficient management of heterogenous energy resources, integrating and combining the management of different energy technologies into the BEMS. A lab setup with a real-time interface and data processing, for monitoring and controlling the power generation and consumption for different type of buildings, will be designed to optimize, test and validate the platform.

Keywords: Building energy management system, Interactive buildings, IoT, Cloud-computing, Digitalization.

1. Introduction

Buildings are a major cause of carbon emissions and building sector is responsible for around 40 % of energy consumption and for about 30 % of CO_2 emissions [1-2].

Three technology factors that make and drive decarbonization feasibility have been identify. There is the transition to a new energy system, new enabling technologies and digitalization [3-4].

Decarbonization is a critical transition that is affecting all businesses and is reshaping the foundations of the energy industry. A key driver of this energy transition is policy, spearheaded on a global scale by the Paris Agreement [5]. In parallel to this, two other pillars transforming the energy landscape, decentralization and digitalization, are significant enablers of decarbonization, making it more technically feasible than ever before. These technical developments are helping overcome some of the challenges of decarbonization and are expanding the opportunities for optimization and new business models.

There is a clear need for accelerating and financing building investments and leverage smart, energy-efficient technologies in the building sector. Smart buildings integrate cutting edge ICT-based solutions for energy efficiency and energy flexibility, which can effectively assist in creating healthier and more comfortable buildings with lower energy consumption and lower CO2 emissions [6].

1.1. Energy Transition

Energy is the lifeblood of an economy and without reliable, sustainable and affordable energy, society cannot prosper. The transition from the old to the new energy systems is done by integrating the renewable energy sources into the new energy systems making decarbonization more feasible.

The energy transition refers to the transition from energy supply from fossil and nuclear fuels to renewable energy sources, with the aim of creating a new, sustainable energy system with almost zero CO_2 emissions.

Europe's ambition is to achieve a secure, sustainable, and affordable energy system. The European Commission has set itself the aim of reducing emissions by 55 % by 2030 and reaching climate neutrality by 2050 [6]. The European Energy Transition Readiness Index highlights the key role infrastructure is playing in driving decarbonization in the region.

1.2. Enabling Technologies

The current technology revolution is leading to unwitnessed shifts in the economy, society, business, and individuals. A great effort is being made worldwide toward clean energy in order to protect the environment and improve operational efficiencies and customer services for better grid availability and reliability.

New enabling technologies contain storage technology and flexible energy loads that help overcome the intermittency issues.

Smart buildings, also known as intelligent buildings or automated buildings, are structures that leverage advanced technologies and systems to enhance the efficiency, comfort, safety, and sustainability of the building and its occupants.

These buildings integrate various interconnected devices, smart sensors, and automation systems to

optimize operations, improve energy management, and provide intelligent services.

This energy transition (transformation) is pushed by several factors, which include electrification, decentralization, and digitalization.

1.3. Digitalization

Digital technologies comprising communications, flexibility dispatch systems, smart meters, data standards, and IT systems constitute a key enabler for flexibility markets. Digital technology is emerging in smart homes to facilitate DSM. Digitalization of the network is an obvious opportunity for cost-effective development and management of the electricity system with high returns in cost and quality to serve.

Digitalization of energy and building technology allows better control of hardware, technologies and software. More than that, digitalization supports electrification and decentralization by having better management, which includes automatic control, consumption real-time optimization, and interaction with customers [7-8].

2. Interactive Buildings and BEMS

Energy consumers are more connected, and the smart building has emerged: with new technologies, such as renewable energy and energy storage located close to or as part of a building's infrastructure (as well as digitalization and connectivity of energy management inside the building), consumers are becoming smarter and transforming the way they can operate.

An interactive building is able to turn buildings into a source of energy, using load management techniques, optimization within buildings and demand flexibility.

Building automation is one of the most important requirements for DR (demand response) and DSM (demand-side management) without which customers could not respond to price signal in real-time.

A typical traditional building has a Building Energy Management System (BEMS) that is limited to HVAC and perhaps lighting, access control, and power monitoring. It is simply control used to monitor for problems and do basic controls. Both societal and technology factors are driving the evolution of BEMSs from being primarily an HVAC control system to being more of a smart building system integration platform for proactive monitoring, control, and automation.

2.1. Demand Response and Demand-Side Management Techniques

Demand Response (DR) programs fall into the category of load-management programs to encourage customers to decrease their electric consumption in response to a change in the price of electricity over time which, in turn, addresses the economic use of the grid. DR programs help utilities reduce the power consumed, preserve energy, redistribute power consumed, enhance system reliability, reduce energy prices, and increase economic efficiency [7, 8].

Demand-side management (DSM) is a group of programs consisting of the planning, implementing and monitoring activities of electric utility that are designed to encourage consumers to modify their level and pattern of electricity usage. The main objective is to provide customers with continuous and efficient energy in the long term with the less costs. In fact, DSM contains two main principles for achieving supply-demand balancing, load shifting and energy efficiency.

DR and DSM are two distinct procedures, DR ensures short-term load response to improve the energy consumption profile while DSM is applied for long-term planning, such as for shifting the load peak over time. Anyway, they are capable of being used together in synchronicity.

2.2. Next-Generation Building Energy Management Systems (BEMSs)

Building owners and system integrators face increasing pressure to save more energy, reduce costs, and maintain availability all while enhancing occupant experience and well-being. Achieving these objectives is best solved by a new type of BEMS available today that goes well beyond HVAC controls. These modern next-generation BEMSs benefit stakeholders by being a more open integration platform that uses IoT, cloud computing, data analytics, and artificial intelligence technologies to get more out of your available resources and connected systems.

The building energy management system (BEMS) is a critical tool for operating a building safely, efficiently, and reliably. However, focusing on energy efficiency and sustainability, combined with fundamental changes in resident needs and expectations, are straining traditional BEMS implementations pushing them to grow and evolve. At the same time, advancements in cloud computing, IoT, analytics, and artificial intelligence are leading to new and broader capabilities, such as increasing demand for energy efficiency and sustainability, changing occupant requirements and expectations, and emergence of newer IT, IoT, and smart building technologies to being more of a smart building system integration platform for proactive monitoring, control, and automation.

3. IoT Communication Platform-based Cloud Computing Solutions

The IoT is a pretty new concept in the architecture of communication devices and connects sensors and devices such as local battery storage, rooftop solar PV, home appliances and smart meters (SMs) through the internet, enabling information gathering and exchange. The IoT is basically composed by digitization of assets, collection of data and computational algorithms

to control the system. Cloud-based control systems would enable the management of these devices.

The IoT framework is equipped to handle large volumes of data generated by multiple DERs (distributed energy resources) within future smart energy systems via additional tools based AI algorithms. In this context, cloud-based platforms are key players in storing and intelligently using the data generated by the IoT in a highly flexible manner and deploying a multitude of applications in parallel.

Cloud platforms bring computation robustness and flexibility for interfacing multiple technologies and data based algorithms while providing on-demand parallel computing resources.

Multiple industrial communication protocols enable device-to-device, device-to-gateway, and gateway-to-cloud communication, depending on bandwidth, security, resilience to noise, losses, error detection or interoperability.

4. Design Procedure, Modeling Approach and Workflow Management

In order to develop an IoT platform and to provide end-to-end solutions for customers' energy management needs, based on demand side management for energy & cost savings, we started with a detailed modelling approach for an electric water heater (EWH) for DR based on one- and two-dimensional parabolic Partial Differential Equation (PDE). EWHs have a great potential in implementing DR control strategies because the power consumption has a high correlation with daily load patterns and can be used as energy storage devices when is needed [9]. The dynamic behavior of EWHs is essential for designing successfully DR controls. We developed the models in MATLAB and Simulink software tools, before to integrated with dSPACE RTI, as can be seen in Fig. 1.

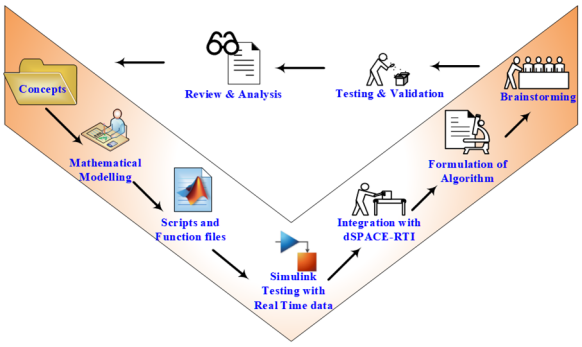

Fig. 1. Workflow management.

The smart heater we modeled, validated by measurements, and tested can estimate and regulate its stored energy (state-of charge) based on the temperature measurement, the inflow of water, and the heater power.

The state of charge in the tank is the energy left, which is the initial energy in the tank $E0$ plus the change in energy divided by the maximum energy:

$$SOC = \frac{E_0 \cdot \frac{dE}{dt}}{E_{\max}} \cdot 100[\%], \quad (1)$$

where the initial energy and maximum energy can be calculated as follows:

$$E_0 = m_0 \cdot c \cdot T_0, \quad (2)$$

where m_0 and T_0 are the initial water mass and water temperature respectively.

$$E_{\max} = m_{\max} \cdot c \cdot T_{\max} \quad (3)$$

where $mmax$ and $Tmax$ are the maximum capacity and maximum temperature of the water tank respectively.

Next step was to design and build a controller in order to minimizing the cost of energy consumption for the price signal while maintaining the user comfort level, as shown in Fig. 2. The comfort parameter quantifies the tradeoff between cost savings and user comfort. For optimal operation states of EWH based on forecasting price we used a ML algorithm developed in Python and integrated with our previously developed MATLAB-Simulink model, as co-simulation environment.

It also incorporates demand side management features meaning that it can be optimized through a machine learning algorithm to improve the energy efficiency and reduce the energy consumed by 20 % [10].

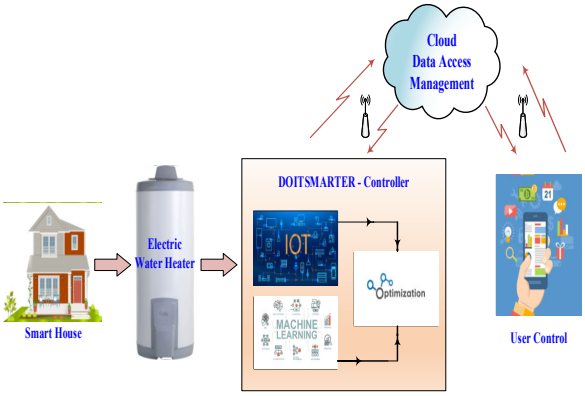

Fig. 2. A basic block diagram representation.

5. Performance Evaluation and Testing Procedure

The lab setup based on an IoT communication platform it is shown in Fig. 3. The setup is based on a real-time interface (RTI) with a graphical user interface (GUI) called dSPACE ControlDesk.

This platform is generated via MATLAB-Simulink software program and can be used, among other things, for algorithms development and testing. IoT sensors signal conditioning and data analytics can also be performed. The sensor signals are replicated with a Tektronix AFG31000 series, and the signals are given into the control panel of the dSPACE for RTI based analysis of the model.

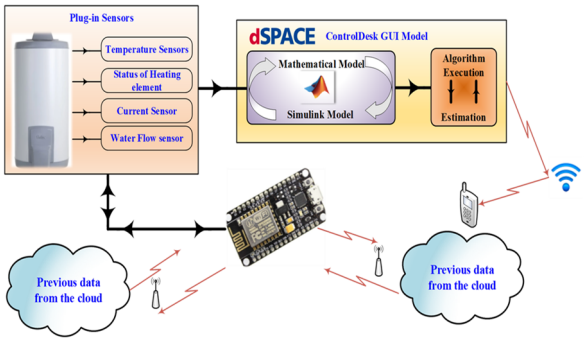

Fig. 3. An experimental lab setup based on an IoT platform designed for testing different components/devices of a BEMS.

In parallel with the experimental lab setup, we developed a cloud computing solution's including data from the hot water heater, as shown in Fig. 4. The smart meter is monitoring the data in real-time and send it to the cloud via a HAN adaptor.

DR can achieve the supply–demand balance through controlling the electric consumption which is monitored through the smart meter. The BEMS (aggregator control) makes the decision based on control signals from service provider after comparing the demand and PV generation in order to achieve market balance with supply–demand balance.

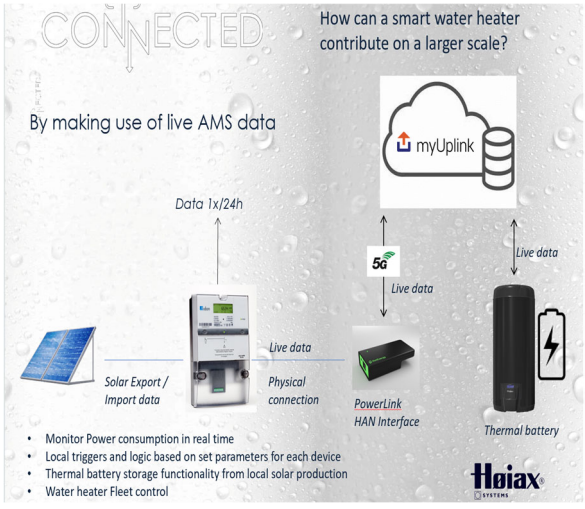

Fig. 4. IoT platform-based cloud-computing approach.

The platform will include a completely new generation of water heater, capable of storing energy like a thermal battery, that allows control from mobile devices and the app myUplink.

The water heater can function as an energy battery, because of information from the smart home system it can store hot water when electricity is cheapest. Electricity prices often vary a lot over the course of a day, often depending on how heavy the load is on the electricity grid. When the electricity is at its most affordable or you have access to self-produced electricity via a solar cell system, you can choose for the boiler to raise the temperature in the tank automatically in relation to what you usually have as a set point. In other words, you only use energy when it is cheapest. When the water reaches a given temperature, it switches off and does not need to be switched on again for many hours. When you draw water at a time when electricity is expensive, the temperature in the water heater gradually drops without switching on. This way you avoid using energy on the hot water during this period.

As the boilers can be connected to a smart house system, they can be integrated into the management of the entire house, then you will get the most out of the opportunities this provides.

The proposed platform is based on the most popular standards Z-wave and Zigbee, which can be connected to third-party products and applications via a single app. Smart home solutions that can be controlled with apps are currently in great demand, and this innovation enables them to adapt to both customer groups and a general desire for a better climate.

Via the app for the smart house system, you can control the smart water heater together with other electricity consumption in the home, such as electric cars and space heating.

6. Conclusions

The goal of this work was to highlight the energy transition, new enabling technologies and digitalization of energy in interactive buildings and to present an IoT communication platform developed for testing practical solutions for a BEMS. The envisioned and targeted energy optimization solutions include the development of an innovative Internet of Things (IoT) algorithm system awareness, considering a secure communication and data processing approaches, reducing energy demand and equivalent CO2 emissions. The developed solution will bring novelty based on Edge computing and AI and will integrate sensors and building functionalities into one common gateway, giving the possibility for different service providers to operate on the same hardware, with open data source and scalability.

Acknowledgements

This work was supported in part by EEA Grants, DOITSMARTER and Increased knowledge on RES and Energy Efficiency.

References

[1]. IEA. Electricity information: Overview. Paris, France, 2021, http://www.iea.org/reports/electricity-information-overview.

[2]. IRENA. Global Renewables Outlook. Energy Transformation 2050, *International Renewable Energy Agency*, Abu Dhabi, 2020.

[3]. Y. Wu, Y. Wu, J. M. Guerrero, J. C. Vasquez, Digitalization and decentralization driving transactive Energy internet: key technologies and infrastructure, *International Journal of Electrical Power and Energy Systems*, 126, A, 2021, 106593.

[4]. What digitalization can do to alleviate the energy crisis, *Siemens report*, 2022, Switzerland, www. siemens.com/smartinfrastructure

[5]. Paris Agreement, Web Portal (https://climate.ec.europa.eu/eu-action/international-action-climate-change/climate-negotiations/paris-agreement_en).

[6]. European Commission services towards the development of a smart readiness indicator for buildings, Support for setting up a Smart Readiness Indicator for buildings and related impact assessment, December 2017.

[7]. Shady S. Refaat, Omar Ellabban, Sertac Bayhan, Haitham Abu-Rub, Frede Blaabjerg, Miroslav M. Begovic, Smart Grid and Enabling Technologies, *Wiley,* 2021.

[8]. Salman K. Salman, Introduction to the Smart Grid-Concepts, Technologies and Evolution, *IET*, 2017.

[9]. Z. Xu, R. Diao, S. Lu, J. Lian, and Y. Zhang, Modeling of Electric Water Heaters for Demand Response: A Baseline PDE Model, *IEEE Transactions on Smart Grid,* Vol. 5, No. 5, September 2014, pp. 2203 - 2210.

[10]. A. F. Meyabadi, and M. H. Deihimi, A review of demand-side management: Reconsidering theoretical framework, *Renewable and Sustainable Energy Reviews,* 80, 2017, pp. 367-379.

(034)

Geospatial Sensor-based Approach to Provide Defibrillators by using Drones in Mountain Areas: A Study Case in South Tyrol, Italy

E. Fajardo-Figueroa [1], R. Mendicino [1], S. Tritini [1], M. van Veelen [2], G. Vinetti [2], G. Ristorto [3], S. Mayrgündter [4], G. M. Bianco [5], L. Meng [6] and A. Mejia-Aguilar[1]

[1] Eurac Research, Center for Sensing Solutions, Drususallee 1, 39100, Bozen, Italy
[2] Eurac Research, Mountain Emergency Medicine, Drususallee 1, 39100, Bozen, Italy
[3] MAVTech s.r.l., Via Ipazia 2, 39100, Bozen, Italy
[4] NOI Techpark, Volta-Straße 13/A, 39100, Bozen, Italy
[5] University of Rome Tor Vergata, Civil and Computer Science Engineering, Rome, Italy.
[6] Technical University of Munich, Chair of Cartography and Visual Analytics, Munich, Germany
Tel.: + 39, fax: + 87654321
E-mail: abraham.mejia@eurac.edu

Summary: The use of geospatial infrastructure supported by novel sensors, autonomous and piloted aerial platforms, and computational tools are impacting civil applications such as risk management, particularly interesting in mountain rescue operations. Here, we propose a semi-automatic geospatial system able to identify the coordinates of a distress call, map them in the entire Province of South Tyrol, identify possible areas to execute the maneuvers of drone operations, and generate the drone flight plan able to identify possible obstacles and keeps a relative height of flight following normative or user configuration to harmonize joint missions (e.g., helicopters). The hardware component consists of a drone platform (MAVTech), RGB and thermal cameras, and a light defibrillator. A remote user interface confirms the coordinates by detecting the victim (thermal) and providing situation awareness (RGB) to the operators to finally drop the defibrillator.

Keywords: Geospatial system, Drones, Sensor imagers, Defibrillator.

1. Introduction

During the last years, the introduction of drones in risk management protocols has dramatically opened new possibilities to assist people in danger [1], to determine the nature and extent of risk (eg. natural hazards [2]), to effectively coordinate first responder teams [3] and to provide assistance by means of small first-aid packages [4].

In addition, novel sensors such as infrared cameras [5], long-range communication protocols [6], new computational methods, have contributed to accelerating the traditional methods of rescue operations.

However, operations in hostile environments, such as mountain scenarios, require complex methods, high-skilled responders, and usually the complete chain of rescue depends on weather conditions, and optimal performance of technology. In the end, time is the main factor to overcome to successfully give support to any victim.

Therefore, in this work we propose a combined approach based on geospatial infrastructure (GIS technology), open data models that are used to map emergencies in the alpine region of South Tyrol, Italy, and sensor-based data fusion to optimally fly an aerial platform, to identify, localize and confirm any victim, and to provide a basic package that contains one defibrillator to be used in case of cardiac arrest.

The main novelty of this work relies on two aspects: the semi-automatic GIS system is able to identify the area of a distress call, map it, suggest a possible area to execute the Aerial Unmanned Vehicle (UAV) maneuvers (eg. parking), and to create the flight plan. The file is uploaded in-site and the mission is automatically performed, supervised by an operator (due to legislation). The system fusion the data coming from the distress call, the actual flight plan (telemetry), integrates thermal and visible range imagery to detect the victim and provide a situational awareness to the pilot who transmits such information to the hospital and/or medical assistance.

2. Study Area

For this study, we selected two representative mountain scenarios in the alpine Province of South Tyrol, Italy, in the Corvara in Badia municipality (latitude 46.539885°, longitude 11.896100°, elevation 1800 m.a.s.l.), for two different seasons (summer and winter). The selected areas are highly visited by tourism, and attracted by the hiking and skiing seasons respectively (Fig. 1).

3. Method

As an initial step, we elaborate a cartographic approach consisting of the identification of suitable places to perform the maneuvers of drones for mountain rescue operations. These places, or drone-ports, have a relatively small area of operations, with access to electricity to charge batteries and good phone signal coverage and preferably close to roads where ambulances can assist the victim. To elaborate it, we

use the landuse and landcover products from the Province of South Tyrol. We used open- access remote sensing data (Sentinel, digital surface models) and available public datasets of the Province of South Tyrol [7]. Then, we overlayed this product to the regulated areas for flying civil drones in Italy. Despite the fact that first responders have an allowance to fly drones in emergencies at any elevation, we suggest keeping the civil rules of flying in the direction of future normative identified as U-Space where any aircraft should maintain a minimum and maximum elevation to share the volume of airspace [8]. The suggested approach will overcome many of these difficulties.

Fig. 1. Corvara in Badia, South Tyrol, Italy.

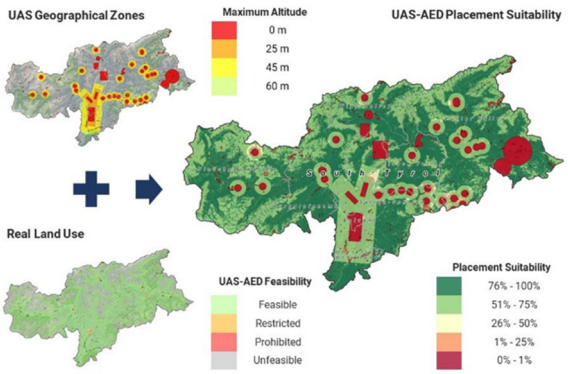

Fig. 2. Cartographic approach to localize drone-ports to execute autonomous missions.

Then, to attend the distress call, we made use of the GeoResq application widely used by the Italian mountain rescue teams [9]. Georesq is based on the activation of the internal GPS installed in most modern cell phones. Once the distress call is activated, the system sends the actual position to a central emergency station. It is possible to indicate the type of emergency, such as a cardiac arrest.

With this coordinate, our proposed method identifies the most suitable place drone-port, assuming it is operative and ready to operate. Then, it was possible to create a flight plan, whose origin starts in a parking spot, reaching as a final point the coordinate of the victim. It is a sequence of points, that contain a theoretical model for coordinate, elevation, and speed with respect to ground.

The tested drone for this study is a MAVTech Q4X equipped with a RGB camera and disposable defibrillator delivered by an automatic parachute system with an autonomy of 32 min. Its navigation system includes different accessories, including strobe lights, RTK GPS, a secondary GPS antenna, and a First Person View (FPV) camera [10], Fig. 2. In addition we used an infrared camera to detect and localize the victim.

Fig. 2. UAV Platform, MAVTech, model Q4X (curtesy of MAVTech).

3. Preliminary Results

We tested the above-mentioned approach in summer conditions. Using a simulated coordinates distress call, the system elaborated the flight plan by maintaining the U-space regulations Fig. 3.

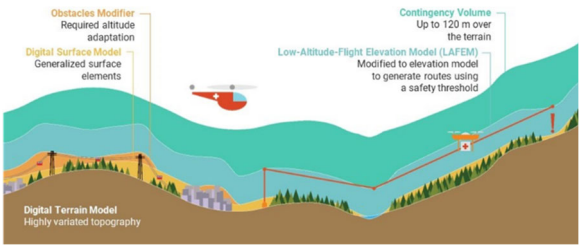

Fig. 3. U-space regulations and UAVflight plan strategy.

We use a telemetry approach based on the sensor data provided by the UAV (instrumentation on board) that consists of an Inertial Measurement Unit (IMU), compass, GPS. These data are collected, and transferred to a central station via 3G/4G communication router, in a dedicated online repository. It is based on the Internet of Things simplified approach able to combine diverse typologies of information (sensor-based) as well as actuators (defibrillator provision) [11]. It also includes raster information provided by the thermal (FLIR Vue Pro) and RGB cameras.

We fusion the imagery with the simplified IoT telemetry information (Fig. 4) provided by the UAV to

confirm the position of the victim. With the approximate height, the coordinates, the attitude of the drone, and the characteristics of the optics (field of view) [12].

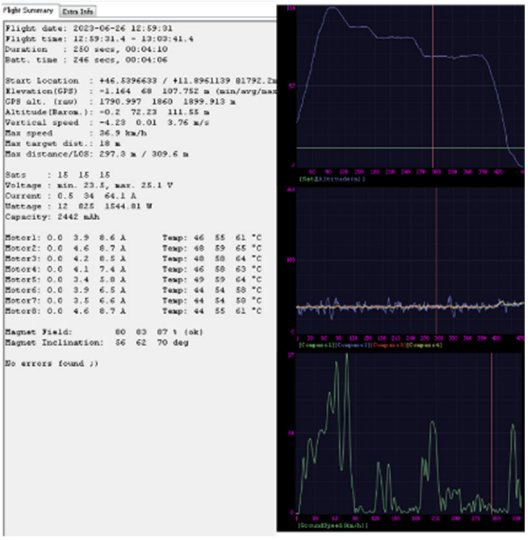

Fig. 4. Simplified IoT application with compass, altitude and ground speed information.

Later, we identify a thermal anomaly Fig 5a, and confirm the discrepancies on visible image Fig 5b.

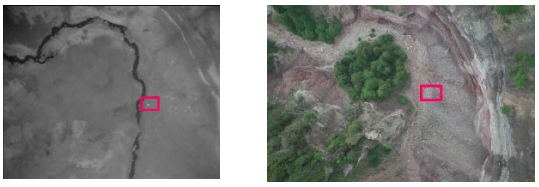

Fig. 5. (a) Infrared and (b) visible imagery.

Finally, we determine and confirm the position projected to the pixel information to deliver the AED to the victim (Fig. 6)

(a) (b)

Fig. 6. Provision of the AED (a) view from the ground (victim) and (b) from the drone.

4. Conclusions

It has been demonstrated the capacity to improve the localization of a potential victim in need of a defibrillator with the support of modern geospatial tools (GIS) and modern platforms and sensors (UAV+dedicated payload). The capacity to transfer the actual information of the drone to central stations (telemetry) opens opportunities to use such platforms in emergencies such as earthquakes, eruptions, fires, and mountain emergency accidents as described here.

Acknowledgements

The research leading to these results has received funding from the South Tyrol FUSION grant program under the project “DRONE-AED” funded by Cassa di Risparmio Foundation and from Eurac Internal Project “ESLAB@NOI” 2023.

References

[1]. A. Kobaszyńska-Twardowska, J. Łukasiewicz, P.W. Sielicki, Risk Management Model for Unmanned Aerial Vehicles during Flight Operations, *Materials* (Basel), 15, 7, 2022, p. 2448.

[2]. A. Román, A. Tovar-Sánchez, D. Roque-Atienza, I.E. Huertas, I. Caballero, E. Fraile-Nuez, G. Navarro, Unmanned aerial vehicles (UAVs) as a tool for hazard assessment: The 2021 eruption of Cumbre Vieja volcano, La Palma Island (Spain), *Science of The Total Environment*, Vol. 843, 2022, 157092.

[3]. J. Lemayian, J. Hamamreh, First Responder Drones for Critical Situation Management, in *Proceedings of the Innovations in Intelligent Systems and Applications Conference*, 2019, pp. 1-6.

[4]. M. J. van Veelen, G. Roveri, A. Voegele, T. Dal Cappello, M. Masè, M. Falla, I. B. Regli, A. Mejia-Aguilar, S. Mayrgündter, G. Strapazzon, Drones reduce the treatment-free interval in search and rescue operations with telemedical support – A randomized controlled trial, *The American Journal of Emergency Medicine,* Volume 66, 2023, pp. 40-44.

[5]. T. M. Dawdi, N. Abdalla, Y.M. Elkalyoubi, B. Soudan, Locating victims in hot environments using combined thermal and optical imaging, *Computers and Electrical Engineering,* 85, 2020, 106697.

[6]. G. M. Bianco, R. Giuliano, F. Mazzenga, G. Marrocco, A. Mejia-Aguilar, LoRa System for Search and Rescue: Path Loss Models and Procedures in Mountain Scenarios, *IEEE Internet of Things Journal*, 8, 3, 2021, pp. 1985 - 1999.

[7]. Rete civica dell’Alto Adige, *GeoCatalogo*, 2023. http://geokatalog.buergernetz.bz.it/

[8]. European Union Aviation Safety Agency (EASA), Commission Implementing Regulation (EU) 2021/664 of 22 April 2021 on a regulatory framework for the U-space, 2023.

[9]. Corpo Nazionale Soccorso Alpino e Speleologico, GeoResq, Google Play, 2023. https://web.georesq.it/

[10]. MAVTec s.r.l., 2023. https://www.mavtech.eu/

[11]. Damaševičius, R., Bacanin, N.; Misra, S., From Sensors to Safety: Internet of Emergency Services (IoES) for Emergency Response and Disaster Management, *J. Sens. Actuator Netw.,* 12, 3, 2023, 41.

[12] Sandino, J., Maire, F., Caccetta, P., Sanderson, C., Gonzalez, F., Drone-Based Autonomous Motion Planning System for Outdoor Environments under Object Detection Uncertainty, *Remote Sens.,* 2021, 13, 4481.

(035)

Zinc Tin Oxide Nanostructures Synthesized by the Microwave Hydrothermal Method Applied to Gas Sensors

R. A. Silva [1], M. G. Masteghin [2] and M. O. Orlandi [1]
[1] São Paulo State University, Engineering, Physics and Mathematics Department, Araraquara, Brazil
[2] University of Surrey, Advanced Technology Institute, Guildford, United Kingdom
Tel.: +55 1633019892
E-mail: ranilson.angelo@unesp.br

Summary: Semiconductor metal oxide materials with ternary or quaternary type structures have been highlighted by the properties resulting from the type of structural alignment of the constituent elements. This work reports the growth mechanism of zinc tin oxide-based structures synthesized by microwave-assisted hydrothermal methods and gas sensing performance for NO_2, H_2, and CO gases. The materials were characterized by X-ray diffraction (XRD), scanning and transmission electron microscopy (SEM and TEM). $ZnSn(OH)_6$, $ZnSn(OH)_6/ZnSnO_3$, and Zn_2SnO_4/SnO_2 structures were obtained varying the synthesis time of 4h, 12h, and 24h, respectively. Gas sensor measurements showed $ZnSnO_3$ a lower detection limit to NO_2, in which a 12-fold increase in electrical resistance is estimated in the presence of 1 ppb NO_2. Moreover, the Zn_2SnO_4/SnO_2 exhibited higher selectivity and a sensor response to NO_2 relative to H_2 and CO. Hence, the results demonstrate that ultra-selective and high-performance gas sensor devices can be created through nanostructures growth engineering.

Keywords: Gas sensor, Semiconductor metal oxide, Nitrogen dioxide, Environmental pollutant, Microwave-assisted hydrothermal.

1. Introduction

The growing demand for high-performance devices for detecting harmful gases to humans and the environment has encouraged the research of new materials with different electrical properties and unique morphologies. Among the leading gases monitored nowadays are carbon monoxide (CO), nitrogen dioxide (NO_2), and hydrogen (H_2), all coming mainly from burning fossil fuels. The chemo-resistive semiconducting metal oxide (SMO_x) nanostructures have been highlighted for gas detection due to their low cost and scalability. These devices generally present high sensitivity; however, the selectivity must be improved for the sensor responses to be reliable.

Tin dioxide (SnO_2) and zinc oxide (ZnO) are the most used gas-sensing materials [1,2]. SnO_2 nanostructures in the presence of 100 ppm of NO_2 and CO gases showed a sensor response (R_{NO_2}/R_{air} and R_{air}/R_{CO}) of 65 and 1.5, respectively [3]; while "flower"-like ZnO structures presented R_{NO_2}/R_{air} = 70 and R_{air}/R_{CO} = 2 for the same concentrations of the analytes [4]. On the other hand, studies have shown that SnO_2/ZnO heterostructures exhibit promising properties for gas detection. SnO_2/ZnO nanostructures showed an increase of about 16- and 32-fold in sensor response for 10 ppm NO_2 compared to pure SnO_2 and ZnO [5]. For zinc tin oxide (ZTO) nanostructures such as $ZnSnO_3$ and Zn_2SnO_4, an anti-moisture behavior was observed, i.e., the sensor response was minimally affected by water vapor [6]. Although ZTO shows interesting properties so far, few studies are available for gas sensing due to its challenging synthesis and the thermodynamic instability of the metastable $ZnSnO_3$ phase. Therefore, this study evaluates the structural properties and sensing response of ternary compounds $ZnSn(OH)_6$, $ZnSnO_3$, and Zn_2SnO_4/SnO_2 with unique morphologies obtained from microwave-assisted hydrothermal synthesis.

2. Experimental

2.1. Synthesis of the ZnO and ZTO Nanostructures

For the ZnO synthesis, the precursor's zinc acetate dihydrate ($Zn(CH_3CO_2)_2{\cdot}2H_2O$) and sodium hydroxide (NaOH) in a molar ratio of 1:14 were placed inside a sealed polytetrafluoroethylene (PTFE) reaction cell. The synthesis was conducted in a microwave for 20 minutes at 120 ˚C.

A mixture of ZnO nanostructures with tin (IV) chloride pentahydrate ($SnCl_4{\cdot}5H_2O$) were used as precursors in synthesizing ZTO nanostructures using the procedure previously described for the reaction times of 4 h, 12 h and 24 h at 170 °C.

2.2. Structural and Morphological Characterizations

The synthesized materials' phase and crystallinity were analyzed by XRD using a Rigaku RINT2000 diffractometer and a TEM using a Philips CM200 microscope with a 200 keV beam. The materials morphology was examined in a JEOL JSM-7500F microscope (FEG-SEM).

2.3. Gas sensing Measurements

Gas sensing measurements have been carried out using NO_2, H_2, and CO as analyte gases, with concentrations ranging from 5 to 100 ppm diluted in dry synthetic air via mass flow controllers (MKS). The devices were measured at 150 ˚C, 200 ˚C, and 250 ˚C.

The electrical resistance change was monitored by applying a voltage of 0.5 V using a source/measure unit (Agilent 34972A). Sensor responses (signals) were calculated based on the $R_{gas}/R_{baseline}$ (for NO_2) or $R_{baseline}/R_{gas}$ (for reducing gases, CO and H_2), where R_{gas} is the device resistance when exposed to the analyte gas and $R_{baseline}$ corresponds to the steady-state resistance in air reference (baseline). Selectivity was defined as the sensor response in the presence of NO_2 relative to the sensor signal when the device was exposed to reducing gases.

3. Results and Discussion

The XRD structural (Fig. 1) and SEM morphological (Fig. 2) analysis show that after 4h, only the cubic tin zinc hydroxide phase ($ZnSn(OH)_6$) with cuboctahedron shape is obtained, while the synthesis time of 24h resulted in a mixture of the zinc stannate (Zn_2SnO_4) and tin dioxide (SnO_2) phases with a "silver touch" cacti structure. On the other hand, an intermediate time of 12h resulted in a tube-like hollow microstructure obtained from the mixture of $ZnSn(OH)_6$ and zinc tin-oxide ($ZnSnO_3$).

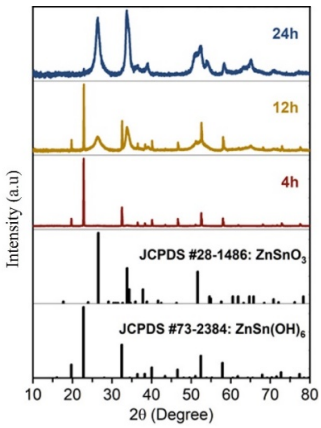

Fig. 1. XRD spectra for samples synthesized for 4 h, 12 h, 24 h, and standard for $ZnSn(OH)_6$, and $ZnSnO_3$.

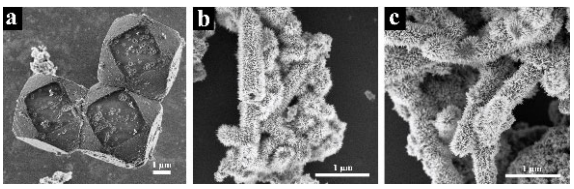

Fig. 2. SEM images of samples a) 4 h, b) 12 h, and c) 24 h.

Fig. 3a compares sensor response to reducing (CO and H_2) and oxidizing (NO_2) gases, showing an expected drop in resistance for an n-type semiconductor in the presence of CO and H_2. Selectivity values under 100 ppm exposure to analyte gas are shown in Fig. 3b. All compositions of the ZTO system showed excellent selectivity for NO_2 about H_2 or CO, notably in the 24h in which the sensor response was ~1600 times greater for NO_2 than for H_2 and ~1500 times greater for NO_2 than for CO.

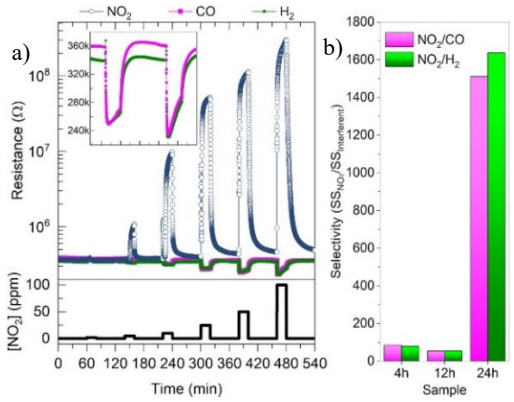

Fig. 3. a) Gas sensing response for the 24h sample device operated at 200 ˚C. b) Selectivity in the presence of NO_2 divided by the sensor signal in the presence of interferent gases.

4. Conclusions

Hierarchical nano-heterostructure proved a promising approach to improve the required selectivity of SMO_x NO_2 sensors. The results showed that the synthesis process for the ZTO nanostructures allowed the transition from the $ZnSn(OH)_6$ phase to the metastable $ZnSnO_3$, which decomposes into Zn_2SnO_4/SnO_2 heterostructures. Regarding gas detection properties, the ultra-low NO_2 detection limit was achieved by the $ZnSnO_3$, while the Zn_2SnO_4/SnO_2 presented superior selectivity towards reducing gases.

Acknowledgments

This work was supported by PROPe – UNESP public notice 13/2022, CNPq, CAPES, and FAPESP.

References

[1]. S. Das and V. Jayaraman, SnO_2: A comprehensive review on structures and gas sensors, *Progress in Materials Science,* Vol. 66, 2014, pp. 112–255.

[2]. Y. Kang, F. Yu, L. Zhang, W. Wang, L. Chen and Y. Li, Review of ZnO-based nanomaterials in gas sensors, *Solid State Ionics,* Vol. 360, 2021, p. 115544.

[3]. P. H. Suman, A. A. Felix, H. L. Tuller, J. A. Varela, M. O. Orlandi, Comparative gas sensor response of SnO_2, SnO and Sn_3O_4 nanobelts to NO_2 and potential interferents, *Sensors Actuators B: Chemical*, Vol. 208, 2015, pp. 122–127.

[4]. M. Chen, Z. Wang, D. Han, F. Gu and G. Guo, High-sensitivity NO_2 gas sensors based on flower-like and tube-like ZnO nanomaterials, *Sensors Actuators B: Chemical,* Vol. 157, 2011, pp. 565–574.

[5]. Z. Zhang, M. Xu, L. Liu, X. Ruan, J. Yan, W. Zhao, J. Yun, Y. Wang, S. Qin and T. Zhang, Novel SnO_2@ZnO hierarchical nanostructures for highly sensitive and selective NO_2 gas sensing, *Sensors Actuators B: Chemical,* Vol. 257, 2018, pp. 714–727.

[6]. L. Du, H. Zhang, M. Zhu and M. Zhang, Construction of flower-like $ZnSnO_3/Zn_2SnO_4$ hybrids for enhanced phenylamine sensing performance, *Inorganic Chemistry Frontiers,* Vol. 6, 2019, pp. 2311–231.

(036)

Replication of a DSC Device Using 3D Computational Modelling: Correction of Heat Flow Diagrams of Selected Geopolymers by Processing the Experimental Data

V. Kočí
Czech Technical University in Prague, Faculty of Civil Engineering,
Department of Materials Engineering and Chemistry,
Thakurova 7/2077, 166 29 Prague 6, Czech Republic
Tel.: + 420 2 2435 7125
E-mail: vaclav.koci@fsv.cvut.cz

Summary: Calorimetric measurements have been still struggling with few challenges, the thermal inertia treatment belongs among the most significant ones, especially in the field of thermal kinetics. Beside neglecting or ignoring its effects, empirical approaches are usually applied by practitioners to deal with it. This paper goes beyond the practice, exploiting an advanced method based on computational replication of the real experimental device including all the heat transfer processes involved during the measuring procedure. An inverse solution of problem enables a direct identification of the heat source in the sample which is the main difference from experimental approaches that rely on delayed/distorted signal readout outside the sample. The modelling results revealed, the thermal inertia neglection might lead to a temperature shifting by up to 15 °C in case of geopolymers tested.

Keywords: Differential scanning calorimetry, Thermal inertia, Geopolymer, Computational modelling, Systematic errors, Heat flow evolution, High temperatures.

1. Introduction

Despite the progress that have been made in the field of calorimetric measurements, there are still some negative factors affecting the results measured. The application of sophisticated electronic devices is very helpful and contributive at the first sight. However, being considered as a gray box, end-user can hardly analyze measuring subprocesses to reveal the origin of measuring errors and to make appropriate actions subsequently to eliminate them. Thermal inertia is one of the most frequently mentioned factors of which effect might be further magnified regarding to specifics of devices, sample size, heating rate, sensors positioning and signal processing in particular [1]. The end-users usually follow producers' guidelines to obey recommended setups and measuring process that that has been empirically identified to be less affected by the systematic errors [2].

Following up on the previous research [3], this paper goes beyond such a practice. A calibrated computational replication (model) of a selected differential scanning calorimeter is used to fit the experimental outputs. Once fitted, the grey-box label can be "removed" by closer looking inside the computational version of the device to analyze such processes that led to the same outputs as the experiment itself. In this way, the effect of the sensors positions, thermal inertia and other sources of errors can be involved enabling correct results to be extracted.

2. Materials and Methods

2.1. Geopolymers Studied

The geopolymer sample used in this research has been taken from the previous research [4] and represents one of the mixtures (labeled as C5 in the original publication) prepared within the course of composition optimization. It is based on ceramic powder (CP) used as the precursor which is activated using sodium water glass (WG, silicate modulus equal to 1.6) and NaOH pellets dissolved in water (W). Standard siliceous sand (S) with the particle size up to 2 mm is used as the filler. The dosage of particular constituents is summarized in Table 1.

Table 1. Geopolymer composition.

CP (g)	S (g)	WG (g)	NaOH (g)	W (g)
403	1097	175	22	152

2.2. Heat Flow Diagrams

Differential scanning calorimetry has been exploited to observe heat evolution difference between reference and measuring crucible, in which the geopolymer sample has been accommodated. The LabSys Evo/DSC calorimeter (Setaram Inc.) has been used for this measurement, exposing 50 μg of the sample to the heating rate of 5 K/min. Using set of thermocouples combined with a calibrated conversion

function, the heat flow curve can be plotted by means of evaluation of the different heat evolution in particular crucibles.

2.3. DSC Model and Data Processing

Regardless of a DSC device type and its data processing precision level, the common weak point of all these devices originates from physical limitations of the thermocouples positioning as they cannot be directly inserted into a sample. They are usually sticked to the outer surface of a crucible in which the thermal process takes place. The heat evolved by the sample must be therefore transferred on a certain path before is detected. Within this transfer, some of the heat can be consumed or redistributed or it easily takes some time which results in signal delay and distortion. The empirical techniques proposed to deal with this phenomenon are well-known, but their versatility and quick application possibility are on expense of accuracy.

Since the mathematical model of the DSC device/sensor replicates single details of the calorimeter so that the modelled heat transfer path is nearly identical to the experimental one (see Fig. 1), the model represents a powerful tool in which such heat function of the reacting sample is sought, that provides the same output (when processed by the model) as the real experimental device. It means, the solution of this inverse problem is basically going deeper in the "grey box" by direct identifying the heat source located exactly in the place of its origin. This is the main difference from the experimental approach in which results rely on the signal (distorted and delayed) readout OF the thermocouples outside the sample. Due to the page limit, please refer to [4] for more details about the model principles, construction, calibration or validation as well as exploitation of a selected advanced seeking method.

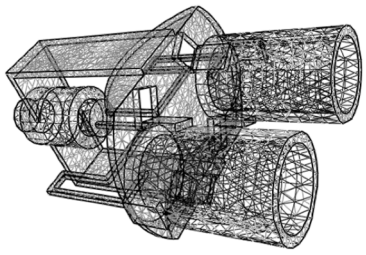

Fig. 1. Computational replication of the DSC sensor (in the device oriented vertically).

3. Results and Discussion

A brief comparison of the modelling and the experimental outputs (see Fig. 2) confirmed the expectations: the corrected output is shifted right along the *x*-axis by approximately 15 °C. This fact indicates the original signal recorded experimentally is linked to temperature values slightly lower than the actual temperature of the sample. The shift might be caused by some heat absorption and/or redistribution by metal components of the DSC, the crucibles walls in particular. The absolute difference of the heat flows detected is relatively small as geopolymers are known to be stable at high temperatures which makes them high-temperature resistant. The evaluation software of the DSC device automatically applies corrections following given empirical rules, but still the data produced is not fully cleaned of systematic errors.

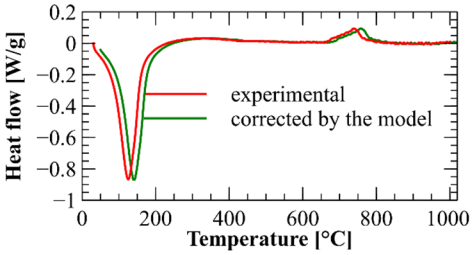

Fig. 2. Heat flow diagrams of the sample studied.

4. Conclusions

The extended abstract presented a computational approach developed for correction of systematic errors typical for calorimetric measurements. As the sample studied, geopolymer mixture has been tested. The modelling procedure led to temperature shift correction by 15 % approximately. The geopolymer studied showed to be thermally stable as not any significant exo/endo reaction have been revealed when exposed up to 10 %. The major heat power peak accounted for less than 1 W/g.

Acknowledgements

This research has been supported by the Czech Science Foundation under project No. 22-03474S.

References

[1]. S. Vyazovkin, How much is the accuracy of activation energy affected by ignoring thermal inertia?, *International Journal of Chemical Kinetics*, Vol. 52, Issue 1, 2020, pp. 23-28.

[2]. V. Kočí, J. Šesták, R. Černý, Thermal inertia and evaluation of reaction kinetics: A critical review, *Measurement,* Vol. 198, 2022, 111354.

[3]. V. Kočí, J. Maděra, A. Trník, R. Černý, Heat transport and storage processes in differential scanning calorimeter: Computational analysis and model validation, *International Journal of Heat and Mass Transfer,* Vol. 136, 2019, pp. 355-364.

[4]. V. Kočí, D. Koňáková, V. Pommer, M. Keppert, E. Vejmelková, R. Černý, Exploiting advantages of empirical and optimization approaches to design alkali activated materials in a more efficient way, *Construction and Building Materials*, Vol. 292, 2021, 123460.

(038)

Exploring Sustainable Printed Paper Sensors for Analyzing Cure Behavior and Detecting Cracks in Composites

A. Mahendran, N. Gupta, C. Koren and H. Lammer
Kompetenzzentrum Holz GmbH, WOOD KPLUS, Altenberger Strasse 69, A-4040, Linz, Austria
Tel.: +43 4212 494-8016
E-mail: a.mahendran@wood-kplus.at

Summary: The article focuses on the application of sustainable printed paper sensors for characterizing the cure behavior and crack detection in fiber-reinforced composites. It highlights the limitations of conventional embedded sensors and introduces printed paper sensors as an alternative solution. These sensors utilize paper as a flexible and low-cost substrate. The study employed printed paper sensors with interdigitated electrodes to monitor the curing behavior of resin-impregnated paper. The feasibility of using printed sensors for crack detection was also investigated. Mechanical tests, including bending and dropping ball tests, were conducted to evaluate the performance of the printed paper sensors. Resistance change was measured as an indicator of sensor response under applied loads. The results showed favorable sensing behavior, with the embedded sensor exhibiting a strong response to applied loads. In conclusion, the study demonstrated that printed paper sensors are suitable for monitoring the cure behavior of composites and can be used for crack detection under impact loading conditions.

Keywords: Printed paper sensor, Cure monitoring, Crack detection, Sustainable, Composites.

1. Introduction

Fiber-reinforced composites are widely employed in various structural applications [1]. Ensuring the safety, reliability, and durability of these composites necessitates structural health monitoring, which involves the detection and evaluation of potential damage, defects, or changes in their condition. Real-time monitoring of the curing process during composite manufacturing is also crucial to determine the time required for complete curing. However, conventional embedded sensors made from polymeric substrates are bulky, act as foreign bodies, and can compromise the mechanical strength of the composites. The state-of-the-art in micro-crack detection is electroluminescence imaging, where conventional electroluminescence was used to inspect the solar cell cracks [2]. Some authors also proposed an approach that utilizes a hybrid combination of deep learning models, including convolutional neural networks and Bayesian probabilistic analysis, for robust vision-based crack detection [3].

Printed paper sensors have emerged as a viable alternative to address these challenges. These sensors leverage the flexibility and cost-effectiveness of paper as a substrate, while benefiting from the functionality provided by printed electronic components [4]. Moreover, printed paper sensors are environmentally sustainable as they can be decomposed at the end of their life cycle. Printing techniques like screen printing, inkjet printing, and flexographic printing enable the deposition of conductive inks, functional materials, and sensing elements onto the paper substrate.

In our recent study, printed paper sensors based on interdigitated electrodes were utilized to predict the curing behavior of phenol and melamine formaldehyde resin-impregnated paper. Additionally, the feasibility of using printed sensors for crack detection was investigated. The crack detection system aims to identify measurable changes that indicate delamination of the composite structure, typically caused by induced force or impact. To achieve this, a complex sensor structure is required, and the "Hilbert Curve," a rectangular structure with space-filling properties, was chosen as the most effective and straightforward design compared to other options [5]. The Hilbert curve was printed on the paper substrate using silver and carbon inks for crack detection purposes.

2. Materials and Methods

The interdigitated electrode paper sensor and its specifications used in this analysis are shown in Fig. 1. These paper sensors were developed at Wood K Plus, Austria, and had an electrode length and spacing of 300×300 µm.

The DEA measurements were conducted using a dielectric analyzer from Novocontrol Technologies (Germany). A sinusoidal voltage at 10000 Hz was applied between the electrodes to generate an electric field. The electrical properties such as permittivity, conductivity, specific resistance, and loss factor were measured as a function of time at that frequency. Conductivity is calculated from the loss factor, directly related to the ions' mobility and the resin's cure state.

To detect cracks, a specific pattern (shown in Fig. 2) consisting of silver and carbon ink was printed onto a thin paper substrate. Subsequently, the printed sensors were embedded within the composites using the vacuum bag technique. The feasibility of the printed paper sensors was assessed through mechanical tests, including bending and dropping ball tests. The resistance change corresponding to the applied load was measured as an indicator of performance.

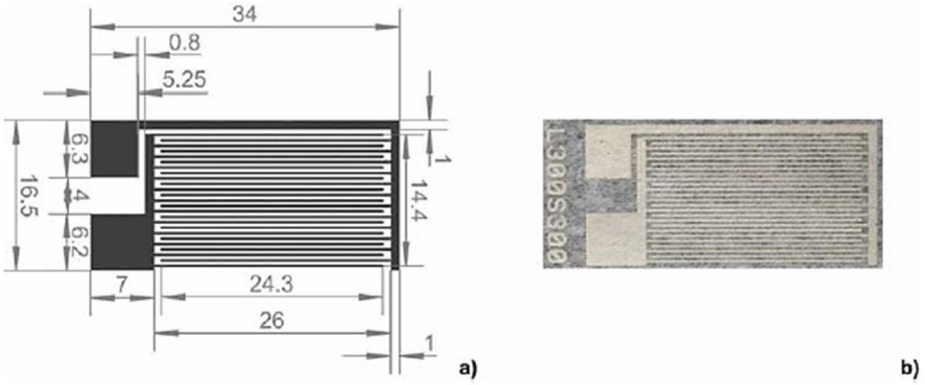

Fig. 1. (a) Sensor design with distances in mm, (b) a silver print of a 300/300 [µm/µm] sensor on paper; Reprinted with the permission of [4].

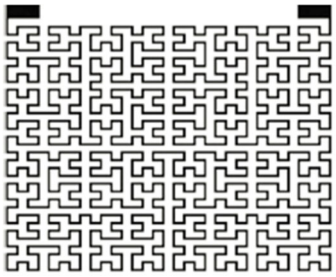

Fig. 2. Space filling Hilber curve pattern on the paper substrate.

3. Results and Discussions

The sensing behavior of the developed paper sensors were compared to commercially available polyimide-based sensors was analyzed. The experiments were done using paper sensors with silver as well as carbon inks and commercial sensors. The results are shown in Fig. 3. It can be observed from Fig. 3a that there are some differences in the maximum conductivities of different sensors, but this difference is attributed to the different initial capacitance of the sensor, which may be different due to the wire connections. To compare the performance of all sensors, the conductivity results were integrated and normalized, as shown in Fig. 3b.

It can be observed that all the sensors including commercial sensor and paper sensors (with silver as well as carbon ink) provides same curing time of resin. In the middle of curing the results are a bit different because of different interaction between resin and substrate as well as ink material. But paper sensors served the purpose by showing the same curing time as commercial ones.

To evaluate the crack detection sensor's performance, compressive and tensile loads were applied. The embedded sensor exhibited a highly favorable response corresponding to the loads applied on the composites as shown in Fig. 4.

Following the dropping ball impact test, certain samples exhibited visible cracks, resulting in a loss of signal. Other samples only displayed changes in resistance values. Fig. 5 illustrates how the damage incurred by the composites led to a loss of connectivity.

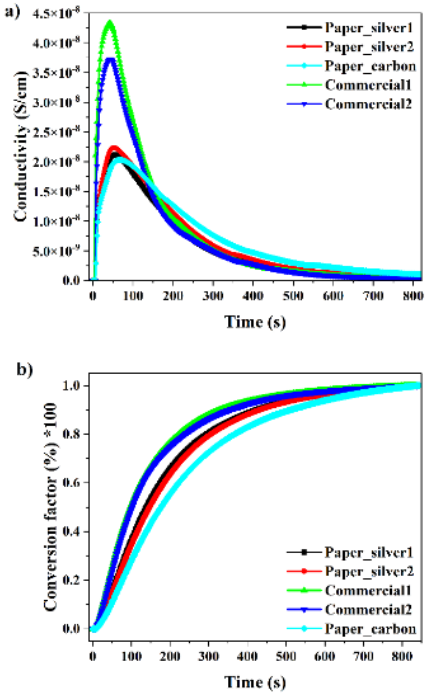

Fig. 3. Dielectric cure monitoring of MF resin-impregnated paper using different sensors: a) Conductivity vs. time, b) Conversion factor vs. time.

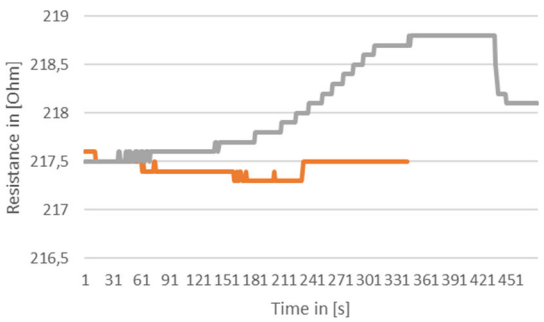

Fig. 4. Change in resistance with respect to type of applied load on the printed crack detecting sensor: (a) Tension- Grey, (b) Compression- Orange.

Fig 5. Microscopic image showcases the composite structure following the drop ball test, exposing the propagation of cracks within the composite material.

4. Conclusions

The cure monitoring application is well suited for the printed paper sensors, which exhibit performances comparable to commercial interdigitated sensors. The initial study indicates the potential of paper sensors for crack detection under impact loading conditions. Notably, the presence of a significant crack resulted in a loss of signal, while minor cracks caused only minimal changes in resistance.

Acknowledgements

This work was supported by the Austrian Research Promotion Agency (FFG) under the project "i^3 Sense". Grant number 888361.

References

[1]. Prashanth, S., Subbaya, K.M., Nithin, K. and Sachhidananda, S. Fiber reinforced composites-a review, *J. Mater. Sci. Eng,* Vol. 6, Issue 3, 2017, pp. 2-6.

[2]. Dhimish, M., Holmes, V., Solar cells micro crack detection technique using state-of-the-art electroluminescence imaging, *Journal of Science: Advanced Materials and Devices,* Vol. 4, Issue 4, 2019, pp. 499-508.

[3]. Fang, F., Li, L., Gu, Y., Zhu, H., Lim, J. H., A novel hybrid approach for crack detection, *Pattern Recognition,* Vol. 107, 2020, pp. 107474.

[4]. T. Stockinger *et al.*, High porous, ultra-thin paper sensors − An option for successful sensor integration, *Sensors Actuators A Phys.*, Vol. 350, 2023, p. 114098.

[5]. Sagan, Hans, Space-filling curves, *Springer*, New York, 1994, pp. 9-30.

(041)

Exploration of Phage Display Peptides as Novel Sensing Materials for Highly Sensitive and Selective Biomimetic Optoelectronic Nose

V. Escobar [1,2], C. Hurot [1], S. Brenet [1], M. El Kazzy [1], N. Scaramozzino [2], R. Mathey [1], A. Buhot [1] and Y. Hou [1]

[1] Grenoble Alpes University, CEA, CNRS, IRIG-SyMMES, 17 Rue des Martyrs, 38000 Grenoble, France
[2] Grenoble Alpes University, CNRS, LIPhy, 38000 Grenoble, France
Tel.: + 33 4 38 78 94 78
E-mail: vanessa.escobar@cea.fr, yanxia.hou-broutin@cea.fr

Summary: The development of a biomimetic electronic nose that can reliably detect and discriminate between Volatile Organic Compounds (VOCs) at a level comparable to biological olfactory system has not yet been achieved and remains a scientific challenge. The present work aims to bridge the gap between the performance of the Surface Plasmon Resonance Imaging (SPRI)-based optoelectronic nose and its biological counterpart by integrating novel sensing materials into a cross-reactive peptide microarray. In particular, novel peptides obtained through phage display were used as selective sensing materials to test VOCs belonging to the BTEX family (Benzene, Toluene, Ethylbenzene, Xylene). Reliable discrimination of VOCs with similar chemical structures, including isomers, was achieved even after three months of initial chip preparation. More than 90 % repeatability was obtained after implementing normalization strategies. We demonstrate that these materials represent a reliable, biomimetic way to sense and differentiate between structurally-similar VOCs.

Keywords: Electronic nose, Volatile organic compounds, Peptide, Phage display, Surface plasmon resonance imaging.

1. Introduction

For decades, biological olfaction has been a source of inspiration for the development of biomimetic systems that can detect and recognize odors through the detection and discrimination of Volatile Organic Compounds (VOCs) [1]. The remarkable capabilities of the mammalian sense of smell were elucidated in 1991 [2]. One of the important conclusions that was drawn is that the majority of olfactory receptors (ORs) act in a combinatorial manner, rather than a specific recognition for odorant molecules. Thus, each aroma is encoded as a distinct "receptor code", making it possible to recognize and discriminate between them. Because of this, a relatively small number of receptors located in the epithelium can detect a quantity of different odors many orders of magnitude higher.

Although the majority of receptors are "generalists" acting in a combinatorial way, there are some "specialist" receptors with a higher degree of selectivity towards certain target molecules [3].

In 2018, our team reported for the first time a highly sensitive and selective opto-electronic nose (opto-eN) based on coupling Surface Plasmon Resonance Imaging (SPRI) and cross-reactive peptide microarrays [4].

The purpose of the present work is to further improve the discriminatory power and limit of detection of our system through the exploration of novel sensing materials taking inspiration from the mechanism of action of the human nose. Herein, we aim to complement the performance of a previously designed array of cross-reactive peptides through the addition of peptides with higher selectivity towards phenyl-containing VOCs belonging to the BTEX family (Benzene, Toluene, Ethylbenzene, Xylene).

For this purpose, novel peptides were obtained through phage display, an *in vitro* technique that exerts selective pressure on the expression of peptides with higher affinity to a target through cycles of high-affinity purification [5] (Fig. 1).

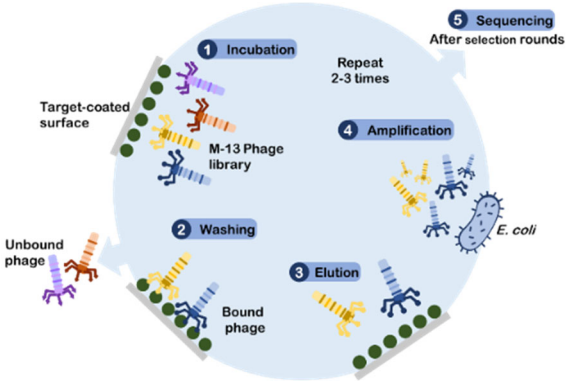

Fig. 1. The five main steps of a phage display experiment.

2. Materials and Methods

Phage Display. For target preparation, gold-coated glass slides were functionalized with aromatic hydrocarbons using thiol-gold chemistry. The Ph.D.™-7 Phage Display Peptide Library (New England Biolabs, Australia) was used according to the protocol provided by the kit. Briefly, the phage library was incubated onto non-functionalized gold plates for a 1 h negative selection. After, the plates were

discarded and the supernatant containing unbound phage was incubated onto functionalized gold plates. After 1h, plates were washed with TBS buffer 10 % Tween-20 10 times, then eluted with Glycine buffer 0.2 M. Bacteriophages were sequenced after four selection rounds. The identified peptides were synthesized and incorporated onto sensor microarray.

Sensor Microarray. 19 biomolecules were chosen as sensing materials, including: an internal negative control (NC) that is known to not be sensitive to VOCs, ten cross-reactive peptides (P1-P10) with different physic-chemical properties (neutral, hydrophobic, hydrophilic, positively and negatively charged) and eight peptides chosen through phage display (P11-P18). Peptides were deposited in quadruplicates onto a gold-coated NBK7 glass prism (Edmund Optics, U.S.) using a noncontact microspotting robot (Scienion AG, Germany) and incubated for 18h to allow for the formation of Self-Assembled Monolayers (SAMs). For confidentiality reasons, the sequences of these peptides are not disclosed herein.

Volatile Organic Compounds. Toluene (99.8 %), m-Xylene (≥ 99 %), p-Xylene (≥ 99 %), o-Xylene (97 %), 1-butanol (99.9 %), 1-hexanol (≥ 99 %), cyclohexane (99.5 %) and methylcyclohexane (≥ 99 %), were purchased from Sigma Aldrich and handled under a fume hood. Samples were mixed into mineral oil to promote gradual evaporation.

Surface Plasmon Resonance Imaging. Our SPRI system is in the Kretschmann configuration, where the gold surface is irradiated through the prism illuminating the whole peptide microarray and variations in reflectivity are captured and measured by a CCD camera. A fluid bench composed of a reference line of dry purified air, and a VOC analyte line, each controlled by a mass-flow controller (El-Flow, Bronkhost) and a pressure controller (El-Press, Bronkhorst), is used for controlled sample injections.

3. Results

Sensor response to different VOCs. Sensorgrams are obtained by plotting Δ%R versus time for VOC injections. At the equilibrium plateau, replicate responses are averaged and a distinct equilibrium pattern is obtained for each VOC. Then, the response is normalized using the following equation:

$$R_{norm} = \frac{\Delta\%R * \sqrt{N}}{\sqrt{\sum_{n=1}^{N} \Delta\%R^2}}, \quad (1)$$

where N is the number of analyzed species.

Principal Component Analysis (PCA). Once normalized, the multidimensional data set is fitted onto a 2D plane using PCA. Fig. 2 shows PCA score plots demonstrating that cross-reactive peptides are not fully able to discriminate in between aromatic ring-containing VOCs (Fig. 2a), contrarily to peptides obtained by phage display (Fig. 2b), which achieve better discrimination even when using less sensors. Thus, it is clearly demonstrated that the introduction of novel peptides on the chip improves the performance of our optoelectronic nose.

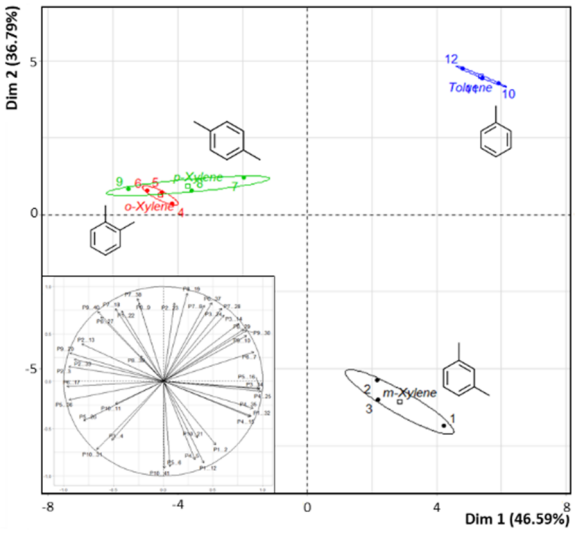

(a)

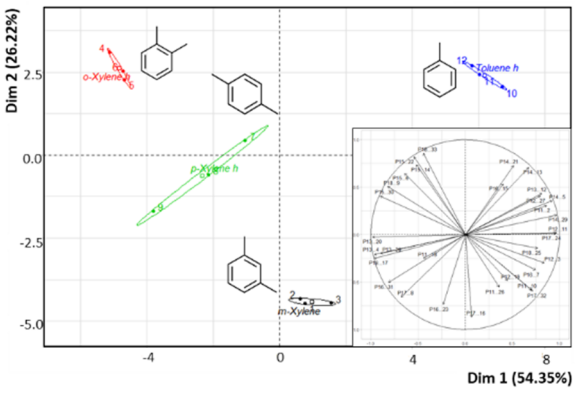

(b)

Fig. 2. PCA score plots for Xylenes and Toluene using a) cross-reactive peptides (P1-P10) and b) phage display peptides (P11-P18). Inset: PCA graphs of variables.

4. Conclusions

In the present work, we demonstrate the excellent discriminatory capabilities of novel materials for the detection and discrimination of VOCs in the BTEX family. Thus, for the first time, we demonstrate the feasibility of coupling highly selective "specialist" peptides with a cross-reactive array of "generalist" peptides to further mimic the mechanism of action of the biological sense of smell and improve the performance of the optoelectronic nose.

References

[1]. M. El Kazzy, et al., An Overview of Artificial Olfaction Systems with a Focus on Surface Plasmon Resonance for the Analysis of Volatile Organic Compounds, *Biosensors*, Vol. 11, Issue 8, 2021, 244.

[2]. L. Buck, R. Axel, A novel multigene family may encode odorant receptors: a molecular basis for odor recognition, *Cell*, Vol. 65, Issue 1, 1991, pp. 175-187.

[3]. J. Bohbot, J. Dickens, Selectivity of odorant receptors in insects, *Frontiers in Cellular Neuroscience*, Vol. 6, 2012.

[4]. S. Brenet, et al., Highly-Selective Optoelectronic Nose Based on Surface Plasmon Resonance Imaging for Sensing Volatile Organic Compounds, *Anal. Chem.*, Vol. 90, Issue 16, August 2018, pp. 9879-9887.

[5]. G. P. Smith, V. A. Petrenko, Phage Display, *Chem. Rev.*, Vol. 97, Issue 2, April 1997, pp. 391-410.

(042)

Calibration of a Hail-Impact Sensor based on Piezoelectric Transducers

F. Blasina, A. Echarri and N. Pérez
Facultad de Ingeniería, Universidad de la República, Julio Herrera y Reissig 565, Montevideo, Uruguay
E-mail: fblasina@fing.edu.uy

Summary: Hail is a climatic phenomenon that poses numerous measurement challenges, hindering the advancement of hail casting compared to other meteorological phenomena. Reliable hail sensors benefit society because, though sporadic, hailstorms are highly damaging, endangering both lives and goods that matter for societal well-being. In recent years, automatic solutions have emerged as viable options, some of which utilize piezoelectric elements. A comprehensive understanding of these sensors, their potential for improvement, and their limitations is vital for informed technology adoption and enhancement. This work presents our studies on the design process and calibration of a hail sensor, examining the outreach of an instrument based on acoustic waves generated by impacts on an exposed structure. Consequently, we developed a disk-shaped hail sensor equipped with two piezoelectric transducers for determining impact energy. We believe that this work contributes to a better understanding of the operation of hail sensors based on acoustic impacts.

Keywords: Acoustic, Automatic, Calibration, Design, Hail, Piezoelectric.

1. Introduction

Automatic hail measurement provides the opportunity to catch up in hail casting capabilities, currently relegated. This work presents the design of an electroacoustic automatic hail sensor that measures impact energy, the hail frequency and registers the beginning and end of events. To record the hail impacts, the sensor uses piezoelectric transducers integrated into a plate that is deliberately placed in exposition to the elements.

Hailstorms are spatiotemporally restricted but intense. The impact energy during the hail events yields a considerable loss of material goods [1, 2]. There are reasonable hypotheses for modeling hailstones: they are taken as homogeneous ice spheres that reach terminal velocity before impact [3].

The classical hail measurement device, the *hailpad,* is a square of foamy material covered with an aluminum sheet, where hailstones leave dents [4]. *Hailpads* are of single-use and must be collected and analyzed after a hailstorm. They do not permit any temporal analysis.

Automatic recording devices have been developed for long time, but those using acoustic signal processing are state of the art. Acoustoelectric hail sensors rely on the impact of hailstones against a mechanical embodiment that is exposed to the storm. As a consequence of each impact, waves are generated within the embodiment, which is called an acoustical cavity. The waves are converted to electrical signals by means of transducers, for which piezoelectric diaphragms are an excellent choice: when a strain is applied on them, they generate a voltage signal.

2. Sensor Design

We designed a hail sensor prototype focusing in the acoustical cavity characteristics for estimating the energy of the impacts regardless the point on the plate where the hits occur (Fig. 1). There are crucial considerations to take, such as material, shape, size, disposition of the piezoelectric transducers, and holding of the instrument.

The experience of prospective experimentation showed us that simple shapes make it easier to model the behavior of the signals. At first, we considered that signals with a richer frequency spectrum would contain more information regarding the energy of the impact, so we experimented with shapes and materials that favored multiple incidences of the waves on the borders of the plate before reaching the transducer, such as steel and aluminum squares and non-regular geometrical shapes. After careful analysis of the obtained signals, the conclusion was that the waves with fewer incidences on the borders are good enough as to estimate the energy, whereas having shorter signals (Fig. 2) is an advantage to separate the signals from different impacts that are close in time. Particularly, the central symmetry of a circle helps to decide where to situate the piezoelectric elements. Therefore, the shape of our sensor embodiment is a 25 cm-diameter disk.

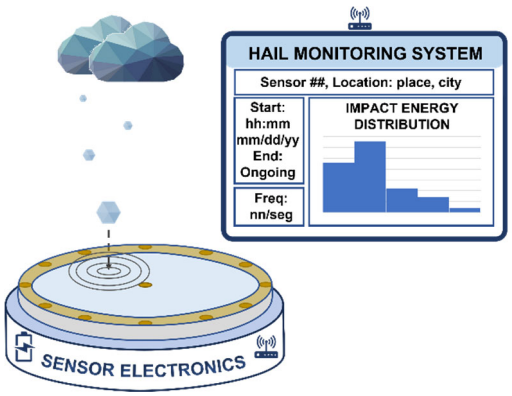

Fig. 1. Left: Hail sensor we designed. Right: Monitoring interface that uses the information yielded by the hail sensor.

Some solutions that have recently appeared commercially, such as *Hailflow HF-4*[1] *(ISAW Products), Hailsens IOT*[2] *(Hyquest Solutions)*, and *Hail Sensor HDI*[3] *(Sommer)* do also use disks as resonant cavities. Within the academic references, more complex shapes such as octagonal plates [5] and tridimensional objects [6] were preferred.

The material of our sensor is acrylic, which has enough weather [7] and impact resistance when the disk is sufficiently thick, to fulfill the requirement of a lifespan for many years. This material is highly standardized in composition, affordable, and easy to work with. The piezoelectric diaphragms can be easily embedded, obtaining a waterproof design. We constructed a device that is a total of 1.4 cm thick, where the upper layer is 1 cm thick and two thin layers contain and protect the transducers. The damping of this material attenuates a typical signal in less than 20 ms, allowing us discern up to 50 impacts per second. Metals such as aluminum and steel were discarded due to lower damping.

The acrylic plate is fixed with its whole bottom face resting on a base, with a homogeneous foam that isolates the mechanical waves produced by the impacts from other hard volumes. We considered using punctual supports such as in a table, but this provokes an undesired variety of vibration modes depending on the position of the impact concerning the stands. Having equal support for the whole face is the way of having the simplest model for the waves' behavior.

The principal transducer of the sensor is a single *Murata 7BB-12-9*[4] piezoelectric placed at the center of the plate. We use the signals generated by this transducer to measure impact frequency and estimate impact energy.

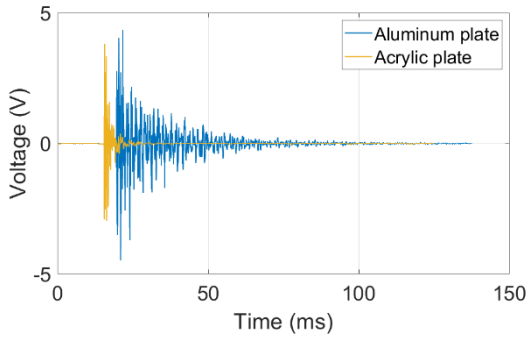

Fig. 2. Comparison of signals obtained when using aluminum and acrylic as materials for the plate. When using acrylic, the signal is much shorter, which favors distinguishing impacts that occur close in time.

We noticed the importance of considering the attenuation of the signals that reach the transducer for impacts of equal energy but at different distances of the transducer, which can affect the result by up to 90%. Therefore, we included an auxiliary transducer, that is a piezoelectric ring situated at the edge of the plate, which is used only to determine the distance of interest by means of the difference of times of flight between transducers and compensate for the damping.

3. Mathematical Models

The relationship between the energy of the acquired signals and the impact energy is given by:

$$E_{impact} = G_{EE} E^{c}_{signal} / A(d), \qquad (1)$$

where E_{impact} is the quantity of interest, E^{c}_{signal} is the energy of the signal generated by the impact of a stone when hits the center of the plate, and d is the distance between the actual point of impact and the center of the plate. The constant G_{EE} takes electric energy into impact energy for the constructed device, considering its electric circuitry and must be calibrated. The function $A(d)$ models the wave attenuation:

$$A(d) = \alpha + (1 - \alpha) e^{-\beta d}, \qquad (2)$$

where α and β are parameters that must be calibrated. For automatically recognizing the distance d, we use the difference of times of flight, Δt, of the waves to the border and the center of the disk. Modeling the central piezoelectric as a punctual element and the auxiliary piezoelectric as a narrow ring at the edge of the plate, the relationship is

$$\begin{cases} d = \gamma - \delta \Delta t \\ \Delta t = t^{Border}_{Flight} - t^{Center}_{Flight}, \end{cases} \qquad (3)$$

where γ is a parameter that should be approximately half of the radius of the plate, and δ is a calibrated parameter since the speed of propagation of the waves on the material is nontrivial. The absolute times of flight from the point of the impact to the border, t^{Border}_{Flight}, and to the center, t^{Center}_{Flight}, are unknown, but their difference can be computed by using cross-correlation or custom signal-processing techniques.

4. Calibration

We performed the calibration by dropping steel balls that impact with known energy. In this stage, we considered the bounce energy employing high-speed camera videos, to accurately estimate the amount transferred to the plate. The method of dropping steel balls, usually referred as *Energy Matching*, is of regular use in hail-sensor calibration [8].

[1] isaw-products.com/rainflow-rf4/
[2] hyquestsolutions.com.au/products/hardware/meteorology/hailsens-iot-hail-monitoring-system
[3] sommer.at/en/products/wind-weather/hail-sensor-hdi
[4] murata.com/en-global/products/productdetail?partno=7BB-12-9

To control the impacts, we designed and constructed a device we named *SGran* [9]. One advantage of this device is that it lets us perform up to seven identical impacts in a row, remotely commanding the device from a user interface. The device uses electromagnets to drop the steel balls with null initial velocity, achieving an excellent impact-point and impact-energy repetitiveness, which is crucial for calibrating (1) – (3).

A detailed work on the calibration process has been submitted for revision at this moment. The values of the calibrated parameters are in Table 1, whereas the obtained curves are shown in Figs. 3 - 5.

4. Conclusions

We designed and constructed an acoustoelectric sensor prototype that automatically estimates the impact energy of projectiles. The transducers we used are piezoelectric diaphragms.

Table 1. Values of the calibrated parameters.

Parameter	Value	Unit
G_{EE}	5.70	Dimensionless
α	0.0237	Dimensionless
β	0.0368	mm^{-1}
γ	44.9	mm
δ	149	mm/ms

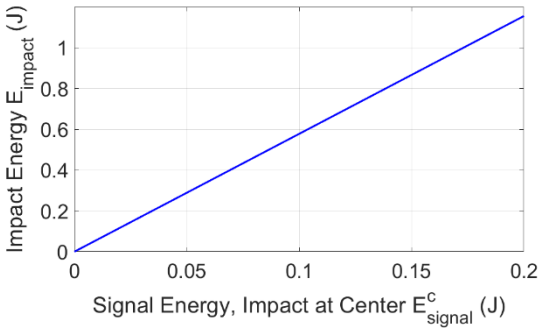

Fig. 3. Calibration curve. Estimated impact energy for a given signal energy, when the impact occurs at the center of the plate. Corresponds to (1) when $d = 0$.

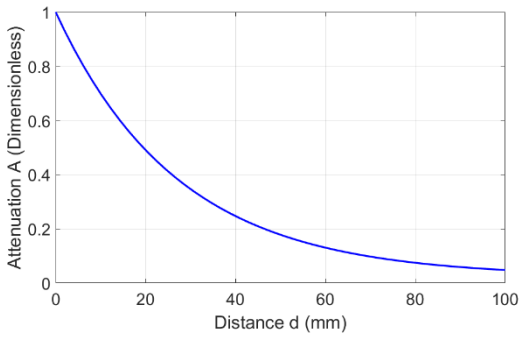

Fig. 4. Calibration curve. Signal attenuation factor regarding distance of the impact point to the center of the plate. Corresponds to (2).

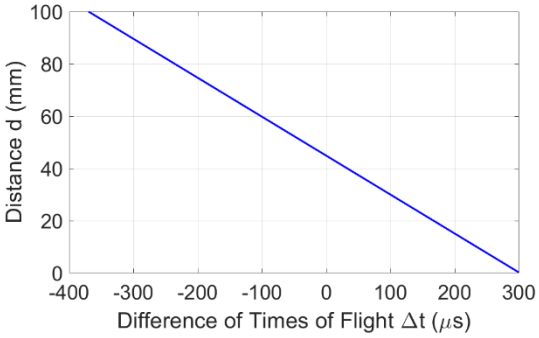

Fig. 5. Calibration curve. Distance of the impact point to the center the plate, estimated using the difference of times of flight of the generated wave from the impact point to each of the transducers. Corresponds to (3).

We observed that using a disk for the shape of the acoustical cavity of the sensor has advantages regarding simplicity in signal processing.

Since having shorter signals facilitates the distinction of impacts that occur close in time, we chose acrylic as the material for the disk.

We present the basics of the calibration process and the obtained curves, and explain the considerations for a reliable estimator.

While calibrating, we recorded high-speed camera videos that showed that the error introduced by not considering the bounce of the projectile is insignificant in most of the cases.

References

[1]. T Marshall and S Morrison, Hail damage to built-up roofing, in *Proceedings of the 22nd Conference on Severe Local Storms*, 2004, P9.3.

[2]. Yaojie Yue, Lan Zhou, A-xing Zhu, and Xinyue Ye, Vulnerability of cotton subjected to hail damage. *PLOS One*, 14, 1, 2019, pp. 1–21.

[3]. R. Schleusener and P. Jennings. An energy method for relative estimates of hail intensity, *Bulletin of the American Meteorological Society*, 41, 7, 1960, pp. 372–376.

[4]. A. Long et al., The hailpad: construction and materials, data reduction, and calibration, *Citeseer*, 1979.

[5]. M. Löffler-Mang, D. Schön, et al. Characteristics of a new Automatic Hail Recorder, *Atmospheric Research*, Vol. 100, No. 4, 2011, pp. 439–446.

[6]. J. Lane, R. Youngquist, et al. A Hail Size Distribution Impact Transducer, *The Journal of the Acoustical Society of America*, Vol. 119, No. 3, 2006, pp. 47–53.

[7]. L. McKeen, The Effect of UV Light and Weather on Plastics and Elastomers, 3rd ed. *William Andrew*, 2019.

[8]. D. Vento, The Hailpad Calibration for Italian Hail Damage Documentation, *Journal of Applied Meteorology*, Vol. 15, 1976, pp. 1018–1022.

[9]. F. Blasina, A. Echarri, N. Pérez, et al., Implementation and Evaluation of a Hail-impact Simulation Device, *Memoria Investigaciones en Ingeniería*, No. 23, 2022, pp. 135–150.

(045)

Terahertz Sensor System with Dual Mode Operation

Janez Trontelj, Andrej Švigelj, Domen Višnar and Janez Trontelj jr.
Faculty of Electrical Engineering, University of Ljubljana, Trzaska 25, 1000 Ljubljana, Slovenia
E-mail: janez.trontelj1@guest.arnes.si

Summary: New THz applications are emerging fast into our everyday life. Due to its ability to penetrate harmlessly through many media, for instance through textile which not transparent to light, but also the Styrofoam which is a perfect thermal insulator and not transparent to visible light, it is perfectly transparent to THz spectrum. Most of applications rely on measurements and analysis of THz spectrum.

There are two types of THz measurements set-ups. A time domain set- up TDS and Frequency Domain System, FDS The TDS is a more mature measurement, typically the results are more accurate, but the at the cost of more expensive measurements set up and is more time consuming. It is normally performed on optical tables and is not portable. The FDS is on the contrary based on solid state technology, the measurement equipment cost is much lower, and is capable to perform measurement on the spot.

Keywords: THz sensor, THz detection, Compact THz system, Portable THz system.

1, Introduction

We propose a compact THz sensor system, that is capable to operate in both tine-domain and frequency domain modes. It consists of an array of single sensors with equal or properties or of different ones, but providing a separate output for each sensor. This allows grouping the sensor area to patches, detecting the THz spectrum of bio-response of reflecting THz from the sample in vivo, or the transmitting signal in vitro.

The sensor system is compact, and is connected to laptop by USB for providing the power and simultaneously signal transferring. It also includes signal input for synchronization possibility and square signal output with selectable frequency.

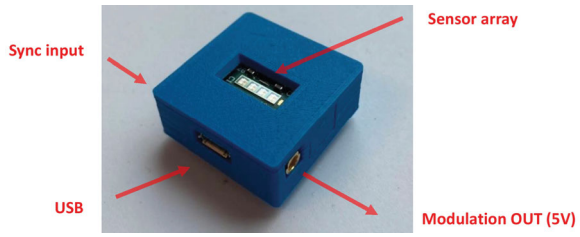

Fig. 1. Photo of compact THz detection system.

The sensor system processes each pixel individually and therefore it can be used both in time domain and in frequency domain. It can also be used as a THz spectrometer when a narrow band pixel is used with different central THz frequency in the array. This means, that when illuminated with the THz source with a wide band spectrum, the different pixel is responding differently according the received spectral frequency. Such spectrometer is an enormous advantage over typical TDS systems, which can be time consuming, clumsy, and inadequate set-up. It works well for food quality control on running industrial conveyor belts to detect THz spectral response of unhealthy food.

The detection system is a compact size of 30×30×12 mm, easy to use, and simple to program for detection the anomaly in the THz spectra.

2. Hardware

The main objective of the hardware optimization is the possibility to use it at an affordable cost so it can be used in mass production for different applications such as industrial quality control. Fig. 2 presents a general block diagram of the detection system.

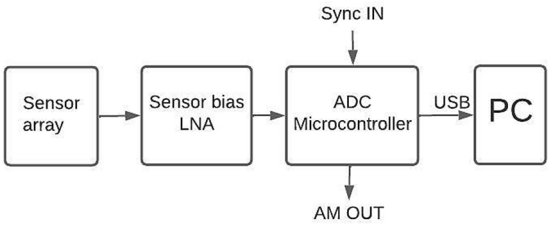

Fig. 2. Block diagram of the detection system.

Sensors are developed and produced in LMFE.

They are grouped in to an array of four sensors with fixed position and sensor types. The sensors are antenna-coupled microbolometer type.

The developed antenna can be narrow frequency band to be used as band-pass filters for selectively chosen for different applications [1]. We have developed and produced the 0.1 THz, 0.3 THz and 0.6 THz narrow band antennas. In addition, we have developed broadband antennas with the frequency band from 100 GHz to 1 THz with reasonably flat response. It turned out that the response of this antenna is acceptable also over several THz range. The photo of the antennas is shown on Fig. 3. The energy

absorbed by the antennas is released on the intermediate microbolometer element which results in its temperature change and its resistance accordingly. [2, 3] The computer simulation of the microbolometer temperature is shown o Fig. 4.

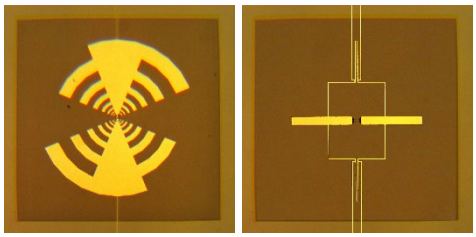

Fig. 3. Photo of broadband and narrow band antenna.

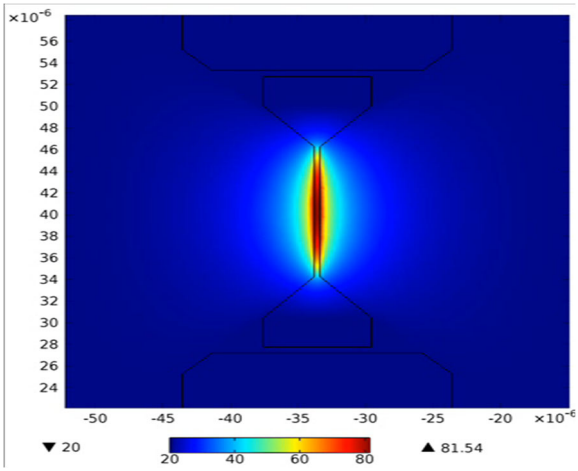

Fig. 4. Thermal simulation of LMFE microbolometer.

The low noise amplifier was designed and fabricated in 0.35 um analog process of TSMC. The layout was combining four LNAs with connections optimized for connections to the sensors as shown on Fig. 5.

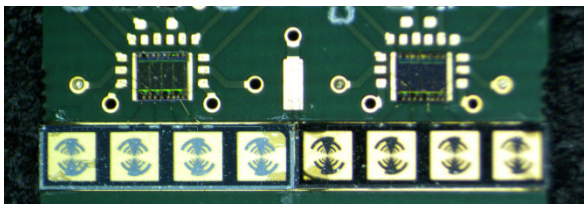

Fig. 5. Photo of sensor line and integrated LNA.

The amplifiers gain can be set to 1000, 500 or 250 by single control signal. The IC also includes sensor bias circuit. The bias current can be selected between values of 150 uA, 200 uA and 250 uA. Fig. 6- shows noise levels of the analog part of the system. 1/f noise is clearly dominant below 1 kHz frequency. Above 1 kHz the noise levels drop below 22 Nv/√Hz as here on the thermal noise of the circuit is the only main contributor.

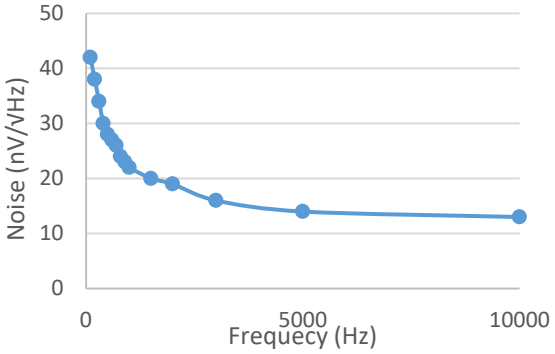

Fig. 6. Measured results of LNA noise including the sensors.

3. Digital Part

All the signals are processed by digital signal processing. The requirements for the analog to digital conversion are 16-bit resolution and sampling rate of up to 200 k samples per second. The sampling rate is limited by the USB transfer rate. The upper limit of THz modulation frequency is defined by the number of sensors. Which is 12.5 kHz for 8 and 25 kHz for 4 sensor system.

Integrated microcontroller also detects trigger input signal and starts the AD conversion of predefined number of samples. It also generates the signal for THz source modulation. The frequency range is programmable from 1 Hz up to 10 kHz.

4. Time Domain Setup

The setup is presented on Fig. 7. It consists of THz source on the left and the proposed THz sensor system on the right with four THz sensors

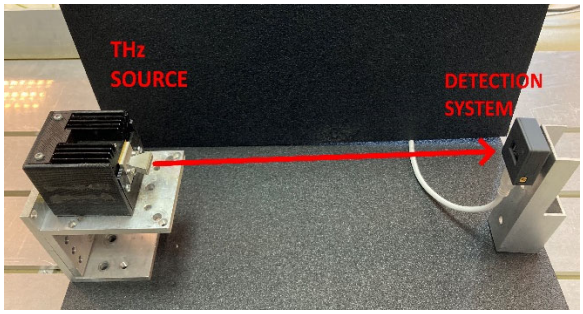

Fig. 7. Time domain setup layout.

Graph shown in Fig. 8 presents signals obtained from the setup in time domain configuration. Each color represents output of each THz sensor. The amplitude difference is due to non-uniform THz beam. The upper graph presents signals in time domain and the lower shows its FFT.

Fig. 8. AM signals from 4 sensors in time-domain configuration with corresponding FFT.

Time domain setup allows instantaneous overview of the measurement scene. It can be used in both transmission and reflection mode.

5. Frequency Domain Setup

In frequency domain setup the THz source needs to be frequency modulated. The frequency ramp is linear with the span of 40 GHz and sweep time 50 ms. A half transparent beam splitter reflects half of the signal directly to sensors. The other half is proceeded to the mirror which reflects with 100 % reflection. The Frequency domain setup is shown on Fig. 9.

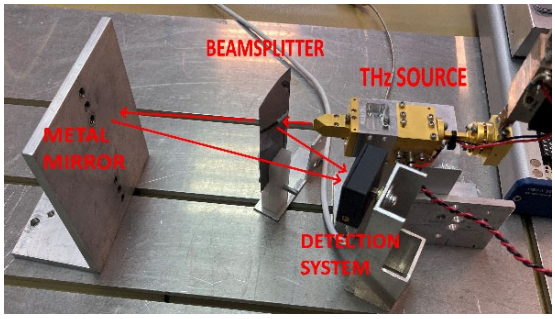

Fig. 9. Frequency domain setup layout.

This means that the sensor received a delayed signal caused by the doubled distance between beam splitter and mirror. Fig. 10 shows signals on the sensor.

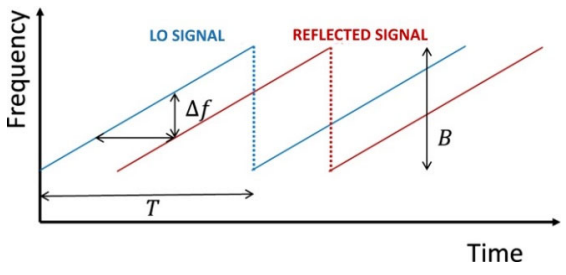

Fig. 10. Signals present on the sensor in time.

Ramp graph is shown in Fig. 4 including the transmitting and receiving signal. The distance D of the mirror can be calculated using Eq. (1).

$$D = \frac{c_0|\Delta f|}{2(\frac{df}{dt})} \quad (1)$$

In Fig. 11 the FFT result of frequency domain setup is shown. Frequency on the graph is directly proportional to the metal mirror distance from the source, although reduced for the for the distance of the beam which is reflected from the beam splitter.

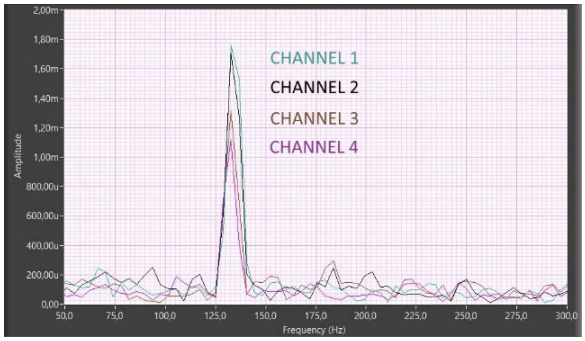

Fig. 11. Graph showing FFT of frequency domain setup result.

Fig. 12 presents measurement results of frequency at different positions of the mirror.

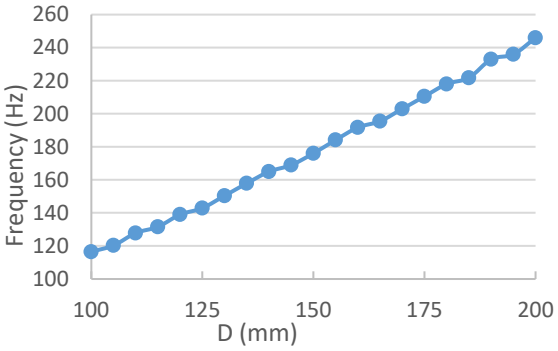

Fig. 12. Frequency results vs distance.

6. Conclusion

The proposed sensor system has some unique functions and is intendent to be used in many applications:

1. Research of new applications is much more user friendly and opens the possibility to large number of scientists, having a limited budget for expensive equipment.
2. Fast diagnosis of both in vitro or in vivo tissue for different irregularity.
3. Detection of voids, foreign objects in products invisible for naked eye or visual spectroscopy.
4. Detection of irregularity of food products vacuum packaged, so no smell detector can't be used.

5. Detection of contents in the pockets of the garments brought to dry cleaning facilities.

And more.....

References

[1]. J. Grade, P. Haydon, D. Van der Weide, Electronics Terahertz Antennas and Probes for Spectroscopic Detection and Diagnostics, *Journal of Applied Physics* Vol. 125, Issue 15, April 2019, 151602,

[2]. J. Lloyd-Hughes, G. Scalari, A. van Kolck, M. Fischer, M. Beck, J. Faist, *Optics Express*, Vol. 17, Issue 20, 2009, pp. 18387-18393.

[3]. K. Hirakawa, Y. Zhang, B. Qiu, T. Niu, R. Kondo, N. Nagai, K. Kuroyama, Fast and sensitive bolometric terahertz detection at room temperature through thermomechanical transduction, in *Proceedings of the 44th International Conference on Infrared and Millimeter and Terahertz Waves (IRMMW-THz'19)*, Paris, 1-6 Sept. 2019, pp. 1-3.

(047)

Physiological Assistance by Climate Comfort: Measurements and Indicators

Bernhard Kurz [1] and Christoph Russ [2]
[1] Institute for Applied Ergonomics, Siedlerstr. 1, 85716 Unterschleissheim, Germany
[2] InsideClimate GmbH, Hilpoltsteinerstr. 1b, 83607 Holzkirchen, Germany
[1] Tel.: + 49 89 62489595, Fax: + 49 89 662065
E-mail: be.kurz@ifaerg.de

Summary: With regard to performance and motivation to perform, in addition to adapted work intensities and social aspects, the environmental conditions (noise, light, climate) in particular must be adapted to the human physiological requirements. At this the ambient climate resp. the resulting microclimate depending on work load, clothing etc. plays the central role, especially in view of increasing global temperatures. These facts underline the importane of skin microclimate as a comfort or discomfort indicator as well as its preventive diagnostics for emerging critical health conditions such as dehydration or hyperthermia. Initially, the measurement of microclimate factors and the determination of suitable comfort indicators under real wearing or working situations represent a particular challenge. For complete physiological assistance with the aim of minimizing the basic physical load (reactive power), heart rate, core body temperature and skin resistance, for example, must also be recorded, preferably by means of textile resp. smart sensors. A disadvantage of climate measurements with test persons is the inter- and intraindividual scattering, which only can be compensated by thermophysiological simulation methods, based on a reproducible and standardized heat and humidity source. So the assessment of the degree of discomfort as well as unhealthy work conditions can be evaluated objectively.

Keywords: climate comfort, physiological assistance, comfort assessment, microclimate measurement

1. Introduction

The requirements addressed on modern work, protective and sports clothing or even on seating and lying systems have changed fundamentally in recent decades. So multifunctionalities are expected of todays clothing systems, which not only fulfill the primary purpose of, for example protection against chemical, mechanical or thermal influences, but also for skin-sensory or haptic benefits, as well as hygiene and cleaning demands or biomechanical requirements with regard to a best fit (see Fig. 1).

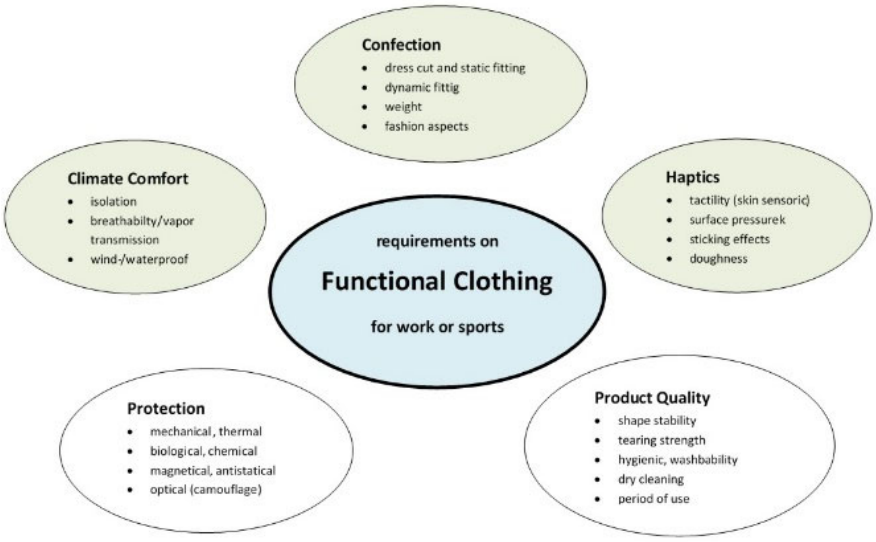

Fig.1. Ergonomic requirements for clothing (green areas with comfort relevance)

2. Climate Comfort and Discomfort

Additionally to the requirement-related functionalities comfort aspects have to be regarded, which can be roughly divided into the two areas of biomechanical and climatic comfort. Furthermore both comfort sectors show strong interactions and mutual influences with corresponding physiological consequences. For example, a poor shoe fit will produce skin irritation and blisters and, in conjunction

with a warm and damp shoe climate, this effects will even be accelerated, because the mechanical properties of the skin are adversely affected (maceration). In addition, it is known that in the first phases of use of clothing components or of sitting and lying systems, the biomechanical conditions initially determine the wearing comfort or, better, the discomfort. But after some time, the climatic factors arise and can sometimes even take on the dominant role. In view of the demand that comfort is ultimately determined by no unpleasant sensations [3, 7], it is also clear that regional discomforts have a decisive influence on the global situation and will directly influence the physical and mental performance as well as the motivation to perform.

In combination with ergonomic and skin-sensory aspects, such as sweat-related adhesive effects or wet spots, climate comfort plays a central role, since the global thermophysiological requirements are only fulfilled by a balanced heat management [2, 4, 9]. This includes a targeted design of the heat transfer, the breathability and the moisture transportation of the textile layers in order to achieve a pleasant local microclimate (see Fig. 2).

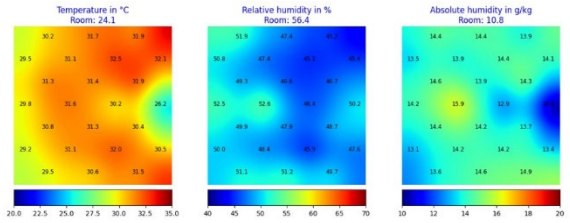

Fig. 2. Heat and humidity profile of a test person on an office chair.

Regarding the partly dramatic changes of the work situations with increasing temperatures (global temperature change) and their physiological consequences the importance of climate comfort will increase in future.

3. Physiological Assistance

In the construction and design as well as assessment of the climaphysiological functions of clothing or body support systems, and incidentally also for actuators and control elements, a multi-stage analysis process is required, i.e.

- Determination of (bio-)physical parameters for the evaluation of thermoregulatory properties (balanced heat management),
- Quantification of the comfort-determining microclimate as a (human-)physiological criterion by standardized testing methodology,
- Use of validated prediction models for comfort prognosis,
- Selected supplementary validation by tests with test persons.

After numerous investigations by a wide variety of industrial and public institutions [1, 6, 8], the skin microclimate is the decisive multi-dimensional indicator for assessing the thermoregulatory function and, in particular, the climatic and ergonomic wearing comfort. This is confirmed in numerous studies with shoes, gloves, clothing or seating and lying systems [5, 10] by the destincted physiological sensitivity for temperature and humidity perception with high correlation to the measured variables temperature and absolute humidity. From this, the approved limits for thermal neutrality of 35 °C and 25 g/kg can be derived, characterized by a balanced heat and sweat control with periodic thermoregulative activities (see Fig. 3). In contrast, increased heat dissipation as well as insufficient cooling effect are recognizable by additional physiological reactions with increased energy expenditure for heat production, sweating and vasodilation/constriction. This “reactive” power, which is useless for the work process, must be minimized in the sense of physiological assistance in order to counteract

- the kidney function impairment due to increased sweating and the resulting loss of electrolytes with subsequent interference of muscle functions, and
- the cardiovascular stress due to increased pump rate.

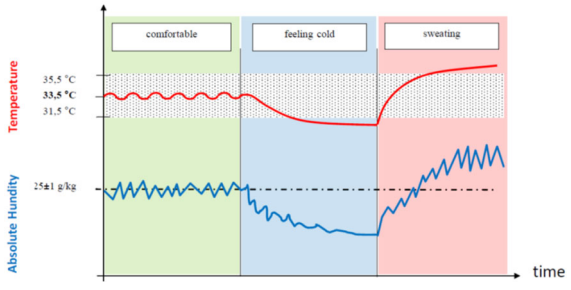

Fig. 3. Thermoregulative phases.

Finally, these facts underline the importance of skin microclimate as a comfort or discomfort indicator as well as its preventive diagnostics for emerging critical health conditions such as dehydration or hyperthermia, especially with the help of additional physiology parameters such as core temperature, skin resistance and heart rate e.g. by means of smart textiles.

3.1. Microclimate Measurement

In addition to a suitable, miniaturized and nearly non-retroactive sensor technology, a key aspect of microclimate measurement close to the skin is the detection of its distribution by means of sensor arrays. Automated cluster analyses are used to determine area-specific parameters without being dependent on a single sensor position or sensor orientation. The SweatLog measurement system offers sensor mats (see Fig. 4) for use on surfaces such as seats or mattresses, as well as sensor grids for clothing analyses, for example with shoes, jackets or headwear.

Fig. 4. SweatLog sensor array as sensor mat.

Fig. 4 shows the results of a proband test with 2 different safety vests, one (blue bars) with PCM (phase change material) the other without (red bars). The tests have been conducted in various room temperatures (25°, 30° und 35° C) on a bike ergometer adjusted to 80 W physical load. The results confirm the cooling effect of the PCM material with its physiological consequence on the resulting heart rate, at least increasing over the lactate threshold (resting pulse plus 40) wearing the vest without the cooling technology.

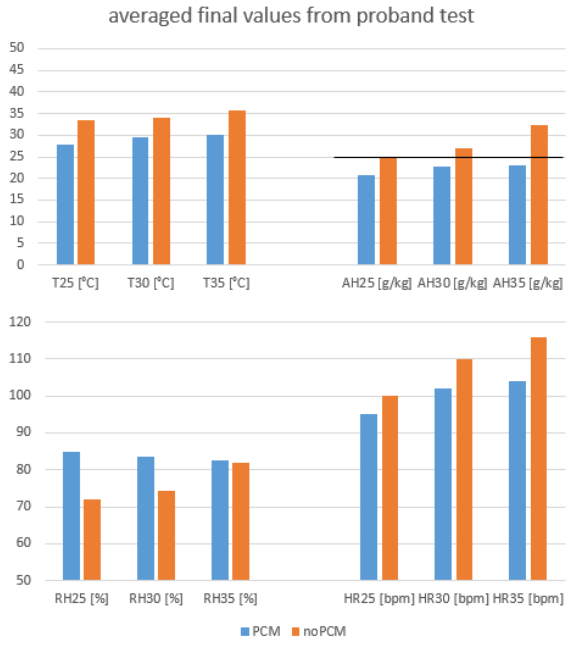

Fig. 5. Safety vests: microclimate (Temperature T, absolute (AH) resp. relative humidity (RH)) and heart rate (HR) from proband test in different ambient temperatures (25°, 30°, 35°C).

Thus, the assessment of the thermoregulatory situation can be derived from the obvious relationships between

- Objective physiological reactions (dehydration, rise in core temperature, heat exhaustion);
- Subjective comfort perceptions (hot spots, wet spots, clothing stickiness);
- And the correlating microclimate parameters temperature and absolute humidity.

3.2. Standardized Heat and Sweat Source

A disadvantage of measurements with test persons is the not inconsiderable inter- and intraindividual scattering, which requires many test persons for reproducible and statistically reliable statements. With the help of thermophysiological simulation methods, which are used as a reproducible and standardized heat and humidity source [11], the assessment of the degree of discomfort can be achieved also from the measurement of temperature and absolute humidity of the simulated microclimate.

According to the best possible replication of the physiological human evaporation and the combination of heat and humidity emissions the SWEATOR technology has been developed [4]. This technology is based on a water-filled, heat controlled hollow body with a special water vapor permeable membrane coating. The test specimens can be manufactured in different shapes (see Fig. 6), with different permeable membranes and without or with different surface perforations. The heating and water circulation are controlled by a touch screen control unit. In the boundary layer between SWEATOR surface and material probe the microclimate distribution is measured with a SweatLog sensors array (see Chapter 3.1). The test trials take place under climatically defined room conditions including additional convections, if necessary. The SWEATOR technology thus enables realistic test conditions and non-destructive testing options with ready-made products.

Fig. 6. SWEATOR torso with test jacket, SWEATOR foot and SWEATOR head with safety helmet.

Fig. 7 shows the results of simulation tests with the SWEATOR head in various protective caps. The differences in the type of textile layer used and in the perforation of the protective cap are assigned as follows:

- REF: Cotton/Jersey textile, no impact protection
- Blue: identical to REF but with perforated plastic (ABS) shield
- Black: identical to REF with non-perforated ABS shield.

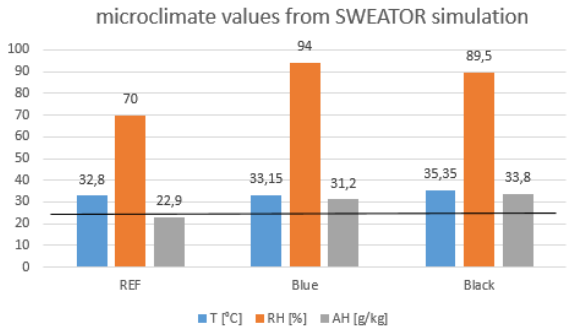

Fig. 7. Bump caps: microclimate (Temperature T, absolute (AH), relative humidity (RH)) from SWEATOR test under 21°C ambient temperature

The effect of the impact shield (ABS plastic) is clearly recognizable for Blue as well as Black with higher temperatures and higher humidities compared to the reference cap (REF). The perforation of the ABS shield (Blue) results in more convenient microclimate than with the Black cap, but still in the discomfort range because of a high microclimate temperature in the case of Black and increased absolute humidity in the case of Blue and Black. Compared to any proband test, such simulation methods are a cost-efficient, highly reproducible and meaningful alternative.

4. Conclusions

Climatic comfort involves physiological relevance and influences performance and motivation to perform and has to be differed into global and regional comfort as well discomfort perceptions. In order to achieve a balanced heat and moisture management the thermoregulative reactive power must be thermoregulate minimized resp. avoided due to cardiovascular stress or kidney function impairments.

Comfort perception, especially in clothing components or on seating/lying surfaces, can be quantified at a high correlation level by measuring the temperature and absolute humidity in the skin microclimate, measured as climate distribution by several sensors resp. sensor arrays (SweatLog system).

To compensate the inter- and intraindividual influences on the appearing microclimate any simulation processes like the SWEATOR technology are preferable, but must ensure a thermophysiologically adjustment and a highly reproducible and, of course, an easy handling.

Selected research projects in the fields of work clothing components (bump helmets, protection vests e.a.) emphasize the applicability of required climate measurement as well as climate simulation technology. The result confirm the informative value of microclimate indicators on comfort or discomfort perception and, maybe much more important, on critical physiological situations.

References

[1]. Y. Epstein, D. S. Moran, Thermal Comfort and Heat Stress Idices, *Industrial Health*, 44, 2006, pp. 388-398.

[2]. R. F. Goldman, B. Kampmann, *Handbook on Clothing 2nd ed., in Proceedings of the International Conference on Environmental Ergonomics (ICEE),* 2007, pp. 2/1-2/19.

[3]. T. H. E. Hertzberg, Seat Comfort, *WADC Technical Report,* 1958, pp. 30-56.

[4]. B. Kurz, Ch. Russ, Climate Comfort and Product Testing, *Technical Textiles,* 4/5, 2020, pp. 172-174.

[5]. B. Kurz, S. Langenmeir, C. Zimmermann, W. Uedelhoven, M. Rottenfusser. Klimamanagement im Schuh, *Orthopädieschuhtechnik*, 11, 2012, pp. 42-51.

[6]. A. Psikuta, L. C. Wang, R. M. J. Rossi, Prediction of the Physiological Response of Humans Wearing Protective Clothing Using a Themophysiological Human Simulator, *J. Occup. Environ. Hyg*., 10, 4, 2013, pp. 222-232.

[7]. A. Ulherr, K. Bengler, Bewertung von Sitzen – Eine kritische Betrachtung von Komfort und Diskomfort Modellen, *Z. Arb. Wiss.,* 72, 2019, pp. 104-110.

[8]. K. H. Umbach, Die physiologische Funktion der Bekleidung, P. Knecht (ed.), Funktionstextilien, High-Tech-Produkte bei Bekleidung und Heimtextilien, 2003, pp. 43-56.

[9]. L. Wang (ed.). Performance Testing of Textiles, *Woodhead Publishing of Elsevier*, Cambridge, 2016.

[10]. C. Zimmermann, W. Udelhoven, B. Kurz, K. -J. Glitz. Thermal comfort range of a military cold protection glove: database by thermophysiological simulation, *Eur J Appl Physiol,* 104, 2008, pp. 229-236.

[11]. DIN EN ISO 11092:2014-12. Textilien - Physiologische Wirkungen – Messung des Wärme- und Wasserdampfdurchgangswiderstands unter stationären Bedingungen (sweating guarded hotplate test), 2014.

(048)

Internet of Things-based Geo-awareness System for Civilian Drones

S. Kunze
Deggendorf Institute of Technology, Institute for Applied Informatics,
Grafenauer Str. 22, 94078 Freyung, Germany
Tel.: +49 8551 91764-33, fax: +49 8551 91764-69
E-mail: stefan.kunze@th-deg.de

Summary: With the increasing adoption of civilian drones, technical solutions for managing the traffic in the lower airspace are becoming increasingly important. Pure transponder solutions which only allow monitoring of the movement will not be sufficient for safe drone operation in the future. Instead, the situation in the lower airspace must be continuously analyzed, based on transponder data from the drones as well as information from various other sensors and data sources. Whenever potentially dangerous situations are identified, a means to interact with the affected drones (either by updating the autopilot or warning and guiding the human) is also essential. In the SIMULU project, such a system is prototypically implemented with a strong focus on the scalability and modularity of the approach. The implementation is presented in this paper.

Keywords: Unmanned aerial systems, Drones, U-Space, Internet of Things.

1. Introduction

In recent years, numerous new applications for civilian drones have emerged. However, with the increasing numbers of unmanned aerial systems (UAS), the need for regulating the lower airspace also has become a pressing issue. In the European Union (EU) the term U-Space is used for UAS traffic management (UTM). Transponders will be an important part of any future UTM implementation. But for reliable and safe drone operation a way to interact with the UAV (unmanned aerial vehicle) or its pilot is needed. In The SIMULU project, a prototypical geo-awareness system (GAS) for civilian drones is implemented. It features a bi-directional communication link between the UTM system and the UAS. This allows interaction with the drone's pilot or autopilot in case of dangerous situations. In order to identify potentially dangerous situations, not only the transponder messages from the connected drones but also information from various other sensors and information sources are taken into account. For the prototype, Internet of Things (IoT) techniques and protocols are used. In this paper, the implementation of SIMULU's geo-awareness system is presented.

2. Related Work

A central aspect of UTM systems is the transponder which allows the drone to transmit its position (and other telemetry data) to the UTM. In manned aviation, this is done using the Automatic Dependent Surveillance – Broadcast (ADS-B) standard. The feasibility of ADS-B with reduced transmit power for UAV applications has been shown by Duffy and Glaab [1]. However, the ADS-B frequency band is becoming increasingly congested [2]. Hence, it doesn't seem to be a suitable choice for widespread use in UTM systems. The authors of [3] propose an ADS-B-like communication using various communication channels like 4G, Zigbee, or LoRa. They further present a prototypical UTM system using the ADS-B-like transponders [4]. This system also incorporates a UTM-based detect and avoid mechanism. It recognizes when two drones are approaching one another in the same airspace. "Traffic alerts to pilots via personal mobile phones will be sent by voice calls from UTM controller for avoidance" [4].

The Single European Sky ATM Research Programme (SESAR) demonstration project EuroDRONE implements some key UTM features of Europe's U-space programme. It did include a hardware box that serves as a transponder and for flight clearance. However, a means for interacting with the drone or its pilot during the flight was not part of the project [5].

The Commission Implementing Regulation EU 2021/664 which is the regulatory framework for the U-space, is currently being passed into the national laws of the member states. It is stated that a U-space service provider must be able to alert the UAS operator and update or withdraw a flight authorization if it is at risk. Examples of this are conflicts with manned air traffic or the detection of non-cooperative drones [6].

While cooperative drones regularly transmit their position to the UTM via their transponders, uncooperative drones won't do so. However, the existence of these uncooperative drones, which don't adhere to the regulations should also be accounted for when designing UTM applications, as they can severely impact safe drone operation. This threat has created a demand for civilian drone detection systems. A wide range of methods (acoustical, optical and infrared-based, radio frequency-based, and radar) has been researched [7]. Some detection systems for civilian drones are already commercially available.

For the design of the proposed system, privacy is also important. All future U-Space implementation also must adhere to the regulations of the EU's General

Data Protection Regulation (GDPR). A UTM system handles sensitive and personal data. For example, the drone owners and pilots must be registered in the system. Anonymization of the data can be an important step to assure sufficiently high levels of privacy and security. An overview of various levels of anonymization based on [8] is shown in **Table**.

Table 1. Levels of data anonymization, in accordance with [8].

Classification		Definition
Identifiable data		Contains obvious identifiers of individuals.
Reversibly	Pseudo-nymized	Obvious identifiers are removed and replaced with code; reidentification is possible with a key.
Reversibly	Pseudo-anonymized	Directly identifiable information is removed, and no key exists to map the records back to respective individuals. However, linkage to other available data sets could enable reidentification.
Irreversibly anonymized data		Reidentification of individual is no longer possible
Anonymous data		Data has been collected on an anonymous basis or has been aggregated and reidentification of individual is not possible

3. Implementation

The goal of the SIMULU project is to collect relevant data from all connected drones (in the form of regular transponder messages), various other sensors, and information sources. All this data is fused to monitor the air traffic in the lower air space and identify potentially dangerous situations. The system shall be able to interact with the UAS to restore safe flying conditions. The implementation of the geo-awareness system is based on the previously published concept [9]. The project focuses on a scalable solution based on open interfaces, that can either run in the cloud or on-premises. The backend communication is mostly based on MQTT. The system architecture is shown in Fig. 1 and consists of the following components:

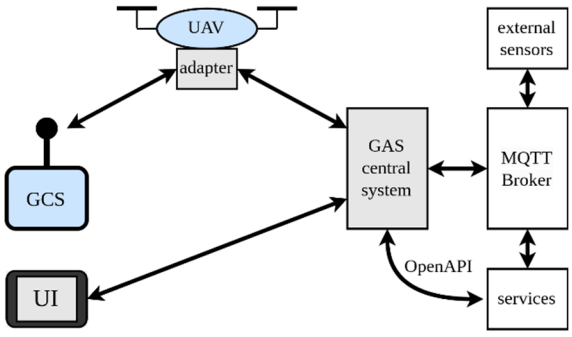

Fig. 1. System architecture.

GAS Central System: This component handles the incoming transponder messages from all connected drones and retrieves other relevant data from the connected sensors and services. By fusing the data from the different sources, a clear picture of the current situation is created. Based on the fused data, potential dangers are identified. Such potentially dangerous situations may include but are not limited to UAVs on a collision course, UAVs in the flight path of a pre-planned and approved mission of another drone, or UAVs in a no-fly zone. These no-fly zones can either be static (e.g., the area around airports) or dynamic. The latter ones can be set up to temporarily close specific parts of the lower air space for civilian drone traffic. This allows the UTM service to account for events like mass gatherings (e.g., demonstrations, concerts, etc.) or police and rescue service operations.

For drones guided by autopilot, the mission may be updated directly. This way the drone will automatically change its course, speed, or altitude to evade the danger. In case the UAV is controlled by a human pilot, warnings and instructions are transmitted to the user interface (UI) of the pilot. The prototype in SIMULU is implemented using Node-RED and provides a dashboard view for the UTM controller.

MQTT Broker: This is the central component of MQTT communication, as the clients don't communicate with each other directly. Instead, information is published to the broker on a specific topic. All other clients that have subscribed to this topic will receive a copy of the message from the broker.

Depending on the Quality of service (QoS) setting, the level of delivery guarantee for messages can be set [10]: For QoS 0 a best-effort mechanism without any acknowledgment is used. The sender will send each message only once. Thus, message loss is possible. If QoS 1 is selected, the recipient will reply with a PUBACK message. If the sender doesn't receive this PUBACK, it will retransmit the message. With QoS 2 it is assured, that the message is received exactly once. For this, a four-part handshake is used. While QoS 0 provides the fastest way of communication, messages might get lost. The GAS uses this setting for the regular transponder messages of the drone. The system can cope with losing some transponder updates. On the other hand, this keeps the overhead for most of the communication very small. A higher QoS level increases the overhead but assures the message delivery. For this reason, the GAS uses these settings for transmitting important data, like mission updates or warnings for pilots.

UAV adapter: This device is the part of the GAS that interfaces the UAV. It consists of a radio module and an embedded PC which is connected to the drone's flight controller. Through this connection, it has access to the sensor data (e.g., GPS position, etc.) of the drone, as well as its autopilot (if available). From this information, the UAS adapter creates transponder messages (based on the MAVLink protocol), which are regularly transmitted to the central system. The

update interval of the transponder messages can be configured in the software.

The prototype of the UAV adapter is implemented for a quadcopter using a Pixhawk Cube Orange flight controller. In addition to the existing setup required for operating the drone, the components of the UAV adapter are integrated into the UAS as shown in **Fig.**. The second telemetry port of the Pixhawk is connected to a Raspberry Pi embedded PC. Through this interface, the same MAVLink messages that are sent to the ground control station (GCS) are also available on the Raspberry Pi. From this information, the transponder messages are created and then transmitted to the central System of the GAS. For this radio transmission, RFD868 radio modules are used. These modules operate in the license-free 868 MHz ISM frequency band. This radio link provides a bidirectional channel between the UAV and the central system. It is used for all GAS-related communication, like transponder messages and flight plans in the uplink (UAV to UTM), but also for warnings and mission updates in the downlink (UTM to UAV). The prototype of the geo-awareness system uses the same radio modules that are used for the telemetry link between the drone and GCS. The power supply for the Raspberry Pi and the additional radio module is provided by the drone's battery.

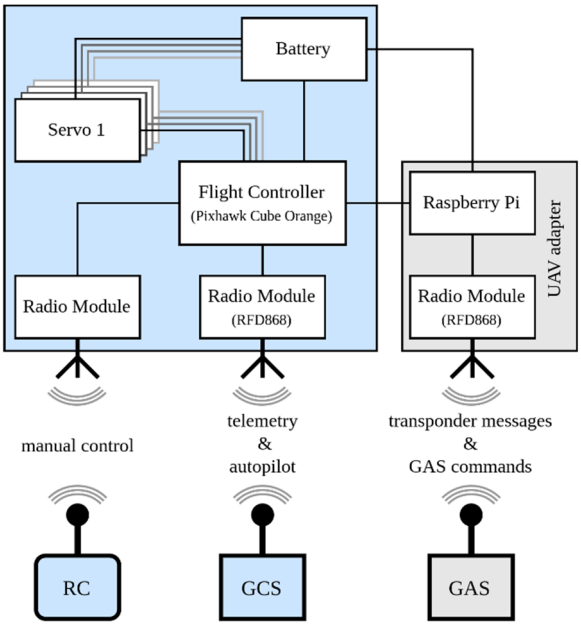

Fig. 2. UAV Adapter for drone with Pixhawk.

Alternatively, a 4G/5G modem could be used for communication utilizing the public cellular network. In this case, MQTT could also be used for the transponder messages. The device is powered by the drone's battery. The UAS adapter can also be implemented as a pure hook-on device, with its own power supply and sensors. In this case, no direct interaction with the drone is possible. Instead, only messages to the pilot or GCS may be sent. However, this type of device can be retrofitted to any UAV.

User Interface: The UI displays relevant information for the pilot. It shows the position and status (telemetry and other sensor data) of the pilot's own drone. The map also shows the position of other nearby UAVs, (dynamic) no-fly zones, and the flight paths of upcoming registered flights. The prototype in SIMULU is implemented in Node-RED. A screenshot of the UI is shown in **Fig.**. The information can either be relayed through a radio link from the central system via the UAV adapter, or the UI can subscribe directly to the relevant MQTT topics if it has an Internet connection.

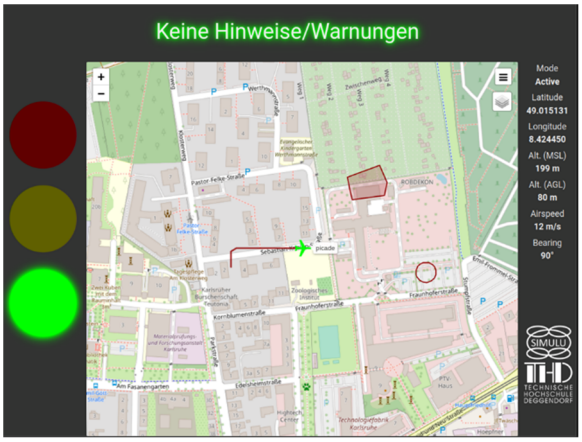

Fig. 3. Screenshot of user interface.

The UI can also provide an audio output to improve the usability. This way the pilot can concentrate on the drone in the air, rather than permanently checking the display.

External sensors: For the safe operation in the lower airspace not only the transponder messages from the connected cooperative drones are relevant. The threat posed by non-cooperative drones (i.e., drones that don't comply with the regulations) must also be considered. In the SIMULU system, a radar-based solution was used as an exemplary detection system. Information on detected signals (non-cooperative drones, but also bird swarms) is published to the MQTT broker. Another example of an external type of sensor that can provide valuable information is a weather station, as especially the wind speed is an important factor for safe drone operation. Using the modular MQTT-based IoT approach, the system can easily be extended with further sensors.

Services: The SIMULU system also features several services that can provide further important information for the situation analysis. Several prototypical services are implemented in the project. They can either be interfaced via MQTT or an OpenAPI interface.

The drone register provides detailed information on the UAV itself, like type, weight, and payload capacity. It also contains information on the owner of the UAS. Finally, each drone gets a unique ID which is used to identify it in the communication with the UTM. Since this is partially sensitive data, there are two different APIs for accessing the information. The

uav-model-api gives access to generic data on the drone type, while the *uav-object-api* gives access to sensitive data.

The pilot register contains information on the user of the drone. It also allows the pilots to upload certifications and permits. This data is highly sensitive and is not accessed by the geo-awareness system. However, it is required for other aspects of a full UTM implementation.

In the flight register, information on planned missions and approved flights is stored. This data serves as the basis for the geo-awareness system to clear flight corridors for pre-approved flights. For example, human pilots maybe warned, that a planned flight will lead through the nearby airspace. By informing the pilot of temporary altitude restrictions a save passing can be assured.

Another service keeps track of existing no-fly zones. Besides the static no-fly zones (e.g., at airports), the SIMULU project also considers dynamic ones. Since these can't be hardcoded into the firmware of the drone, it's up to the GAS to inform the connected UAS of these dynamic no-fly zones. The positions, altitude limitations and time limits of all the respective no-fly zones can be accessed from this service.

Privacy considerations: Any future U-Space system must be compliant with the EU's GDPR. While the proposed prototypical system is not GDPR-compliant, some privacy considerations were nevertheless taken into account. Access to the services is based on a user's role. For example, in the pilot's UI only a drone icon is shown. The icon can be dependent on the type of UAV (fixed-wing or multi-copter), as this information is relevant for the pilot. Other information, like the owner of the drone, is not relevant to the functionality of the UI. In the central system of the GAS all connected drones are identified by their unique ID. This is necessary to obtain information from the drone register on the type of drone, weight, autopilot capability etc. However, a UTM operator using the monitoring system does not need to know who the drone with a given ID belongs to. For other U-Space-related services, like billing or handing out fines for infractions, the owner of the drone can be identified by the drone's ID. Depending on the user role, the user rights can be scaled, so that they only have access to the data that is relevant for them.

In the radio transmissions of the UAV adapter and the central system, only the drone ID is sent. This follows the concept of pseudonymization as described in [8], as the sensitive private data can only be obtained with the according user rights.

4. Test & Evaluation

The prototypical implementation of the SIMULU system was tested during real drone flights, to test the features of e.g., automatically updating an autopilot mission during the flight to evade no-fly zones or other drones.

With the following exemplary test flight, the basic functions of the GAS can be summarized nicely. After turning on the drone, it automatically begins sending transponder messages (containing its position and status) to the GAS. Once, the autopilot mission is uploaded from the GCS to the flight controller, the mission details are automatically passed along to the GAS as well. After taking off, the drone began to follow the preplanned path. At that time, a dynamic no-fly zone was activated. In **Error! Reference source not found.**a. the original waypoints of the drone and the no-fly zone are illustrated. The central system of the GAS recognized that the original mission of the drone would lead through the prohibited area. Therefore, new waypoints for the autopilot were calculated and transmitted to the drone. The drone successfully updated its autopilot mission midflight and followed the new waypoints, as shown by the track of the drone's flightpath in **Error! Reference source not found.**b.

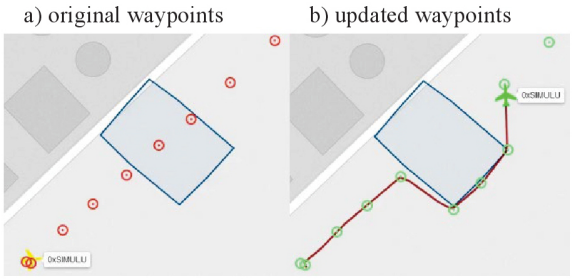

Fig. 4. Mission update.

The test flight also included a second, manually piloted drone, which was positioned in the flight path of the original drone. The system reacted to this by warning the pilot of the second drone and imposing an altitude limit on him. At the same time the mission of the first drone was updated again, to increase the altitude and allow a safe passage of the two drones.

To better test and evaluate the behavior of the GAS in dangerous situations, emulated drones were also used for the evaluation process. These drones were emulated with Hardware in the loop (HiL) using AirSim or purely in Software. Additionally, a radar emulator was used to replay the previously recorded track of real drones. The radar measurements were performed in cooperation with the project partner Fraunhofer IOSB at their facility in Karlsruhe. Afterward, the recorded radar tacks can be replayed by publishing the radar data to the MQTT broker with the original timing. These detections are treated as uncooperative drones by the GAS and the emulated drones in the area are warned and guided away from them.

For the performed evaluation flights and simulations, the update interval for the transponder messages was always set to one second. For the performed tests this provided a good balance between the temporal resolution of the data, the congestion of the radio channel, and system performance. However, the implementation of dynamic transponder intervals

might increase the performance of the system, especially when sharply increasing the number of drones. The frequency of the regular transponder messages could increase with the threat level (green / yellow / red) of the UAS. It could also be increased only in specific cases (e.g., UAVs on a collision course) where a better temporal resolution are beneficial. On the other hand, for drones that are flying alone and far away from any potential risks, the update period could be considerably lengthened.

5. Conclusions & Future Work

The test and evaluation of the SIMULU geo-awareness system has shown the functionality of the design. In contrast to traditional drone transponder designs with information flow only from drone to UTM, the central aspect of the proposed system is a bidirectional communication link. During the evaluation, the monitoring of the drone traffic, the recognition of potentially dangerous situations by the central system, as well as updating of the autopilot mid-flight worked well. In the case of manually piloted drones, the GAS provides a way to interact with human pilots in a simple way during the flight. Providing live support to human pilots will become increasingly important with the rising number of UAVs and UAS applications. Many pilots use their drones for recreational purposes and may not do so on a regular basis. They may also not be familiar with the latest regulations. Due to these factors, human pilots may quickly become overburdened in dangerous situations.

In conclusion, the SIMULU project has shown the value of a bidirectional channel for UTM-related communication. It provides a means to directly interact with or influence the drones in the U-Space, which can significantly increase safety in the lower airspace.

However, there are several steps to be taken in the future work. The next step towards a real-world application is increasing the number of drones as well as the area covered by the system. So far, the integration into the autopilot has only been implemented for one system (Pixhawk flight controller). Other flight controller systems should be incorporated into the system as well. In terms of communication, the radio modules could be replaced by a 4G/5G-based solution. This would eliminate the need for a dedicated communication infrastructure.

The usability of the user interface could be increased by using augmented reality to implement a head-up system for the pilot. This would keep the focus of the pilot on the airborne drone while providing important information at the same time.

To improve the situation analysis and recommendations of the GAS, further services could be connected. Examples are the integration of weather services, or a service that links the U-space to manned aviation. One application for this could be to clear flight paths and landing spots for rescue helicopters. Additionally, the path planning for updating autopilot missions is quite rudimentary, so far. More sophisticated algorithms that also consider the flight trajectories of different drone types could be used instead.

Acknowledgements

The work presented in this paper is part of the SIMULU project, which was funded by the German Federal Ministry for Digital and Transport.

References

[1]. B. Duffy, L. Glaab, Variable-power ADS-B for UAS, in *Proceedings of the IEEE/AIAA 38th Digital Avionics Systems Conference (DASC'19)*, San Diego, USA, September 2019, pp. 1-6.

[2]. A. Baltaci, E. Dinc, M. Ozger, A. Alabbasi, C. Cavdar, D. Schupke, A Survey of Wireless Networks for Future Aerial Communications (FACOM), *IEEE Communications Surveys & Tutorials*, Vol. 23, Issue 4, 2021, pp. 2833–2884.

[3]. C. E. Lin, C.-S. Hsieh, C.-C. Li, P.-C. Shao, Y.-H. Li, Y.-C. Yeh, An ADS-B Like Communication for UTM, in *Proceedings of the Integrated Communications, Navigation and Surveillance Conference (ICNS'19)*, Herndon, USA, April 2019, pp. 1-12.

[4]. C. E. Lin, T. Chen, P. Shao, Y. Lai, T. Chen, Y. Yeh, Prototype Hierarchical UAS Traffic Management System in Taiwan, in *Proceedings of the Integrated Communications, Navigation and Surveillance Conference (ICNS'19)*, April 2019, pp. 1-13.

[5]. V. Lappas, *et al.*, EuroDRONE, A European UTM Testbed for U-Space, in *Proceedings of the International Conference on Unmanned Aircraft Systems (ICUAS'20)*, Athens, Greece, September 2020, pp. 1766-1774.

[6]. Acceptable Means of Compliance and Guidance Material to Regulation (EU) 2021/664 on a Regulatory Framework for the U-Space, Annex to ED Decision 2022/022/R, Issue 1, *European Union Aviation Safety Agency (EASA)*, December 2022.

[7]. A. Holland Michel, Counter-Drone Systems, Center for the Study of the Drone at Bard College, Feb. 2018, http://dronecenter.bard.edu/counter-drone-systems/

[8]. K. N. Vokinger, D. J. Stekhoven, M. Krauthammer, Lost in Anonymization – A Data Anonymization Reference Classification Merging Legal and Technical Considerations, *Journal of Law, Medicine & Ethics*, Vol. 48, Issue 1, 2020, pp. 228-231.

[9]. S. Kunze, A. Weinberger, Concept for a Geo-Awareness-System for Civilian Unmanned Aerial Systems, in *Proceedings of the 31st International Conference Radioelektronika*, April 2021, pp. 1-6.

[10]. MQTT Version 5.0, OASIS Standard, *Organization for the Advancement of Structured Information Standards*, 2019.

(049)

Hyperspectral Imaging Microscopy for Single-cell-analysis

Wolfgang Kurz, Aaron Flügge Arus, Emre Kariper, Olcay Akgün, Edwin Adisoemarta, Martin Jakobi and Alexander W. Koch
Technical University of Munich, Institute for Measurement Systems and Sensor Technology,
Arcisstraße 21 80333 Munich, Germany
Tel.: + 4989 289-23354
E-mail: w.kurz@tum.de

Summary: Hyperspectral imaging (HSI) is an imaging technology that can capture images of a wide range of electromagnetic wavelengths, providing high-resolution spectral data that can be used to identify subtle differences in a scene. This technology is being used in a wide range of applications, including remote sensing, agriculture, astronomy, forestry, food quality, and cultural heritage preservation. Due to recent advances in this technology, it is also possible to scan objects in the micro- and nanometer range, so called hyperspectral microscopy. This adjustment allows studying nanoparticles, biological samples or processes and providing spectral information, as conventional microscopy only presents an image in the visible range. The spectral information can differentiate certain materials, which is usually difficult to achieve using conventional microscopy. Alternatively, it may help identify the cellular structures of a single cell or cell culture and avoid the challenging process of labelling for fluorescence microscopy. This work presents the modification of a hyperspectral imaging setup for microscopy.

Keywords: Hyperspectral imaging, Hyperspectral microscopy, Spectral analysis, Spectral fingerprint.

1. Introduction

Hyperspectral imaging (HSI) collects and processes information across the electromagnetic spectrum [1]. It combines spectroscopy and digital photography. Hyperspectral imaging aims to acquire the spectrum of each pixel in an image of a scene to discover objects, identify materials, or detect processes [2]. Hyperspectral cameras use specialized hardware to capture hundreds of bands for each pixel, which can be interpreted as a full spectrum. Therefore, an object of interest is scanned, and an image for every wavelength is created. These images are stored in a so-called hypercube and allow the analysis of the spectral distribution of a single pixel (Fig. 1) [3].

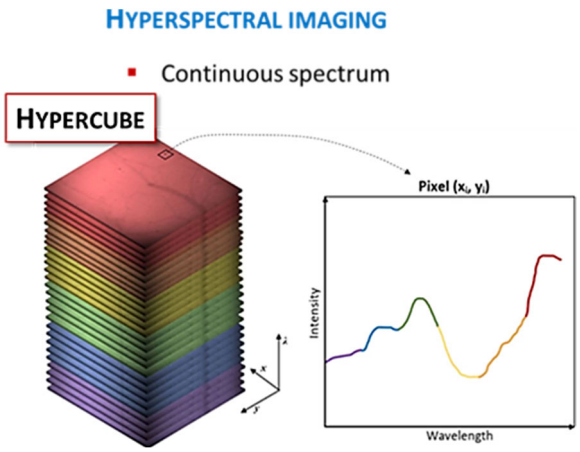

Fig. 1. Hypercube of a hyperspectral imaging scan and its pixel analysis [3].

The entire electromagnetic spectrum of the inspected object is used to find so-called fingerprints, which are unique spectral signatures [4]. With these distinctive marks, objects can be differentiated due to their spectral features in the non-visible electromagnetic spectrum range. Therefore, hyperspectral imaging is used in many fields of application like remote sensing, agriculture, astronomy, forestry, food quality and cultural heritage preservation, and biomedical imaging. The field of application of this technology is shifting more and more from macroscale down to micro- and nanoscale, where additional spectral information can help with the analysis and characterization in molecular biology or of nanoparticles where conventional microscopy mostly presents only spatial information [5].

2. Hyperspectral Microscope Setup

Section 2 presents the hyperspectral Imaging setup built for the micro- and nanoscale to perform microscopic analysis.

Fig. 2 shows the schematic representation of the hyperspectral imaging microscope. The system includes a stage controller, an optical path with the optical components, a hyperspectral imaging camera with a spectral range of 325-1056 nm, and a data processing unit (Matlab GUI). A broadband LED light source is used as illumination source (wavelength range 470-850 nm).

The light (“green” path) from the light source is partially reflected (50:50) by the beam splitter 1 and then projected onto the microscope objective as illumination. The light that is reflected (in yellow)

from the sample travels through the objective and the beam splitter 1 and is then focused by the cylindrical achromatic lens through a slit onto a diffraction grating inside the spectrograph to disperse the light into its constituent wavelengths.

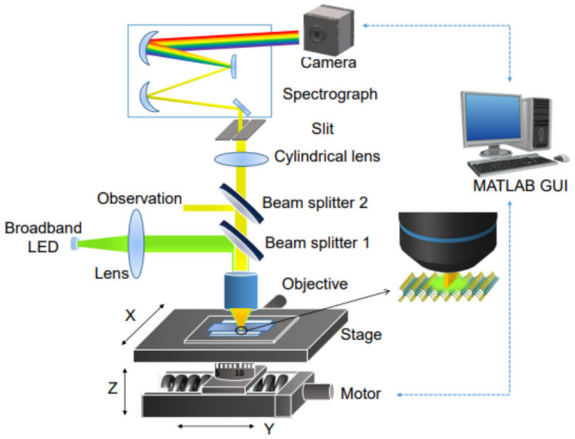

Fig. 2. Schematic setup of the hyperspectral microscope [6].

The light reflected by the beam splitter 2 is used for visual observation. When the area of interest is positioned, the second beam splitter is removed to increase the amount of light reaching the sensor of the camera.

The motorized positioning platform performs scans of the object of interest in y direction. The scans were performed with an x63 plan-appochromat objective reaching a total system resolution of 0.3 $\frac{\mu m}{pixel}$.

3. Hyperspectral Microscopic Scan

Fig. 3 shows a successful scan of a dead single-cancer cell and a gold nanoparticle and displays the representative spectra on the right side. The colors in the left image represent the reflectance intensity, with yellow standing for the strongest and blue for the weakest reflectance. The marks on the left side depict the pixel position, where the spectra for the right side were chosen. The orange and purple mark represent the center and border of the cancer cell, whereas the yellow mark displays the gold particle, and the blue shows the background spectrum. It is apparent that the gold particle reflects the light resulting in a higher peak of intensity, whereas the cell absorbs more light resulting in a valley whereby the border absorbs weaker as the cell structure becomes shallower.

4. Conclusions

The hyperspectral microscope used in this project proofed to do high-resolution scans down to the nanometer scale and distinguish the objects in a scanned scene by their spectral distribution. Therefore, this system enables the acquisition of nanoparticles, single-cells, cell cultures, and their processes in multiple spectral bands, which can be used to further analyze a sample's components and structure.

One potential application is the diagnosis of cancer. By using hyperspectral imaging to scan tissue samples, it may be possible to identify cancer cells based on their spectral signatures. Also, detecting foreign matter in a biological sample could be possible, as the spectrum clearly indicates a different specimen, whereas just an image in the visible range could complicate the differentiation if no experienced expert is conducting the analysis.

The promising results obtained demonstrate the great potential of a hyperspectral microscope system. Robust and reliable algorithms for the image processing and segmentation are necessary and can lead to significant advances in the understanding of processes on this scale.

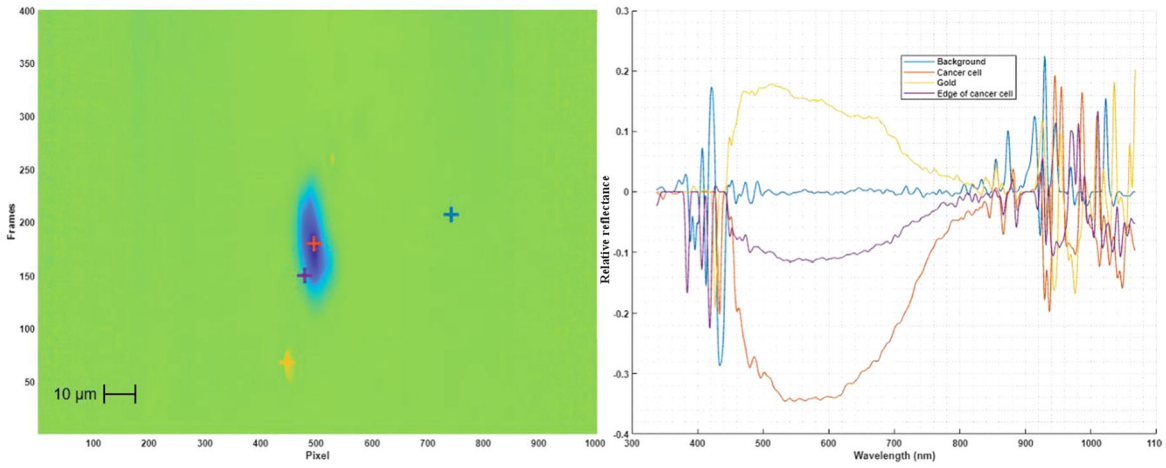

Fig. 3. Nanoparticle and Single-Cell Scan (left) with a x63 magnification and its representative spectrum (right).

References

[1]. C.-I Chang, Hyperspectral Imaging: Techniques for Spectral Detection and Classification, *Springer US*, 2003.

[2]. P. Geladi, H. F. Grahn, Techniques and Applications of Hyperspectral Image Analysis, *John Wiley Sons Ltd*, 2007.

[3]. L. Giannoni, F. Lange, I. Tachtsidis, Hyperspectral imaging solutions for brain tissue metabolic and hemodynamic monitoring: past, current and future developments, *J. Opt*., Vol. 20, 2018, 044009.

[4]. G. Lu, B. Fei, Medical hyperspectral imaging: A review, *JBO Journal of Biomedical Optics*, Vol. 19, Issue 1, 2014, 10901.

[5]. M. W. Hagen, N. Kudenov, Review of snapshot spectral imaging technologies, *Optical Engineering*, Vol. 52, Issue 9, 2013, 090901.

[6]. X. Dong, Hyperspectral Imaging Microscopy for Atomic Layer Mapping of Two-Dimensional Materials, *Technical University of Munich (TUM)*, 2021.

(052)

Development of Bimetallic Zn/Ti-BMOF Thin Film Composite Optical Waveguides for Ethylenediamin Detection at Ambient Temperature

Patima Nizamidin * **and Huifang Chen**

State Key Laboratory of Chemistry and Utilization of Carbon Based Energy Resources; College of Chemistry, Xinjiang University, Urumqi, 830017, Xinjiang PR China
Tel.: 086-15899445904
E-mail: patima207@aliyun.com

Summary: In this case, for the purpose of improve the gas sensing selectivity of monometallic titanium organic framework (MOF, Ti-MOF), the zinc and titanium bi-metal (Zn/Ti) nodes were introduced to the frame to produce specific adsorption site by synergistic effect of them. A graphene-like Zn/Ti-bimetallic MOF(BMOF) thin film fabricated on titanium dioxide (TiO_2) film composite optical waveguide (COWG) substrate using solvothermal method, and the gas-sensing performance at ambient temperature (20°C) for amines and acidic gases were investigated. As a result, Zn/Ti-BMOF completed its graphene-like structure with uniform small pores (D=60 nm) after 5h of continuous growth at 150°C. Zn/Ti-BMOF thin film COWG exhibited higher refractive index and a positive response to ethylenediamine (EDA) and H_2S gas co-existing with the same concentration (100 ppm) of amines and acidic gases. It is postulated that there are charge transfer and hydrogen bond interaction occurs when the Zn/Ti-BMOF film COWG adsorbs EDA and H_2S gases, respectively, as the Lewis acid-base nature of C=N bond in the Zn/Ti-BMOF. The presented sensor shows a wide detection range (100 ppm –100 ppt), fast (2 s) and stable response to EDA.

Keywords: Bimetallic Zn/Ti-BMOF, Composite optical waveguides, Response selectivity, Ethylenediamine.

1. Introduction

Metal-organic frameworks (MOFs) attracted great attention of researchers for decades due to their tenable structure and reversible host-guest interaction between MOFs and the analyte. The desired frame-work structure can be controlled by adjusting the organic ligand, or the central metal, the solvent, as well as the pH values for its surface moditability, pores distribution uniformity, and excellent physio-chemical activity, which makes MOFs an ideal candidates for gas separation/storage, sensors and devices [1]. Recently, in gas adsorption and gas sensor field, extensive investigations on the design and synthesis of bimetallic-based metal organic framework (BMOF) have exponentially increased owing to their improved adsorption selectivity and structural stability compared to those monometallic MOF, which caused from synergistic functionalities. Yi Xue [2] and co-workers designed a series of Cu/Bi-BMOFs for the selective adsorption of CO_2. The synergistic Co-Mn-MOF-74 [3] exhibits an excellent adsorption characteristics to NO_x. Our research group have been developed monometallic titanium metal organic framework {Ti-MOF, $[Ti_2\text{-}(TpA)_2\text{-}NDI]_n$} based COWG with highly sensitive and multiselective to ethylenediamine (EDA), followed by nitrogen dioxide (NO_2), methylamine and trimethylamine upond exposed to 15 types of benzenes, amines and acidic gases [4]. In this study, in order to improve the response selectivity of Ti-MOF film COWG, the zinc and titanium bi-metal (Zn/Ti) nodes were introduced to the frame, and Zn/Ti-BMOF was prepared for the first time. The optical gas adsorption performance for amines (ammonia, methylamine, dimethylamine, trimethylamine, EDA) and acidic gases (H_2S, SO_2, NO_2, HCl, CO_2) was investigated using self-assembled OWG sensor testing system (Fig.1). Meanwhile, the gas adsorb principles was studied and discussed with respect to optical gas adsorption behaviours of the Zn/Ti-BMOF film COWG.

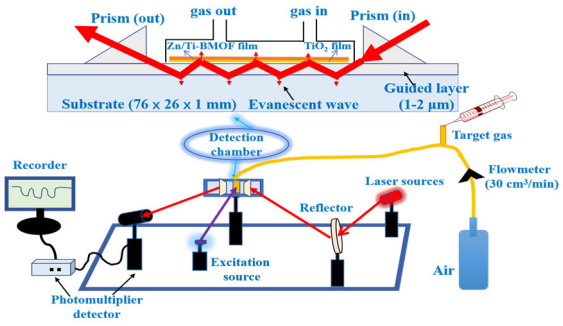

Fig. 1. Schematic view of OWG sensor plate form.

2. Method

Film fabrication: To promote efficient film growth, a titanium dioxide (TiO_2) film with 40 nm thick was fabricated on the tin-diffused glass slide [4] (TiO_2-COWG); then the precursors, $Zn(NO_3)_2{\cdot}6H_2O$, $TiCl_4$, and NDI were mixed in a molar ratio of 1:1:1 and stirred at room temperature for 1 h. The resulting mixture was then transferred to a cylindrical reactor. Simultaneously, the TiO_2-COWG substrate was placed

in the reactor. The Zn/Ti-BMOF film was grown at 150 °C for 5 hour. Finally, the as-grown film was removed, dried under a nitrogen gas flux, and stored in a vacuum desiccator for further investigation.

Gas sensing performance: the obtained Zn/Ti-BMOF films were fixed on the OWG sensor testing plate-form (Fig. 1), and a laser beam with fixed wavelength of 520 nm was introduced by prism coupler, the carrier gas (dry air) flow rate was controlled at 30 ml min^{-1}. For each test, the Zn/Ti-BMOF film COWG was first exposed to dry air to record the baseline output light intensity, denoted as I_{air}. Subsequently, the film was exposed to a given amount of the analyte gas, and the intensity of the output light, I_{gas}, was simultaneously recorded. The optical signal (ΔI, variations in the output light intensities) over the testing time was transmitted to a computer by the photomultiplier tube and recorded. The procedure was performed at ambient temperature (20°C) and normal pressure (0.92 atm). The testing gases (amines and acidic gases) with different concentrations were prepared according to a procedure described in the [4], and their concentrations were determined using gas detection tubes with a detection range of 2–200 ppm.

3. Results and Discussion

The chemical composition and morphology of the Zn/Ti-BMOF were confirmed by Fourier transform infrared spectroscopy (FTIR), X-ray photoelectron spectroscopy (XPS), and field emission scanning electron microscope (FESEM). XPS spectrum (Fig. 2a) shows the characteristic binding peaks of zinc (Zn), carbon (C), nitrogen (N) and oxygen (O), without the Ti binding peaks due to its lower contents. The FTIR characteristic peaks (Fig. 2b) located at 3430 cm^{-1} (O-H), 3074 cm^{-1} (N-H), 1649 cm^{-1} (C=O), 1269 cm^{-1} (O-C-O), and 737 cm^{-1} (C-H) were represents successful construction of Zn/Ti-BMOF. FESEM image revealed a homogeneous graphene-like structure on the surface of the Zn/Ti-BMOF film with an average pore size of 60 nm (Fig. 2c).

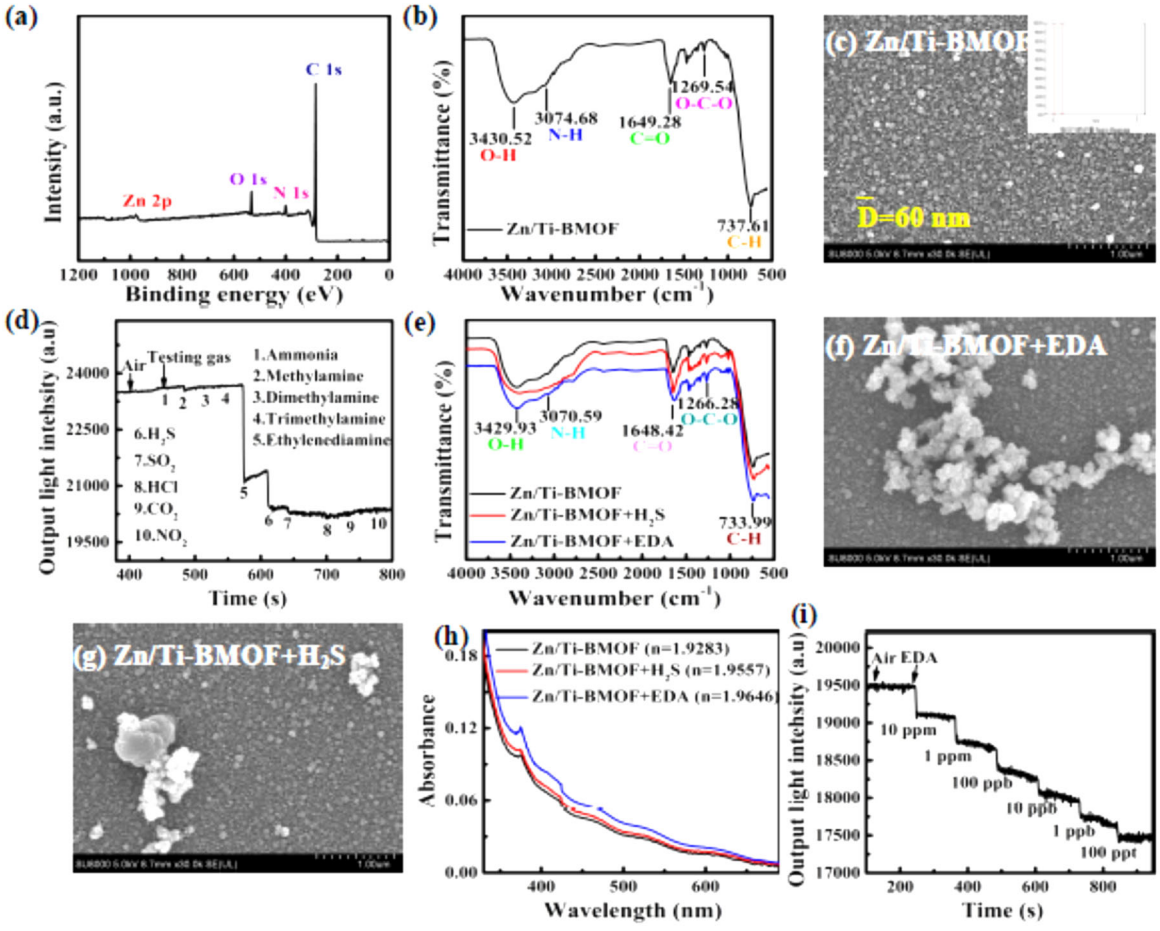

Fig. 2. (a) Full XPS spectrum, (b) FTIR, (c) FESEM image of Zn/Ti-BMOF; (d) Selective response of Zn/Ti-BMOF films OWG to different gases with 100 ppm, (e) FTIR, (f) Absorbance, (g-h) FESEM images of Zn/Ti-BMOF films after exposure to EDA and H_2S, (i) Response diagram of Zn/Ti-BMOF films OWG to different concentrations of EDA gas.

In gas sensing process, the selectivity of the Zn/Ti-BMOF film COWGs for the adsorption of amines and acidic gases were evaluated. The testing result (Fig. 2d) shows that Zn/Ti-BMOF film COWG exhibited a larger adsorption response for EDA, followed by H_2S, upon exposure to 100 ppm of amines and acidic gases.

Compare with monometallic Ti-MOF, the response selectivity was improved due to the synergistic effects of Zn and Ti metals. The FTIR spectrum results (Fig. 2e) of Zn/Ti-BMOF film before and after exposure to EDA and H_2S shows that EDA mainly interacts with C=N side in NDI and induces enhancement of intramolecular hydrogen bond; besides, the O-H (3430 cm^{-1}) and C=O (1649 cm^{-1}) peaks are blue-shifted 11.4 and 21.7cm^{-1}, approximately, which maybe caused from the n-π transfer of lone pair electrons of nitrogen atom to organic ligand NDI. While after the H_2S gas adsorption, there are hydrogen bond interaction between host-guest, resulting reduce in strength of O-H (3430 cm^{-1}) bond vibration. These charge transfer and hydrogen bond interactions were believed to be comes from the Lewis acid-base nature of C=N bond in the Zn/Ti-BMOF [5]. Meanwhile, the host-guest interactions inducing structural stacking of film surface (Fig. 2f-g) and reduction in porosity, thus an increase in film refractive index (Fig. 2h) was participated, which resulting the decrease in output-light intensity. After further study it was proved that, while concentration of analyte gases was reduced to the 1 ppm, Zn/Ti-BMOF film COWG showed a fast (2 s) and unique response with a wide detection range (1 ppm–100 ppt) to EDA gas (Fig. 2i) without the interference of other amines and acidic gases.

4. Conclusions

In this work, we present the fabrication and gas sensing characteristics of Zn/Ti-BMOF film COWG. Zn/Ti-BMOF completed its graphene-like structure after 5h of continuous solvothermal growth, resulting in an uniform small pores (D=60 nm), higher refractive index, and improved selective response to EDA and H_2S gas co-existing with the 100 ppm of amines and acidic gases. When the Zn/Ti-BMOF film COWG adsorbs EDA and H_2S gases, it susceptible to occurs a charge transfer and hydrogen bond interaction, as the Lewis acid-base nature of C=N bond in the Zn/Ti-BMOF. The presented sensor could prob a wide range (1 ppm –100 ppt) of EDA.

Acknowledgements

This study was supported by the National Natural Science Foundation of China (number 22164019) and Natural Science Foundation of Xinjiang Uyghur Autonomous Region (number 2021D01C032).

References

[1]. S. Kevat, B. Sutariya, V.N. Lad, Microfluidics-assisted, time-effective and continuous synthesis of bimetallic ZIF-8/67 under different synthesis conditions, *Journal of Materials Science,* 58, 12, 2023, pp. 5219-5233.

[2]. Y. Xue, C. Li, X. Zhou, et al., MOF-Derived Cu/Bi Bi-metallic Catalyst to Enhance Selectivity Toward Formate for CO_2 Electroreduction, *ChemElectroChem*, 9, 4, 2022, e202101648.

[3]. Z. Wu, Y. Shi, C. Li, et al., Synthesis of Bimetallic MOF-74-CoMn Catalyst and Its Application in Selective Catalytic Reduction of NO with CO, *Acta Chimica Sinica,* 77, 8, 2019, pp. 758-764.

[4]. P. Nizamidin, C. Guo, Q. Yang, et al., Surface-modified Ti-MOF/TiO_2 membrane and its gas-sensing characteristics, *Surface Innovations,* 11, 6-7, 2023, pp. 365-376.

[5]. Z. Meng, K.A. Mirica, Covalent organic frameworks as multifunctional materials for chemical detection, *Chemical Society Reviews,* 50, 24, 2021, pp. 13498-13558.

(056)

Routine Measurement and Monitoring System for the Activity of Elderly People with Dementia: A Systematic Review

Júlia D. Rodrigues, Pedro Morais and Vítor Carvalho
2AI – School of Technology, IPCA, Campus do IPCA, 4750-810, Barcelos, Portugal
Tel.: +351 253 802 260
E-mails: juliadoriarodrigues@gmail.com, vcarvalho@ipca.pt; pmorais@ipca.pt

Summary: This systematic literature review was conducted to explore systems for measuring and monitoring the activity routine of older people with dementia. The review was able to identify and analyze relevant studies that evaluate the effectiveness and usability of these systems in improving the quality of life and well-being of this population. A survey was carried out using the following databases: B-On, Google Scholar, PubMed and Science Direct, within the time frame between 2018 and 2023, considering only the newest studies to be reached. The techniques under study or already developed were presented, along with their results, as well as the characteristics of the study and the characteristics of the technologies. The final sample included 8 articles describing different measurement and monitoring tools. Gaps were identified in this final samples, as well as fields that still need to be addressed. Future research should focus on developing and improving solid, safe and viable tools that can help to improve patients' quality of life and facilitate the work of their caregivers

Keywords: Elderly, Dementia, Routine, Activities, Monitoring, Measurement, Systematic review.

1. Introduction

Dementia is a broad term including several illnesses that affects millions of individuals worldwide, particularly among the elderly population aged 65 years and older [1]. It is characterized by memory loss, cognitive impairment, behavioral changes, and functional limitations. Such symptoms can compromise and prevent the performance of activities of daily living [2].

In addition, according to the World Health Organization, in 2021 about 55 million people were living with dementia [3] and this number is likely to grow more and more with the increase of the elderly population. If the predictions come true, the number of people with dementia could reach the 139 million marks in the next 30 years [4, 5]. In this sense, it is important to find new solutions or strategies that can help these older people to perform their daily activities without needing so much attention or help from their relatives and caregivers, or at least to improve their treatment with information provided on their daily activities. On the other hand, it is important that the people responsible for the care of these patients can also have tools that help them to monitor these activities and facilitate this care. Therefore, recognizing and understanding the specific needs and challenges faced by the target group is crucial for developing adapted interventions and support systems. In this sense, this research sought to understand how systems that can monitor the daily activities of elderly people with dementia, and what they are capable of identifying, as well as their effectiveness in improving the quality of life of these elderly people and their caregivers have been developed.

Through this systematic analysis of existing literature, the review provided an overview of the current state of the art, identifying gaps and limitations of existing studies and highlighted areas for further research and improvement. The results of this review serve as a basis for future evidence-based decision-making in healthcare settings, guiding the development and implementation of more effective and adapted measurement and monitoring systems.

This paper is organized in 5 sections. Section 2 describes the literature review methodology; Section 3 presents the results obtained; Section 4 draws the discussion; and, finally, Section 5 presents the paper final considerations and remarks.

2. Methodology

The literature review commenced by conducting a comprehensive search and analysis of pertinent studies, articles, and reports detailing various systems employed within this particular context. This review also encompassed an exploration of associated challenges, requirements, and the daily experiences encountered by the target demographic.

2.1. Search Strategy

Adhering to the methodological rigor stipulated by the PICO (Population, Intervention, Comparison, and Outcome) framework [6, 7], this strategy was meticulously employed to enhance the transparency, precision, and lucidity of the review process [8]. In this context, the demographic focus group comprises elderly individuals affected by dementia, thus

constituting the population of interest, although it is believed that the results can also be used for future studies with younger age groups, but who are affected by the same disease.

The intervention component concerns the implementation of measurement and monitoring systems, meticulously designed to supervise and track the intrinsic aspects of the daily routines of this population cohort. In the sphere of comparison, an initial inclusion criterion involved studies that cast a comparative lens on different measurement and monitoring methodologies or that evaluated the effectiveness of these systems against prevailing standard care paradigms or alternative interventions.

Ultimately, the most important results were to assess the operational effectiveness of the systems used and to elucidate their role in improving the quality of life, daily functioning and holistic well-being of older people affected by dementia.

2.2. Databases, Keywords and Filters

With the aim of an exhaustive exploration of the literature, a selected set of keywords was used. This list of keywords embraced a spectrum of interconnected concepts that captured the essence of the topic in question. Variations of terms including, but not limited to, "routine measurement", "monitoring systems", "assessment systems", "older people", "dementia", "activities" and "technologies" were incorporated. Through strategic integration with Boolean operators (AND, OR), these keywords were inserted into the search queries, adapted to each particularity of the chosen databases. This strategic orchestration aimed to obtain articles that comprehensively addressed the effectiveness, usability and repercussions of these systems on the designated population.

In addition, in order to rigorously carry out this literature review, an approach involving the use of four different databases was adopted. This broad spectrum included PubMed, Google Scholar, ScienceDirect and the Portuguese platform B-on, ensuring that a wide range of relevant studies were included in combination. Also, a strict focus on relevance and timeliness was maintained, concentrating predominantly on articles published in the English and Portuguese languages, reflecting the primary language proficiency of the research team. And, to safeguard timeliness and contextual appropriateness, a careful publication date filter was used, covering articles published in the time domain ranging from 2018 to 2023. This well-defined time period was selected with the highest precision to cover the latest advances, aligning the review with the contemporary overview of knowledge and technological progress in the field.

A total of 252 articles relevant to the scope were initially identified and exported to the Zotero platform for organization [9]. Following a reading of the titles and a review of the inclusion and exclusion criteria, 68 articles were selected for a reading of the abstracts and conclusions. Subsequently, after a thorough review of abstracts and conclusions, the articles were refined in accordance with the criteria outlined in the forthcoming section.

2.3. Selection Criteria

The definition of inclusion or exclusion criteria for articles discovered through the designated keywords was carried out with the aim of exclusively covering materials that have an immediate link to the intended thematic area and that remain relevant in the contemporary scene.

Therefore, the inclusion criteria were structured to cover articles that were accessible to the research team and that fit into a time period ranging from 2018 to 2023, as previously referred, thus promoting congruence with the current environment. In addition, a key prerequisite involves the peer-reviewed nature of the articles, underlining a commitment to academic rigor.

Also, one of the main inclusion criteria was the selection of articles that provided a specialized exploration in the field of monitoring and measurement systems for daily activities. At the same time, studies that focused on treatment modalities without patient data acquisition, such as musical therapies, were omitted. On this path, the exclusion criteria operated with a precision that aimed to filter out studies carried out on cohorts that go beyond the sphere of the elderly, as well as those that focus on pharmacological or non-technological interventions. Articles written in languages other than English and Portuguese are part of this exclusion list, as are duplicate studies considered redundant in the analytical context. Systematic reviews, meta-analyses, editorials, journal articles, magazine articles and book chapters were also excluded as well as duplicates. These criteria together ensure a precise and exhaustive selection process.

2.4. Quality Criteria

The selection process for the articles in this study was also based on a set of quality criteria, with the aim of guaranteeing the integrity and credibility of the research results. First, priority was given to studies with a representative sample of elderly people with dementia. However, it was realized that large samples became difficult in some studies, due to the lack of necessary authorization from the elderly themselves or their guardians. Therefore, studies that did not need a very large sample to prove their effectiveness were also included, as well as studies that were applied only to caregivers and healthy people.

In addition, the quality criteria gave priority to studies that incorporated meticulously validated and reliable measurement systems, guaranteeing the solidity of the data collected. In addition, the evaluation process embraced studies that employed methodologies capable of minimizing potential bias, both in terms of selection and confounding factors.

Strategies such as randomization and pairing were considered, supporting the commitment to methodological robustness and rigour in the search for meaningful knowledge.

3. Results

After the research process and an exhaustive evaluation, considering all of the stablished criteria, a collection of 8 articles was selected for final analysis. These carefully selected articles will be presented in the following subsection, organized in Table 1 and providing a comprehensive overview of each article.

3.1. Characteristics of the Selected Studies

This section presents a detailed overview of the articles chosen. Table 1 contains vital information, including the titles of the articles, the main characteristics of the studies and the types of technology used. The articles were also identified in the table for future reference in the review. The aim of this tabulated presentation is to provide a clear reference point for next researches and reviews, ensuring easy accessibility to the relevant details. The following subsection will look in depth at the conclusions and results of these studies.

Table 1. Selected articles.

Article	Title	Type of Technology	Characteristics
A1 [10]	Audio Based Action Recognition for Monitoring Elderly Dementia Patients	Audio capture and action recognition with deep learning	Usage of two hardware devices (Raspberry Pi 4B and ReSpeaker sensor). Usage of a Convolutional Neural Network. Usage of MQTT protocol to transmit the data to the backend platform.
A2 [11]	Development of a Sensor-Based Behavioral Monitoring Solution to Support Dementia Care	Wearable Sensor Technology	Study carried out with 5 healthy people, using a smartwatch and a smartphone with google APIS. The research focused on obtaining location, step count and activity recognition data.
A3 [12]	Evaluating the Use of Daily Care Notes Software for Older People with Dementia	Daily notes system via mobile devices and desktops	The survey was carried out using the Yammer Software application, with 18 caregivers, 2 team leaders and 13 patients of a residential home, as well as other health professionals who also had access to the notes.
A4 [13]	Geofencing Technology in Monitoring of Geriatric Patients Suffering from Dementia and Alzheimer	Geofencing surveillance system	Patient monitored by a GPS device. If the monitored area is exceeded, the distance between the elderly person and the nearest caregiver is calculated using the Haversine method.
A5 [14]	Monitoring behavioral symptoms of dementia using activity trackers	Personalized Behavioral Symptom Monitoring with Activity Trackers	9 elderly people and 8 caregivers participated in the study. Two smartwatch models were used to collect data on steps per minute, heartbeats per minute and minutes of sleep. The data sought to evaluate behavioral changes related to dementia in participants in Cognitive Stimulation Therapy using the Eva robot.
A6 [15]	Monitoring Behaviors of Patients with Late-stage Dementia Using Passive Environmental Sensing Approaches: A Case Series	Unobtrusive activity-sensing technologies to track behavioral markers	Platform gathered participant data, including sensors under mattresses, movement sensors and actigraphy devices; other participants used Emerald sensors. Data correlated with medication, assessed by caregivers and doctors.
A7 [16]	Portable EEG monitoring for older adults with dementia and chronic pain - A feasibility study	Pain monitoring through a portable EEG device	Use of a portable headband for EEG measurement. Sample of 5 elderly people in an institution. The device is connected to a smartphone or other device capable of receiving data. The device was placed on different days, monitoring the level of pain perceived by the subjects.
A8 [17]	The feasibility of a vision-based sensor for longitudinal monitoring of mobility in older adults with dementia	Vision-based sensor for tracking	Study with 18 institutionalized elderly people. The setup included a Microsoft Kinect, a laptop computer, a radio frequency identification reader and two circularly polarized UHF antennas. Walking sequences were recorded, analyzed, and gait parameters extracted.

Among the articles identified, a trend emerges in which three of them [12, 16, 17] mainly investigate the feasibility of using the technologies mentioned, rather than the details of the systems themselves. Although these studies do not focus precisely on the architecture of each system, they do shed light on the operational dynamics of such technologies and their potential acceptance by patients. This analysis, which encompasses the evaluation of these aspects, aligns with the focus of this review.

Studies A2, A5, A6, and A7 utilized devices directly connected to the patients. Study A3 was unique in its use of a technology managed solely by caregivers. Additionally, studies A1, A4, A6, and A8 implemented remote monitoring technologies, eliminating the necessity for the elderly to carry a device.

In terms of monitoring methodologies, the research landscape reveals different facets. Study A1 is the only one to propose audio capture and subsequent

recognition for activity assessment. Studies A2 and A4 converge on geolocation strategies adapted to elderly people with dementia. With similar objectives, A2 and A5 orchestrated pedometer technology to assess ambulatory activity. Expanding the research repertoire, A2 emerged as a singular effort to delineate activities through sensor-activated inference. Instead of automated processes, A3 introduced a caregiver-mediated annotation system, facilitated by a smartphone app. Both A2 and A6 orchestrated the acquisition of sleep patterns, while A5 ventured into heart rate monitoring. A6 and A8 used motion sensors to obtain data, although the A8 study tried to track the gait of each patient. Interestingly, A7 made unique use of a portable EEG device to discern pain levels.

3.2. Presentation of Results

While limited in scope, the initial study (A1) [10] achieved a noteworthy 98 % accuracy in the audio capture, forwarding data to discern basic activities. Ongoing enhancements are warranted, including broadening recognized activities and minimizing sensor dimensions.

The second study (A2) [11], although successful in tracking behavior at home and identifying patterns, aiding predictive models and personalized interventions for dementia care, still needs to return this data to the health system in order to prove the real effectiveness of each of them in improving the quality of life of individuals. Furthermore, the success of studies carried out on healthy people may still run into a number of problems if carried out on people who have all the difficulties that dementia can offer.

The A3 study [12], although not giving details of the system adopted, shows the successful adoption of the software by care providers. Positive results include an increase in the volume of daily care notes, improved readability, greater accessibility and better preparation for activities. Usability considerations are highlighted, with the versatility of the software being crucial to overcoming barriers. Furthermore, the alignment of policies and technologies remains a challenge. Finally, as this is a study that relies on manual data input, it still needs research and evaluation of the best ways to maintain the reliability of the information collected,

The fourth study (A4) [13] used the Haversine distance calculation and a notification system to manage proximity between the care provider and the patient. Although generally successful, two trials failed due to inaccuracies in the distance calculation. The dependence of the mobile device system on GPS signals led to lower accuracy. A further disadvantage emerged: the system does not monitor immobile patients. Future research was suggested that could include alerts of dangerous areas and notifications of patient immobility, as well as improving the effectiveness of GPS.

The A5 study [14] demonstrates the successful adoption of activity monitors by patients and caregivers for the assessment of dementia-related symptoms. Activity monitors provide valuable data on behavioral symptoms such as depression and apathy. Incorporating new sensors or raw data could improve the monitoring of other symptoms. Challenges include accuracy due to the limitations of the devices. Future research could explore advanced sensors and environmental data. Accelerometer raw data could estimate physical agitation and spatio-temporal gait parameters related to the risk of depression and dementia. The raw data would also allow for better monitoring of mobility and sedentary activity. The article also suggests incorporating microphones to assess socialization and including waterproof devices that are easier to use.

The sixth article selected (A6) [15] is a case series demonstrating the potential of discrete activity detection technology for monitoring people with dementia in their natural living environments. The technology implemented offered continuous, privacy-preserving data with the appropriate clinical implications, including the identification of behavioral changes and medication effects. The study also identified the need for further research to validate behavioral markers, guarantee privacy and establish transparency.

A7 study [16] suggests that changes in pain-related brain regions are associated with changes in spontaneous brain activity, which may indicate pain processing. Portable EEG devices, such as the one used in the study, could serve as a low-cost, non-invasive tool for assessing pain in people with dementia. However, the small sample size and technical limitations of the study warrant further research for robust clinical applications. The feasibility of obtaining EEG data from residents with dementia was demonstrated, opening up the possibility of EEG being a biomarker of pain for those who are unable to communicate. Finally, the article indicates that larger studies are needed to validate these results and compare portable EEG with medical-grade EEG for pain assessment.

Finally, the last study (A8) [17] demonstrates the feasibility of using the vision-based tool to longitudinally monitor gait in people with dementia. The tool successfully collected and analyzed gait data, providing information on walking patterns and gait measurements. This approach offers potential to improve falls risk assessment in long-term care by detecting changes in mobility patterns that may precede health events. Although portable sensors have limitations, vision-based systems such as AMBIENT are promising. Opportunities for improvement presented include refining participant identification methods, improving sensor placement and automating data processing.

4. Discussion

Emerging technologies designed to measure and monitor activities hold great promise for improving care for older people with dementia, offering transformative improvements in care approaches and

alleviating difficulties for caregivers. Although each study presents its own insights and conclusions, a common thread emerges: technology has the power to improve patient outcomes, simplify processes and provide valuable data for informed decision-making.

The technologies examined in this analysis highlight the diverse range of applications in the field of elderly care. Although the analysis has maintained a specific focus on activity measurement and monitoring systems with data capture capabilities, it is clear that there is a dearth of comprehensive experience and studies in this area. It is undeniable that certain technologies need significant improvement, especially given the specific needs of individuals with dementia. From the discomfort caused by conventional smartwatches [14] to the mobility limitations that arise [13], it is clear that there is an understanding of the specialized obstacles that require resolution.

It is important to note that one of the studies under review focused in particular on the dyadic relationship between people with dementia and their caregivers [12], highlighting the key role of caregiver involvement [18]. This underlines the emphasis of research on the need to adequately prepare and integrate caregivers in the assessment and training of these technologies.

Finally, in the larger context, these technologies have the potential to launch a new era of personalized and economically efficient dementia care, facilitating timely interventions and simultaneously contributing to the reduction of hospitalization rates [15].

5. Final Remarks

The integration of technologies presents a promising avenue for improving the well-being of the geriatric population affected by dementia. Technological implementations show favourable results by providing auxiliary support to the elderly and their caregivers in the field of daily activities, while facilitating the assessment and optimization of medical interventions. Given the rapid pace of demographic ageing, the increasing prevalence of dementia and the concomitant expense of providing care, monitoring technologies are set to play a key role in the daily lives of older people with dementia and their caregivers.

Empirical evidence underlines the satisfactory implications of monitoring paradigms, while at the same time highlighting the need for improvement. The use of pre-existing devices that interact seamlessly with common smartphones and smartwatches is clearly an economical and effective resource. However, the emergence of more sophisticated modalities, such as audio recognition systems, requires greater investment in research to discern their effectiveness. Given the lack of comprehensive experimental research with substantial cohorts of participants, and recognizing the profound implications for older people affected by dementia and their caregivers, the impetus for further exploration in this field is clearly appropriate.

Acknowledgements

This work was financed by the financed by national funds, through FCT - Foundation for Science and Technology and FCT / MCTES under the project UIDB/05549/2020, UIDP/05549/2020, CEECINST/00039/2021 and LASI-LA/P/0104/2020.It was also funded by the Innovation Health From Portugal, co-funded from the "Mobilizing Agendas for Business Innovation" of the "Next Generation EU" program of Component 5 of the Recovery and Resilience Plan (RRP), concerning "Capitalization and Business Innovation", under the Regulation of the Incentive System "Agendas for Business Innovation".

References

[1]. C. Webster, What is dementia, why make a diagnosis and what are the current roadblocks?, *World Alzheimer Report*, 2021.

[2]. J. C. Maia, *et al.*, Tecnologias assistivas para idosos com demência: revisão sistemática, *Acta Paul. Enferm*., Vol. 31, Issue 6, 2018, pp. 651–658 (in Portuguese).

[3]. World Health Organization, https://www.who.int/news-room/fact-sheets/detail/dementia

[4]. M. Matsangidou, *et al.*, 'Bring me sunshine, bring me (physical) strength': The case of dementia. Designing and implementing a virtual reality system for physical training during the COVID-19 pandemic, *International Journal of Human-Computer Studies*, Vol. 165, 2022, 102840.

[5]. T. Fulmer, N. Li, Age-Friendly Health Systems for Older Adults With Dementia, *The Journal for Nurse Practitioners*, Vol. 14, Issue 3, 2018, pp. 160-165.

[6]. H. Donato, M. Donato, Etapas na Condução de uma Revisão Sistemática, *Acta Médica Portuguesa*, Vol. 32, 2019, 227 (in Portuguese).

[7]. C. Okoli, A Guide to Conducting a Standalone Systematic Literature Review, *CAIS*, Vol. 37, 2015.

[8]. A. Pollock, E. Berge, How to do a systematic review, *International Journal of Stroke*, Vol. 13, Issue 2, 2018, pp. 138-156.

[9]. E. Linares-Espinós, *et al.*, Methodology of a systematic review, *Actas Urológicas Españolas (English Edition)*, Vol. 42, Issue 8, 2018, pp. 499-506.

[10]. D. K. Basuki, R. Zull Fhamy, M. I. Awal, L. Hakim Iksan, S. Sukaridhoto, K. Wada, Audio Based Action Recognition for Monitoring Elderly Dementia Patients, in *Proceedings of the International Electronics Symposium (IES'22)*, 2022, pp. 522-529.

[11]. J. R. Thorpe, B. H. Forchhammer, A. M. Maier, Development of a Sensor-Based Behavioral Monitoring Solution to Support Dementia Care, *JMIR Mhealth Uhealth*, Vol. 7, Issue 6, 2019, e12013.

[12]. N. Maiden, K. Pitts, K. Pudney, K. Zachos, Evaluating the Use of Daily Care Notes Software for Older People with Dementia, *International Journal of Human-Computer Interaction*, Vol. 35, Issue 7, 2019, pp. 605-619.

[13]. E. R. Pratama, F. Renaldi, F. R. Umbara, E. C. Djamal, Geofencing Technology in Monitoring of Geriatric Patients Suffering from Dementia and Alzheimer, in *Proceedings of the 3rd International Conference on Computer and Informatics Engineering (IC2IE'20)*, 2020, pp. 106-111.

[14]. J. Favela, D. Cruz-Sandoval, A. Morales-Tellez, I. H. Lopez-Nava, Monitoring behavioral symptoms of dementia using activity trackers, *Journal of Biomedical Informatics*, Vol. 109, 2020, 103520.

[15]. W.-T. M. Au-Yeung, *et al.*, Monitoring Behaviors of Patients With Late-Stage Dementia Using Passive Environmental Sensing Approaches: A Case Series, *The American Journal of Geriatric Psychiatry*, Vol. 30, Issue 1, 2022, pp. 1-11.

[16]. L. Pu, K. M. Lion, M. Todorovic, W. Moyle, Portable EEG monitoring for older adults with dementia and chronic pain – A feasibility study, *Geriatric Nursing*, Vol. 42, Issue 1, 2021, pp. 124-128.

[17]. E. Dolatabadi, Y. X. Zhi, A. J. Flint, A. Mansfield, A. Iaboni, B. Taati, The feasibility of a vision-based sensor for longitudinal monitoring of mobility in older adults with dementia, *Archives of Gerontology and Geriatrics*, Vol. 82, 2019, pp. 200-206.

[18]. A. E. Harper, *et al.*, A Systematic Review of Tools Assessing the Perspective of Caregivers of Residents With Dementia, *J. Appl. Gerontol.*, Vol. 41, Issue 4, 2022, pp. 1196-1208.

(057)

Virtual Reality and Artificial Intelligence as Tools to Aid the Management of Chronic Pain: A Comprehensive Literature Review

Arthur Gomes [1], Anabela Marques [2], Vítor Carvalho [1] and Duarte Duque [1]
[1] 2Ai – School of Technology, IPCA, Barcelos, Portugal
[2] CHEDV - Centro Hospitalar de entre Douro e Vouga, E.P.E.
Tel.: +351 253 802 260
E-mail: a24200@alunos.ipca.pt, anabela.marques@chedv.min-saude.pt, vcarvalho@ipca.pt, dduque@ipca.pt

Summary: Chronic pain is a healthy issue affecting millions of people, in which conventional treatments demand the use of medication and considerable discipline from patients. Emerging technologies based on virtual reality (VR) and artificial intelligence (AI) have the potential to improve the efficiency of such treatments and pain management techniques. To comprehend what are the most promising chronic pain management practices based on these technologies, as well as the gaps in their development, this study aimed to produce a literature review on the subject. We employed a systematic search strategy for peer-reviewed studies, published in English language, from 2018 to 2023, targeting relevant electronic databases and applying a combination of keywords and Boolean operators. VR is proved to distract individuals from their pain, promote relaxation, and enhance engagement in therapeutic activities, while AI algorithms demonstrated the potential to personalize treatment plans. However, new research is necessary to establish the optimal protocols, guidelines, and cost-effectiveness of these interventions.

Keywords: Virtual reality, Artificial intelligence, Chronic pain, Review, Therapy.

1. Introduction

Chronic pain has emerged as a pervasive and complex health challenge, affecting millions of individuals worldwide. Characterized by its persistence and endurance beyond the normal healing process, it exerts a substantial toll on both physical well-being and overall quality of life. Conventional methods of pain management encompass pharmaceutical interventions and physical therapy, aiming to alleviate discomfort and restore functionality. However, the multifaceted nature of chronic pain often demands a more comprehensive and innovative approach.

In recent times, the integration of emerging technologies has stimulated a paradigm shift in chronic pain management. Virtual reality (VR) and artificial intelligence (AI) are at the forefront of this transformative journey, offering promising avenues for addressing the intricate aspects of chronic pain that extend beyond the scope of traditional treatments. VR, which immerses users in simulated environments, and AI, which processes complex data to derive insights, have garnered attention as potential complementary tools in the holistic treatment of chronic pain [1].

As the understanding of this problem deepens, so does the appreciation for treatments that encompass a wider spectrum of approaches. In this context, the integration of VR and AI aligns with the growing emphasis on personalized and patient-centric care. These technologies have the potential to empower individuals by providing tailored interventions that target not only the physical manifestations of pain but also the psychological and emotional dimensions that often accompany it. By engaging patients in immersive experiences that distract from pain or facilitate relaxation, VR offers a novel dimension to management strategies.

Furthermore, AI-driven systems, leveraging data analytics and machine learning, hold promise in optimizing pain assessment and treatment plans. These technologies can decode intricate patterns in pain experiences, enabling healthcare providers to customize interventions that align with the unique needs of each patient. Such tailored approaches are a marked departure from the one-size-fits-all methodologies of the past.

The integration of VR and AI into chronic pain management is not only evidence to the evolving landscape of healthcare but also a reflection of the growing synergy between technology and medicine. These advancements carry the potential to enhance treatment outcomes, reduce reliance on traditional pharmacological interventions, and alleviate the burden of chronic pain on individuals and healthcare systems alike. However, as with any novel approach, thorough investigation, empirical validation, and ethical considerations remain crucial to realizing the full potential of VR and AI in this domain.

The objective of this study is to explore the current state of knowledge regarding the use of VR and AI in the treatment and relief of chronic pain, by conducting a comprehensive literature review. Specifically, the review aims to identify existing research, highlight identified problems, assess the efficacy of different interventions, and identify promising practices to tackle this persistent global health challenge.

To achieve these objectives, a comprehensive search strategy was employed, targeting the relevant electronic databases *B-On* and *PubMed*, where the combination of keywords and Boolean operators "*chronic pain management or chronic pain relief or chronic pain control or chronic pain reduction AND virtual reality or vr or augmented reality or artificial intelligence or ai or a.i.*" was used to select the applicable studies. The search was also limited to peer-reviewed articles, book chapters, and conference papers published in English between 2018 and 2023.

As result of application of the search criteria, 139 studies were found, 32 of which were deemed as eligible and included in review, according to the flow diagram [2] presented in Fig. 1.

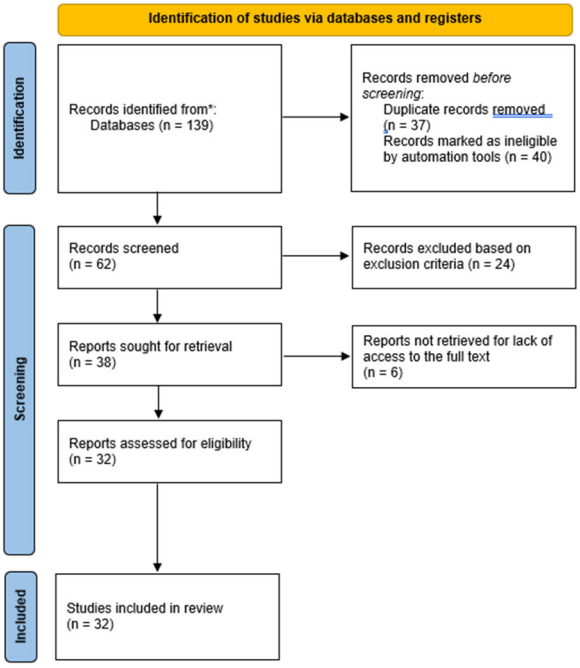

Fig. 1. PRISMA flow diagram for new reviews which included searches of databases.

The paper is organized in 3 sections. Section 2 presents the selected studies included in the literature reviewed performed and Section 3 draws the final comments and remarks of the performed study.

2. Overview of the Included Studies

The 32 eligible studies included in this review encompassed a wide range of research designs, which can be divided in two major groups: (i) Clinical Trials and Pilot Studies on VR/AI Interventions; and (ii) Literature Reviews, Meta-Analyses, and Perspectives on VR/AI in Pain Management.

The use of artificial intelligence in chronic pain assessment and treatment was explored only in one of the included studies, in which D. Kringel et al. [3] demonstrated the AI algorithms potential to identify pain patterns and personalize treatment plans based on individual patient data, including genetic information. Machine learning techniques were employed to analyze large datasets and develop predictive models for pain outcomes. This AI-based approach showed promise in improving pain assessment accuracy and optimizing treatment strategies.

On the other side, the vast majority of the studies explored diverse aspects of using VR as an intervention method in the management and treatment of chronic pain.

2.1. Clinical Trials and Pilot Studies on VR/AI Interventions

This group includes studies that involve conducting clinical trials or pilot studies to evaluate the effectiveness of VR/AI interventions for managing and treating chronic pain.

Most of the studies were designed as Randomized Controlled Trials (RCT), dividing participants into a control group, a VR intervention group, and, in some cases, a traditional treatment group, so the results collected during or after the interventions could be compared.

N. Tuck et al. [4] included patients being aged 18 to 70 years with broad musculoskeletal pain conditions in their trial, while other studies chose to observe the effects of the interventions in a narrower scope of participants, such as pediatric patients [5] or people who suffer from very specific conditions (e.g., pain associated to a disease of rheumatological origin [6], endometriosis-related pelvic pain [7], and chronic joint pain associated with hemophilic arthropathy [8]).

L. Riera et al. [6] and F. J. Perales et al. [9] explored not only the impacts of a VR system for pain management, but also the use of binaural acoustic stimulations during the interventions, what could create an even more immersive environment, finding out that the combination between VR and binaural beats sessions produced a greater decrease in the perception of pain.

H. Fu et al. [10] studied the management of chronic pain through guided meditation enhanced by the use of VR systems. Through the measure of electroencephalograph activity, the study detected that the session altered neurophysiological brain signals, which were not necessarily associated with pain.

B. D. Darnall et al. [11] evaluated the feasibility of a self-administered skills-based VR program, concluding that using VR for pain management was associated with positive outcomes, since participants reported minimal adverse effects, high satisfaction with the VR experience, and improvements in various pain-related measures such as pain intensity, pain interference, sleep, mood, and stress, increasing their overall well-being.

A wide range of VR devices and applications, body sensors, and software have been utilized in pain management and rehabilitation research. These technologies encompass VR headsets produced by

different manufacturers, VR applications available at the market and others developed specifically for the studies, which tried to fill the patients' needs and the circumstances derived from their medical condition.

In this context, P. Brown et al. [12] compared the results achieved by patients submitted to an immersive and interactive experience *vis-à-vis* those submitted to a non-immersive controlled experience with no interaction. The researchers concluded that technological immersion alone is not enough to induce VR-analgesia. It is the kind of content and the degree of presence generated by this content that seems to facilitate the analgesic response.

Performing qualitative research for cancer patients suffering from chronic pain perceptions of VR therapy, B. M. Garrett et al. [13] found out that participants tended to fall into two preference categories: those favoring contemplative and meditative environments, and those engaging in cognitive problem-solving scenarios. Notably, a particular problem-solving game was found to worsen pain for some individuals, indicating that many current VR applications, designed for recreation, might not be suitable for pain management due to their content, while designs integrating positive environments, natural elements, and soothing soundscapes could potentially yield better results.

A. Griffin et al. [5] developed a specific VR intervention application to improve mobility and manage chronic pain among pediatric patients, which was well-received and deemed acceptable, feasible, and engaging by the participating youth. Qualitative feedback from patients and parents highlighted the engagement in previously unattainable activities, the distraction provided by VR, and the perception of therapies with VR as enjoyable and fun.

Several studies reported positive outcomes in using VR for reductions in opioid consumption, pain severity, and pain interference, while improving patients' daily physical activity, strength, sitting and standing tolerances, and confidence.

Moreover, participants generally found the VR experiences engaging, and adherence to VR-based treatments was noted, while collateral effects (e.g., cybersickness, nausea) were deemed unusual. This indicates that VR can be a well-received and feasible option in pain management strategies.

However, due to the lack of long-term follow-up in most of the studies, it is not possible to properly assess if the positive effects observed are sustained in time or if they are limited to a short period.

Nevertheless, a study conducted by F. S. de Vries, R. T. M. van Dongen, and D. Bertens [14] offers insightful observations in this regard. Notably, their study revealed that beyond the treatment phase, a significant portion of the participants experienced a continued reduction in pain intensity. This finding implies the potential for sustained benefits even after the active intervention period, highlighting the need for further investigations that delve into the durability of these effects over extended periods.

2.2. Literature Reviews, Meta-Analyses, and Perspectives on VR/AI in Pain Management

This group encompasses studies that review existing literature, perform meta-analyses, and provide perspectives on the use of virtual reality in pain management.

In this context, P. D. Austin [1] developed a scoping review about the analgesic effects of VR for people with chronic pain. The study covered a range of primary and secondary chronic pain conditions and used a variety of different computer screen and headset protocols, including gaming, mindfulness, exercise, relaxation, and proprioceptive skills.

The researcher concluded that VR is deemed to be an effective analgesic intervention for people with chronic pain, given user satisfaction, a lack of side effects such as cybersickness, and relief of comorbid symptoms, what is agreed by L. Goudman et al. [15]. However, it was pointed out that VR intervention study methods remain heterogeneous and exploratory in design, thus findings should be interpreted with caution.

Huang et al. [16], A. Pourmand et al. [17], and B. Mallari et al. [18], by their turn, alerted that there is insufficient evidence to support lasting analgesic effect in chronic pain, although identified potential to reduce pain in patients with chronic pain during VR exposure.

In the same line, C. Tack [19] affirmed that it was not demonstrated yet whether immersive VR can provide benefits beyond those seen with passive distraction for the treatment and management of chronic low back pain, while S. Grassini [20] noted the positive impact of VR therapy on chronic pain was comparable to that observed with other pain management interventions, such as physical exercise and laser therapy.

M. Alqudimat et al. [21] focused on the utilization of immersive technologies, primarily VR, for the management of pediatric chronic pain. The study reminds that while physical activity for children with this condition often poses challenges due to discomfort, engaging in such activities through immersive technology distracts them from pain, what could potentially improve pain tolerance. Furthermore, it highlights that incorporating features such as music, cues, rewards, and performance metrics in technology can motivate children to engage in painful movements.

The research also indicates that several pilot studies in pediatric populations demonstrated the feasibility and potential benefits of VR in managing pediatric chronic pain, what should be confirmed by further studies. In this sense, it was informed that the INOVATE-Pain consortium has outlined guiding principles for VR interventions in pediatric chronic pain with suggested measures and study procedures.

F. Rousseaux et al. [22] observed immersive VR as a tool for hypnosis techniques applied to the management of pain, reporting that the combination of Virtual Reality Hypnosis (VRH) with daily hypnosis exercises led to a notable reduction of 36 % in pain intensity and 33 % in pain unpleasantness for a patient

with chronic neuropathic pain, as demonstrated across 33 VRH sessions. Similarly, another patient experiencing pain related to gluteal hidradenitis observed a significant decrease in pain intensity within just two days following VRH intervention, resulting in a remarkable 62 % reduction.

In their study, S. O'Connor, A. Mayne, and B. Hood [23] concluded that the utilization of VR in mindfulness practices holds the potential to enhance chronic pain management. However, the review's outcomes were constrained in significance due to the presence of weak study designs and small sample sizes. To further assess its efficacy in enhancing overall health and various outcomes, future research should prioritize the meticulous co-design and thorough testing of VR-based mindfulness applications, engaging closely with individuals enduring chronic pain.

2.3. Challenges and Limitations

Despite the promising findings, several challenges and limitations were identified across the studies. One major limitation was the lack of standardized protocols and guidelines for using VR and AI in chronic pain management. The studies varied in terms of the VR interventions used, the AI algorithms employed, and the outcome measures assessed, making it difficult to compare and generalize the results.

A notable limitation encountered during this literature review was the scarcity of available articles and studies addressing the utilization of AI as a tool for the management and treatment of chronic pain. The dearth of research in this specific domain restricted the depth of analysis and comprehensive understanding that could be achieved, leaving certain aspects of this innovative approach relatively unexplored within the scope of the review.

Many studies faced limitations due to small sample sizes, also impeding the generalization of findings. Future research should prioritize larger multicenter randomized clinical trials with diverse populations to enhance the external validity of results. Addressing the variability of patient experiences with VR programs and considering previous VR exposure in statistical analyses could further refine the understanding of outcomes.

The temporal aspect of VR interventions was often constrained, with evaluations conducted immediately after sessions. Future studies should consider longer follow-up periods to assess both immediate and sustained effects. Incorporating placebo or active control groups can help establish the true impact of VR interventions, discern their most effective elements.

Some studies faced limitations related to the use of VR applications that were not specifically designed for the targeted condition. Future research should consider developing or adapting applications tailored to the specific pain type or context, enhancing the intervention's relevance and effectiveness.

Several studies reported higher attrition rates than anticipated, with reasons ranging from comorbid mental health issues to scheduling conflicts and pandemic-related disruptions. Strategies to improve recruitment and retention rates, such as providing more options for sessions or incorporating patient preferences, should also be explored.

Challenges related to blinding assessors and participants were noted, introducing potential bias. Implementing measures to blind assessors, even partially, and adopting rigorous methodologies can mitigate this limitation.

Lastly, technical issues such as inconsistent Wi-Fi, software timeouts, and lack of "kiosk modes" affected immersion and user experience, for future studies should focus on improving technical reliability and user-friendly interfaces to optimize the intervention's effectiveness.

3. Final Remarks

The results of this review suggest that both VR and AI hold promise for enhancing the management and treatment of chronic pain, even though there is a small number of research encompassing the use of AI. Specifically taking into consideration the studies based on VR interventions, which are broad and heterogeneous, evidence shows that such use can be effective as supplementary strategies across various chronic pain conditions.

The studies reviewed show that VR interventions can serve as distractions from pain owing to their immersive quality and as supportive aids to physiotherapy exercises. However, their efficacy varies based on individual factors such as patients' age, movement constraints, and the severity of underlying diseases. Additionally, the level of customization within VR programs to cater to specific treatment requirements also plays a role in determining their success.

Nevertheless, it is possible to conclude that further research is needed to establish the optimal protocols, guidelines, and cost-effectiveness of these interventions. Notably, it becomes imperative for future studies to extend their focus towards incorporating longer follow-up periods. By doing so, these studies can better evaluate and discern not only the immediate effects, but also the sustained impacts of the interventions being explored.

With continued advancements in technology and research, VR and AI may become integral components of chronic pain treatment and management strategies in the future.

Acknowledgments

This paper was funded by the project "NORTE-01-0145-FEDER-000042", supported by Northern Portugal Regional Operational Programme

(Norte2020), under the Portugal 2020 Partnership Agreement, through the European Regional Development Fund (ERDF).

References

[1]. P. D. Austin, The Analgesic Effects of Virtual Reality for People with Chronic Pain: A Scoping Review, *Pain Medicine*, Vol. 23, Issue 1, 2022, pp. 105-121.

[2]. M. J. Page, et al., The PRISMA 2020 statement: an updated guideline for reporting systematic reviews, *British Medical Journal*, Vol. 372, 2021, n71.

[3]. D. Kringel, et al., A machine-learned analysis of human gene polymorphisms modulating persisting pain points to major roles of neuroimmune processes, *European Journal of Pain*, Vol. 22, Issue 10, 2018, pp. 1735-1756.

[4]. N. Tuck, et al., Active Virtual Reality for Chronic Primary Pain: Mixed Methods Randomized Pilot Study, *JMIR Formative Research*, Vol. 6, Issue 7, 2022, pp. 1-12.

[5]. A. Griffin, et al., Virtual Reality in Pain Rehabilitation for Youth With Chronic Pain: Pilot Feasibility Study, *JMIR Rehabilitation and Assistive Technologies*, Vol. 7, Issue 2, 2020, e22620.

[6]. L. Riera, et al., Advances in the Cognitive Management of Chronic Pain in Children through the Use of Virtual Reality Combined with Binaural Beats: A Pilot Study, *Advances in Human-Computer Interaction*, Vol. 2022, 2022, pp. 1-10.

[7]. B. Merlot, et al., Pain Reduction with an Immersive Digital Therapeutic in Women Living with Endometriosis-Related Pelvic Pain: At-Home Self-Administered Randomized Controlled Trial, *Journal of Medical Internet Research*, Vol. 25, 2023, e47869.

[8]. R. Ucero-Lozano, et al., Approach to Knee Arthropathy through 180-Degree Immersive VR Movement Visualization in Adult Patients with Severe Hemophilia: A Pilot Study, *Journal of Clinical Medicine*, Vol. 11, Issue 20, 2022, pp. 6216-N.PAG.

[9]. F. J. Perales, et al., Evaluation of a VR system for Pain Management using binaural acoustic stimulation, *Multimedia Tools & Applications*, Vol. 78, Issue 23, 2019, pp. 32869-32890.

[10]. H. Fu, et al., Virtual Reality-Guided Meditation for Chronic Pain in Patients With Cancer: Exploratory Analysis of Electroencephalograph Activity, *JMIR Biomedical Engineering*, Vol. 6, Issue 2, 2021, pp. 1-21.

[11]. B. D. Darnall, et al., Self-Administered Skills-Based Virtual Reality Intervention for Chronic Pain: Randomized Controlled Pilot Study, *JMIR Formative Research*, Vol. 4, Issue 7, 2020, e17293.

[12]. P. Brown, et al., Virtual Reality as a Pain Distraction Modality for Experimentally Induced Pain in a Chronic Pain Population: An Exploratory Study, *Cyberpsychology, Behavior, and Social Networking*, Vol. 25, Issue 1, 2022, pp. 66-71.

[13]. B. M. Garrett, et al., Patients perceptions of virtual reality therapy in the management of chronic cancer pain, *Heliyon*, Vol. 6, Issue 5, 2020, e03916.

[14]. F. S. de Vries, R. T. M. van Dongen, D. Bertens, Pain education and pain management skills in virtual reality in the treatment of chronic low back pain: A multiple baseline single-case experimental design, *Behaviour Research and Therapy*, Vol. 162, 2023, 104257.

[15]. L. Goudman, et al., Virtual Reality Applications in Chronic Pain Management: Systematic Review and Meta-analysis, *JMIR Serious Games*, Vol. 10, Issue 2, 2022, pp. 1-21.

[16]. Q. Huang, et al., Using Virtual Reality Exposure Therapy in Pain Management: A Systematic Review and Meta-Analysis of Randomized Controlled Trials, *Value in Health*, Vol. 25, Issue 2, 2022, pp. 288-301.

[17]. A. Pourmand, et al., Virtual Reality as a Clinical Tool for Pain Management, *Current Pain & Headache Reports*, Vol. 22, Issue 8, 2018, pp. 53-60.

[18]. B. Mallari, et al., Virtual reality as an analgesic for acute and chronic pain in adults: a systematic review and meta-analysis, *Journal of Pain Research*, Vol. 12, 2019, pp. 2053-2085.

[19]. C. Tack, Virtual reality and chronic low back pain, *Disability & Rehabilitation: Assistive Technology*, Vol. 16, Issue 6, 2021, pp. 637-645.

[20]. S. Grassini, Virtual Reality Assisted Non-Pharmacological Treatments in Chronic Pain Management: A Systematic Review and Quantitative Meta-Analysis, *International Journal of Environmental Research and Public Health*, Vol. 19, 2022, 4071.

[21]. M. Alqudimat, et al., State of the Art: Immersive Technologies for Perioperative Anxiety, Acute, and Chronic Pain Management in Pediatric Patients, *Current Anesthesiology Reports*, Vol. 11, Issue 3, 2021, pp. 265-274.

[22]. F. Rousseaux, et al., Hypnosis Associated with 3D Immersive Virtual Reality Technology in the Management of Pain: A Review of the Literature, *Journal of Pain Research*, Vol. 13, 2020, pp. 1129-1138.

[23]. S. O'Connor, A. Mayne, B. Hood, Virtual Reality-Based Mindfulness for Chronic Pain Management: A Scoping Review, *Pain Management Nursing*, Vol. 23, Issue 3, 2022, pp. 359-369.

(058)

Using Machine Learning to Classify Network Abnormalities into Legitimate or Assault in IoT-based Cyber Physical System

Stephen Afrifa [1,2], Vijayakumar Varadarajan [3,4,5], Peter Appiahene [2] and Tao Zhang [1]
[1] Department of Information and Communication Engineering, Tianjin University, Tianjin 300072, China
[2] Department of Computer Science and Informatics, University of Energy and Natural Resources, Sunyani 00233, Ghana
[3] School of Computer Science and Engineering, University of New South Wales, Sydney, NSW 2052, Australia
[4] International Divisions, Ajeenkya D. Y. Patil University, Pune 412105, India
[5] School of Information Technology, Swiss School of Business Management, 1213 Geneva, Switzerland
Tel.: + 233247498261, + 919942057843
E-mails: afrifastephen@tju.edu.cn, v.varadarajan@unsw.edu.au

Summary: The use of Internet of Things (IoT) devices is a result of the massive number of messages carried through the internet. One of the most serious IoT threats is the botnet attack, which aims to commit legitimate, profitable, and effective cybercrimes. Three machine learning (ML) techniques are used in this study to create a system that detects legitimate or malicious communication in linked computer networks. The findings showed that random forest (RF) performed the best, with a coefficient of determination (R^2) of 0.9958. Despite the models produced considerable results, it was recommended that RF be utilized when detecting legitimate or malicious networks in IoT-connected computer networks. This research is critical for making educated decisions for long-term growth in industrial and educational networks.

Keywords: Machine learning, IoT, CPS, Deep learning, Network traffic.

1. Introduction

Cyber Physical Systems (CPS) are a synergistic blend of computing, networking, and physical processes. CPS models a wide range of systems, including intelligent critical infrastructures [1]. Indeed, the broad integration of CPS in vital infrastructures has increased their significance in assuring economic development, and as a result, their security and resilience have become important in many aspects of modern life. Researchers and developers discovered a means to fulfill Industry 4.0 goals by combining machine learning (ML) approaches with industrial processes that include intelligence [2]. The Internet of Things (IoT) is made up of millions of physical objects that are linked to the Internet through a network and execute tasks autonomously with little human intervention [3]. The proliferation of Internet of Things (IoT) technologies and their integration with CPS allows for improved monitoring, control, and administration of these systems [4]. However, due to the nature of the integrated IoT devices, such systems are becoming increasingly vulnerable to component failures as well as security assaults, since the underlying communication protocols employed might bring such new vulnerabilities into the system.

We examine how to distinguish component failures (which alter regular network behavior) from network assaults by evaluating channel characteristics in a computer networked system using unique machine learning models. The following are the primary contributions of this study, as adopted from [5, 6]:

1. We present an overarching Machine Learning (ML) framework that makes use of data gathered from computer networked IoT devices.
2. We use a simulation framework as well as a real-time testbed to assess the proposed framework for a variety of different classification algorithms.
3. We give cutting-edge contemporary performance assessment criteria for evaluating the performance of machine learning algorithms.

2. Related Works

A lot of researchers have conducted experiments to evaluate the resilience of CPS systems in IoT devices using ML models. To begin with, Khan et al. [7] proposed an innovative and safe architecture with a standardized process hierarchy/lifecycle for dispersed small and medium sized enterprises (SMEs) based on collaborative blockchain, internet of things (IoT), and artificial intelligence (AI) with machine learning (ML) techniques. They designed "BSMEs," a blockchain with an IoT enabled permissionless network topology that gives solutions to cross chain platforms. The B-SMEs handle the registration of participating SMEs, day-to-day information administration and exchange between nodes, and analysis of partnership exchange related transaction data before they are recorded on the blockchain immutable storage. In the IoT, Al-Wesabi et al. [8] developed a Pelican Optimization Algorithm with Federated Learning Driven Attack Detection and Classification (POAFL-DDC). For IoT threat detection, the POAFL-DDC approach used decentralized on-device data. Last but not least,

Alghamdi and Bellaiche [9] provided a multi-pronged classification strategy for a deep ensemble-based intrusion detection system (IDS) employing Lambda architecture. To distinguish between malicious and benign traffic, binary classification uses Long Short-Term Memory (LSTM), whereas multi-class classification employs an ensemble of LSTM, Convolutional Neural Network, and Artificial Neural Network classifiers to detect the kind of attack.

3. Materials and Methods

3.1. Data Collection

It is difficult to find an adequately tagged dataset for botnet identification. This study is based on a publicly available dataset from the FigShare data repository, which may be downloaded at https://doi.org/10.6084/m9.figshare.21769658.v1 (accessed on July 1, 2023). The dataset has already been labeled and is being analyzed for botnet identification. The data provided are used as a standard in the present study.

3.2. Data Preprocessing

The dataset was preprocessed in order to transform raw data into useful information for machine learning algorithms to grasp [10]. It is claimed that the data is generally incomplete and rife with inaccuracies. Handling null or missing values, label encoding, and feature selection are all processes in the preprocessing stage.

3.3. The Proposed Architecture

Fig. 1 depicts the proposed architecture for the study. The proposed machine learning models, which comprise the random forest (RF), support vector machine (SVM), and naïve bayes models, were used to train the dataset. The outcome shows either real or botnet traffic. This delivers an artificial intelligence-powered system that can detect it in real-time behavioral analysis, block it, and end any botnet activity.

3.4. The Data Division

The data was separated into training (70 %) and testing (30 %) sets. These are hyperparameters whose values govern the learning process and determine the model parameters that a learning algorithm learns [11]. The testing dataset aids in evaluating the models' performance.

3.5. The Machine Learning Algorithms

This study makes use of three conventional machine learning classifiers: RF, SVM, and NB. To create predictions or classifications, RF employs an ensemble of many decision trees. The random forest technique produces a more accurate result by mixing the outputs of various trees [12]. The SVM algorithm's purpose is to find the optimum line or decision boundary for categorizing n-dimensional space so that we may simply place fresh data points in the proper category in the future. A hyperplane is the optimal choice boundary [13]. Additionally, NB is a probabilistic classifier, which means it predicts based on an object's likelihood [14]. The developed algorithms can determine whether a network is real or botnet traffic to assist enterprises, government, and organizations in making educated judgments.

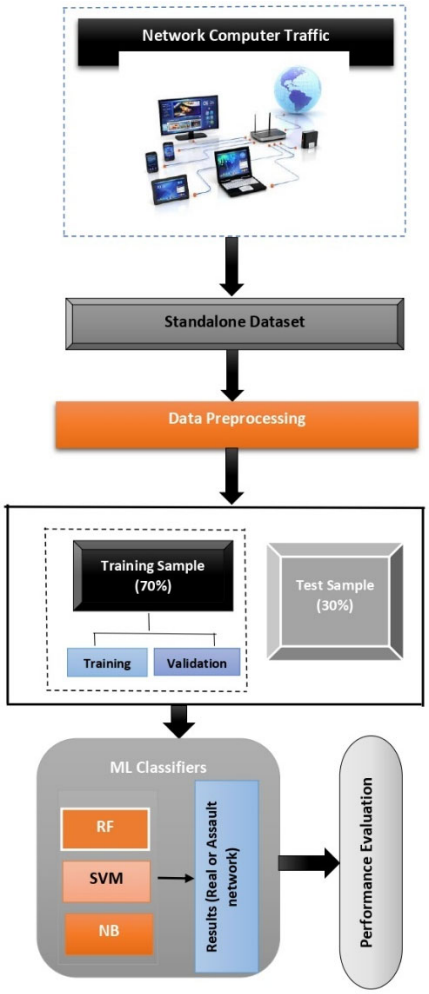

Fig. 1. The proposed architecture of the study.

3.6. Performance Evaluation Measures

The root mean squared error (RMSE), mean absolute error (MAE), mean absolute percentage error (MAPE), and coefficient of determination (R^2) were used to evaluate the performance of the machine learning models in the present study. The higher the R^2, thus, as it approaches 1, the better the accuracies and the lower the error scores, the better the performance of the models. The RMSE, MAE, MAPE, and R2 are represented by equations 1, 2, 3, and 4, respectively.

$$RMSE = \sqrt{\sum_{i=1}^{n} \frac{(y_{observed} - \hat{y}_{predicted})^2}{n}}, \quad (1)$$

$$MAE = \frac{1}{n} \sum_{i=1}^{n} \left| y_{observed} - \hat{y}_{predicted} \right|, \quad (2)$$

$$MAPE = \frac{100\,\%}{n} \sum_{k=1}^{n} \left| \frac{y_{observed} - \hat{y}_{predicted}}{y_{observed}} \right|, \quad (3)$$

$$R^2 = \left(\frac{\sum_{i=1}^{n} (y_{observed} - y_{average})(\hat{y}_{predicted} - \hat{y}_{average})}{\sqrt{\sum_{i=1}^{n} (y_{observed} - y_{average})^2 \sum_{i=1}^{n} (\hat{y}_{predicted} - \hat{y}_{average})^2}} \right)^2, \quad (4)$$

where $y_{observed}$ represents the observed values, $\hat{y}_{predicted}$ is the predicted values, n is the number of samples, $y_{average}$ and $\hat{y}_{average}$ represent the average observed and predicted values, respectively.

4. Experimental Results and Discussion

This section presents the results gained from the ML algorithms employed for the present study.

4.1. Performance of the ML Algorithms

The performance of various single machine learning models in the proposed architecture is shown in Table 1. Model performance differed little between the employed algorithms. According to the data, the RF had the highest performing metrics in terms of R^2 (0.9958) and the lowest error scores in all other metrics, including RMSE (0.0025), MAE (0.0652), and (0.0852).

Table 1. ML models performance and evaluation.

Model	Metrics	Results
RF	R2	0.9958
	RMSE	0.0025
	MAE	0.0652
	MAPE	0.0852
SVM	R2	0.9025
	RMSE	0.0035
	MAE	0.0721
	MAPE	0.8200
NB	R2	0.9159
	RMSE	0.0042
	MAE	0.0755
	MAPE	0.0865

According to Table 1, the NB obtained the second-best performing ML model. The NB had an R^2 of 0.9159, whereas the SVM had an R^2 of 0.9025. In terms of other performance categories, the NB also had the second-best error scores. Although all of the models earned substantial scores in all of the performance measures, the SVM performed the worst. According to this study, the RF is the best ML algorithm for recognizing legitimate or malicious communication in a linked computer network.

Additionally, the study's findings were compared to the state-of-the-art to assess the robustness of the models used. The RF used in the study outperformed a comparable study by Vimont et al. [15], while the NB outperformed Disha and Waheed [16] in accomplishing the same goal as this study. Furthermore, the study found that it is required to regularly check the functioning of connected computer networks in order to facilitate and improve communication. Computer networks are critical to modern society because they enable the transmission and sharing of information between individuals, groups, and objects.

5. Conclusion and Future Works

Computer networks have had a huge impact on society by providing global connectivity and information exchange. The utilization of Internet of Things devices has greatly changed communication, and hence digital communication. This study demonstrated that machine learning techniques are effective in detecting actual or malicious traffic in a connected computer network. The models used in this study produced considerable results, and their influence on providing a benchmark analysis for decision making is enormous.

The authors want to use deep learning techniques such as convolutional neural networks (CNN) and hybrid models such as random forest-convolutional neural network (RF-CNN) in the future.

Acknowledgements

The authors would like to express their appreciation to Adwoa Afriyie for her advice and help during the study. Our heartfelt thanks also go to Eric Afrifa and Malcolm Afrifa for their encouragement.

References

[1]. J. Vrchota, P. Řehoř, M. Maříková, M. Pech, Critical Success Factors of the Project Management in Relation to Industry 4. 0 for Sustainability of Projects, *Sustainability*, Vol. 13, Issue 1, 2021, 281.

[2]. D. Chatziparaschis, M. G. Lagoudakis, Aerial and Ground Robot Collaboration for Autonomous Mapping in Search and Rescue Missions, *Drones*, Vol. 4, Issue 4, 2020, 79.

[3]. J. Almalki, *et al.*, Enabling Blockchain with IoMT Devices for Healthcare, *Inf.*, Vol. 13, Issue 10, 2022, 448.

[4]. D. Shiny Irene, S. Indra Priyadharshini, R. Tamizh Kuzhali, P. Nancy, An IoT based smart menstrual cup using optimized adaptive CNN model for effective menstrual hygiene management, *Artif. Intell. Rev.*, Vol. 56, Issue 7, 2022, pp. 6705-6722.

[5]. S. Afrifa, V. Varadarajan, Cyberbullying Detection on Twitter Using Natural Language Processing and Machine Learning Techniques, *Int. J. Innov. Technol. Interdiscip. Sci.*, Vol. 5, Issue 4, 2022, pp. 1069-1080.

[6]. S. Afrifa, V. Varadarajan, P. Appiahene, T. Zhang, E. A. Domfeh, Ensemble Machine Learning Techniques for Accurate and Efficient Detection of Botnet Attacks in Connected Computers, *MDPI Eng*, Vol. 4, Issue 1, 2023, pp. 650-664.

[7]. A. A. Khan, A. A. Laghari, P. Li, M. A. Dootio, S. Karim, The collaborative role of blockchain, artificial intelligence, and industrial internet of things in digitalization of small and medium-size enterprises, *Sci. Rep.*, Vol. 13, Issue 1, 2023, 1656.

[8]. F. N. Al-Wesabi, *et al.*, Pelican Optimization Algorithm with Federated Learning Driven Attack Detection model in Internet of Things environment, *Futur. Gener. Comput. Syst.*, Vol. 148, 2023., pp. 118-127.

[9]. R. Alghamdi and M. Bellaiche, An ensemble deep learning based IDS for IoT using Lambda architecture, *Cybersecurity*, Vol. 6, 2023, 5.

[10]. S. Afrifa, T. Zhang, P. Appiahene, V. Vijayakumar, Mathematical and Machine Learning Models for Groundwater Level Changes : A Systematic Review and Bibliographic Analysis, *Futur. Internet*, Vol. 14, Issue 9, 2022, 259.

[11]. W. K. Adu, P. Appiahene, S. Afrifa, VAR, ARIMAX and ARIMA models for nowcasting unemployment rate in Ghana using Google trends, *J. Electr. Syst. Inf. Technol.*, Vol. 10, 2023, 12.

[12]. S. Afrifa, T. Zhang, X. Zhao, P. Appiahene, M. S. Yaw, Climate change impact assessment on groundwater level changes: A study of hybrid model techniques, *IET Signal Process.*, Vol. 17, Issue 6, 2023, e12227.

[13]. J. W. Asare, P. Appiahene, E. J. Arthur, S. Korankye, S. Afrifa, and E. T. Donkoh, Detection of anemia using conjunctiva images: A smartphone application approach, *Med. Nov. Technol. Devices*, Vol. 18, 2023, 100237.

[14]. P. Appiahene, J. W. Asare, E. T. Donkoh, G. Dimauro, R. Maglietta, Detection of iron deficiency anemia by medical images: a comparative study of machine learning algorithms, *BioData Min.*, Vol. 16, 2023, 2.

[15]. A. Vimont, H. Leleu, I. Durand-Zaleski, Machine learning versus regression modelling in predicting individual healthcare costs from a representative sample of the nationwide claims database in France, *Eur. J. Heal. Econ.*, Vol. 23, Issue 2, 2022, pp. 211-223.

[16]. R. A. Disha, S. Waheed, Performance analysis of machine learning models for intrusion detection system using Gini Impurity-based Weighted Random Forest (GIWRF) feature selection technique, *Cybersecurity*, Vol. 5, 2022, 1.

(059)

Vehicle Speed Measurement through Ground Vibrations Induced by Transverse Rumble Strips

D. Thanglerdsumpan [1], P. Wardkein [2] and L. Kirasamuthranon [3]
[1] Ruamrudee International School, Bangkok, Thailand
[2] Department of Telecommunications Engineering, School of Engineering,
King Mongkut's Institute of Technology Ladkrabang, Bangkok, Thailand
[3] Department of Electronics Engineering Technology, College of Industrial Technology
King Mongkut's University of Technology North Bangkok, Bangkok, Thailand
E-mail: [1] dhiraththanglerdsumpan@gmail.com, [3] Lersonk@kmutnb.ac.th

Summary: The likelihood and severity of a crash are directly related to the speed of vehicles. Therefore, vehicle speed measurement is crucial to ensuring road safety as they are key to enforcing speed limits. This paper proposes two new methods of vehicle speed measurement utilizing a novel means of ground vibrations induced by transverse rumble strips. A transverse rumble strip is a group of equally spaced raised strips perpendicular to the traffic. These strips serve as a safety measure to alert drivers of potential hazards on the road by inducing noise and vibrational feedback when driven over. The ground vibrations can be monitored by a geophone sensor and processed to obtain the time taken by a vehicle to travel from one strip to another. By knowing the time taken to travel over a certain distance between each strip, the proposed methods in this paper are able to calculate the speed of a passing vehicle. The two methods proposed in this paper differ in the way in which they obtain that time: one processes the time domain signal of ground vibrations directly, while the other processes the frequency domain signal obtained through a fast Fourier transform (FFT) algorithm.

Keywords: Rumble strips, Transverse rumble strips, Geophones, Frequency-domain, Time-domain, Vehicle speed measurement, Ground vibrations.

1. Introduction

According to the World Health Organization, "the number of road traffic deaths continues to rise steadily, reaching 1.35 million in 2016" [1]. Vehicles traveling at high speeds are among the deadliest things on the road. The vehicle's speed directly influences the crash's severity and the likelihood of death. As a result, many roads have speed limits. However, without proper enforcement, these speed limits render useless. Therefore, vehicle speed measurement is crucial to transportation engineering, as it helps enforce speed limits and ensure road users' safety. A wide variety of vehicle speed measurement methods are currently used today, radar sensors, embedded sensors, magnetic sensors, and monitoring of pavement deflections. Nonetheless, each of these methods has its advantages and disadvantages.

Currently, radar sensors are among the most popular methods of vehicle speed measurement. These sensors direct electromagnetic waves at a moving vehicle and observe a Doppler shift in the reflected wave to calculate the vehicle's speed [2]. This method is widely used since it is easy to use, relatively accurate, and available as a hand-held speed gun. However, these speed sensors' accuracy can suffer greatly depending on the weather. Moreover, these devices are exceedingly expensive to purchase and maintain.

Embedded sensors are another commonly used method. This method works by embedding two sensors — usually inductive loops, piezoelectric tubes, or pneumatic tubes [3] — a certain distance apart into the pavement. The vehicle's speed is calculated by dividing the distance between the two sensors by the difference in time between when the first and second sensors detect it. However, embedding these sensors into the pavement is a costly and disruptive process, as it requires cuts in the pavement.

Monitoring pavement deflections [4] is a comparatively novel method that uses geophones set a certain longitudinal distance apart on a stretch of pavement to obtain the difference in time that the different geophones detect
deflection at different points of the pavement. One key advantage of this approach is that it is non-intrusive, meaning it does not require a line of sight to the vehicle. However, a significant drawback of this method is that it requires bitumen pavements that are flexible enough for a passing vehicle to cause significant deflection. This method was first proposed by Ngoc Son Duong et al. in 2021.

Another relatively new method is the portable roadside magnetic sensor system for vehicle counting, classification, and speed measurement [5] developed by Saber Taghvaeeyan and Rajesh Rajamani in 2014. The sensor system consists of wireless anisotropic magnetic devices that are not required to be embedded in the roadway. Speed measurement is based on calculating the cross-correlation between longitudinally spaced sensors using frequency-domain signal processing techniques.

This research paper presents two new approaches for measuring vehicle speed. The methods are based on monitoring ground vibrations as vehicles drive over transverse rumble strips.

Transverse rumble strips are a set of equally spaced raised strips across the road that induces noise and vibration [6] when a vehicle passes over them. These strips serve as a safety measure to alert drivers of potential hazards on the road and prevent accidents. They are commonly found in urban areas, especially ahead of crosswalks, to warn drivers of pedestrians crossing the road. As proposed in this paper, the ground vibrations generated by vehicles passing over rumble strips can be used to measure vehicle speed.

There are a few similarities between the proposed methods in this paper and existing methods in the literature review. One is the utilization of geophones, similar to the monitoring pavement method [4], to monitor the pavement's motion caused by passing vehicles. One of the proposed methods also resembles the portable roadside magnetic sensor system for vehicle counting, classification, and speed measurement [5], using frequency-domain signal processing techniques to determine the speed of passing vehicles. These similarities suggest that the new methods may offer an alternative solution to existing methods and contribute to reducing the number of road traffic deaths by enforcing speed limits and ensuring road users' safety.

This paper is organized as follows. In Section 2, the scientific principles relating to the proposal of this paper, including the generation of ground vibrations when a vehicle passes over a set of rumble strips, the kinematic principle of speed, the mechanism of a geophone, and the amplifier circuit, are discussed. In Section 3, the two new methods of vehicle speed measurement — processing the time-domain signal of ground vibrations generated by a vehicle passing over transverse rumble strips and processing the frequency-domain signal of ground vibrations generated by a vehicle passing over transverse rumble strips — are proposed. In Section 4, the experimental results of speed measurements are presented, and conclusions are discussed Section 5.

2. Principles

2.1. Rumble Strips Induced Ground Vibrations Generated from Wheels Impacting the Pavement

As the tire rolls across a set of transverse rumble strips, it rolls up the raised surface of each strip and then falls back down, generating a peak in ground vibrations upon each impact with the ground [7], as seen in Fig. 1. The ground vibrations are captured in an electrical signal in relation to time. By obtaining two values: the distance d between identical points of two consecutive strips and the time T taken to travel that distance found in the time period of the electrical frequency, (1) can be used to calculate the speed s of the vehicle.

$$s = \frac{d}{T} \tag{1}$$

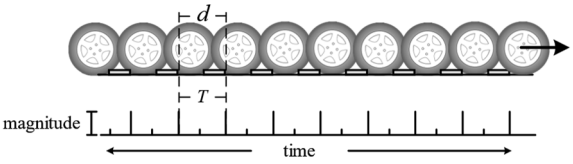

Fig. 1. Relationship between the movement of the tire across rumble strips and magnitude of ground vibrations in the time domain.

2.2. Capturing Ground Vibrations

Multiple methods exist for capturing ground vibrations; however, this research paper utilizes geophones placed on the ground for capturing ground vibrations generated by a moving vehicle across a set of rumble strips. The internal structure of a geophone comprises a conductive coil wrapped around a mass that is suspended over a stationary magnet placed in the center of the conductive coil, as depicted in Fig. 2. As the mass suspended over the magnet moves up and down due to ground vibrations, it causes electrons to move through the conductive coil, inducing a current. The resulting current produces an electrical signal corresponding to the ground's vibration.

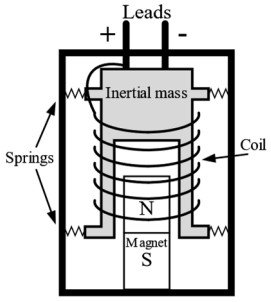

Fig. 2. Structure of a Geophone.

2.3. Amplifying Circuit

Due to the minuscule magnitude of ground vibrations induced by transverse rumble strips, an amplifying circuit is employed to amplify the voltage of the output signal from the geophones in the proposed methods of this paper. This amplifying circuit is an instrumentation amplifier, which is a type of differential amplifier [8]. Owing to its exceptional noise reduction capabilities, the instrumentation amplifier is the optimal choice for amplifying low magnitude ground vibrations from busy roads flooded with vibrational noise.

Fig. 3 displays the schematic of the most commonly used instrumentation amplifier, while (2) expresses the gain of the circuit.

$$Gain = \left(1 + \frac{2R_1}{R_G}\right)\frac{R_3}{R_2} \tag{2}$$

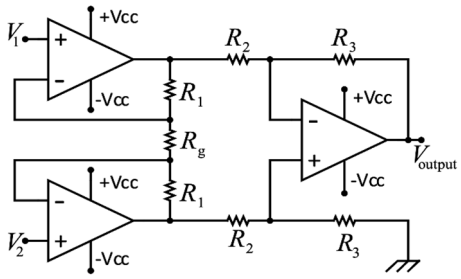

Fig. 3. Schematic of instrumentation amplifier.

3. Proposed Methods

This paper proposes two innovative methods for measuring vehicle speed, both utilizing a novel technique of using ground vibrations generated by a vehicle passing over a set of transverse rumble strips as a means of speed measurement. Despite both acquiring the ground vibration signal through a geophone and amplifying it, the two methods differ in the process of obtaining the time taken by the vehicle to travel from one strip to another. The first method calculates the time taken by processing signals in the time domain, while the second method calculates the time taken by processing signals in the frequency domain.

As noted in the principles section, when a vehicle traverses a set of rumble strips, it generates ground vibrations. To capture these ground vibrations, a geophone is placed on the roadside in a location relative to the rumble strips, as depicted in Fig. 4. The geophone produces an analog signal that is amplified by an instrumentation amplifier.

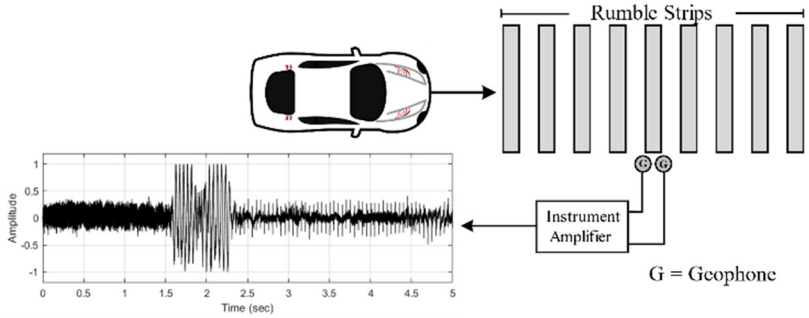

Fig. 4. Placement of geophones for vibration detection through the instrumentation amplifier. The analog signal is then converted into a digital signal using a sound card. The two methods differ after a digital signal is obtained.

3.1. Time Domain Processing

In this approach, the signal is plotted in the time domain and subsequently analyzed to determine the time t_T taken by the vehicle to travel from one strip to another. The principle of vibrations generated from wheels impacting the ground is applied to determine the time t_T. Specifically, t_T is calculated as the difference in the horizontal axis of two adjacent zero-crossings in the graph, as illustrated in Fig. 5. The obtained value of t_T is then utilized in (1) to compute the speed s, where d represents the distance from the start of one strip to the next.

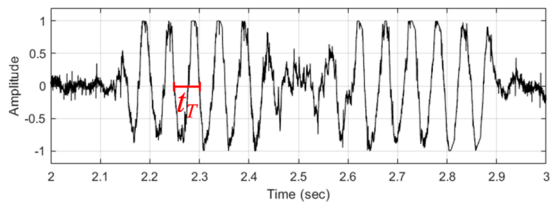

Fig. 5. Signal from the Geophones in the Time Domain.

3.2. Frequency Domain Processing

In contrast to the time domain processing method, this method obtains the value that is to be substituted into (1) for variable t through a spectral analysis rather than an analysis of the signal in its time domain. A spectrum is first obtained using the Fast Fourier Transform (FFT) algorithm to convert the signal into a frequency domain graph. The spectrum is then analyzed to determine the frequency of the highest magnitude, which would correspond to the frequency of the vibrations generated by the car going the rumble strips. From the frequency, the time which the car takes to travel from one strip to the next t_F can be substituted into (1) for variable t to calculate the speed s of the vehicle.

4. Experimental Results

Experiments were conducted to assess the accuracy of the proposed methods. This section presents the performance of the instrumentation amplifier used in the experiments and an analysis of the accuracies of the two proposed methods based on the results of the experiments.

4.1. Instrumentation Amplifier

An instrumentation amplifier is implemented in the experiment as proposed in the Principles section and as depicted in Fig. 3. The instrumentation

From Fig. 3, there are 7 resistors in the circuit of this instrumentation amplifier; in this experiment, R_1, R_2, and R_3 all have a resistance value of 10k ohm, while a variable resistor that has a range of resistance from 0 to 100 ohm is used for R_G. As a result of this specific design for the instrumentation amplifier, (2) can be rewritten as (3) to match the experiment.

$$Gain = 1 + \frac{20000}{R_G} \tag{3}$$

To determine the frequency response of the instrumentation amplifier, the amplifier was given an input of sinusoidal waves of 500 mV_{pp} amplitude with frequencies ranging from 0.1 to 10000 Hz. The experimental results of the frequency response of the instrumentation amplifier are displayed in Fig. 6. From Fig. 6, the amplifier used in this experiment has a constant gain for all frequencies under 10 kHz. As a result, this amplifier is suitable for the purpose of this research as the maximum frequency input to the amplifier is no more than 50 Hz.

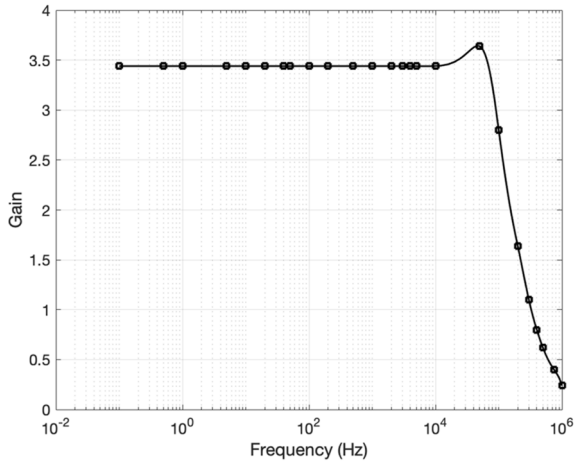

Fig. 6. Frequency Response of Instrumentation Amplifier.

4.2. Speed Measurement

In the experiments, the speed of a moving vehicle was measured using four different methods. Two of those methods were the two proposed in this paper. Meanwhile, the other two methods were looking at the vehicle's speedometer and using a radar gun. The driver used the speedometer to gauge the speed of the car while driving. On the other hand, the radar gun was used to obtain a reference speed to analyze the accuracy of the results of the proposed methods. The instrumentation includes:

- Two geophones placed 0.15 m apart in the center of the set of rumble strips.
- An instrumentation amplifier receiving input from the geophone and outputting to a soundcard in a computer.
- A set of rumble strips, as modeled in Fig. 7, containing nine strips.

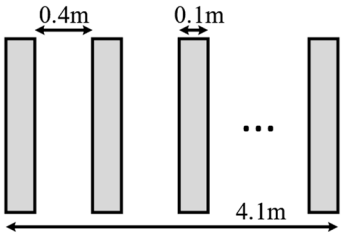

Fig.7. Diagram of Rumble Strips in Experiments.

Fig. 8 and Table 1 represent the results of the experiment. Fig. 8 shows examples of plotted signals that were used in the speed calculations. Each row contains signals of different speeds read from the speedometer. The top, middle, and bottom rows display the signals for 30, 40, and 50 km/h, respectively. Meanwhile, the left column shows the signals in the time domain, and the right column shows the signals in the frequency domain. From top to bottom, the time period for each time domain graph is 0.07, 0.05, and 0.04 seconds, respectively. On the other hand, from top to bottom, the tallest peak for the frequency domain graphs are 13.9, 19.3, and 24.5, respectively. Table 1 presents the average speed measured from the radar gun, time-domain method, and frequency-domain for each speedometer speed across the three trials.

The speedometer was used in the experiment to allow the driver to gauge their speed. However, the speed displayed on the speedometer does not reflect the true speed of the vehicle due to several reasons, such as changes in tire circumference due to use and environmental conditions. Therefore, measurements from a radar gun are used as the reference speeds instead. Fig. 9 presents the error or difference in kilometer per hours between the speed measured from the radar gun and the speeds measured from the time domain and the frequency domain methods. The time domain method had the smallest error (0 km/h) at 17 and 36 km/h and the largest error (-2 km/h) at 56 km/h. On the other hand, the frequency domain method had the smallest error (0 km/h) at 17 km/h and the largest error (-5 km/h) at 47, 56, and 75 km/h.

5. Conclusion

Vehicle speed measurement is crucial to ensuring traffic safety for road users, especially in urban areas where the number of vehicles and pedestrians is high. However, another thing that is also abundant in urban areas is transverse rumble strips, which are used to alert drivers of potential hazards ahead. This paper proposes two new speed measurement methods that utilize this abundance of transverse rumble strips by using geophones to collect the ground vibrations generated by a vehicle passing over them. The two methods — processing the time-domain and frequency-domain signals — are simple, inexpensive, portable, and can work in any weather conditions.

Moreover, the only sensors used in the methods are geophones, which are passive sensors, and therefore, allow the system to operate on low power until the process of signal processing and computations. Based on the outcomes of the experiments, the errors of the proposed vehicle speed measurement methods compared to a conventional radar gun fall within a range of 0 to 5 km/h difference. These variations are of minor magnitude, sufficiently validating the role of the proposed methods in contributing to traffic accident warning and preventative systems.

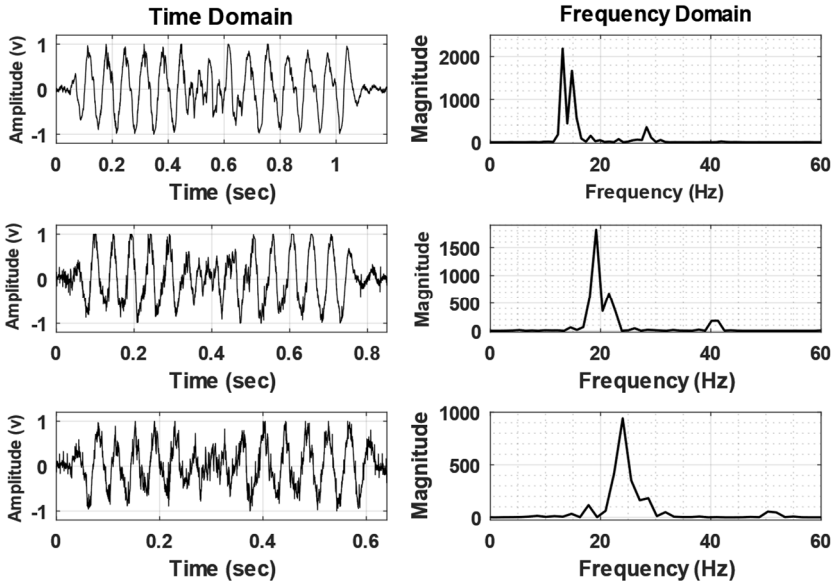

Fig. 8. Signals from Experiment.

Table 1. Average Frequencies and Speeds from Experiment.

Speedometer (km/hr)	Radar Gun (km/hr)	Time domain		Frequency domain	
		Speed (km/hr)	*Frequency (Hz)*	*Speed (km/hr)*	*Frequency (Hz)*
20	18	18.27	10.15	17.72	9.84
30	26	26.88	14.93	24.91	13.84
40	37	36.59	20.32	35.65	19.80
50	47	48.08	26.70	42.49	23.61
60	56	53.89	29.94	50.95	28.31
70	66	64.56	35.86	67.70	37.61
80	75	73.54	40.85	69.83	38.79

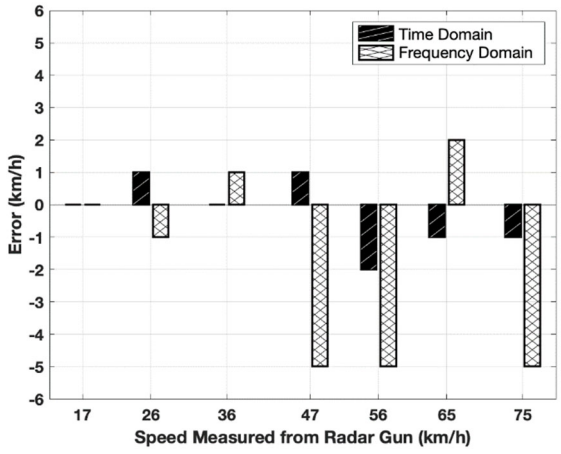

Fig. 9. Bar Graph Displaying Average Error of the Proposed Methods Compared to a Radar Gun from Experiment.

References

[1]. World Health Organization, Global status report on road safety 2018, *World Health Organization*, Geneva, 2018, December 2018, pp. 2-13.

[2]. IEEE Standard for the Performance of Down-the-Road Radar Used in Traffic Speed Measurements, IEEE Std 2450™-2019, *IEEE Instrumentation and Measurement Society*, November 2019.

[3]. M. Akram Adnan, N. Izzah Zainuddin, N. Sulaiman, and T. Badrul Hisyam Tuan Besar, Vehicle Speed Measurement Technique Using Various Speed Detection Instrumentation, in *Proceedings of the IEEE Business Engineering and Industrial Applications Colloquium (BEIAC' 2013)*, Langkawi, Malaysia, 07-09 April 2013, pp. 668-672.

[4]. N. S. Duong, J. Blanc, P. Hornych, F. Menant, Y. Lefeuvre, B. Bouveret, Monitoring of pavement deflections using geophones, *International Journal of Pavement Engineering*, Vol. 21, Issue 9, 7 Jun 2021, pp. 1103-1113.

[5]. S. Taghvaeeyan and R. Rajamani, Portable Roadside Sensors for Vehicle Counting, Classification, and Speed Measurement, *IEEE Transactions on Intelligent Transportation Systems*, Vol. 15, No. 1, Feb 2014, pp. 73-83.

[6]. R. L. Pimentel, R. A. Melo, I. A. Rolim, Estimation of increases in noise levels due to installation of transverse rumble strips on urban roads, Elsevier, *Applied Acoustics*, Vol. 76, Feb. 2014, pp. 453-461.

[7]. M. S. Zaina, M. H. Othmanb and *et al*, Evaluation of Ground Vibration Resulting from a Heavy Vehicle Passing Over Transverse Rumble Strips: A Case Study in Kluang Road FT050, *Jurnal Kejuruteraan*, Vol. 33, No. 3, 2021, pp. 654-650.

[8]. R. Boylestad, L. Nashelsky, Op-Amp Applications, in Electronic Devices and Circuit Theory, 11th ed., *Pearson*, 2009.

(061)

Static and Dynamic Calibration of Pneumatic Pressure Sensors and Instruments

José Dias Pereira [1,2] and Octavian Postolache [3]
[1] Instituto Politécnico de Setúbal, ESTSetubal, Sustain.RD, Setúbal, Portugal
[2] Instituto de Telecomunicações, Lisboa, 1049-001, Portugal
[3] Instituto de Telecomunicações IT-IUL, Instituto Universitário de Lisboa, Portugal
E-mail: dias.pereira@estsetubal.ips.pt

Summary: Static and dynamic calibration of industrial devices is a key factor regarding the process performance, in terms of quality and reliability, and obviously in the return on investment and companies' profits. The importance of the calibration is even more important for continuous industrial processes where online condition-based maintenance enables to monitor and spot upcoming equipment failure and triggers maintenance within a long enough time before failure. In this paper a particular attention is dedicated to static and dynamic calibration of pneumatic pressure devices, such as, industrial transmitters that are used in a large number of industrial instrumentation applications to measure different physical quantities, not only for pressure measurements, but also for indirect measurements such as flow rates of liquids and gases. The paper includes simulation and experimental results associated with static dynamic calibration of pneumatic pressure sensors and instruments.

Keywords: Pressure sensors, Industrial instrumentation, Calibration, Pressure regulators.

1. Introduction

Regarding dynamic pressure calibration techniques, it is important to underline those sensors are typically calibrated by varying the input signal amplitudes, rather that its frequency. A challenge of this calibration techniques is to cover the dynamic range of the sensing pressure devices according their working principles and applications. Regarding aperiodic calibration techniques, there exist two main techniques, one known as step input and other known as impulse input [1]. In the first case, the calibration is based on the response of the sensing device to a quick rise in the applied pressure and in the second case a quick rise and fall input pressure signals are used. Regarding application fields, there are several areas where dynamic measurements and calibrations are an important issue [2], such as: hydraulic piping and pumps, medical cardiac probes, control of medical balloon manufacturing, angioplasty catheters, gas turbines, intake and exhaust flow engines, engines combustion chambers, wind tunnels, specific aeronautic instrumentation, synchronized hydraulic and pneumatic systems and explosions' detection, among others. The response time of a pressure measuring system with a connecting tube, that is widely used in several instrumentation devices, must also be analyzed since the dynamic characteristics of connecting tubes, namely their lengths and diameters, can affect, substantially, pressure measurement accuracy [3]. This paper is organized as follows: section is the introduction; section two includes the hardware and software description of the proposed static and dynamic calibration system; section three includes experimental results and their discussion, and the last part, section four, is dedicated to conclusions.

2. System Description

This section includes the description of the main characteristics of the HW and SW of the proposed static and dynamic calibration system and flowchart of the implemented calibration procedure.

2.1. Hardware

The block diagram of the electro-pneumatic pressure regulator (EPPR) [4] used to generate the static and dynamic pressure signals, used for calibration purposes, includes, mainly: a pneumatic pressure transducer (PT), a miniature electro-valve (VENT), used for speed up pneumatic air discharge and for zero calibration purposes, that means offset calibration, a miniature proportional valve (MPV) and some elementary conditioning circuits, namely, a comparator and a voltage follower. Fig. 1 represents the block diagram of the EPPR. The setpoint signal, used to define the pressure applied to the DSUT, is generated by multifunction data acquisition board with 12-bit resolution; a maximum sample rate of 50 kS/s and output DAC voltage range varying between 0 and 5 V.

2.2. Software

The software of the proposed system includes several routines used for: configuration of the calibration signal; data processing for evaluation of static and dynamic calibration parameters [5]; storage of calibration data and generation of calibration reports. As an example, Fig. 2 represents the front

panel of the LabVIEW program that was developed to configure parameters of the pressure signal used for calibration purposes. The main configuration parameters, visible in the front panel of the virtual instrument (VI), include: the definition of waveform settings, namely the frequency, amplitude and offset of the control voltage signal that corresponds to the setpoint of the pneumatic loop represented in Fig. 1; the definition of the main characteristics of the pressure calibration pattern, that include the number of bursts, the number of pulses per burst and inter-burst pause duration, and a burst modulation parameter of the multiples patterns included in the calibration pressure signal. In the example, represented in Fig. 2, the calibration pressure signal includes 4 burst patters; a number of 9 pressure pulses per burst; an inter-burst pauses equal to 3 s; a sinusoidal pattern waveform, with frequency and amplitude equal to 1 Hz and 1 V, respectively, and an offset value equal to 0.25 V.

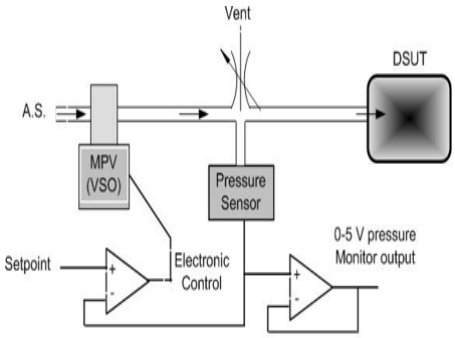

Fig. 1. Block diagram of the electro-pneumatic pressure regulator with internal vent (MPV- miniature proportional valve; DSUT- device system under test).

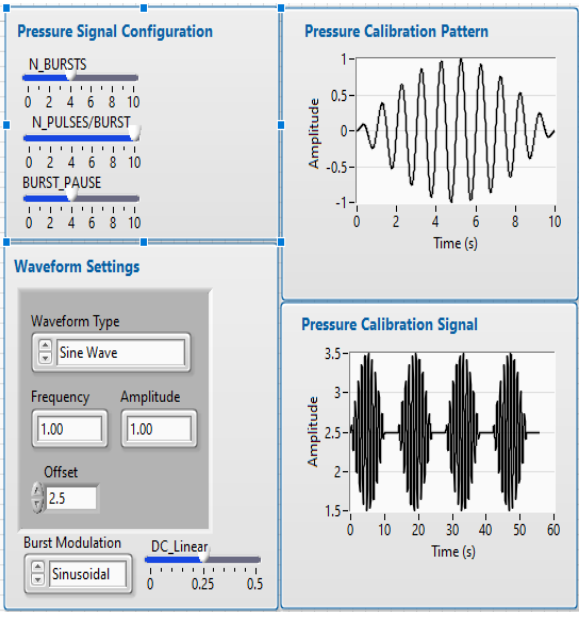

Fig. 2. Calibration pressure signal associated with a burst suction signal characterized by: 4 burst patterns; 9 pressure pulses per burst; inter-burst pauses equal to 3 s and a sinusoidal pattern waveform.

Another example, considering a more realistic situation, is represented in Fig. 3 where the calibration pressure signal includes 8 burst patters; a number of 4 pressure pulses per burst; an inter-burst pauses equal to 8 s; a triangular pattern waveform and with the same values of frequency, amplitude and offset, that were previously considered. In this case, the time constant for increasing the pressure is much higher than the time constant for pressure discharge.

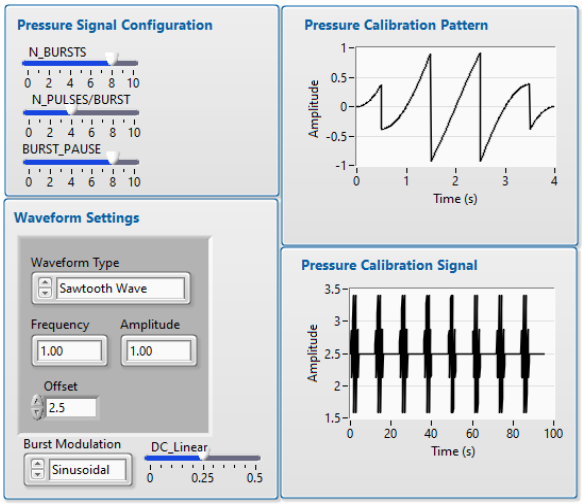

Fig. 3. Calibration pressure signal associated with a burst suction signal characterized by: 8 burst patterns; 4 pressure pulses per burst; inter-burst pauses equal to 8 s and a triangular pattern waveform.

2.3. Calibration

Whenever dynamic calibration of pressure devices is essential, it is important to underline that the pressure device to be calibrated includes not only the sensing element, for examples a piezoelectric or piezoresistive element, but also the connecting devices, such as tubing and others pneumatic interconnections, and the pneumatic fluid, itself. The dynamic response is affected not only by frequency variations bout also by amplitude variations. Thus, the dynamic calibration of pressure sensors is typically performed by varying, not only the frequency, but also the amplitude of the pneumatic signals. Fig. 4 represents the flowchart of the calibration procedure that includes the evaluation of the static calibration coefficients (SCC), on the left side of the figure, and the evaluation of the dynamic calibration coefficients (DCC), on the right side of the same figure.

3. Results

Regarding static calibration test results, Fig. 5 represents the results that were obtained when the input control voltage of the EPPR varies between its minimum and maximum values, 0 V and 5 V, respectively. As it is clearly visible from Fig. 4, the EPPR presents high linearity and its sensitivity is about

1 p.s.i. per Volt, which agrees with the datasheet specifications of the device [4].

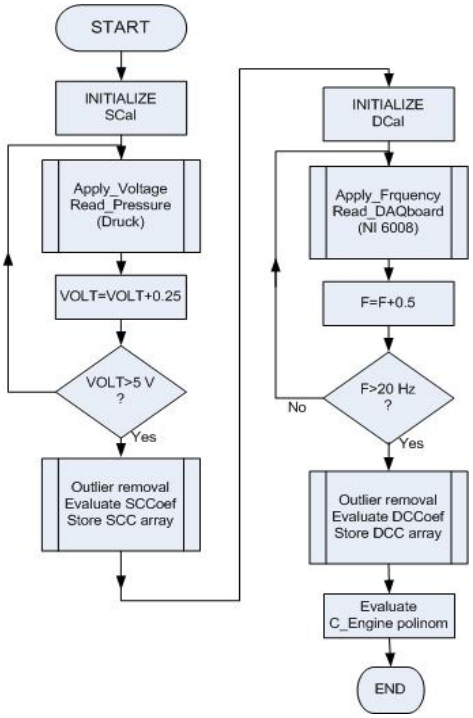

Fig. 4. Calibration flowchart (SCC- static calibration coefficients, DCC- dynamic calibration coefficients).

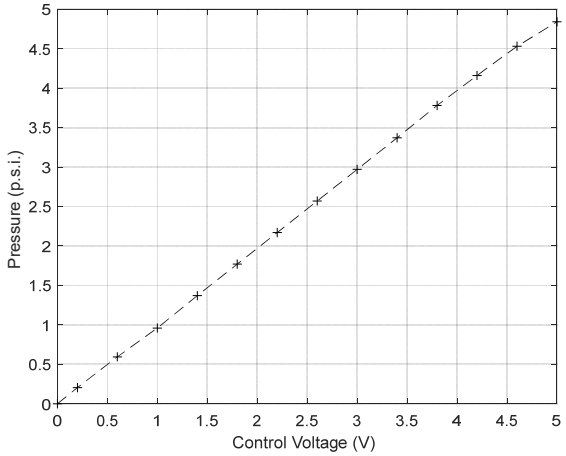

Fig. 5. Static calibration test results of the EPPR.

Fig. 6 represents the relative error of the output pressure amplitude taking as reference its theoretical value. From the results it is possible to conclude that, after offset and gain compensation of the static calibration test results, the absolute value of the relative error is always lower than 0.3 %, being the correlation coefficient between measured and theoretical values equal to 0.9828, and the offset error value lower than 0.0051 p.s.i.. These error values are low enough to perform the laboratory calibration of the majority of the industrial pressure instrumentation that typically presents an overall measurement error higher that 1 %. Additional tests were performed with time-variable pressure signals thar are required for dynamic calibration purposes. Some of these tests were performed with sinusoidal control voltage signals and it was verified, as expected, that the frequency response has a low-pass filter behavior. Fig. 7 represents experimental test results for a set of sinusoidal signals with offset and amplitude values equal to 2.5 V and 1 V, respectively, and frequencies equal to {0.1; 0.2; 0.5; 1.0; 2.0; 5.0; 10.0; 20.0; 50.0} Hz. Using the polyfit function of MATLAB, it was obtained the following filter characteristics: a unitary static gain and a cutoff frequency (fc) approximately equal to 7.2 Hz. As previously referred, it is important to underline that the value of the cutoff frequency depends significantly on the characteristics of the pneumatic system, connected to the output of the EPPR, namely, the pneumatic tubes' lengths and diameters, together with the limitation imposed by air compressibility and the dynamic characteristics of the EPPR.

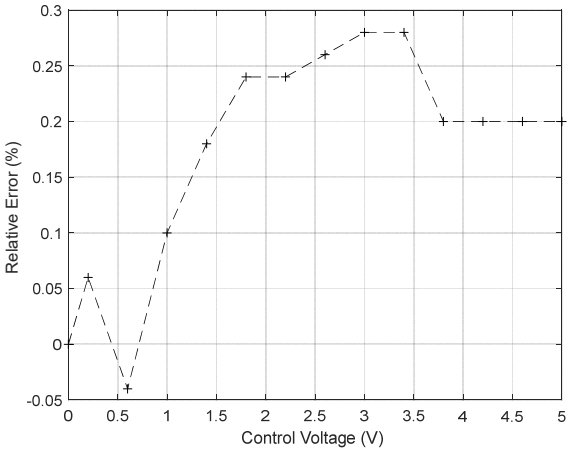

Fig. 6. Relative error between measured and theoretical.

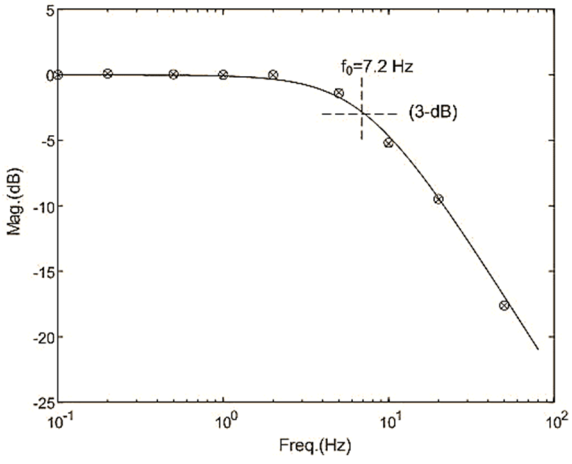

Fig. 7. Bode diagram of the electro pneumatic based system (circle symbol- experimental data, continuous line- LMS curve fitting of the experimental data).

Finally, regarding time domain characterization, Fig. 8 represents the dynamic calibration results that were obtained with three square pressure control signals with a common frequency equal to 5 Hz and

amplitudes equal to 0.25, 0.5 and 1 V. As it is clearly visible, the maximum relative errors increase with the amplitude of the signals being its maximum absolute value lower than 1.2 % for the first two smaller amplitudes and about 8 % for the higher square wave amplitude. The relative errors are referenced to the full-scale range of the EPPR, that is equal to 5 p.s.i., and the theoretical sensitivity of the pressure regulator, used for testing purposes, which is equal to 1 p.s.i./V.

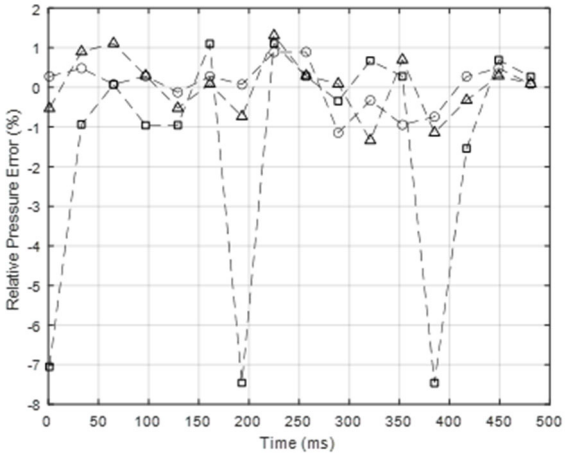

Fig. 8. Dynamic calibration results for a set of three-square voltage control signals with a frequency equal to 5 Hz and three different amplitude values (o- 0.25 V and Δ- 0.5 V and □- 1 V).

4. Conclusions

This paper presents a low-cost and flexible electro pneumatic based system that can be used for static and dynamic calibration of pneumatic pressure sensing devices. Regarding flexibility capabilities, the proposed system enables that different parameter, such as, amplitude, frequency, waveform, number of pulses per burst, burst rate, and amplitude burst modulation of the generated pressure signals be adjusted in real time, according to users' needs and application fields of the devices under calibration, namely according the application field of industrial measurement pressure applications. The main advantages of the proposed static and calibration system include: its low-cost implementation with COTS components; flexible configuration; self-test capabilities and an acceptable performance for the large majority of industrial pressure instrumentation devices.

References

[1]. L. M. Léodido, C. Sarraf, J. Damion, Caractéristiques Dynamiques des Capteurs de Pression en Milieu Hydraulique, in *Proceedings of the International Metrology Congress*, Paris, France, 22-25 June 2009.

[2]. A. C. G. C. Diniz, et al., Dynamic Calibration Methods for Pressure Sensors and Development of Standard Devices for Dynamic Pressure, in *Proceedings of the XVIII IMEKO World Congress – Metrology for a Sustainable Development*, 17-22 September, 2006, Rio de Janeiro, Brazil.

[3]. I. Bajsic, J. Kutin, T. Zagar, The response time of a pressure special issue intelligent sensing and decision-making, in Advanced Manufacturing, Instrumentation Science and Technology, Vol. 35, *Taylor and Francis*, 2007, pp. 399-409.

[4]. Miniature Electronic Pressure Controller, Part Number: 990-005103-005, https://www.parker.com/content/dam/Parker-com/Literature/Precision-Fluidics/Electronic-Pressure-Controllers/OEM-Data-Sheet.pdf

[5]. J. P. Damion, Moyens d'Étalonnage Dynamique des Capteurs de Pression, *Bulletin du Bureau National de Métrologie*, Vol. 8, Issue 30, 1977.

(062)

APHRODITE: Design and Preliminary Tests of an Autonomous and Reusable Photo-sensing Device for Immunological Test aboard the International Space Station

L. Nardi[1], N. Maipan Davis[1], S. Sansolini[1], T. B. De Albuquerque[1], M. Laarraj[1], D. Caputo[2], G. de Cesare[2], S. R. Shariati Pour[3], M. Zangheri[3], D. Calabria[3], M. Guardigli[3], M. Balsamo[4], E. Carrubba[4], F. Carubia[4], M. Ceccarelli[4], M. Ghiozzi[4], L. Popova[4], A. Tenaglia[4], M. Crisconio[5], A. Donati[4], A. Nascetti[1] and M. Mirasoli[3]

[1] School of Aerospace Engineering, Sapienza University of Rome, Via Salaria 851, I-00138, Rome, Italy
[2] Department of Information Engineering, Electronics and Telecommunications, Sapienza University of Rome, Via Eudossiana 18, I-00184, Rome, Italy
[3] Department of Chemistry "Giacomo Ciamician", Alma Mater Studiorum – University of Bologna, Via Selmi 2, I-40126, Bologna, Italy
[4] Kayser Italy s.r.l., Via di Popogna 501, I-57128, Livorno, Italy
[5]ASI, Italian Space Agency, Via del Politecnico, 00133 Rome, Italy
Tel.: + 39 3924573881
E-mail: lorenzo.nardi@uniroma1.it

Summary: Preliminary results of the design and manufacturing of APHRODITE, a compact and versatile device for carrying out analyses of biological fluids during space missions that will be used as a technological demonstrator on board the International Space Station (ISS) for the quantitative determination of salivary biomarkers indicators of alterations of functionality of the immune system. The paper addresses the design of the main subsystems of the analytical device and the preliminary results obtained during the first implementations of the device subsystems and testing measurements. In particular, the system design and the experiment data output of the lab-on-chip photosensors and of the front-end readout electronics are reported in detail.

Keywords: Lab-on-chip, Chemiluminescence, Hydrogenated amorphous silicon photosensors, Biosensor, International space station.

1. Introduction

The APHRODITE analytical device, developed collaboratively by the School of Aerospace Engineering (SIA), Sapienza University of Rome, the University of Bologna, and Kayser Italia, funded by ASI, aims to design and manufacture a technology demonstrator for salivary biomarker analysis on the International Space Station (ISS). The system employs a lab-on-chip (LoC) with thin-film sensors for dual-analyte chemiluminescence immunoassay. Long-duration space travel necessitates health protection and prevention methods due to microgravity-induced health issues like muscle atrophy, metabolic changes, and increased cancer risk [1]. Traditional space activity has been within low orbit, but future missions demand *in situ* diagnostics and prevention methods due to non-viable sample return. In response, diagnostic tools usable during space missions are a new aerospace priority. The LoC technology, with its microfluidic approach, is a fitting design choice because it enhances analytical efficiency, reduces sample size, response time, and cost, and increases automation.

Such devices have already been used on Earth in numerous biomedical applications and have recently been validated in orbit [2, 3].

In this paper, we report the system design and preliminary results of an innovative platform conceived to enhance space exploration by permitting the detection of numerous target analytes of interest in microgravity.

2. System Overview

APHRODITE is a compact biosensor (Fig. 1) designed for ISS deployment to analyze cortisol and dehydroepiandrosterone (DHEA) levels in astronaut saliva. The biosensor incorporates microfluidics, functionalized microbeads (MBs), and a-Si:H photodiodes for detection, a detection method already validated in microgravity [4,5].

Its components include a disposable cartridge, detection subsystem, fluidic dispensing subsystem, control electronics, and mechanical housing. The biosensor's design emphasizes space application requirements such as compactness, weight reduction, and radiation resistance. Its subsystems include a disposable cartridge with reagent reservoirs, a detection subsystem with a microfluidic chip and photosensor array, a fluidic dispensing subsystem, control electronics, and mechanical housing.

The immunological analysis protocol employs a luminol/H_2O_2 reaction catalyzed by Horseradish

Peroxidase for detecting cortisol and DHEA. The analyte-specific capture antibodies are immobilized on MBs [6], which are then loaded in the chip channel, kept in position using permanent magnets, and then eliminated by removing the magnetic field and washing, leaving the system clean and ready for the next analysis, unlike in other LoC systems [7].

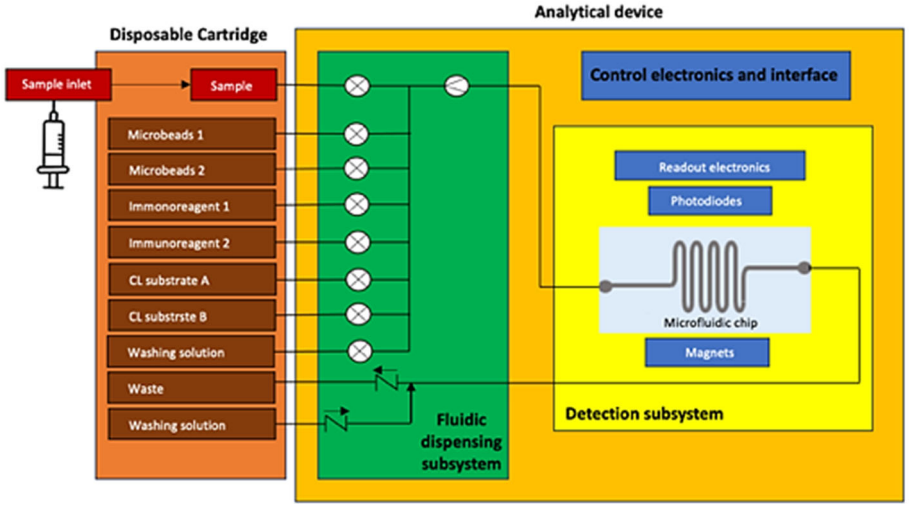

Fig. 1. APHRODITE block diagram.

3. Results and Discussion

Initial experiments verified the system's concept were carried out by the University of Bologna to select the most suitable buffer, on MBs stability, functionalization protocol, and the cross-reactivity between DHEA and cortisol.

In addition, an integration test demonstrated APHRODITE's performance with a fluidic dispensing subsystem and disposable cartridge prototype. The chemiluminescence (CL) signal was successfully detected (Fig. 2), with attention to microbead distribution during analysis. This experiment included the detection of DHEA without saliva sample and demonstrated the successful operation of the core subsystems, including microfluidic channels, valves, and cartridge components. The typical behavior of CL signal curve after stop flow condition was observed in the data.

4. Conclusions

The APHRODITE biosensor's design was validated through preliminary tests and subsystem integration. Future steps involve deploying a ground model for measurements with actual saliva samples and qualifying the device for ISS flight. Once proven, APHRODITE could contribute to studying space's impact on human health and be adapted for other biomarker analyses.

Acknowledgments

The authors acknowledge the Italian Space Agency (ASI) that funded the system development and future flight to the ISS in the frame of the program «Ricerche e dimostrazioni tecnologiche sulla Stazione Spaziale Internazionale – VUS3: ISS4EXPLORATION».

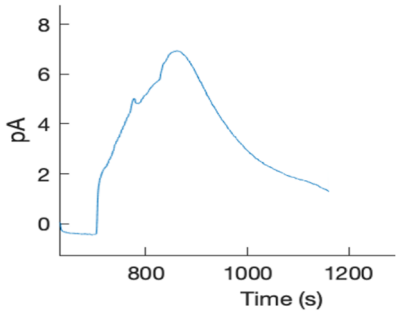

Fig. 2. DHEA run output signal.

References

[1]. Afshinnekoo, E., Scott, R. T., MacKay, M. J., Pariset, E., et al., Fundamental Biological Features of Spaceflight: Advancing the Field to Enable Deep-Space Exploration, *Cell*, Vol. 183, 2020, pp. 1162–1184.

[2]. Burklund, A., Tadimety, A., Nie, Y., Hao, N., Zhang, J.X.J., Advances in diagnostic microfluidics, in: Advances in Clinical Chemistry, 2020, *Elsevier*, pp. 1–72.

[3]. Calabria, D., Trozzi, I., Lazzarini, E., Pace, A., et al., AstroBio-CubeSat: A lab-in-space for chemiluminescence-based astrobiology experiments. *Biosensors and Bioelectronics,* 2023, Vol. 226, 115110.

[4]. Zangheri, M., Mirasoli, M., Guardigli, M., Di Nardo, F., et al., Chemiluminescence-based biosensor for

monitoring astronauts' health status during space missions: Results from the International Space Station. *Biosensors and Bioelectronics*, 2019, Vol. 129, pp. 260–268.

[5]. Fereja, T. H., Hymete, A., Gunasekaran, T., A Recent Review on Chemiluminescence Reaction, Principle and Application on Pharmaceutical Analysis, *ISRN Spectroscopy*, 2013, pp. 1–12.

[6]. Khizar, S., Ben Halima, H., Ahmad, N.M., Zine, N., Errachid, A., Elaissari, A., Magnetic nanoparticles in microfluidic and sensing: From transport to detection. *Electrophoresis*, Vol. 41, 2020, pp. 1206–1224.

[7]. Nascetti, A., Mirasoli, M., Marchegiani, E., Zangheri, M., et al., Integrated chemiluminescence-based lab-on-chip for detection of life markers in extraterrestrial environments, *Biosensors and Bioelectronics*, 2019, Vol. 123, pp. 195–203.

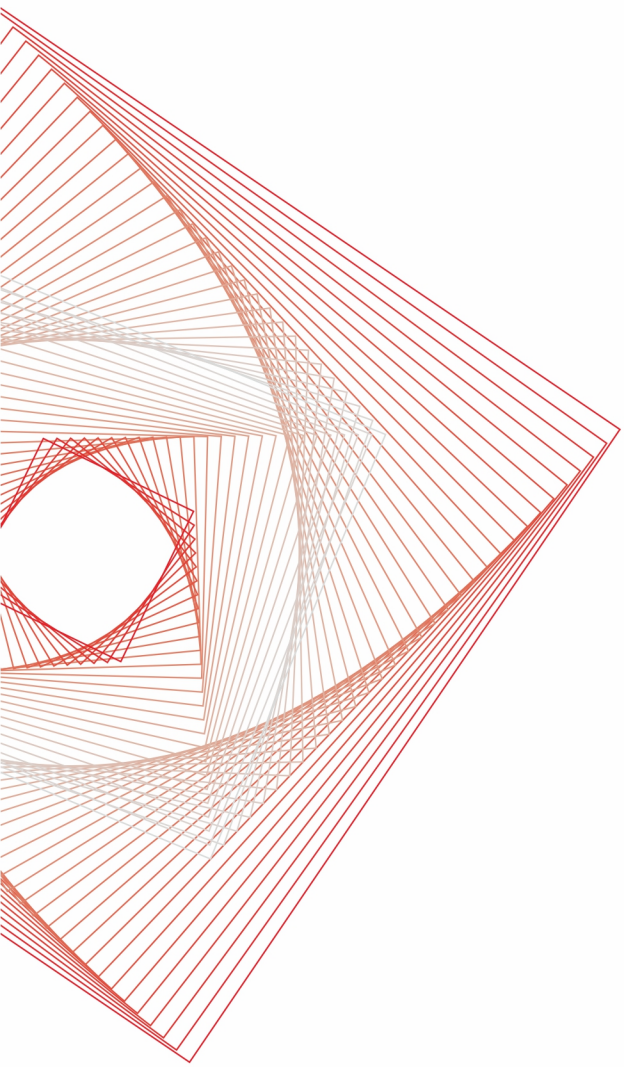

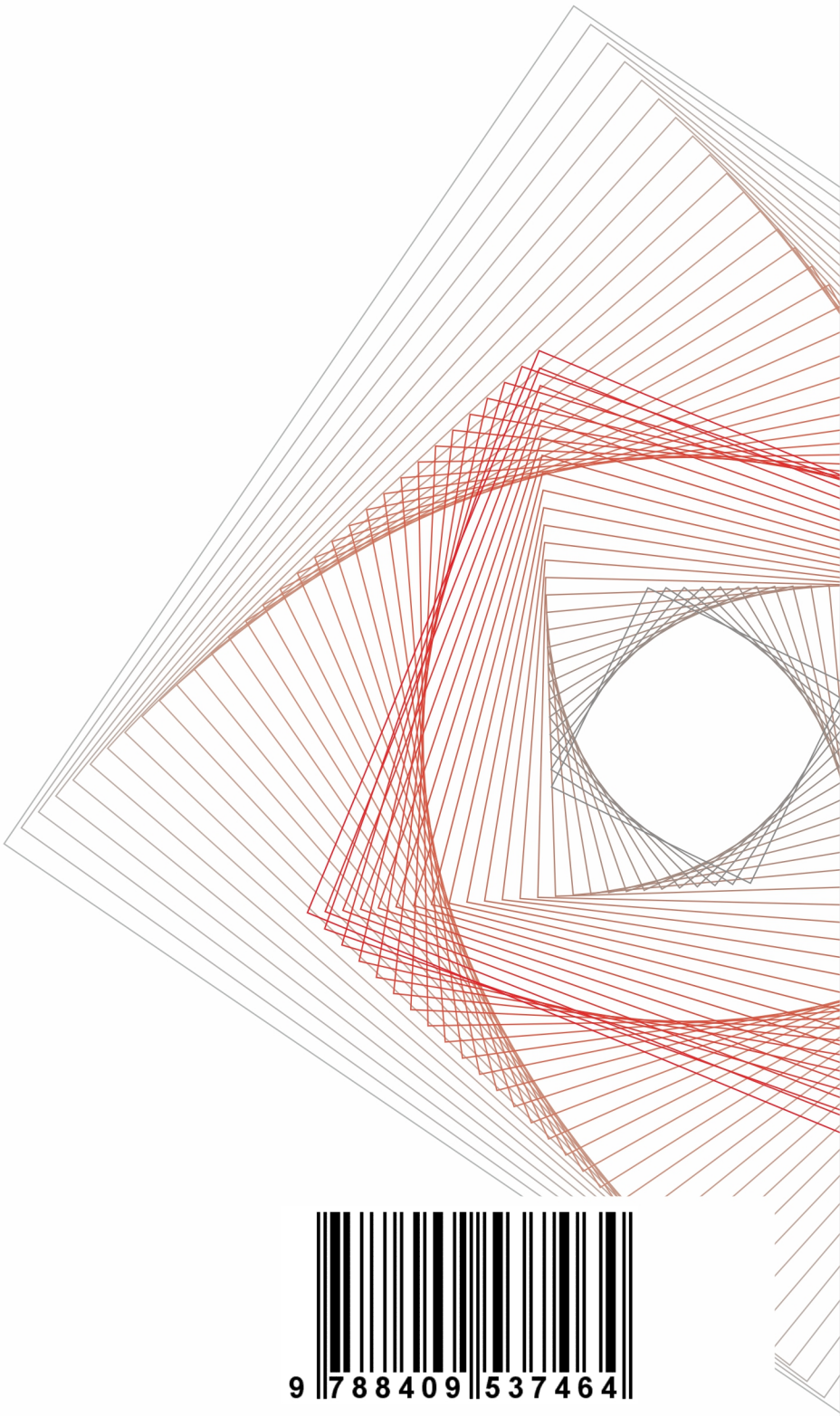

9 788409 537464